

**Some pages of this thesis may have been removed for copyright restrictions.**

If you have discovered material in Aston Research Explorer which is unlawful e.g. breaches

copyright, (either yours or that of a third party) or any other law, including but not limited to those relating to patent, trademark, confidentiality, data protection, obscenity, defamation, libel, then please read our takedown policy and contact the service immediately ([openaccess@aston.ac.uk](mailto:openaccess@aston.ac.uk)).

# **Design and Algorithm-based optimisation of Axial ORC turbine and transient cycles incorporating novel machine Learning tools.**

**Yohan Cyrus Engineer**  
**Doctor of Philosophy**

**Aston University**  
**March 2022**

©Yohan Cyrus Engineer, 2022

Yohan Engineer asserts his moral right to be identified as the author of this thesis.

This copy of the thesis has been supplied on condition that anyone who consults it is understood to recognise that its copyright belongs to its author and that no quotation from the thesis and no information derived from it may be published without appropriate permission or acknowledgement.

# **Design and Algorithm-based optimisation of Axial ORC turbine and transient cycles incorporating novel machine Learning tools.**

Yohan Engineer

Doctor of Philosophy

2022

## **Summary**

The flue gas stacks of industrial steam boilers can be considered an untapped waste heat source, which is characterised as highly intermittent. Although Organic Rankine Cycles pose strong potential to reuse such low-grade heat, the component and system levels analysis of ORCs to efficiently utilise these highly intermittent heat sources in a techno-economic fashion is still an unanswered research question. Such a holistic approach ultimately expedites the commercial adoption of ORCs to utilise a broader range of waste heat sources achieving the highest possible techno-economic benefits. To answer this research question, emphasising scale ORCs that employ axial flow turbines owing to their scalability and superior isentropic efficiency, this thesis undertakes turbine and cycle configuration optimisation by integrating the Craig and Cox loss model to simulate a small-scale axial flow ORC turbine. The transient waste heat of an actual industrial steam boiler stack was employed as a heat source to investigate ten novel cycle configurations. The optimisation was undertaken using parametric, metaheuristic (nature-inspired) and mathematics-based optimisers. Artificial Neural Networks (ANNs) and genetic algorithms (GAs)-based on the loss model led to an optimised turbine configuration that improved turbine total-to-static efficiency and cycle efficiency by 5.2% and 0.24%, respectively. The recuperative cycle proved the optimal thermodynamic configuration, with a 26.5% increase in mean power generation. Furthermore, a multi-objective analysis revealed the recuperative cycle integrated with an air preheater as the optimum thermo-economic configuration, with a 48.9% improvement in the combined overall value of the multiple objectives, including the Specific Investment Cost and mean power, achieving the final payback within 1.72 years. The ideal configuration was observed as a strong function of the Levelized cost of fuel and electricity prices. Application of a mathematical technique based on the non-linear programming by quadratic Lagrangian algorithm was validated for single- and multi-objective cycle configuration optimisations, providing results comparable to the well-established metaheuristic-based genetic algorithm, with a computational efficiency of greater than one order of magnitude. The overall approach of the direct loss model, artificial neural network- and genetic algorithm-based turbine optimisation, parametric cycle pre-optimisation, mathematical technique-based component optimisation and payback evaluation can be considered a blueprint for the future evaluation and design of organic Rankine cycles utilising transient waste heat sources

# Acknowledgements

First, I am indebted and thankful to my supervisor Dr Ahmed Rezk, whose perseverance, attention to detail, vast academic experience and kindness have been invaluable to me. It is only due to his timely guidance and inspirational enthusiasm that I have been able to complete my thesis.

I would also like to warmly thank Dr Philip Davies for providing direction during the formative years of my thesis and introducing me to the scientific approach. Dr Abul Hossain has provided constant feedback for the structure of my thesis, based on his immense scientific experience, for which I am grateful.

I wish to express my warm and sincere thanks to my employers Industrial Boilers and IB Turbo, for supporting me financially, allowing time to undertake this thesis and providing unrestricted access to design and operational data. Mr. P.P. Goel (Technical Director at IB Turbo) has provided invaluable guidance on turbine design techniques.

Lastly, my family has been a pillar of constant support. My wife Sharleen has provided me with emotional support and assistance with the thesis presentation. My parents, uncle Rohinton and brother Zaraan have motivated me to complete my thesis while producing quality work for which I owe them my gratitude.

# Publications

Y. Engineer, A. Rezk, and A. K. Hossain, "Energy analysis and optimization of a small-scale axial flow turbine for Organic Rankine Cycle application," *International Journal of Thermofluids*, vol. 12, p. 100119, 2021.

# Table of Contents

Abbreviations.....	9
Nomenclature.....	10
List of Figures.....	13
List of Tables.....	16
<b>1 Chapter 1 Introduction.....</b>	<b>18</b>
<b>1.1 Importance of energy .....</b>	<b>18</b>
<b>1.2 Historic global energy scenario.....</b>	<b>18</b>
<b>1.3 Current energy trends .....</b>	<b>19</b>
<b>1.4 Future energy trends, renewables and ORC.....</b>	<b>20</b>
<b>1.5 History of ORC.....</b>	<b>21</b>
<b>1.6 Introduction to the ORC cycle.....</b>	<b>22</b>
<b>2 Chapter 2 Literature Review .....</b>	<b>24</b>
<b>2.1 Introduction.....</b>	<b>24</b>
<b>2.2 Equation of State (EoS).....</b>	<b>26</b>
<b>2.3 Comparison between steam and ORC cycles .....</b>	<b>27</b>
2.3.1 Classification based on heat source temperature .....	27
2.3.2 Comparison between steam and organic Rankine expanders.....	29
<b>2.4 Current ORC applications.....</b>	<b>30</b>
2.4.1 Geothermal waste heat recovery .....	30
2.4.2 Biomass .....	31
2.4.3 Solar thermal energy .....	32
2.4.4 Waste heat recovery .....	33
<b>2.5 Working fluids .....</b>	<b>37</b>
2.5.1 Thermodynamic factors.....	38
2.5.2 Safety and environmental factors .....	40
2.5.3 Selection of working fluid based on heat source and sink .....	43
<b>2.6 Classification of ORC expanders .....</b>	<b>45</b>
2.6.1 Volumetric expanders.....	46
2.6.2 Velocity-based expanders (turbines).....	49
<b>2.7 Non-dimensional parameters .....</b>	<b>54</b>
2.7.1 Volumetric flow ratio.....	54
2.7.2 Size parameter .....	54
2.7.3 Reynolds number .....	54
2.7.4 Velocity ratio.....	55
2.7.5 Specific speed.....	56
2.7.6 Specific diameter.....	57
2.7.7 Pressure ratio.....	57
2.7.8 Stage loading coefficient .....	57
2.7.9 Flow coefficient.....	58
2.7.10 Degree of reaction.....	58
2.7.11 Zweifel loading coefficient .....	60
2.7.12 Solidity.....	60
2.7.13 Aspect ratio.....	60
2.7.14 Mach number .....	61

<b>2.8</b>	<b>Turbine efficiency</b>	<b>62</b>
2.8.1	Design point loss models	62
2.8.2	Off-design point loss models	63
<b>2.9</b>	<b>Cycle configuration based on operating conditions</b>	<b>65</b>
<b>2.10</b>	<b>Economics</b>	<b>66</b>
<b>2.11</b>	<b>Machine learning for turbine design</b>	<b>67</b>
<b>2.12</b>	<b>Optimisation</b>	<b>70</b>
2.12.1	Mathematical techniques	71
2.12.2	Metaheuristic optimisers	72
2.12.3	Multi-objective optimisation	73
<b>2.13</b>	<b>Aim and objectives of the study</b>	<b>74</b>
<b>2.14</b>	<b>Research gap and contribution to the field</b>	<b>74</b>
<b>2.15</b>	<b>General outline and structure of thesis</b>	<b>76</b>
<b>2.16</b>	<b>Summary of literature review</b>	<b>77</b>
<b>3</b>	<b>Chapter 3 Methodology</b>	<b>78</b>
<b>3.1</b>	<b>Introduction</b>	<b>78</b>
<b>3.2</b>	<b>Loss models</b>	<b>79</b>
3.2.1	Soderberg loss model	79
3.2.2	Craig and Cox loss model	84
3.2.3	Off-design loss model	90
<b>3.3</b>	<b>Machine learning</b>	<b>91</b>
<b>3.4</b>	<b>Optimisation approach</b>	<b>91</b>
3.4.1	Mathematical-technique-based optimiser	92
3.4.2	Metaheuristic optimisers	93
<b>3.5</b>	<b>Conclusion</b>	<b>93</b>
<b>4</b>	<b>Chapter 4 Artificial Neural Network-based Turbine Optimisation</b>	<b>95</b>
<b>4.1</b>	<b>Introduction</b>	<b>95</b>
<b>4.2</b>	<b>Working fluids</b>	<b>96</b>
<b>4.3</b>	<b>Loss models</b>	<b>97</b>
4.3.1	Soderberg Loss model	97
4.3.2	Craig and Cox loss model	97
4.3.3	Cycle thermodynamic modelling	98
4.3.4	Neural network and optimisation approach	99
<b>4.4</b>	<b>Assumptions</b>	<b>102</b>
<b>4.5</b>	<b>Validation</b>	<b>102</b>
<b>4.6</b>	<b>Results and discussion</b>	<b>105</b>
4.6.1	Effect of turbine inlet temperature	105
4.6.2	Effect of pressure ratio on the turbine's efficiency	110
4.6.3	Turbine optimisation	114
<b>4.7</b>	<b>Conclusion</b>	<b>117</b>
<b>5</b>	<b>Chapter 5 Single Objective Thermodynamic Cycle Optimisation</b>	<b>119</b>
<b>5.1</b>	<b>Introduction</b>	<b>119</b>
5.1.1	Heat source	120
5.1.2	Assumptions	123
<b>5.2</b>	<b>Methods and materials</b>	<b>124</b>
5.2.1	Cycle architecture	124

5.2.2	Thermodynamics.....	130
5.2.3	NLPQL optimisation.....	134
5.2.4	Materials and components.....	134
5.2.5	Optimisation.....	144
<b>5.3</b>	<b>Validation.....</b>	<b>146</b>
<b>5.4</b>	<b>Results and discussion.....</b>	<b>147</b>
5.4.1	Parametric cycle evaluation.....	147
5.4.2	Optimisation study results.....	158
<b>5.5</b>	<b>Conclusion.....</b>	<b>163</b>
<b>6</b>	<b>Chapter 6 Thermo-Economic Optimisation.....</b>	<b>165</b>
<b>6.1</b>	<b>Introduction.....</b>	<b>165</b>
<b>6.2</b>	<b>Methodology.....</b>	<b>166</b>
6.2.1	System description.....	166
6.2.2	Problem definition.....	167
6.2.3	Multi-objective optimisation approach.....	167
6.2.4	Specific investment cost.....	168
6.2.5	Payback.....	170
6.2.6	Optimisation.....	171
6.2.7	Assumptions.....	171
<b>6.3</b>	<b>Results and discussion.....</b>	<b>172</b>
6.3.1	Individual objective trade-off.....	173
6.3.2	Heat exchanger sizing.....	176
6.3.3	Thermal energy recovery.....	177
6.3.4	Pump sizing.....	180
6.3.5	Payback analysis.....	181
6.3.6	Optimiser comparison.....	182
<b>6.4</b>	<b>Conclusion.....</b>	<b>183</b>
<b>7</b>	<b>Chapter 7 Conclusions and Prospects.....</b>	<b>184</b>
<b>7.1</b>	<b>Introduction.....</b>	<b>184</b>
<b>7.2</b>	<b>Conclusions.....</b>	<b>184</b>
<b>7.3</b>	<b>Prospects.....</b>	<b>187</b>
<b>8</b>	<b>References.....</b>	<b>189</b>
	<b>APPENDIX 1.....</b>	<b>209</b>
	<b>Polynomial Equations of the Craig and Cox Loss Model.....</b>	<b>209</b>
	<b>APPENDIX 2.....</b>	<b>216</b>
	<b>Engineering Equation Solver (EES) Code for the Craig and Cox Loss Model.....</b>	<b>216</b>
	<b>APPENDIX 3.....</b>	<b>229</b>
	<b>Engineering Equation Solver (EES) Code for the Soderberg loss model.....</b>	<b>229</b>

# Abbreviations

AI	Artificial Intelligence
ANN	Artificial Neural Network
APH	Air Preheater
CEPCI	Chemical Engineering Plant Cost Index
CFC	Chlorofluorocarbon
CFD	Computational Fluid Dynamics
CHP	Combined Heat and Power
COP	Coefficient Of Performance
EES	Engineering Equation Solver
EPA	Environmental Protection Agency
EoS	Equation of State
FC	Fluorocarbon
GA	Genetic Algorithm
GWP	Global Warming Potential
HCC	Hydrochlorocarbon
HCHC	Hydrochlorofluorocarbon
HCFO	Hydrochlorofluoroolefin
HFE	Hydrofluoroether
HFO	Hydrofluoroolefin
IC	Internal Combustion
KKT	Karush Kuhn Tucker
LAR	Least Absolute Residual
LCOE	Levelised Cost of Electricity
LCOF	Levelised Cost of Fuel
LHTES	Latent Heat Thermal Energy Storage
LMTD	Logarithmic Mean Temperature Difference
MFR	Mass Flow Rate
MOGA	Multi-Objective Genetic Algorithm
MOO	Multi-Objective Optimisation
NLPQL	Non-Linear Programming by Quadratic Lagrangian
NPSH	Net Pressure Suction Head
NSGA	Non-dominated Sorting Genetic Algorithm
ODP	Ozone Depletion Potential
OMTS	Octamethyltrisiloxane
ORC	Organic Rankine Cycle
OTEC	Ocean Thermal Energy Conversion
PCC	Perchlorocarbon
PEL	Permanent Exposure Limits
PFCs	Perfluorocarbons
PR	Pressure Ratio
RDF	Refuse-Derived Fuels
RMSE	Root-Mean-Squared Error
SAFT	Statistical Associating Fluid Theory
SIC	Specific Investment Cost
SNAP	Significant New Alternatives Policy
SP	Size Parameter
SQP	Sequential Quadratic Programming
VFR	Volumetric Flow Ratio
VDI	Verein Deutscher Ingenieure
WHR	Waste Heat Recovery

# Nomenclature

Symbol	Quantity	Unit
$\epsilon H_{recovery}$	Value of thermal energy recovery	(€)
$\epsilon W_T$	Value of electricity generation by the turbine	(€)
$\epsilon W_P$	Value of electricity consumption by the pump	(€)
$A_{HX}$	Heat transfer area of the heat exchangers	(m <sup>2</sup> )
$a_{acentric}, b_{acentric}$	Equation of state acentric factors	(-)
$b_B$	Backbone length	(m)
$C$	Fluid velocity	(m/s)
$C_p$	Specific heat	(J/kg-K)
$CR$	Contraction ratio	(-)
$clearance_{shr}$	Shroud to casing clearance	(m)
$D$	Diameter	(m)
$DoR$	Degree of reaction ( $DoR$ )	(-)
$E_{nb}$	Axial gap between nozzle and blade	(m)
$f_{Dff}$	Darcy friction factor	(N)
$F_L$	Lift parameter	(-)
Factor $\alpha_{Tc}$	Critical temperature equation of state factor	(-)
$G$	Craig and Cox loss coefficient	(-)
$G^*$	Soderberg basic loss coefficient	(-)
$G_1$	Soderberg corrected loss coefficient	(-)
$GCV$	Gross Calorific value	(kJ/kg)
$h$	Specific enthalpy	(kJ/kg)
$ht_b$	Height	(m)
$htr$	Heat transfer resistance of fluid	(K/W)
$K$	Orifice pressure drop coefficient	(-)
$ks$	Relative surface roughness of the blade	( $\mu$ m)
$KW e_{pump}$	Pump power consumption	(kW)
$L$	Length	(m)
$LC_m$	Modified lift coefficient	(-)
lossincr	Trailing edge loss increment	(-)
$M$	Mach number	(-)
$\dot{m}$	Mass flow rate	(kg/sec)
$Mach_{outisen}$	Outlet isentropic Mach number	(-)
$MM$	Molar mass	(g/mol)
$N$	Rotation speed	rpm
$N_{Saspectrat}$	Aspect ratio loss	(-)
$N_{pi}$	Incidence loss	(-)
$N_{pr}$	Reynolds number loss	(-)
$N_{pt}$	Trailing edge thickness loss	(-)
$P$	Pressure	kg/cm <sup>2</sup>
$Pr$	Prandtl number	(-)
$Pwr$	Power output	(kW)
$Q$	Heat	(kJ)
$Q^*2$	Reduced squared quadrupole moment	(-)
$R$	Universal gas constant	(J/K-mol)
$Re$	Reynolds number	(-)
$ReCF$	Soderberg's Reynolds number correction factor	(-)
$S$	Entropy	(J/K-mol)
$s$	Blade pitch	(m)

$spec$	Specific	(-)
$SS$	Speed of sound	(m/s)
$\Delta T_{lm}$	Logarithmic mean temperature difference	(-)
$T$	Temperature	C
$te$	Trailing edge thickness	(m)
$thr$	Throat width	(m)
$thr_{shr}$	Shroud thickness	(m)
$U$	Moving blade velocity	(m/s)
$U_0$	Convective heat transfer coefficient	(W/ms <sup>2</sup> /°K)
$V$	Relative velocity	(m/s)
$\dot{V}$	Specific volume	(m <sup>3</sup> /kg)
$V$	Molar volume	(m <sup>3</sup> /mol)
$V_{molar}$	Velocity ratio	(-)
$VR$	Work done	(J)
$W$	Specific work done	(J/sec)
$\dot{W}$	Annulus loss	(-)
$X_{a1}$	Profile loss	(-)
$X_p$	Secondary loss	(-)
$X_s$	Blade back radius loss	(-)
$\Delta X_{Pse}$	Mach number loss increment	(-)
$\Delta X_{pm}$	Zweifel coefficient	(-)
$Z$		

### Greek Symbols

$\alpha$	Absolute fluid flow angle	(°)
$\beta$	Relative fluid flow angle	(°)
$\beta_M$	Absolute metal angle	(°)
$\varepsilon$	Deflection	(°)
$\eta$	Efficiency	(-)
$\gamma$	Specific heat ratio ( $\gamma$ ),	(-)
$\mu$	Dynamic viscosity ( $\mu$ )	kg/m-s)
$\mu^*2$	Reduced squared dipole moment	(C-m)
$\Phi$	Flow coefficient ( $\Phi$ )	(-)
$\rho$	Density	kg/m <sup>3</sup>
$\psi$	Stage loading coefficient	(-)

## Subscript

<i>a</i>	Axial velocity component
<i>B</i>	Blade
<i>C</i>	Critical
<i>CEPD</i>	Condensate extraction pump fluid discharge
<i>char</i>	Characteristic for BACKONE EoS
<i>det</i>	Determiner
<i>Group1</i>	Group 1 loss
<i>h</i>	Hydraulic
<i>in</i>	Inlet
<i>is</i>	Isentropic
<i>le</i>	Leading edge
<i>LPT</i>	Low pressure turbine
<i>K</i>	Kelvin
<i>k<sub>ap</sub></i>	Pressure drop gain across the orifice
<i>N</i>	Nozzle
<i>out</i>	Exhaust
<i>P</i>	Pump
<i>p</i>	Primary loss
<i>RG</i>	Regenerator discharge
<i>S</i>	Isentropic
<i>s</i>	Secondary loss
<i>spec</i>	Specific
<i>T</i>	Turbine
<i>stg – In</i>	Stage inlet
<i>stg – Out</i>	Stage outlet
<i>W</i>	Radial velocity component
1	Before nozzle
2	Between nozzle and blade
3	After blade

# List of Figures

Figure 1-1: Edison’s Jumbo steam turbine was installed between 1882 and 1885 in the Holborn Viaduct Station in London and in the Pearl Street Generating Station, Manhattan, New York [6].....	19
Figure 1-2: Increase in global fossil fuel consumption from 1800 to 2019 year, measured in terawatt-hours (TWh) [13] .....	20
Figure 1-3: Expected rise of renewable energy in the twentieth-first century [10] .....	21
Figure 1-4: Pictorial view of 145 kW turbine-driven ORC solar pond power plant at Ein Bokek, Dead Sea, Israel, commissioned in 1979 [26].....	22
Figure 1-5: Exemplar of a sub-critical organic Rankine cycle with a superheater (a) T-s Diagram, (b) Components flow diagram [30] .....	23
Figure 2-1: Approach of the literature review .....	25
Figure 2-2: Validation of enthalpy of vaporisation for R1234yf using BACKONE EoS validated by experimental data [57].....	27
Figure 2-3: T-s diagram of steam and commonly used ORC fluids [60] .....	28
Figure 2-4: Classification of thermodynamic waste heat recovery cycles based on heat source and plant size by Liu et al. [61].....	29
Figure 2-5: Existing ORC heat source classification based on total number of installations .	30
Figure 2-6: Binary cycle-based geothermal ORC system [69] .....	31
Figure 2-7: Solar thermal ORC with binary heat transfer loops and latent heat thermal energy storage (LHTES) systems in conjunction with high-grade collectors [79] .....	33
Figure 2-8: Sectoral shares of waste heat distribution by temperature [82].....	34
Figure 2-9: Classification of steam Rankine and organic Rankine cycles for WHR applications based on heat source temperature and power generation [84] .....	34
Figure 2-10: Typical WHR ORC application [84].....	35
Figure 2-11: Classification of existing ORC units utilise waste heat sources by installation capacity. Total installation capacity of WHR ORC is 349.1 mWeI [94] .....	36
Figure 2-12: Wet, isentropic, and dry expansion [44].....	39
Figure 2-13: Comparison of subcritical and supercritical expansion of ORC Fluids [15] .....	40
Figure 2-14: False-colour image showing ozone concentration above the continent of Antarctica on 2 October 2015 [135] .....	41
Figure 2-15: Working principle of a scroll expander [162].....	46
Figure 2-16: Exploded view of a typical twin-screw expander [165] .....	47
Figure 2-17: Working principle of reciprocating piston expander with a double valve reciprocating expander [166].....	48
Figure 2-18: Working of a rotary vane expander [170].....	49
Figure 2-19: (a) Components of the two-stage axial turbine [172] (b) pictorial view of four stage impulse biased axial steam turbine .....	50
Figure 2-20: Construction of a single-stage radial inflow turbine [172] .....	51
Figure 2-21: Craig and Cox correlated the effect of the surface finish with its induced profile losses [181] .....	55
Figure 2-22: Velocity ratio for single stage impulse (Rateau wheels), two-stage impulse (Curtis wheels) and reaction disc axial stages [183] .....	56
Figure 2-23: Max turbine efficiency versus specific speed for radial inflow turbine [158] .....	56
Figure 2-24: Efficiency correlation for expanders based on specific speed and specific diameter [186] .....	57
Figure 2-25: The Smith chart provided the correlation between the load coefficient, flow coefficient and efficiency [187, 189] .....	58
Figure 2-26: Isentropic enthalpy drop for (a) a pure impulse turbine with DoR 0% and (b) a high-reaction turbine with DoR 50%.....	59
Figure 2-27: Correlation of Mach number with profile efficiency [181] .....	61
Figure 2-28: Craig and Cox calculated the positive and negative incidence loss independently [181].....	63
Y. C. Engineer, PhD Thesis, Aston University, 2022	13

Figure 2-29: The primary loss correlation provided by Ainley-Mathieson [209] (a), and Mukhtarov-Krichakin [212] (b) was improved upon by Moustapha et al. [210] (c) .....	64
Figure 2-30: The secondary loss correlation provided by Ainley-Mathieson (a) [209], and Mukhtarov-Krichakin [212] (b) loss was improved upon by Moustapha et al.[210] in (c) .....	65
Figure 2-31: Typical ANN structure .....	68
Figure 2-32: Structure of a simple decision tree .....	68
Figure 2-33: Linear regression on a typical data set .....	69
Figure 2-34: Typical Bayesian network .....	69
Figure 2-35: Directed acyclic graph .....	69
Figure 2-36: Classification of mathematical technique and metaheuristic-based optimisers.	70
Figure 3-1: Variation of basic loss coefficient with increase in deflection angle for various ratios of maximum profile thickness to overall profile length [206] .....	81
Figure 3-2: Velocity triangles of the flow across blades .....	82
Figure 3-3: Blading loss distribution as per Craig & Cox [24] .....	85
Figure 3-4: Impact of blade surface finish and Reynolds number on profile loss ratio observed by Craig and Cox [23] .....	87
Figure 3-5: Lift parameter determined deviation as a function of fluid inlet and outlet angle [23] .....	87
Figure 3-6: The basic profile loss was determined as a function of the modified profile loss, pitch, backbone length and contraction ratio [23] .....	88
Figure 3-7: Annulus wall loss was a function of the profile height and gap between the fixed and moving blades [23] .....	89
Figure 3-8 :Flowchart of cycle-level optimisation using the NLPQL algorithm .....	92
Figure 3-9: The basic structure of the genetic algorithm .....	93
Figure 4-1: (a) Components of a superheated ORC; (b) T-s diagram of superheated ORC for dry fluid R245fa .....	98
Figure 4-2: Architecture of the ANN used .....	99
Figure 4-3: Layout of the optimisation procedure .....	102
Figure 4-4: Pictorial view of the simulated steam turbine operating in a rice mill firm at Karnal, India (permission granted for image) .....	103
Figure 4-5: The influence of turbine inlet temperature on (a) total-to-static efficiency, (b) power, (c) cycle efficiency, (d) relative stage outlet isentropic Mach number, (e) U/C2 ratio and (f) flow coefficient .....	106
Figure 4-6: Converging area of the moving blade section .....	107
Figure 4-7: The influence of turbine inlet temperature on the loss coefficients for all six working fluids .....	109
Figure 4-8: The influence of pressure ratio on: (a) Exhaust temperature; (b) Total-to-static efficiency; (c) Power output; (d) Cycle efficiency .....	111
Figure 4-9: Variation of total loss coefficient with change in pressure ratio .....	112
Figure 4-10: Variation of nozzle primary loss coefficient with change in pressure ratio .....	112
Figure 4-11: Variations in blade primary loss coefficients with change in pressure ratio .....	113
Figure 4-12: Variations in nozzle secondary loss coefficients with change in pressure ratio .....	113
Figure 4-13: Variations in blade secondary loss coefficients with change in pressure ratio .....	113
Figure 4-14: Variations in nozzle outlet isentropic Mach number with change in pressure ratio .....	114
Figure 4-15: Variations in blade outlet isentropic Mach numbers with change in pressure ratio .....	114
Figure 4-16: (a) RMS error after 1000 iterations; (b) ANN training performance .....	115
Figure 5-1: (a) Steam boiler considered for study; (b) Boiler coal feeding mechanism; (c) Micro co-generation steam turbine .....	121
Figure 5-2: Flue gas path of the micro co-generation steam boiler .....	121
Figure 5-3: (a) Mass flow rate of the flue gas; (b) Input energy to system from the flue gas .....	123
Figure 5-4: Conventional ORC .....	124

Figure 5-5: Superheated ORC: (a) Schematic; (b) Simcenter AMESIM cycle block diagram .....	125
Figure 5-6: Superheated ORC with thermal storage: (a) Schematic; (b) Modelled using Simcenter AMESIM.....	125
Figure 5-7: Superheated ORC with air preheating: (a) Schematic; (b) Modelled using Simcenter AMESIM.....	126
Figure 5-8: Superheated ORC with recuperation: (a) Schematic; (b) Modelled using Simcenter AMESIM.....	126
Figure 5-9: Superheated ORC with thermal storage and recuperation: (a) Schematic; (b) Modelled using Simcenter AMESIM.....	127
Figure 5-10: Superheated ORC with air pre-heating and recuperation: (a) Schematic; (b) Modelled using Simcenter AMESIM.....	127
Figure 5-11: Superheated ORC with regeneration (a) schematic (b) modelled using Simcenter AMESIM.....	128
Figure 5-12: Superheated ORC with thermal storage and regeneration: (a) Schematic; (b) Modelled using Simcenter AMESIM.....	128
Figure 5-13: Superheated ORC with air preheating and regeneration: (a) Schematic (b) Modelled using Simcenter AMESIM.....	129
Figure 5-14: Superheated ORC with recuperation and regeneration: (a) Schematic (b) Modelled using Simcenter AMESIM.....	129
Figure 5-15: Variations in pump outlet pressure with increasing displacement .....	135
Figure 5-16: Proposed integration of an ORC boiler with an existing boiler flue gas circuit	136
Figure 5-17: Variations in power output with increasing ORC boiler heating surface area..	137
Figure 5-18: Turbine efficiency contours for pressure ratio and turbine inlet temperature plotted for turbine inlet pressure of (a)16 Bar, (b) 20 Bar and (c) 24 Bar.....	141
Figure 5-19: Variations in turbine power output with increasing turbine displacement .....	141
Figure 5-20: Variations in power output with condenser heat transfer area.....	142
Figure 5-21: Variations in power output with recuperator heat transfer area .....	143
Figure 5-22 Flue gas schematic with integration of ORC and the air preheater .....	144
Figure 5-23: T-s diagram of the optimal ORC, validated against the study by Maraver et al. [280] .....	147
Figure 5-24: Flue gas temperatures observed before and after the use of the ORC boiler .	148
Figure 5-25: (a) Absolute and (b) nominal power output achieved by various parametrically optimised ORCs .....	149
Figure 5-26: Normalised variation in turbine efficiency .....	150
Figure 5-27: Normalised Variations in turbine inlet superheat for multiple cycle configurations with respect to (WRT) conventional ORC .....	151
Figure 5-28: Increases in exhaust superheat temperature noted for all cycles.....	152
Figure 5-29: Increases in feedwater temperature achieved when energy recovery was employed .....	153
Figure 5-30: Increases in flue gas temperature noted due to reduced ORC boiler LMTD ...	154
Figure 5-31: Thermal load of condenser compared for all configurations.....	155
Figure 5-32: Thermal energy gain in APH-based cycles.....	156
Figure 5-33: Fuel consumption estimated for all cycle configurations .....	157
Figure 5-34 (a): Turbine inlet superheat maintained with addition of thermal mass (b): Steady turbine isentropic efficiency achieved with the help of thermal mass.....	158
Figure 5-35: Comparison of convergence time required for NLPQL and GA optimisers .....	159
Figure 5-36: NLPQL algorithm achieved convergence within 48 iterations .....	159
Figure 5-37: Pareto spread of GA population improvement in objective function over 624 iterations .....	160
Figure 5-38: Normalised power output gains of all cycles with optimisers compared .....	160
Figure 5-39: Variations in turbine isentropic efficiency noted for all cases .....	161
Figure 5-40: Thermal energy captured by APH-based cycles .....	163

Figure 6-1: Expected Pareto front for two objective optimisations [20]. Cases A–H represent individual iterations, wherein A–D represent Pareto optimal cases .....	171
Figure 6-2: Pareto front for conventional ORC cycle with NLPQL optimisation. The considered objectives are mean power and specific investment cost.....	173
Figure 6-3: T-s Diagram for (a) NLPQL-optimised APH cycle; (b) NLPQL-optimised recuperative APH cycle.....	177
Figure 6-4: High effectiveness of an air pre-heater demonstrated for an APH-based cycle	178
Figure 6-5: (a) Sensible heat recovery by the recuperative APH cycle; (b) Latent heat recovery using multiple pinch points and large heat exchangers.....	179
Figure 6-6: Peak boiler performance achieved with an air temperature of 97°C [37] .....	180
Figure 6-7: (a) Higher mass flow rate; (b) Higher turbine inlet pressure observed for a NLPQL-optimised regenerative APH cycle .....	181
Figure 6-8: Convergence time required for multi-objective optimisation .....	183

# List of Tables

Table 2.1: Safety and Environmental classification of organic fluids, in increasing order of global warming potential .....	42
Table 2.2: Working fluid properties of fluids operating between 140°C and 30°C .....	44
Table 2.3: Summary of the comparison of expanders .....	52
Table 2.4: Comparison of machine learning algorithms.....	68
Table 3.1: Parameters required for Soderberg's loss model.....	80
Table 3.2: Parameters required for Craig and Cox loss model .....	84
Table 4.1: Artificial neural network and genetic algorithm setup parameters.....	100
Table 4.2: Turbine optimisation constraints for the genetic algorithm.....	101
Table 4.3: A comparison of the results of the validation .....	104
Table 4.4: Genetic algorithm (GA)-optimised parameters and test results .....	116
Table 4.5: A comparison of losses optimised by ANN and GA .....	117
Table 4.6: The range of parameter variations provided by optimised solutions.....	117
Table 5.1: Flue gas parameters .....	122
Table 5.2: Variation of core component sizing provided to optimiser.....	144
Table 5.3: Setup parameters for the NLPQL algorithm.....	145
Table 5.4: Optimisation setting of GA .....	146
Table 5.5: Results of conventional ORC validation comparison .....	147
Table 5.6: Optimised component sizes provided by parametric optimisation, NLPQL and genetic algorithm.....	162
Table 6.1: Cycle configuration and variables .....	166
Table 6.2: Range of variables considered.....	167
Table 6.3: Component and labour costs .....	169
Table 6.4: Diameter and length of working fluid piping .....	170
Table 6.5: Material cost of equipment before optimisation.....	172
Table 6.6: Improvement in composite objective Function and SIC values achieved by optimiser .....	174
Table 6.7 Component size for optimised configuration .....	175
Table 6.8: Reduced cooling water evaporation loss and pump consumption for ORC with APH.....	176
Table 6.9: Material cost of the APH cycle after optimisation.....	178
Table 6.10: The total heat exchanger cost in Euros for the regenerative APH and recuperative APH cycles .....	179
Table 6.11: Payback calculations for the most feasible ORC with APH combination .....	181

# Chapter 1 Introduction

## 1.1 Importance of energy

Energy is one of the most vital resources for our continued existence on Earth. In addition to nuclear and geothermal energy, the sun is the major source of energy. In 1964, Nikolai Kardashev developed the Kardashev scale which has since been widely used as a method of measuring a civilisation's level of technological advancement [1, 2]. He defined a type 1 civilisation as one that can harness all the energy received by a planet from its parent star. Earth receives  $\approx 1.74 \times 10^{17}$  Watts annually. The world's current annual consumption is  $\approx 2 \times 10^{13}$  Watts, which is lower by about four order of magnitudes. According to theoretical physicist and futurist Michio Kaku, humanity is expected to attain type 1 status within the next 100–200 years [3].

Countries with high energy consumption have a greater per capita income. Developed economies have demonstrated a 50-fold increase in energy consumption since the 1860s [4]. This has led to increased focus on electricity generation and a similar trend is now being witnessed in developing economies. Studies have also correlated an increase in energy consumption with an improved quality of life, enhanced social progress index and higher industrial production [5].

## 1.2 Historic global energy scenario

Energy in thermal form was first harnessed by primitive humans when they were able to use fire for heating, cooking and illumination—all essentials for survival. The principles of electricity generation were based on the principles of electromagnetism discovered by Michael Faraday in the 1820s. Mining technology improved to ensure coal replaced timber as the primary fuel for combustion in the 1780s. The Edison Electric Light Station in London was the world's first coal-fired public power station, built in 1882 (Figure 1-1) [6].

The combination of the development of prime movers, fuel sources and electricity generation led to the first Industrial Revolution in the late eighteenth century, which resulted in a significant increase in energy demand. Coal was the fuel of choice for power generation during the first industrial revolution. The chemical energy from the coal combustion was converted to electricity using steam engines and later, steam turbines.

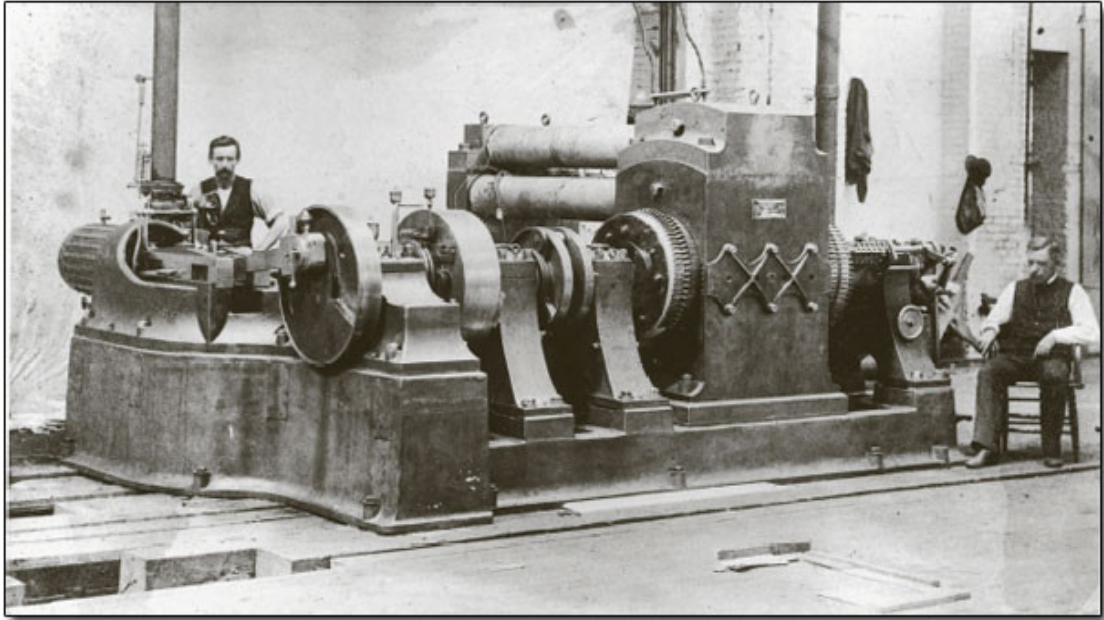


Figure 1-1: Edison's Jumbo steam turbine was installed between 1882 and 1885 in the Holborn Viaduct Station in London and in the Pearl Street Generating Station, Manhattan, New York [6]

### 1.3 Current energy trends

Traditionally, oil and natural gas resources are concentrated across the Middle East, North America, Russia and South America [7]. In contrast, coal is the most abundant fossil fuel, with an estimated 100 trillion tons worldwide [8]. The International Energy Agency (IEA) observed that the energy demands for coal-dependent countries like China and India has been increasing by 7% on a yearly basis [9]. The report also predicted a global annual increase in the primary energy demand by 1.15% until 2035, this mainly due to the increased energy demands of the industrial sector as well as the changes in patterns of heating and cooling demand. In addition, the transportation sector has witnessed significant growth and an escalation in energy consumption due to increased globalisation. Increased electrification has led to a six-fold increase in fossil fuel consumption since the 1950s [10]. In 2018, global energy consumption grew by 2.3%, twice as fast as the average rate over the previous 10 years [11]. During the same year the demand for electricity grew by 4%, faster than all other forms of energy [11]. It is acknowledged that oil industry has a cycle life of 300 years, of which over 150 years have already elapsed. Currently, natural gas is witnessing a dramatic increase in consumption patterns as it is considered the cleanest fossil fuel (Figure 1-2). In addition, natural gas-based power plants provide grid stability for simultaneous operation with renewables due to their quick response times and high turndown ratios.

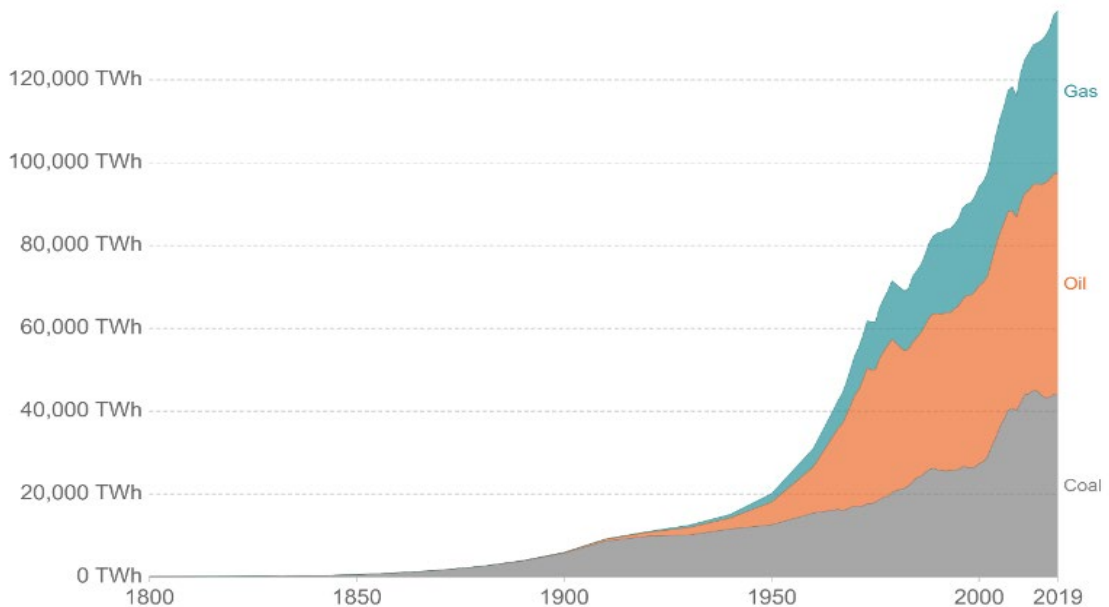


Figure 1-2: Increase in global fossil fuel consumption from 1800 to 2019 year, measured in terawatt-hours (TWh) [13]

## 1.4 Future energy trends, renewables and ORC

Whereas coal is the fuel of the past and natural gas of the present, the future will involve a mix of renewables (Figure 1-3). Environmental concerns caused due to fossil fuel combustion cannot be ignored anymore due to the associated impacts of global warming. Studies have highlighted the need to reduce the equivalent greenhouse gas emissions by 50%, equivalent to 40–48 billion tonnes of carbon dioxide, to restrict average global temperature rise within 2°C [12]. A reduction in the combustion of fuels will lead to a decline in greenhouse gas emissions and airborne-suspended particulate matter. It is expected that oil, gas, coal and renewables will meet 32.6%, 23.7%, 30.0% and 13.7% of global energy needs, respectively, in the near future [8].

Despite the advances in technology and imaging, medium-to-long range weather forecasts suffer from inaccuracy [13]. Studies have pointed to a 10-day forecast having an accuracy of less than 50% [14]. Recent developments include the use of artificial intelligence algorithms [15]. As the majority of renewables depend upon the weather, the intermittency posed by renewable energy sources has led to operating them alongside fossil fuel-based power plants to compensating their short-term instability [16]. This requires the fossil fuel-based plant to operate in idle mode as a standby to renewable energy sources resulting in reduced part load efficiency and increased capital expenditure.

The next century is expected to have a threefold increase in electricity consumption. However, it has been widely acknowledged that the renewables alone will not meet the entire demand of the future [17]. Equally, the variations in power generation by typical renewables is a serious

impediment, limiting our dependence on them. At this crucial juncture, this study wishes to consider the contribution of ORCs to the global energy mix. As such, Organic Rankine cycles (ORCs) stand out as one of the unique tools of renewable energy utilisation which can provide reliable and continuous power generation. Compared to typical renewable energy sources, ORCs offer flexibility to adapt to an ever-increasing range of heat source temperatures; this freedom offered by virtue of the different ORC working fluids. The present installed capacity of ORCs was merely 2.75 gW in the year 2017, compared to 4282 gW for fossil fuels, pointing towards significant additional untapped potential [18, 19].

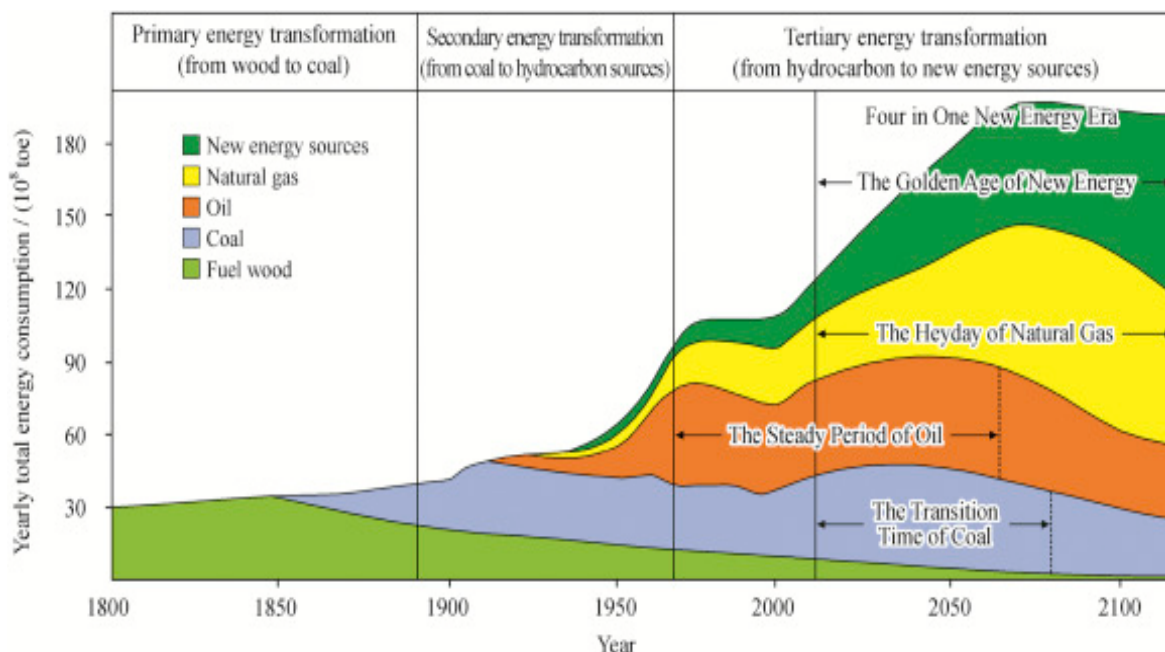


Figure 1-3: Expected rise of renewable energy in the twentieth-first century [10]

## 1.5 History of ORC

The concept of the organic Rankine cycle was established in 1824 by Sadi Carnot [20]. Since the rules of thermodynamics themselves were evolving during that time, the concept remained theoretical. Condensation at pressures greater than atmospheric was required due to gland-sealing issues caused by the poor vacuum systems for early steam turbines, which led to a rise in the condensing temperature. ORCs were first manufactured for waste heat recovery from these primary expanders as an alternative to vacuum systems [21]. Du Tremblay developed the first ORC as a bottoming cycle on a passenger ship with ether as the working fluid. An accident in 1856 at the port of Bahia, possibly due to the volatility of ether, stopped any further developments for a long time [22]. Willisie developed the next ORC for a 4.5 kW plant in St. Louis, Missouri, and an 11 kW plant in Needles, California [23, 24] after a 50-year gap with sulphur dioxide as the working fluid along with a solar heat source. Prof. Luigi D'Amelio developed the first ORC with a turbo expander and high molecular weight working fluid [25]. These fluids led to a simpler system with lower enthalpy drop across the expander, lower operational speed, reduced diameter and lesser number of stages.

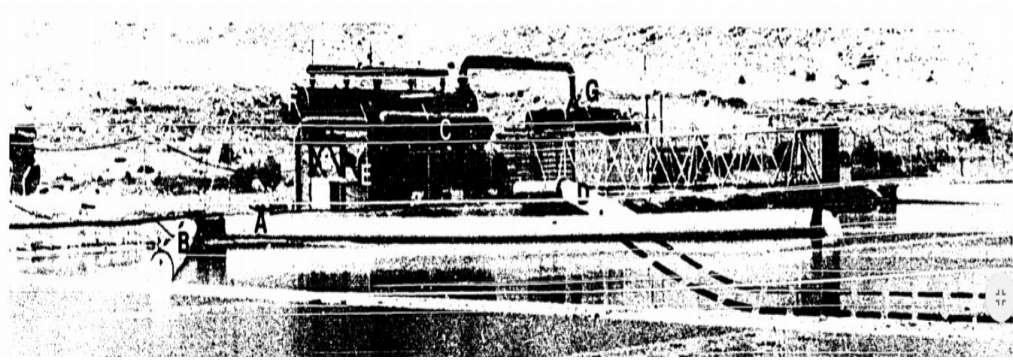


Figure 1-4: Pictorial view of 145 kW turbine-driven ORC solar pond power plant at Ein Bokek, Dead Sea, Israel, commissioned in 1979 [26]

Between 1958 and 1961, Tabor and Bronicki undertook detailed studies of working fluid thermodynamic properties, thermal stability tests and their selection based on the heat source and sink slopes, which in turn were based on the limited number of working fluids available at that time [27]. They observed that the number of atoms within the fluid molecule determined its state after the expander. Fluids with fewer than 10 atoms moved towards wetness on the saturation scale and heavier fluids having greater than 10 atoms moved towards dryness or superheat. Tabor and Bronicki were the first to propose the use of recuperators for ORCs and turbines instead of reciprocating engines (Figure 1-4).

Italian institutes have contributed significantly towards modern commercial ORC development. The Polytecnico di Milano carried out work toward this end from the 1970s onwards, pioneering the modern-day, packaged ORC powerplants. They studied the suitability of the radial outflow turbine and developed the first ORCs for commercial geothermal energy sources [28, 29].

## 1.6 Introduction to the ORC cycle

The fundamental components of an ORC are similar to steam-based Rankine cycle, except that an organic fluid with a higher molecular mass and a lower boiling point is circulated through it. The properties of the fluid allow for the utilisation of lower-grade heat sources, which allows ORCs to avoid combustion, as is the case with most steam-based Rankine cycles (other than nuclear fission). As a result, they are suitable for converting low-grade heat into useful work in the form of mechanical shaft power or electricity.

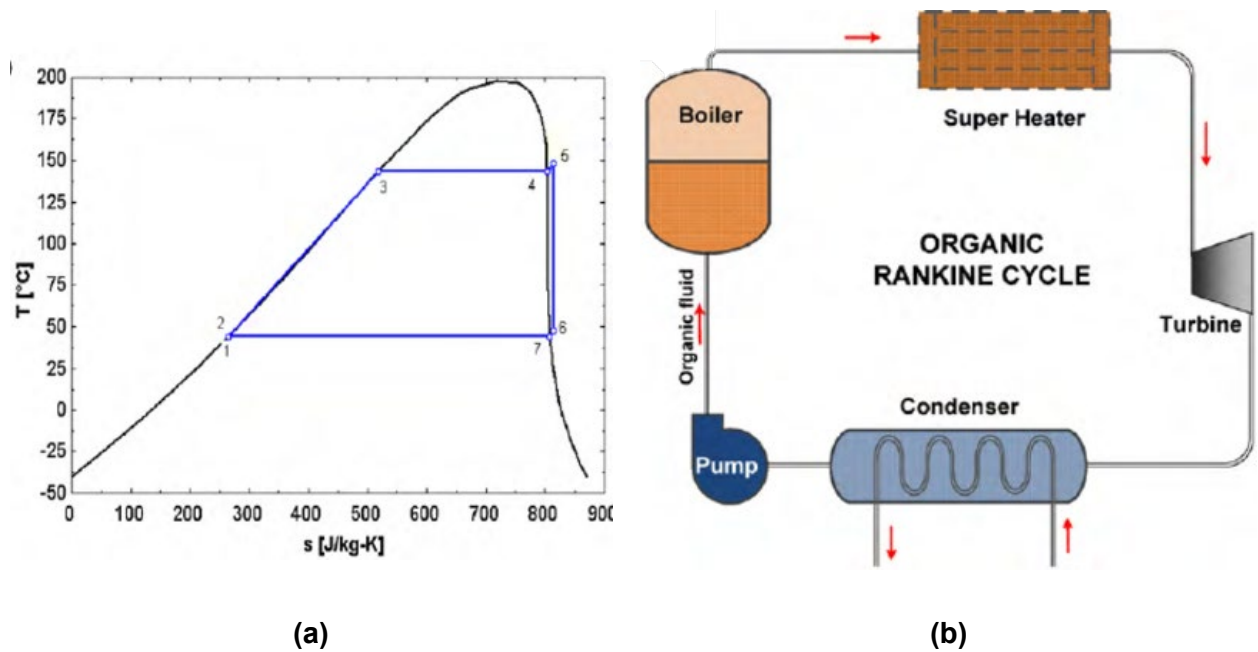


Figure 1-5: Exemplar of a sub-critical organic Rankine cycle with a superheater (a) T-s Diagram, (b) Components flow diagram [30]

The working fluid operates in a closed loop, consisting primarily of four components: a feed pump, an evaporator, a turbine (i.e., expander) and a condenser (Figure 1-5(a)). Based on the type of working fluid and expander chosen, the fluid might operate in the superheated or wet regimen after expansion. A superheater might be provided (Figure 1-5(b)), to protect against blade erosion, as some expanders, particularly turbo expanders, are unable to handle wet fluids. ORC condensers are usually plate or shell and tube heat exchangers. Heat is rejected from the condenser using a cooling circuit, with water as its working medium. The high latent heat of water provides maximum heat dissipation along with minimum evaporation loss in the cooling tower. Whereas condensers for steam-based Rankine systems typically work at 0.1 Bar(a) in tropical conditions and 0.07 Bar(a) in temperate conditions and marine environments, commercial organic Rankine cycle systems operate with condensation pressures greater than atmospheric [21]. This helps ORCs avoid additional working fluid-based sealing arrangements for the expander and condensate recovery pump shafts, necessary to avoid air ingress into the system. The temperature difference between the heat source, and heat sink of the cooling fluid in the condenser determines the exergy efficiency of the cycle. Improving cycle efficiency was typically done by regeneration and recuperation of the working fluid.

# Chapter 2 Literature Review

## 2.1 Introduction

Based on the previous chapter, it can be safely concluded that there is an increasing interest in Organic Rankine cycles (ORCs) vis-à-vis utilising renewable and waste thermal energy. The variety of potential working fluids provides ORCs with the flexibility to adapt to a wide range of heat source and heat sink temperatures compared to steam-based cycles. In the past, ORC systems were widely used to generate power from bio-heat [30-33], geothermal [34-40], ocean thermal (OTEC) [41], solar thermal [42-45], combined heat and power (CHP) [46] and waste heat [47-72] sources. Waste heat recovery (WHR) applications are of particular interest as they provide untapped heat sources, which contribute to global warming and energy loss. Industrial waste heat sources are readily available and contain steady streams with large quantities of low- and medium-grade heat energy at easily accessible locations. The saturation curve of an ORC working fluid expansion varies depending on the choice of working fluid, which leads to a variety of expander designs. Certain working fluids complete the expansion phase in a two-phase state, which limits the choice of expanders for a given application. Considering the variations in ORC plant size, heat grade and working fluids, a variety of expanders were used by previous studies. Zhao et al. noted that turbines, such as axial and radial turbines, were used for 69.96% of overall ORC publications whereas scroll, screw, vane and piston expanders were used in 14.23%, 6.12%, 5.32%, 4.39% of the studies, respectively [73]. Although research on ORC turbines and cycles has been multidirectional, there has been limited research on the use of novel optimisation techniques.

The aims of this literature review chapter are as follows, and a brief overview of the chapter is shown in Figure 2-1:

- Review the available working fluids and classify them based on environmental and thermodynamic factors including their expansion behaviour.
- Compare steam- and organic fluid-based cycles based on heat source temperature and expander suitability.
- Identify previously untapped ORC sources, including WHR applications.
- Classify ORC expanders, identify non-dimensional parameters and suitable loss prediction models for design & off-design efficiency.
- Study the suitable combinations of machine learning and optimisation algorithms for turbine efficiency, cycle efficiency and multi-objective thermo-economic feasibility.

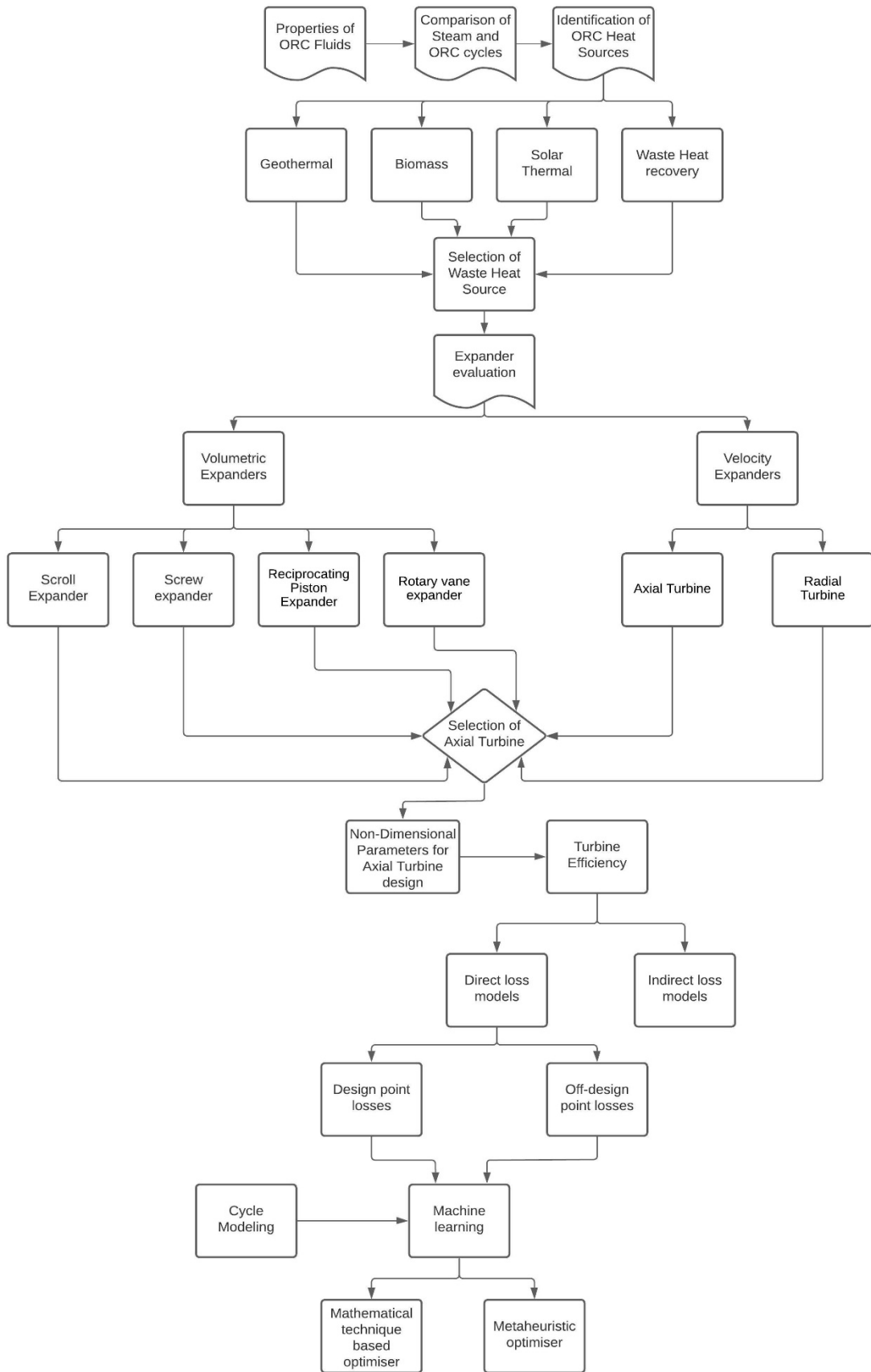


Figure 2-1: Approach of the literature review

## 2.2 Equation of State (EoS)

The equation of state (EoS) is a correlation developed to determine the pure fluid or zeotropic mixture properties in a state of thermodynamic equilibrium [74]. Zeotropic mixtures are a mixture of pure fluids with physical properties between their individual constituents, their composition varied based on the application. Computational solvers use EoS instead of lookup tables. At the time of this study, there was no existing EoS that could accurately predict the working fluid properties for all fluids under all conditions [75]. Previous studies widely employed cubic equations of state such as the Redlich-Kwong-Soave or the more advanced statistical associating fluid theory (SAFT) working fluid modelling [76-80].

The Peng-Robinson EoS, as stated in equation 2.1 was developed by Ding-Yu Peng and Donald Robinson at the University of Alberta in 1976. Compared to later models, it offers a simpler generalisation of the working fluid, while accounting for fluid compressibility and maintained accuracy near the critical point [81, 82]. It is also known for its suitability for gaseous mixtures involving a combination of compounds[83]. Previous studies also validated the suitability of the Peng Robinson EoS while operating with refrigerants [77].

$$P = \frac{RT}{V_{molar} - b_{acentric}} - \frac{a_{acentric} \times \text{Factor}\alpha_{Tc} \times T_K}{V_{molar}^2 + 2 \times b_{acentric} \times V_{molar} - b_{acentric}^2} \quad 2.1$$

Where  $P$  is the pressure in Pa,  $R$  is the universal gas constant in J/(mol K),  $T_K$  is the temperature in Kelvin,  $V_{molar}$  is the molar volume in m<sup>3</sup>/mol. Acentric factors  $a_{acentric}$  and  $b_{acentric}$  and critical temperature factor  $\text{Factor}\alpha_{Tc}$  are functions of fluid-specific critical pressure  $P_{crit}$  and critical temperature  $T_{crit}$ . The second order polynomial was used to characterize the working fluid's saturation dome.

The BACKONE EoS considers the Helmholtz energy ( $F$ ) and depends on the characteristic intermolecular interactions that were physically determined using extensive molecular simulations [80, 81]. The Helmholtz energy ( $F$ ) is determined as the sum of individual contributions. For dipolar fluids, the internal energy is defined as in equation 2.2, where FH is the hard-body contribution, FA is the attractive dispersion force contribution and FD is the dipolar contribution.

For quadrupolar fluids, the QUADBACKONE equation uses FQ as the quadrupolar contribution, as depicted in equation 2.3. This EoS considered four substance-specific parameters: characteristic temperature  $T_{char}$ , characteristic density  $\rho_{char}$ , anisotropy parameter  $A$  and either reduced squared dipole moment  $\mu^*2$  or reduced squared quadrupole

moment  $Q^2$  [81]. The equations have been validated for property accuracy in the range of  $\pm 1.5\%$  with modern ORC working fluids like R1234yf, as shown Figure 2-2 [80, 82].

$$\frac{F}{RT} = \frac{F_H}{RT} + \frac{F_A}{RT} + \frac{F_D}{RT} \quad 2.2$$

$$\frac{F}{RT} = \frac{F_H}{RT} + \frac{F_A}{RT} + \frac{F_Q}{RT} \quad 2.3$$

The simpler Peng Robinson EoS was used for component-level simulation in the study (see Chapter 4), where phase change was not undertaken within the turbine and its simpler generalisation was adequate. The REFPROP database incorporating QUADBACKONE EoS was used for cycle-level simulations in this study (see Chapters 5 and 6), due to its better enthalpy conversion and phase change prediction [84].

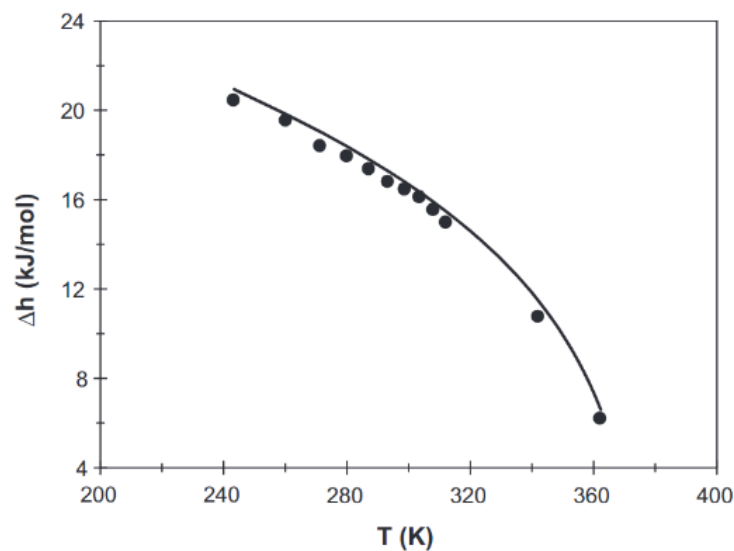


Figure 2-2: Validation of enthalpy of vaporisation for R1234yf using BACKONE EoS validated by experimental data [57]

## 2.3 Comparison between steam and ORC cycles

### 2.3.1 Classification based on heat source temperature

The choice between steam or organic fluids is based on the heat source temperature, which is classified as low-grade for a heat source temperature up to  $70^\circ\text{C}$ , medium-grade for a heat source temperature between  $70^\circ\text{C}$  and  $350^\circ\text{C}$  and high-grade for a heat source temperature above  $350^\circ\text{C}$ . In the case of low-grade heat sources, ORCs demonstrate lower exergy destruction in the evaporator as the temperatures of the working fluid are close to the heat source temperature. Low-grade applications usually have a larger heat source mass flow rate per unit power generation, which results in a smaller working fluid temperature increase across the evaporator [85]. Low- and medium-grade sources are suited to ORCs as the boiling point

of pressurised water is 265°C at 51 kg/cm<sup>2</sup> and 284°C at 69 kg/cm<sup>2</sup>, the typical pressures considered for small steam-based power plants. In addition, steam-based systems require a mandatory superheater for turbine efficiency and wetness constraints, which increases the typical steam temperature above 350°C. The wet fluid behaviour exhibited by water (shown by the slope of the expansion curve in Figure 2-3), was compared to that of ORCs, which also demonstrated wet, dry and isentropic behaviour [86].

Hung et al. concluded that steam Rankine cycles were not suitable for operation with heat sources below 370°C [53]. Additionally, the higher specific volume of low-pressure steam relative to organic fluids led to a significant increase in equipment sizing and costs. The pinch point limitation and associated intermittency at the heat source are the biggest issues in the design of steam-based systems operating on low-grade heat sources [58].

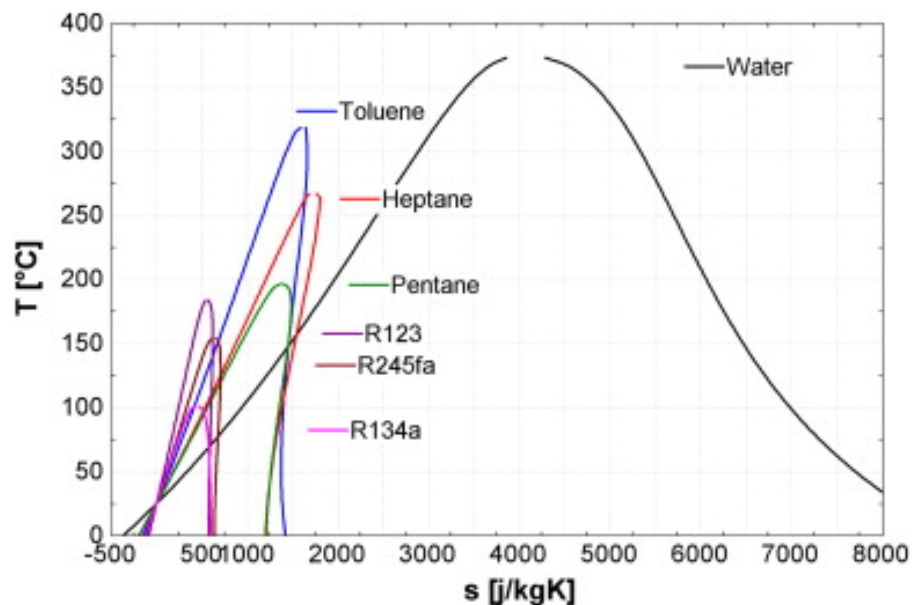


Figure 2-3: T-s diagram of steam and commonly used ORC fluids [60]

As the temperature of the heat source increases, the feasibility of a steam Rankine cycle vis-à-vis organic Rankine cycles improves due to their higher Carnot efficiency and simple architecture. Park et al. mentioned that few ORC studies were conducted for heat source temperatures above 300°C and observed the abundance of steam-based cycles at higher temperatures [85].

The shallow gradient of the expansion slope allowed the use of a large degree of superheat for steam Rankine cycles [86]. The majority of organic fluids also suffered from a thermal stability limit near 380°C [85]. Due to this limitation, intermediary fluids such as thermal oils or pressurised water were employed in an additional heat transfer loop for applications that involved high-grade heat sources [49, 85].

Liu et al. classified waste heat recovery cycles based on heat source temperatures and plant scale, as shown in Figure 2-4 [87]. They concluded that steam Rankine cycles were best suited for medium to high heat source temperatures above 300°C. Lower scale and lower temperature steam cycles for waste heat sources were less cost-effective and experienced surface corrosion issues, caused by carbonic ( $H_2CO_3$ ) and sulphuric acid ( $H_2SO_4$ ) formation below the dew point [88]. Waste heat source temperatures between 90°C and 250°C were observed to provide competitive cycle efficiency for ORC turbines [61].

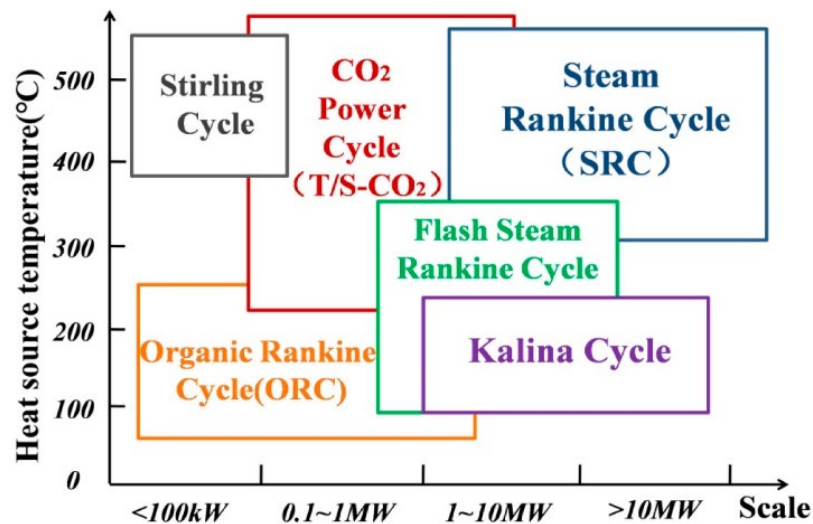


Figure 2-4: Classification of thermodynamic waste heat recovery cycles based on heat source and plant size by Liu et al. [61]

### 2.3.2 Comparison between steam and organic Rankine expanders

A detailed comparison of expanders for ORCs and steam cycles for energy recovery from low- to medium-grade heat sources was undertaken by Bao et al. that concluded the following [89]:

- For a finite temperature difference across the heat source and sink, ORCs demonstrate reduced specific power generation, usually 16-40% lower [90]. This is due to the reduced expansion ratio, smaller change in specific volume and corresponding enthalpy drop across the expander for the working fluid across ORC expanders.
- The low expansion ratios, usually between 2.5 and 4, allow ORC expanders to operate at higher isentropic efficiency.
- Owing to higher density, and consequently, lower specific volume of organic fluids, the required expander volume is smaller for ORCs. This manifested itself as increased partial admission and secondary blade losses in the case of ORC turbines. Due to the higher molar mass of organic fluids, the speed of sound in ORC fluids is much lower compared to steam, which resulted in predominantly supersonic flow across ORC

expanders. This led to additional primary losses during design point and off-design operation.

- Most organic fluids are dry, which results in superheated exhaust from the expander hence additional heat load on the condenser. Steam usually exits the expander during the wet phase.
- Leakage control was crucial in the case of utilising toxic, flammable, explosive or carcinogenic-behaviour organic fluids.

## 2.4 Current ORC applications

ORCs are commercially successful in the small- and medium-scale conversion of thermal energy to electricity for a variety of heat sources, where conventional steam powerplants could not provide viable solutions. Based on the intermittency of the heat source temperatures, ORCs provide flexibility of operation by providing subcritical and trans-critical cycles [91]. The choice of working fluids with variable boiling points allows ORC compatibility with a variety of heat sources. Existing commercial ORC installations on the basis of total number of installations were summarised in Figure 2-5 [92]. Seventy-three percent of the gross power generation from ORCs is carried out using geothermal sources. This can be attributed to the larger scale of geothermal ORC installations compared to other sources [93].

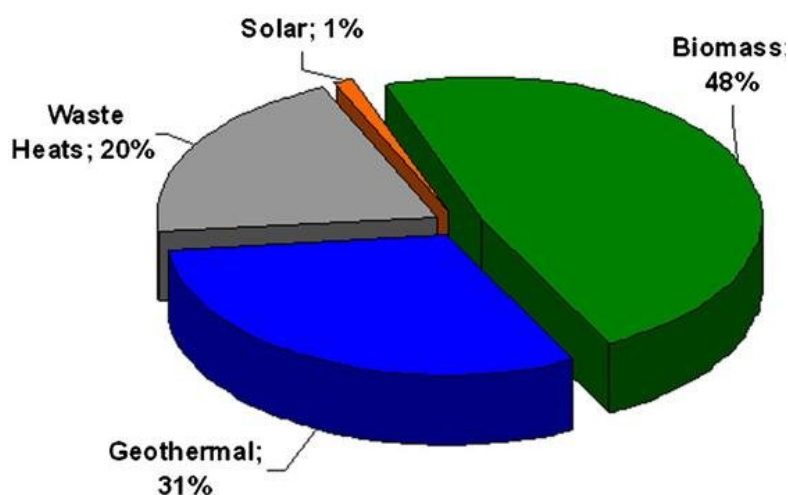


Figure 2-5: Existing ORC heat source classification based on total number of installations

### 2.4.1 Geothermal waste heat recovery

Geothermal locations demonstrate a temperature increase between 30°C and 90°C for every 100 m depth. Typical heat source temperatures vary between 50°C and 350°C. High-grade sources commonly utilise steam Rankine cycles using flash and dry steam systems. Low- and medium-grade geothermal sources are more abundantly available [35]. The use of

supercritical cycles has also been recommended to limit pinch point restrictions, providing a 15% increase in gross power output [39].

Geothermal ORCs incorporate the indirect utilisation of the extracted fluid, using a binary cycle, as shown in Figure 2-6 [36]. The geothermal brine extracted transferred its heat to the ORC working fluid with the help of a heat exchanger and was then reinjected below the surface [94]. Typical geothermal ORC heat sources have a temperature of around 300°C, and brine temperature between 100°C and 190°C. As the pumping of brine is energy intensive, the efficiency of heat source utilisation is important for geothermal ORC plants, limiting commercial applications to higher-grade heat sources. Worldwide power generation from binary geothermal ORCs is about 700 mWe—approximately 8% of the total power production from all geothermal sources [95].

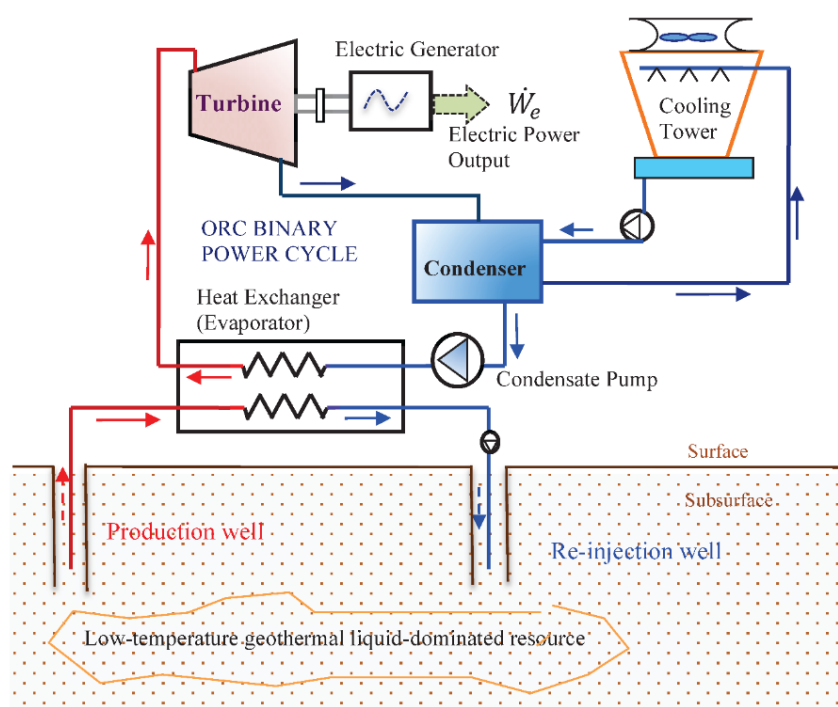


Figure 2-6: Binary cycle-based geothermal ORC system [69]

#### 2.4.2 Biomass

Biomass combustion achieves temperatures up to 1200°C, with an excess air ratio of 2 [96]. Due to the high temperature of bioheat source, biomass ORC power plants are limited to those plants considered too small for steam-based systems. The higher volumetric flow rate allows for an increased expander size in the case of ORCs, which improves expander efficiency and turndown ratio [97]. Steam Rankine cycles demonstrate higher cycle efficiency with higher working fluid pressure, temperature, and mass flow rate, typical of larger power plants. They also require additional capital investment, and greater safety measures, which negates their benefits and feasibility for smaller generation plants. In 2011, only 14% of the gross power

generation from ORCs utilised bioheat, mainly due to subsidies offered by the European Union (EU) for small biomass ORC plants [33]. This validated the greater suitability of steam-based cycles for biomass power plants [93]. Wood pellets were reported as the main biofuel for over 73% of biomass ORC applications within the European Union [98-101].

Despite the high temperatures generated by combustion, biomass ORCs suffer from low energy conversion efficiency (that is, 2nd law) due to the limitations imposed by the thermal decomposition of working fluids [96]. The use of thermic oil, siloxanes and unbranched long-chain alkanes has been suggested for the high-temperature loop of binary biomass ORCs [32]. Many existing plants utilise octamethyltrisiloxane (OMTS) as a working fluid, due to its high evaporation temperature and thermal stability despite its poor heat transfer ratio at elevated temperatures, which eliminates the requirement for an intermediary fluid such as thermal oil [31, 32].

### 2.4.3 Solar thermal energy

Solar thermal energy offers flexibility of heat source temperatures depending on the type of collectors and the receiver area. Mixed results were obtained about the impact of superheating on the energy conversion efficiency of the solar thermal ORC cycle as an increased collector temperature resulted in an increase in convection loss [102]. Solar collectors were classified based on the working fluid temperature generated. Conventional flat plate solar collectors were classified as low-grade, with a fluid output temperature between 75°C and 150°C, and without any degree of concentration [103]. They are seldom used for commercial applications due to their relatively poor viability [104].

Medium-grade solar collectors, such as the evacuated tube, achieve working fluid temperature between 130°C and 150°C. High-grade solar collectors, with working fluid temperature above 150°C, such as the Fresnel Lens and Parabolic cylindrical trough collectors, are widely used commercially [103]. Both single loop and binary loop configurations are used, with pressurised water or thermal oil as the binary loop. Thermal energy storage systems are also integrated with solar thermal ORC systems, to mitigate the variation of solar radiation received during the day and unavailability after sunset, as shown in Figure 2-7 [105].

Solar thermal ORCs have been widely used in cogeneration desalination applications, as an alternative to pure membrane desalination. They are particularly useful for coastal rural locations without access to fresh water, electricity and abundant water supply [106]. The ORC system powers the desalination operation, while working fluid at the expander exhaust provides thermal energy for the desalination plant. The economic feasibility of this system is comparable to a solar photovoltaic-based system [107].

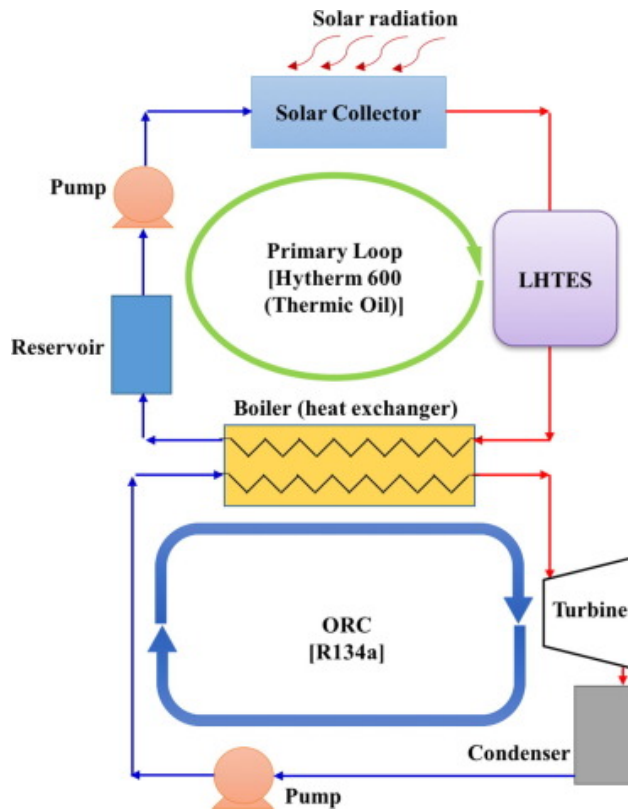


Figure 2-7: Solar thermal ORC with binary heat transfer loops and latent heat thermal energy storage (LHTES) systems in conjunction with high-grade collectors [79]

#### 2.4.4 Waste heat recovery

Whereas steam Rankine cycles can be used for waste heat recovery, they are not suitable for low- and medium-grade waste heat sources due to their high saturation temperature. Medium- to low-grade heat (200-50°C) accounts for 50–66% of the waste heat from the industrial sector (Figure 2-8), as industries reject over 54% of input energy [108, 109]. Such a significant amount of heat rejected into the environment leads to profound thermal pollution, if not adequately recovered. ORCs are better suited for energy recovery from medium- to low-grade streams as well as smaller-sized plants (Figure 2-9), due to their simplicity and compactness [14, 34]. The investigation of ORCs for waste heat recovery applications has previously been undertaken for IC engine exhausts [110], transport vehicles [52], gas turbines [111], cement plants [112], casting plant furnaces [113] and smelting furnaces [114] and industrial sources [90, 115-118]. The choice of working fluids allows cycle properties suited to optimising expander isentropic efficiency, optimal matching of the heat release curve with the fluid saturation curve and operation with transient waste heat sources to maintain the working fluid within the vapour phase at the turbine's moving blades [119].

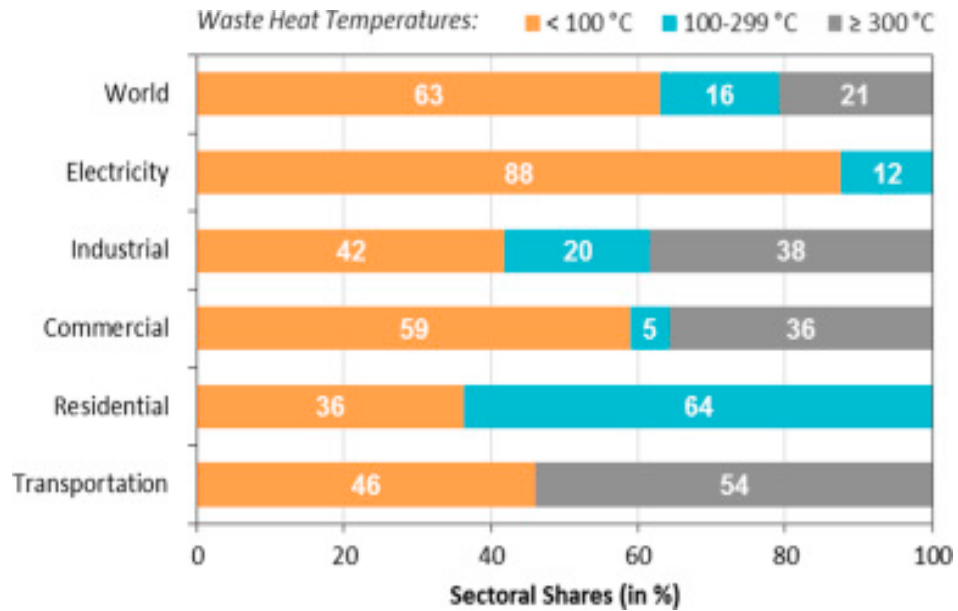


Figure 2-8: Sectoral shares of waste heat distribution by temperature [82]

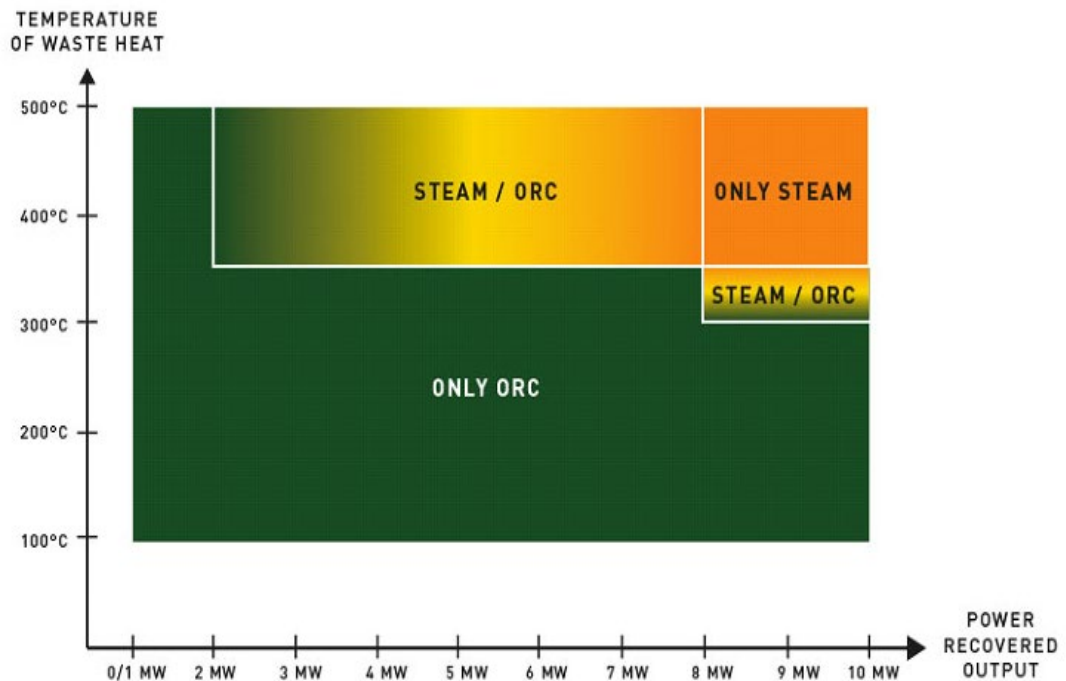


Figure 2-9: Classification of steam Rankine and organic Rankine cycles for WHR applications based on heat source temperature and power generation [84]

Figure 2-10 illustrates a typical WHR ORC application. WHR-based ORCs provide additional power without any additional fuel costs, which is a factor of increasing importance in a world with rising energy prices [53, 120]. ORCs are scalable, operated at lower pressures, with minimum human intervention and are safe for operation with fluctuating waste heat sources [58, 62]. Park et al. reported that the existing experimental studies on WHR ORCs focussed on small-scale applications using repurposed and renovated expanders and limited work has been done in the field, despite the abundant availability of low-grade waste heat suitable for exploitation by ORCs [85].

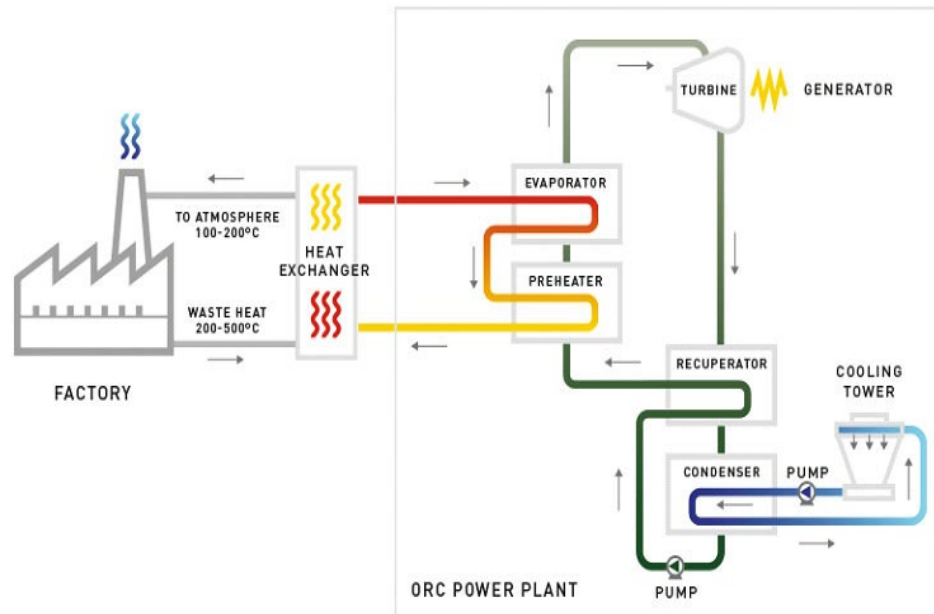


Figure 2-10: Typical WHR ORC application [84]

Figure 2-11 classifies WHR ORC power generation based on heat source. Diesel engines and gas turbines are the most common heat sources [59]. Heat is extracted from the combustion product stream, exhaust gas recirculation stream and coolant stream. It was reported that ORCs improved the fuel economy for long-haul trucks by up to 10% on a commercial scale [121]. The work output from the ORC was used to aid the mechanical power of the diesel internal combustion engine, generate electricity for on-board requirements or combined with a hybrid powertrain [122]. Similar to other waste heat recovery applications, previous studies suggested that the variations in the operational profile of the heat source are of critical importance for IC Engines and gas turbines [59].

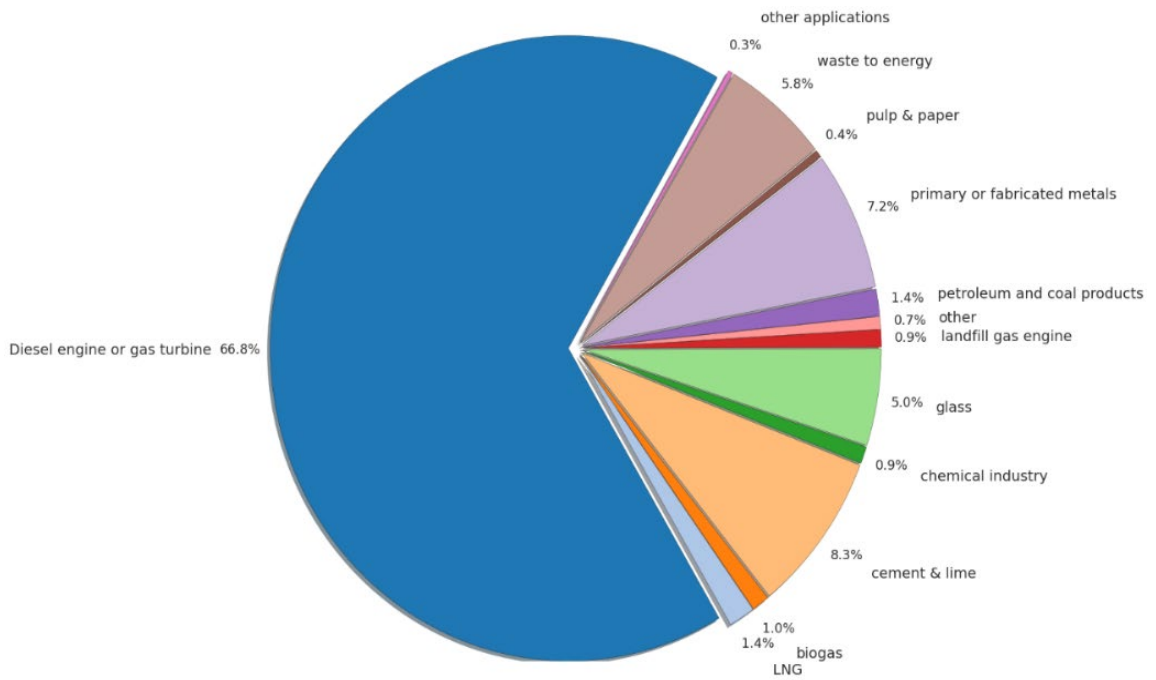


Figure 2-11: Classification of existing ORC units utilise waste heat sources by installation capacity. Total installation capacity of WHR ORC is 349.1 mWe [94]

Cement and metal plants have the second- and third -largest installed WHR ORC user base, at 8.3% and 7.2%, respectively (Figure 2-11). Cement plants are considered suitable for modular ORCs due to their similar plant layout, high-grade waste heat and continuous operation at stable parameters. Steel plants are greater in number and provide three different waste heat sources; these are after the furnace (300°C to 1600°C), before the quenching tower (200°C to 900°C) or indirect heat recovery from the cooling fluid used for the quenching tower [49]. The potential for ORC in steel plants has been reported as 2705 mWe in Europe [49].

WHR ORCs with unconventional heat sources have also been modelled. Singh et al. combined a solid oxide fuel cell and gas turbine cycle along with a medium-grade ORC bottoming cycle [123]. They concluded that the addition of an ORC bottoming cycle led to a 4% improvement in cycle efficiency, along with a 33% reduction in the cost per kW, over a ten-year life span. Song et al. reported that a recompression S-CO<sub>2</sub> cycle demonstrated a 1.3% improvement in cycle efficiency when combined with a bottoming ORC, while simultaneously eliminating the need for a compressor pre-cooler [124]. The researchers then optimised the degree of recuperation of the S-CO<sub>2</sub> cycle to achieve an additional 0.4% improvement in cycle efficiency.

Ziółkowski et al. considered an ORC bottoming cycle as a replacement to a traditional condenser in a supercritical steam cycle [71]. They achieved 1.25% improvement in cycle efficiency, and a 15-fold reduction in the swept area of low-pressure turbine blades and the surface area of the surface steam condenser. Chacartegui et al. concluded that the ORC recuperated gas turbine combined cycles achieved an efficiency improvement around 3% [72].

Y. C. Engineer, PhD Thesis, Aston University, 2022

higher than the optimised conventional gas turbine combined cycles [90]. Muhammad et al. combined a binary loop ORC with a natural gas liquefaction plant with an intermittent steam demand [61]. The ORC used steam that would otherwise be vented to the atmosphere.

Steam is the most used heat transfer medium for process industries due to its favourable latent heat thermal characteristics, non-reactive nature with a wide range of materials, non-toxicity, low cost, widespread availability, suitability for food grade products, flexibility with direct and indirect heating along with an established supply chain for components and ease of operation [115, 116]. Sub-critical industrial boilers are widely utilised by process industries and power generation plants for steam generation using fossil fuels, biomass and refuse-derived fuels (RDF) [117, 118]. Typical industrial boilers reject up to 22% of input heat as low-grade stack losses directly into the environment; this is between 140°C and 200°C for solid fuel-fired boilers, having an estimate installed user base too large to be quantified [62, 125]. These untapped lower-grade waste heat sources can be used for the installation of WHR ORCs, although this heat source has not been investigated in detail previously [126].

## 2.5 Working fluids

As discussed in the preceding section, the flexibility provided by the working fluid offers a great degree of flexibility for an ORC. As ORCs operate across a wide range of heat grades, over 600 pure and zeotropic mixtures were investigated by previous studies; their feasibility depended on their suitability to the cycle characteristics. At the same time, the ORC industry is not unanimous on the choice of fluids for the same application [91]. This study considered multiple fluids, some of them outside the realm of traditional ORC Fluids. Organic compounds frequently studied included alkanes, alkenes, alcohols, fluorocarbons (FCs), chlorofluorocarbons (CFCs), perfluorocarbons (PFCs), perchlorocarbons (PCCs), hydrochlorocarbons (HCCs), hydrochlorofluorocarbons (HCFCs), hydrochlorofluoroolefins (HCFOs), carboxylic acids, fluoroketones, ethers, aromatic hydrocarbons, carbonate esters, hydrofluoroethers (HFEs), hydrofluoroolefins (HFOs), halons and xylenes.

The basic constituents for HFCs, CFCs and HFOs are hydrogen, fluorine and carbon. Whereas HFCs and CFCs consist of saturated organic compounds, HFOs are alkenes constituted of unsaturated organic compounds composed of hydrogen, fluorine and carbon [127]. The utilised inorganic compounds included hydroxides, hydrogen nitrides (ammonia), halogens and nitrogen oxides. Siloxanes and refrigerants are classified as both organic and inorganic compounds. Previous research work conducted pertained mainly to the study of suitable working fluids for the best cycle efficiency [34, 38, 40, 51, 55, 57, 128-134]. Based on this previous research, this thesis undertook a study to establish the desirable properties of ORCs, focussing on thermodynamic, expansion, safety and environmental factors.

### 2.5.1 Thermodynamic factors

The working fluid density, latent heat of vaporisation, liquid heat capacity, viscosity, thermal conductivity, freezing point temperature, critical pressure and temperature, maximum operating pressure and mass flow rate are the key thermodynamic parameters, as elaborated below [40, 135].

- Higher fluid density results in smaller component sizing, particularly, of the expander, valves and pipeline. However, it leads to a reduction in the amount of enthalpy extracted by the expander and lower expander operating speed [130]. Lower density leads to a larger volumetric flow rate, which improves the efficiency of the turbine and pumps but leads to larger component sizes [32, 64, 136].
- Higher latent heat of vaporisation enables a larger amount heat transfer during the phase change of the fluid in the evaporator [60]. High latent heat also tends towards more isentropic expansion of the fluid, reducing condensation during expansion and entropy loss during condensing.
- Lower liquid specific heat capacity results in a vertical saturated liquid line with benefits similar to high latent heat of vaporisation, but increases the pump work [89].
- Lower value of viscosity reduces pump power consumption [137]. It also increases the conduction heat transfer coefficient, which reduces the heat exchanger area.
- Higher value of thermal conductivity reduces the heat exchanger area [67].
- The freezing point temperature at the condensing pressure needs to be lower than the minimum annual ambient temperature, to ensure that the stored working fluid remains in the liquid phase and ensures its circulation.
- For subcritical cycles, the critical pressure and temperature needs to be higher than the maximum operating temperature. While operating near the critical pressure, minor changes to the temperature results in large changes in working fluid pressure, which make the behaviour of the system difficult to predict. For practical sub-critical industrial systems, the working pressure at the upper limit of the cycle does not exceed 70% of the critical point of the fluid at that given temperature [102]. Higher critical pressures allows higher operating pressures and cycle efficiency [32].
- Higher operating pressure allows higher fluid temperature, thus leading to higher expander inlet enthalpy, pressure ratio and power output. Hung et al. reported that the cycle efficiency is a strong a function of inlet temperature, which in turn is a function of operating pressure on saturated working fluids [53].
- For a given amount of electrical output, the mass flow rate of fluid depends on the cycle efficiency. The cycle efficiency in turn is a function of the expander and pump efficiency. Lower mass flow rates ensure smaller and more economical component sizes, less space requirement and reduced operating costs.

### 2.5.1.1 Expansion behaviour of working fluids

Fluids are classified based on their saturated liquid-vapour line in the T-s Diagram, as shown in Figure 2-12. Isentropic fluids are those fluids having a vertical line with an infinite slope for the liquid-vapour line [44]. In an isentropic expander, the working fluid exits the expander in the same phase as that in which it enters. Wet fluids demonstrate a negative state of phase line along the T-s gradient [138]. Fluids of this type have the working fluid exiting the expander in a wet state after isentropic expansion, which helps release greater enthalpy to the expander but could lead to expander damage due to the wetness created at the expander exhaust; this can be avoided by superheating. Fluids that are following a positive slope for the saturated liquid-vapour line are known as dry or overhang type slopes. After undergoing isentropic expansion, the working fluid leaves the expander in a superheated state. ORCs operating with dry fluids typically use a recuperator or pre-condenser to reduce the temperature of the working fluid after the expander and before the condenser. Lecompte et al. reported that the potential for dry fluids in recuperative ORC cycles is only limited by a heat exchanger cooling limit [58].

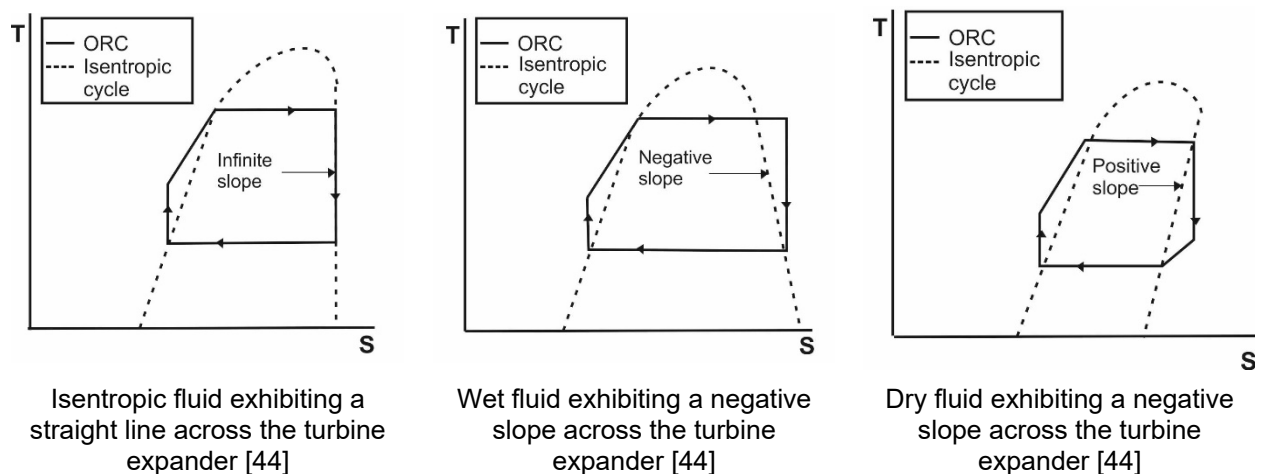


Figure 2-12: Wet, isentropic, and dry expansion [44]

Supercritical cycles use higher evaporation pressure and heat the working fluid directly to a superheated vapour phase (that is, above the critical point of the fluid), as shown in Figure 2-13. They do not demonstrate a typical phase change in the evaporator and vapour-liquid separation in the evaporation drum. Also, they do not undergo multiple thermosyphon-based recirculation cycles in the evaporator tubes and drum as is seen in saturated fluids [139]. Instead, they pass once through the evaporator and immediately enter the supercritical phase. Due to the poor heat transfer coefficients of a gas medium, they require a greater heat transfer area [44].

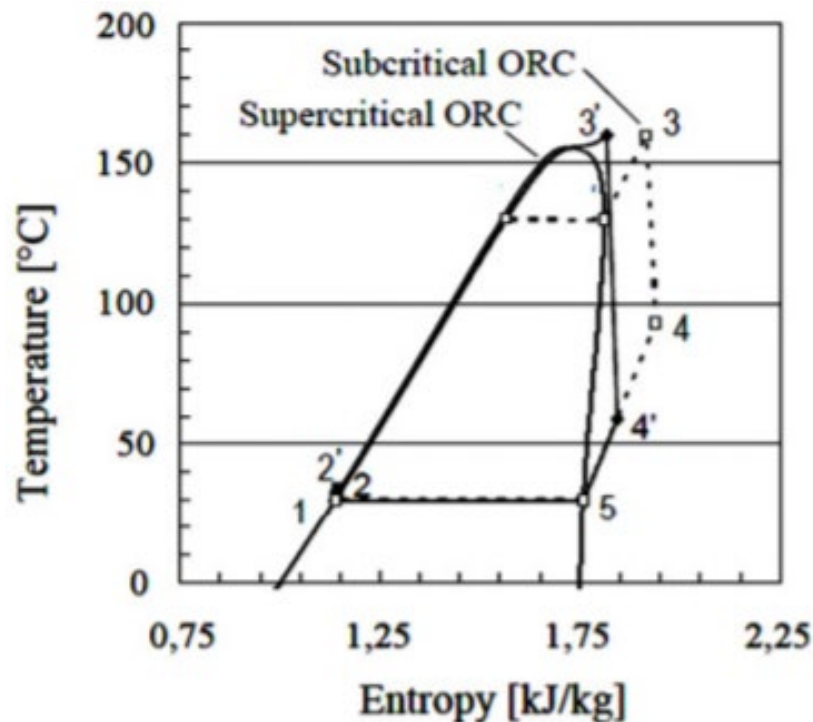


Figure 2-13: Comparison of subcritical and supercritical expansion of ORC Fluids [15]

## 2.5.2 Safety and environmental factors

Ozone depletion potential (ODP) determines the damage caused by a fluid's molecules to ozone molecules in the upper atmosphere. Pronounced thinning of the ozone layer has taken place in polar regions, particularly Antarctica, as illustrated in Figure 2-14 [140]. Therefore, it is advisable to choose a fluid with low or zero ODP, which could continue in production for the foreseeable future [141]. CFCs are high in ODP and were banned by the Montreal Protocol of 1989 [142]. CFCs were replaced by HCFCs, which demonstrated at least six times lower global warming potential (GWP) [143].

The United States Environmental Protection Agency's (EPA's) Significant New Alternatives Policy (SNAP) plans to phase out hydrochlorofluorocarbons (HCFCs) with hydrofluorocarbons (HFCs) after 2024 [144, 145]. As per the Kigali Amendment, HFCs will further be phased out by developed countries before 2036, to reduce projected global average warming by 0.2–0.4°C in 2100 [146]. Hydrofluoroolefins (HFOs) have been developed as low ODP replacements for HFCs and HCFCs. Working fluid manufacturers recently developed a new generation of HFOs such as R1234yf, R1234ze(E) and R1234ze(Z) [147] to replace HFCs and HCFCs globally.

The GWP determines the potential contribution of a fluid towards global warming, which has been described as the largest threat to life on Earth [148-151], due to which this study restricts itself to low GWP fluids. The release of working fluids into the atmosphere usually occurs

through leakage during operation and at the end of their service life [152]. The additional hydrogen atom possessed by HCFCs decreases their stability; the shorter atmospheric lifespan prevents them from reaching the ozone layer [153]. Common parameters used to monitor the fluid toxicity level include LC50 (lethal concentration for 50% of animals), IDLH (concentration deemed to be immediately dangerous to life and health), permanent exposure limits (PEL) and carcinogenicity [154].

Flammability is a major hazard if lower chain hydrocarbons are used, as ORCs operated at elevated temperatures might exceed a hydrocarbon's autoignition temperature [155], that is, the lowest temperature at which a fluid spontaneously bursts into flames, without any external energy source [156]. Thus, the ODP, GWP, toxicity and flammability are critical safety and environmental parameters, summarised for thermodynamic suitable working fluids in Table 2.1

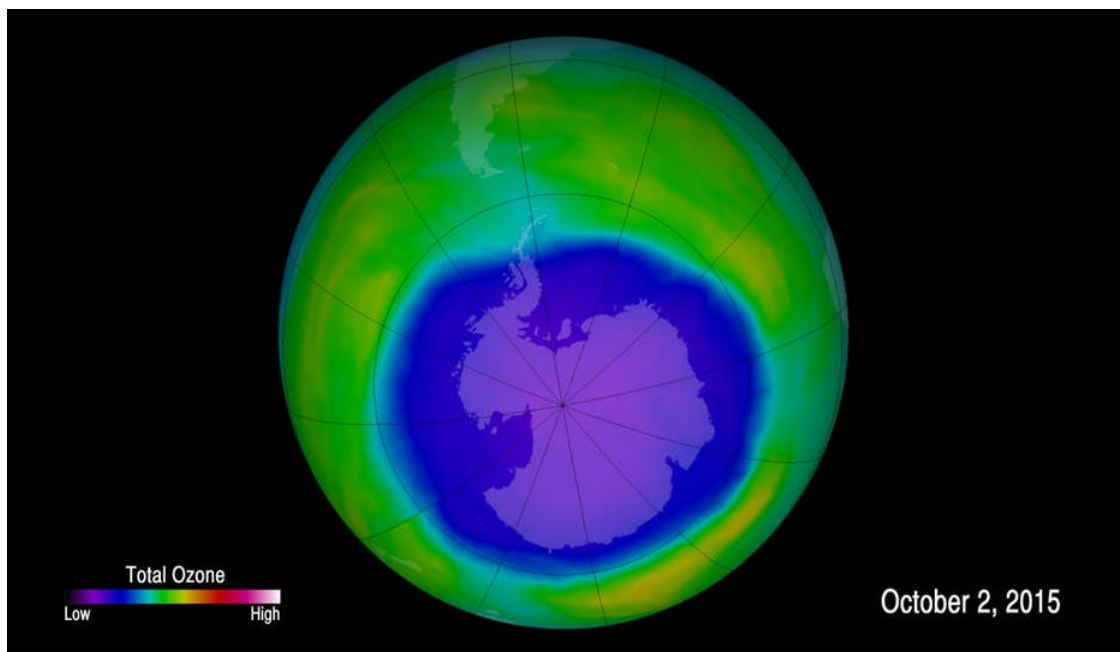


Figure 2-14: False-colour image showing ozone concentration above the continent of Antarctica on 2 October 2015 [135]

Table 2.1: Safety and Environmental classification of organic fluids, in increasing order of global warming potential

<b>Fluid</b>	<b>GWP [157, 158]</b>	<b>ODP [157, 159]</b>	<b>Flamm- ability [160]</b>	<b>Toxicity [160]</b>	<b>Carcino- genicity [161]</b>	<b>Volatility [40]</b>	<b>Atmos- pheric Life [157, 159]</b>
NOVEC 649/1230	1	0	No	No	No	No	5 days
Isobutane (R600a)	3	0	Highly	No	No	Yes	12 years
Butane (R600)	4	0	Highly	No	No	Yes	12 years
Pentane (R601)	4	0	Highly	Yes	No	Yes	12 years
Isopentane (R601a)	4	0	Highly	Yes	No	Yes	12 years
Cyclopentane	4	0	Highly	No	No	Yes	3 days
R 1234yf	4	0	Mildly	No	No	No	11 days
R 1234ze-E	6	0	Mildly	No	No	No	14 days
R 1234ze-Z	6	0	Mildly	No	No	No	14 days
HDR 14	7	N.A.	No	No	No	No	35 days
HFE 7000	530	0	No	Low	No	High	5 years
R141b	725	0.11	No	No	No	Yes	9.3 years
R365mfc	782	0	No	No	No	No	8.6 years
R245fa	930	0	No	Low	No	No	7.6 years
SES 36	1000	0	No	No	No	No	8.6 years
R134a	1300	0.0001	No	No	No	No	13 years

R134a was the most widely used fluid for heat sources up to 110°C. R134a will be phased out after 2024 from its primary purpose as a refrigerant, due to its high GWP (13000), although it was the first chlorine-free HFC replacement for R12 [162, 163]. R245fa was developed by Honeywell, primarily as a non-ozone depleting alternative for closed cell foam spray insulation and a medium-grade ORC working fluid. It has been widely used for heat temperatures up to 150°C [164]. In spite of its ideal thermodynamic properties, R141b had to be excluded from this study due to its high GWP [165]. R12, R113, R114 and R500 were not considered due to their high ODP and GWP values [43]. R1234yf, R1234ze-E and R1234ze-Z were developed as low GWP replacements for R134a as low-grade working fluids [166]. R1234ze-Z is an isomer of R1234ze-E, with greater prospects for lower heat source temperatures of up to 183°C [167]. HD-R14 is another working fluid under development, which can serve as a replacement for R245fa. The limited details obtained demonstrated promising properties [158].

### 2.5.3 Selection of working fluid based on heat source and sink

As ORCs operate within finite heat source and sink temperatures, maximising the pressure drop between these temperatures is vital for working fluid selection. Rowshanie et al. [168] concluded that the optimum working pressure and temperature were key determiners for cycle efficiency. These parameters vary for different working fluids based on their T-s diagram. Assuming a heat source temperature of 165°C and pinch point of 5°C, a working fluid temperature of 160°C could be attained. 20°C of superheating was considered, due to which the saturation pressure at 140°C was noted. Superheating allows for the safe operation of working fluids during transient flow conditions.

The heat sink temperature was assumed as 25°C, along with a pinch point of 5°C. This restricted the saturation pressure of the working fluid at the expander outlet to the equivalent of 30°C saturation temperature [169]. At this temperature, most fluids were observed at a pressure greater than atmospheric; this eliminated the requirement for a vacuum system. The saturated temperature at atmospheric pressure was used to evaluate the fluid phase during storage at room temperature. Pressure ratios and ideal cycle efficiency were calculated based on the saturation pressures corresponding to 140°C and 30°C; these used for expander efficiency and overall cycle loss determination.

This study preferred subcritical cycles as their heat exchangers were easier to design and tolerated heat source intermittency. Fluid classifications based on their isentropic expansion behaviour identified the suitability of energy recovery devices downstream of the expander. Working fluid properties were incorporated from the REFPROP database into an Engineering Equation Solver (EES) model [84, 170]. Table 2.2 features the thermodynamic properties of working fluid

Table 2.2: Working fluid properties of fluids operating between 140°C and 30°C

Refrigerant	Critical pressure	Critical temperature	Saturation pressure at 160°C	Saturation pressure at 140°C	Saturation pressure at 30°C	Type of fluid	Pressure ratio	Saturation temperature at atmospheric pressure	Ideal cycle efficiency
Units	kg/cm <sup>2</sup>	°C	kg/cm <sup>2</sup>	kg/cm <sup>2</sup>	kg/cm <sup>2</sup>		-	°C	%
R134a	40.6	101	Critical	Critical	7.706	Wet		-26.37	Critical
R245fa	36.5	154	33.81	28.15	1.772	Dry	15.89	14.86	8.241
R141b	42.5	204.2	21.1	14.9	0.92	Slight Dry	16.20	31.7	8.771
HFO R1234yf	33.8	94.7	Critical	Critical	7.835	Isentropic		-29.78	Critical
HFO R1234ze-E	36.3	109	Critical	Critical	75.796	Isentropic		-19	Critical
HFO R1234ze-Z	35.3	150.1	35.25	29.49	2.112	Wet	13.96	8.9	8.577
SES36	28.49	177.6	21.04	14.62	0.8298	Slight Dry	17.62	35.34	7.872
NOVEC 1230	18.69	168.7	15.9	10.81	0.4965	Very Dry	21.77	48.67	6.572
HFE 7000	24.8	164.6	22.84	15.8	0.8682	Very Dry	18.20	33.82	7.461
Butane	37.96	152	Critical	31.14	2.84	Dry	10.96	-0.8	8.369
Isobutane	36.4	134.7	Critical	Critical	4.04	Dry		-12	8.237
Pentane	33.6	196.5	18.92	13.29	0.826	Dry	16.09	35.49	8.275
Isopentane	33.7	187.2	22.02	15.7	1.09	Dry	14.40	27.48	8.229
Cyclopentane	45.7	238.6	13.97	9.716	0.5135	Dry	18.92	48.86	8.926
R365	32.7	186.9	20.37	13.97	0.6923	Dry	20.18	39.82	8.082

## 2.6 Classification of ORC expanders

Expander selection was previously identified as the most important contributor to cycle efficiency [86]. Expander type selection for medium-sized, low- to-medium-grade heat sources is controversial [171-178]. The technical criterion deemed important by this study were the expander efficiency, internal leakages, rotational speed, scalability, equipment size, off-design operation, complexity and torque variation across a revolution. The commercial criterion considered were the acquisition cost, maintenance cost, operator supervision requirement, ease of availability and proven track record for industrial use.

The expanders were broadly categorised as volumetric and velocity-based expanders [89]. Volumetric expanders are positive displacement expanders that undergo a pressure drop by increasing the volume of the expansion chamber along the passage of flow. The ratio between the chamber volume at the beginning and end of the expansion process is known as the volume ratio, and is typically between 2 and 6 [55]. The volume ratio of such expanders is fixed, integral to expander design and defines the maximum amount of work per cycle. A complete redesign of the expander is required for a change in operating parameters. This also causes over- and under-expansion losses if the expander runs at off-design conditions, limiting its suitability for transient heat sources [179].

Limited operational flexibility is provided by varying the operating speed. Additionally, since all volumetric expanders are positive displacement machines, they suffer a performance drop during operation with low density working fluids. Volume-based expanders include reciprocating piston expanders, scroll expanders and screw expanders, which are discussed in detail in the next section. Compared to velocity-based expanders, volumetric expanders are more suitable for dealing with higher pressure ratios and operated at lower rotational speeds and flow velocities.

Velocity-based expanders undergo expansion by passing flow through a row of nozzles. The reduction in pressure and temperature converts the flow energy of the fluid into kinetic energy by increasing the velocity. The kinetic energy is captured by the moving blades, and then rotated and converted into shaft power. As the speed of the moving blades is proportionate to the fluid velocity, velocity-based expanders operate at higher speeds than volume-based expanders, typically requiring speed reduction gearboxes, but reducing the number of moving parts.

An effective increase in volumetric flow rate is generated by increasing the flow velocity and vane area. The change in the vane geometry allows a single turbine frame to cater to a variety of fluid flow conditions.

## 2.6.1 Volumetric expanders

### 2.6.1.1 Scroll expander

Scroll expanders use two interleaved scrolls, with the first scroll being fixed, and the second scroll orbiting eccentrically around the first scroll, as shown in Figure 2-15. In this study, it was observed that pockets of fluid were trapped between the scrolls and underwent expansion. Previous studies observed that high expansion efficiency, tolerance to two-phase flow and low rotating speeds benefit scroll expanders [180]. Scroll expanders have been used for ORC applications on a microscale from 0.1 kW up to 10 kW [174, 181]. Empirical simulation models have achieved isentropic efficiency up to 68% [136]. Kaczmarczyk et al. undertook a trial of a 1.1 kW ORC system by running scroll expanders in both series and parallel operations, and found an increase in expander efficiency with a series combination of 11.6% as compared to an 10.8% in parallel operation [182].

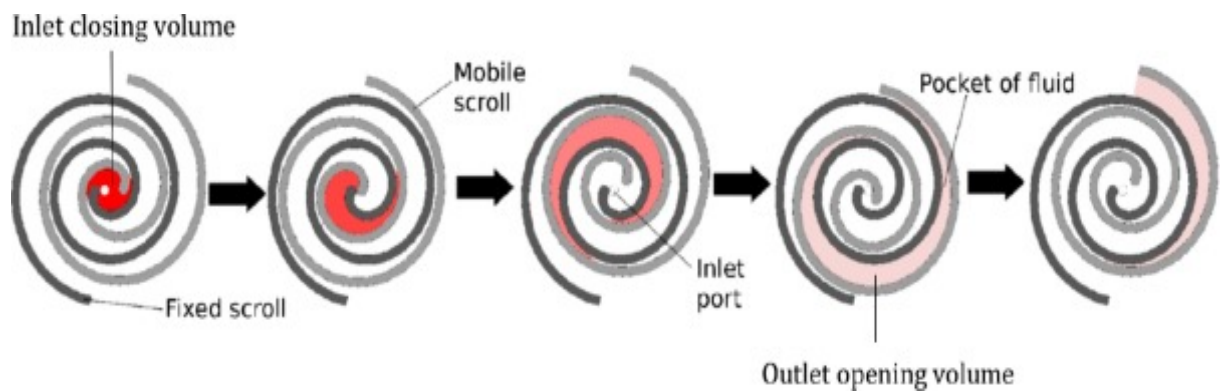


Figure 2-15: Working principle of a scroll expander [162]

Scroll expanders are limited by design to a fixed volumetric expansion ratio and under- and over- expansion losses at part load conditions. They are best suited for applications with a high-pressure ratio. External leakage occurs between the top or bottom plate and the shaft of the scroll, and an internal leakage occurs between the flanks of the scroll and the scroll housing, contributing to a significant proportion of the performance loss. The internal leakage increases exponentially with increase in pressure ratio [183]. Scroll expanders require continuous lubrication between the fixed and moving scrolls. A technical benefit is the ability to modify commercial scroll compressor seals, ports and added pressurised oil lubrication systems to operate them as expanders [174].

### 2.6.1.2 Screw expanders

Screw expanders utilise two helical screws, due to which the expansion of working fluid between the passage created is converted into shaft power, as shown in Figure 2-16. Gearing between both the screws ensures that the expansion timing and clearances between the screws is maintained. Compared to scroll expanders, screw expanders are more suitable for larger volumetric ratios (greater than 5), demonstrating high reliability and proven operating performance, as screw compressors usually operate at 1500 or 3000 rpm [164].

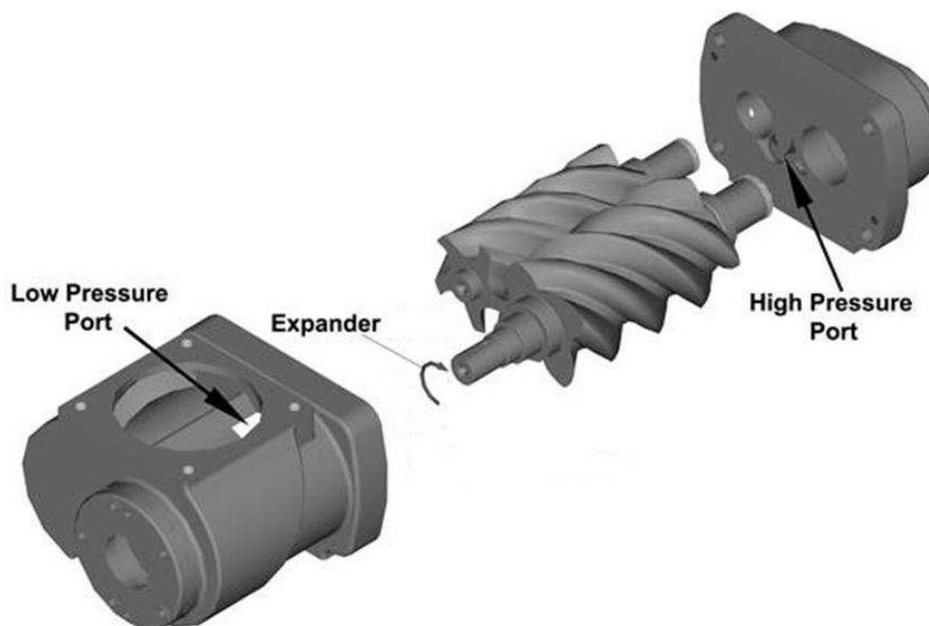


Figure 2-16: Exploded view of a typical twin-screw expander [165]

Screw expanders require lubrication via a mixture of working fluid and oil. The heat generated by the localised bearing friction causes the working fluid to evaporate and the residual oil is used for lubrication. This limitation restricts the choice of working fluids at the high-pressure end bearing to a temperature lower than the bearing oil temperature. Oil-free designs are currently under development.

Screw expander efficiency is sensitive to the clearance and volumetric flow rate. A clearance of the order of 50 microns is usually maintained between the screws and the outer housing [176]. This clearance is practically difficult to achieve for larger machines due to manufacturing limitations. An increased clearance leads to an increase in leakage flow to unacceptably high values which limits expander suitability for medium- and large-sized systems. Larger machines require a larger screw diameter or operating speed, which leads to higher tip velocity and generates additional secondary losses. Previous studies considered a tip velocity of 60 m/s as the upper limit without a significant compromise in leakage flow, which limited the male rotor diameter to 420 mm, for a 3000 rpm machine [176].

### 2.6.1.3 Reciprocating piston expanders

Two stroke reciprocating piston expanders have been used for expanding steam for over 140 years and are now witnessing renewed interests vis-à-vis ORCs [171, 177]. The fluid undergoes expansion, pushes the piston in the outward direction to convert the potential energy of the fluid to linear kinetic energy (Figure 2-17), which is then converted to rotational shaft power by the crankshaft. The working fluid is vented through the exhaust port during the return stroke. Larger piston expanders use multiple pistons and synchronise the port timing with the help of a camshaft. All cylinders are connected to the crankshaft, which transmits the mechanical shaft power generated.

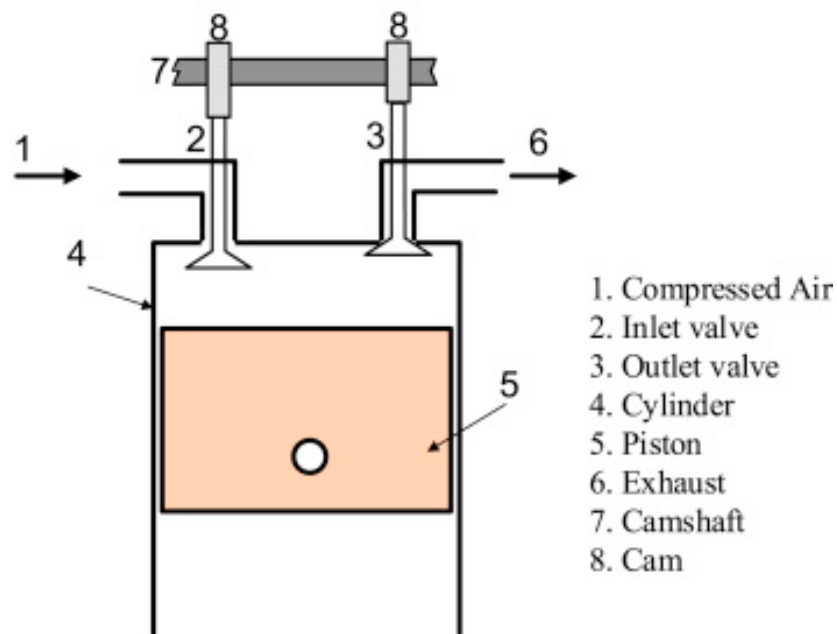


Figure 2-17: Working principle of reciprocating piston expander with a double valve reciprocating expander [166]

Reciprocating piston expanders have the advantages of a matured manufacturing setup and the ability to work at high-pressure ratios. However, the system is inherently unstable, as energy is transferred in one of the two strokes. The primary output is generated in a linear motion, and then converted to rotary output. Balancer shafts are usually required to counter the weight imbalance of the piston and crankshaft. This expander has the highest number of moving parts, resulting in large frictional losses. Piston expanders also require overhauling at regular intervals. In addition, they undergo torque pulsation, despite optimised cylinder timing sequences, due to the limit in the number of pistons, instead of providing continuous torque over a complete rotation like all the other expanders considered. They are suitable for 20 to 100 kWe [184].

#### 2.6.1.4 Rotary vane expanders

Rotary vane expanders are typically used for expanding air in high-risk spark-free environments. They operate with a single rotor along with moving vanes in a circular orbit (Figure 2-18); the multiple vanes providing steady torque. Rotary vanes are reported to handle pressure ratios up to 10 [180]. They have the advantages of a linear power curve, self-priming and operation at typically low speeds up to 3000 rpm [89]. Fukuta et al. experimentally determined the leakage of working fluid across the vanes, which played a major role in determining expander efficiency [185]. Yang et al. developed an experimental expander that used springs to minimise fluid flow leakage between the vanes and boundary walls [173]. Despite this, the maximum expansion efficiency attained so far has been 29%, and scalability beyond microgeneration remained a serious issue, with the largest possible size estimated at 10 kWe [186].

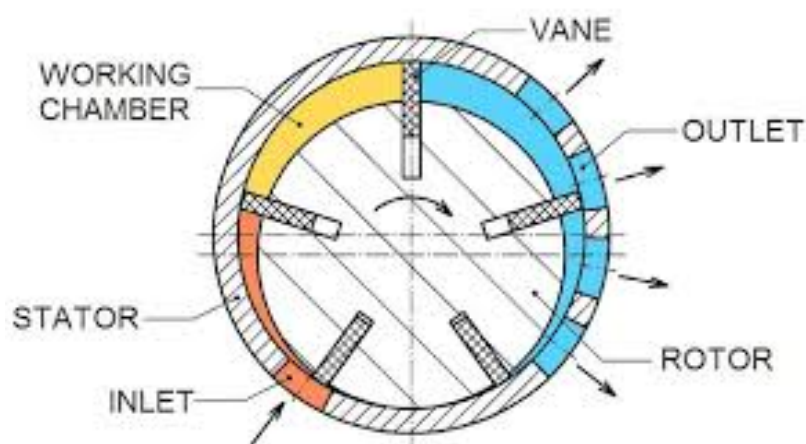


Figure 2-18: Working of a rotary vane expander [170]

#### 2.6.2 Velocity-based expanders (turbines)

Whereas volumetric expanders varied the size of the expansion chamber, turbines undertook expansion by imparting velocity to convert the static enthalpy of the working fluid into kinetic energy using the stationary nozzles, which was then recovered by the turbine's moving blades. Weiß concluded that compared to volumetric expanders, turbines offered superior reliability, greater scalability with volumetric flow rate, greater scalability with pressure ratios, relatively simpler sealing systems, reduced wear and tear, similar tolerance to wetness and minimum vibration, but were limited by lower operation speeds [178].

They demonstrated high flexibility to accommodate various expansion ratios by varying blade geometry. As impulse turbines could operate with variable admission arcs, they were better suited for part load operation than volumetric expanders [187]. The turbines can be broadly classified into axial flow, radial flow, and mixed flow machines, all regarded as highly reliable after a century of operation in steam, gas, nuclear and combined cycle-based power plants

[187]. ORC turbines differ due to their fluid properties and more critical sealing requirements but have similar overall dimensions.

### 2.6.2.1 Axial turbine

Axial turbines enable the entry and exit of flow parallel to the shaft of rotation (Figure 2-19). Single-stage axial flow turbines are used for fluids with a lower pressure ratio. A single set of stationary and moving blades demonstrates optimum performance up to pressure ratio of 4 [180]. Axial turbines offered higher scalability for volumetric flow than volumetric expanders by varying greater blade heights to improve overall profile efficiency and eliminating partial admission-induced pumping losses.

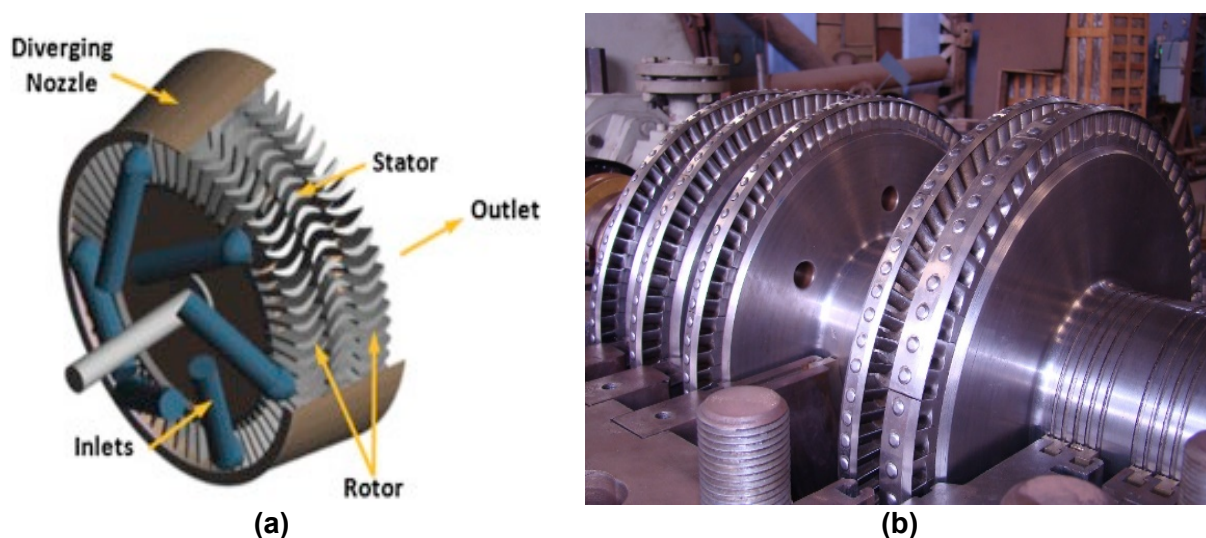


Figure 2-19: (a) Components of the two-stage axial turbine [172] (b) pictorial view of four stage impulse biased axial steam turbine

### 2.6.2.2 Radial turbine

Radial turbines enable the entry of working fluid in the radial direction, otherwise called radially inward turbines, whereas those operating with the direction of working fluid flow away from the shaft are called radially outward turbines (Figure 2-20). While the axial turbine rotor is 'impacted' by the flow of working fluid, the radial turbine uniformly orients the flow perpendicular to its axis, reducing mechanical stresses and unbalance. This was particularly important in the case of high-density fluids [180]. Compared to single stage axial turbines, radial outflow turbines are better suited to lower volumetric flow rates and higher pressure ratios, this because the flow towards a larger radius leads to an increase in flow path cross-sectional area [130]. However, radial flow turbines are not suitable for handling two-phase flow [188]. The complex vanes integral to the radial turbine rotors contribute to a significant increase in manufacturing cost when compared to axial turbines [61]. Radial turbines are less suited to transonic and supersonic flows as these flows face choking at the rotor vanes [178]. Lemort

and Quoilin [134] developed operating maps of the radial inflow turbine for various ORC working fluids. Alshammari et al. studied ORC expander design and found radial turbines suitable for micro- and small-scale ORC-based waste heat recovery applications [172]. Shao et al. developed a 1.884 kWe experimental radial ORC turbine using R123, noting that an increase in heat source temperature led to an increase in the efficiency of the radial turbine [189].

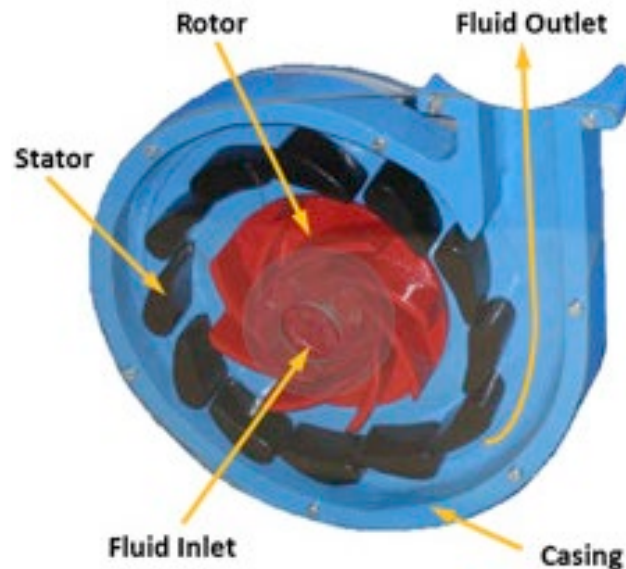


Figure 2-20: Construction of a single-stage radial inflow turbine [172]

### 2.6.2.3 Comparison between axial and radial turbines

Zhao et al. reported that axial turbines are generally rated for a higher power output [73]. Pethurajan et al. reported that previous ORC radially inward turbines are limited to experimental designs and a maximum power output of 5 kWe [180]. They also stated the tendency of the blades to heat up when operated at high temperatures. Blade cooling for radial turbines is generally more difficult than for axial turbines [180]. Al Jubori et al. conducted a mean line analysis of axial flow and radial inlet ORC microturbines, using the Moustapha et al. and Whitfield & Baines loss models. They validated the analysis using Computational Fluid Dynamics (CFD) modelling [190].

The reported peak isentropic efficiency for the axial and radial turbine was 82.5% and 79.05%, respectively. The efficiency deviation between loss models and CFD simulation was 3.84% for axial flow turbines and 3.38% for radial inflow turbines. Axial flow turbines are more widely used for ORC application due to their higher efficiency, superior reliability, design simplicity, reduced capital cost, relatively less wear and tear due to the reduced moving parts, minimum vibration and greater scalability for pressure ratios and volumetric flow rate [178]. Scalability is considered as a factor of paramount importance as the industrial grade heat source considered by this study could vary by quantity. A summary of all the expanders considered by this study is presented in Table 2.3.

Table 2.3: Summary of the comparison of expanders

Type	Capacity range (kW) [191]	Rotational speed (rpm) [191]	Cost	Advantages	Disadvantages
Axial Turbine	20 +	3000-14000	Medium	Flexibility for part load operation, highest upward scalability, widely proven, established manufacturing, limited tolerance to two-phase flow, small size	Downsizing for smaller sizes, limited tolerance for two-phase flow, gearbox typically required [178]
Radial turbine	1–100	8000–80,000	High	Lightweight, mature, high efficiency, widely proven, natural flow direction for radially outward turbine [178], small size	High cost, complex manufacturing, low efficiency in off-design conditions, limited to subsonic flow (Mach No. 0.85)[178], unsuitable for two-phase flow [180], gearbox typically required [178]
Scroll expander	1–10	<6000	Low	Medium efficiency, simple manufacturability, established manufacturing lightweight, low rotational speed, highest tolerance to two-phase flow [178], gearbox not required	Sealing issues, scalability, off- design performance

Type	Capacity range (kW) [191]	Rotational speed (rpm) [191]	Cost	Advantages	Disadvantages
Screw expander	15–200	<6000	Medium	High efficiency, simple manufacturability, established manufacturing, lightweight, low rotational speed, high tolerance to two-phase flow [178], gearbox not required	Sealing issues, unsuitable for transient operation
Reciprocating piston expander	20–100	<6000	Medium	High pressure ratio, mature manufacturability, established manufacturing, low rotational speed, adaptable to variable working condition, gearbox not required	Inherently unbalanced with heavy vibration, Torque pulsation, high maintenance, heavyweight, complexity, off-design performance, unsuitable for two-phase flow [178]
Rotary vane expander	1–10	<6000	Low	Stable torque, tolerance to two-phase flow, simple construction, low cost and noise, gearbox not required	Sealing issues, low capacity, low efficiency, unproven, less manufacturing setup

## 2.7 Non-dimensional parameters

Noting the advantages of the axial turbine, a detailed investigation into their design parameters was undertaken. The use of non-dimensional parameters was considered as a suitable approach for their scalability, unit-free approach and ease of understanding. They provided a preliminary approach to predict characteristics within a wide input parameter band for a typical machine within a reasonable limit. Dimensional approaches were seldom used to characterise turbomachines due to variations in working fluid, application and machine size.

### 2.7.1 Volumetric flow ratio

Volumetric flow ratio (*VFR*) refers to the ratio of specific volume of fluid at the exhaust ( $\dot{V}_{out}$ ) and inlet ( $\dot{V}_{in}$ ) of the turbine (equation 2.4) [190]. It accounts for fluid compressibility and density [60]. Lower volumetric flow rate results in greater blading efficiency, but not necessarily greater power output [77]. A higher volumetric flow rate suggested a higher enthalpy drop, hence, a greater likelihood of a multistage turbine, along with a larger diametric variation between the first and last stage. The larger number of stages increases the rotor manufacturing difficulty, cost, and the likelihood of critical speed related issues.

$$VFR = \frac{\dot{V}_{out}}{\dot{V}_{in}} \quad 2.4$$

### 2.7.2 Size parameter

Size parameter is defined as a function of the volumetric flow rate of the fluid at the expander exhaust  $\dot{V}_{out}$  and isentropic enthalpy drop  $\Delta h_{is}$  in equation 2.5 [191]. It is used for predicting the efficiency penalties due to flow compressibility and reduced blade heights. The enthalpy drop provides properties of the inlet and outlet fluid conditions, and the volumetric flow correlates the size parameter with the mass flow rate. ORC turbines usually maintain a size parameter between 0.02 and 1 [192-194].

$$SP = \sqrt{\frac{\dot{V}_{out}}{\Delta h_{is}}} \quad 2.5$$

### 2.7.3 Reynolds number

The Reynolds number (*Re*) is the ratio between inertial and viscous forces in the turbine flow passage. Arithmetically, it is a function of passage hydraulic diameter and fluid density ( $\rho$ ), velocity ( $v$ ) and dynamic viscosity ( $\mu$ ) (equation 2.6). It bears an implication in fluid flow and heat transfer governing equations and is used to predict flow behaviour patterns, classified as laminar, transient or turbulent.

Turbulence is generated due to differences in the fluid's relative speed that leads to the increase of inertia force in the direction of flow and causes eddy currents, which in return, cause churning in the flow and increase its entropy because of high intermolecular chaotic

motion. Previous studies determined that the Reynolds number had a significant effect on profile losses [192]. At high Reynolds numbers, the relative surface roughness of the blade ( $k_s$ ) played an important role, as it controlled the boundary layer of the flow (Figure 2-21) [193].

$$Re = \frac{\rho v D_H}{\mu} \quad 2.6$$

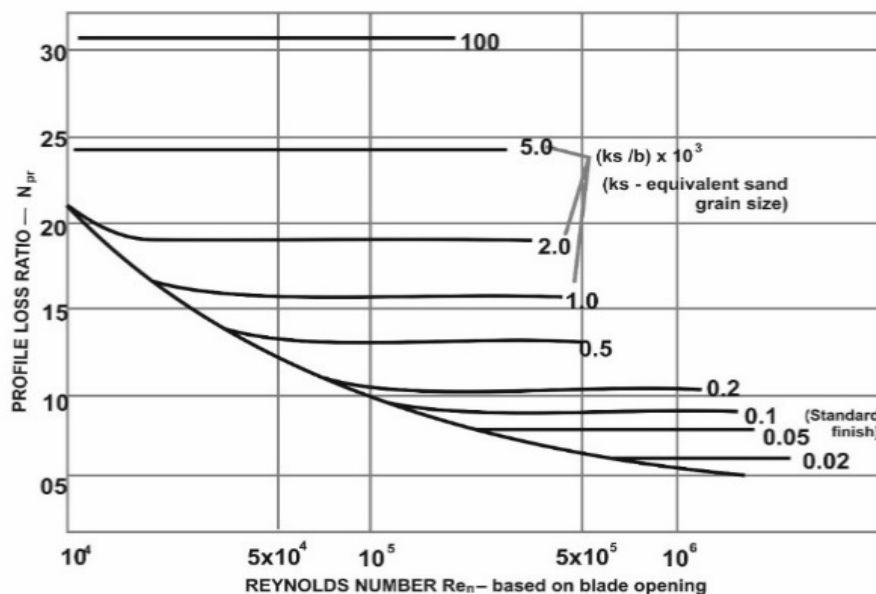


Figure 2-21: Craig and Cox correlated the effect of the surface finish with its induced profile losses [181]

#### 2.7.4 Velocity ratio

The velocity ratio ( $VR$ ) (equation 2.7) is the ratio between the velocity of the moving blade ( $U$ ) to actual velocity of the fluid passing across it ( $C_2$ ). It is significant in the case of ORCs as high  $C_2$  values are unavoidable due to low specific volumes and large volumetric expansion ratios [191]. Impulse turbines achieve a higher pressure drop per stage and are more cost effective, easier to operate and better suited for high velocity applications such as ORCs than reaction stages. As the velocity that can be captured by each row of moving blades is limited, two row and three row impulse designs were developed to capture larger enthalpy drops, albeit with a drop in efficiency. Kearton [197] stated that ideal values of velocity ratio for axial machines range between 0.2 and 0.3 for two row moving blade impulse biased Curtis stages, between 0.4 and 0.5 for a single row impulse machines and between 0.7 and 1.0 for 50% reaction stages, as shown in Figure 2-22 [194].

$$VR = \frac{U}{C_2} = \frac{\cos\beta_2}{\cos\beta_1} \quad 2.7$$

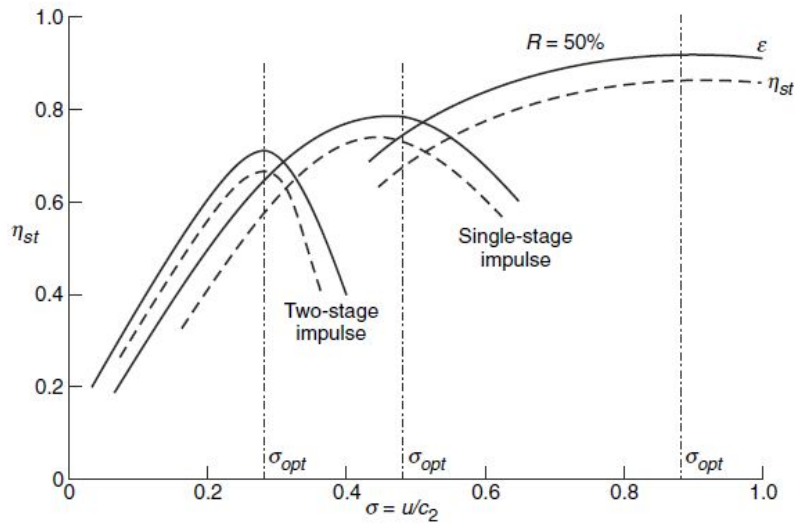


Figure 2-22: Velocity ratio for single stage impulse (Rateau wheels), two-stage impulse (Curtis wheels) and reaction disc axial stages [183]

### 2.7.5 Specific speed

Specific speed is used to scale turbomachinery independent of size, without impacting efficiency, for reasonable limits of Reynolds number. It considers the exhaust volumetric flow rate ( $\dot{V}_{out}$ ), rotational speed ( $N$ ) and isentropic enthalpy drop ( $\Delta h_{is}$ ), as in equation 2.8. Typical preliminary design of new turbines consider two of the three parameters as constraints, and an ideal value of specific speed is specified to obtain the third parameter [186]. Dixon reported that radial turbines performed efficiently at specific speeds between 0.3 and 0.9, as shown in Figure 2-23 [198].

$$N_{spec} = \frac{60 \times N \times \sqrt{\dot{V}_{out}}}{(\Delta h_{is})^{0.75}} \quad [199] \quad 2.8$$

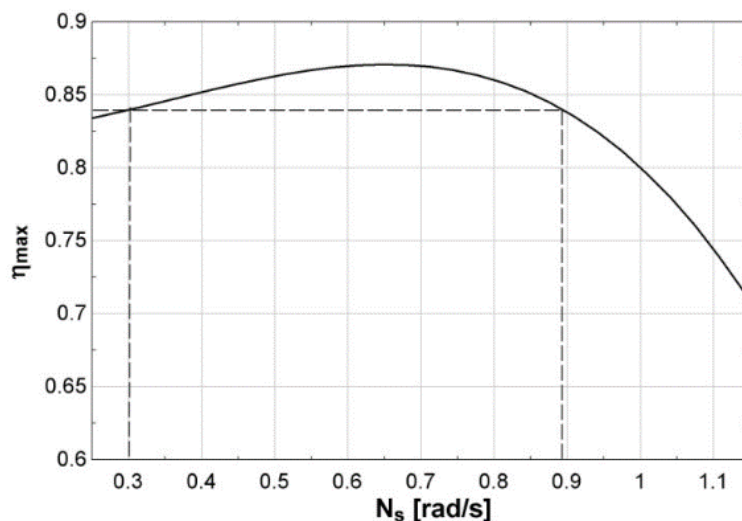


Figure 2-23: Max turbine efficiency versus specific speed for radial inflow turbine [158]

## 2.7.6 Specific diameter

The specific diameter ( $D_{spec}$ ) (equation 2.9) is used in conjunction with the specific speed, as Figure 2-24. It is used to determine the mean flow path diameter ( $D$ ), using the exhaust volumetric flow rate ( $\dot{V}_{out}$ ) and isentropic enthalpy drop ( $\Delta h_{is}$ ) [200]. Practical values for specific diameter tended to be slightly higher than those suggested by the Cordier line. The velocity ratio, specific speed and specific diameter are interdependent.

$$D_{spec} = \frac{D \times \Delta h_{is}^{0.25}}{\dot{V}_{out}^{0.5}} \quad [199] \quad 2.9$$

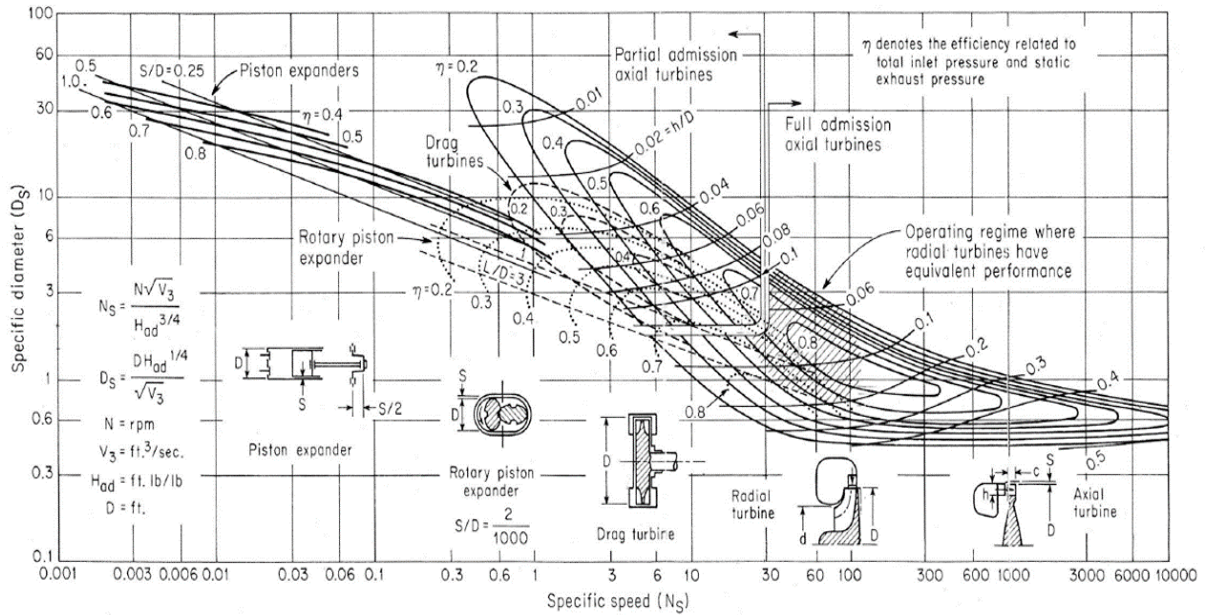


Figure 2-24: Efficiency correlation for expanders based on specific speed and specific diameter [186]

## 2.7.7 Pressure ratio

Pressure ratio is the ratio between the stagnation pressure at the outlet ( $P_{stg-Out}$ ) and inlet ( $P_{stg-In}$ ) of the turbine, as shown in equation 2.10. A higher-pressure ratio means an increase in enthalpy drop and work done by the turbine, leading to higher flow and load coefficients. The compatibility for expanders with pressure ratios has been discussed above in section 2.6

$$PR = \frac{P_{stg-Out}}{P_{stg-In}} \quad 2.10$$

## 2.7.8 Stage loading coefficient

The stage loading coefficient ( $\psi$ ) is used for deciding the number of stages. As the amount of turning work done by the fluids across the profile increases beyond the ideal loading coefficient, a great probability of primary flow detachment emerges, hence, increasing the secondary losses.

$$\psi = \frac{\Delta h_0}{(U_{in})^2} \quad 2.11$$

### 2.7.9 Flow coefficient

Flow coefficient ( $\Phi$ ) is the ratio of the fluid axial velocity after the stationary blades ( $C_{a2}$ ) to the meridional blade rotational speed ( $U$ ). Figure 2-25 shows the Smith chart [195] prepared in 1965, that is widely used for preliminary design by correlating the load and flow coefficients [196]. A reduction in enthalpy drop per stage leads to lower values of flow and load coefficient, thus improving efficiency. However, additional stages are required to accommodate the increased enthalpy drop. Alternatively, the flow coefficient can be reduced by reducing the axial component of velocity. For a given volumetric flow, this is compensated by an increase in blade height.

$$\Phi = \frac{C_{a2}}{U} \quad 2.12$$

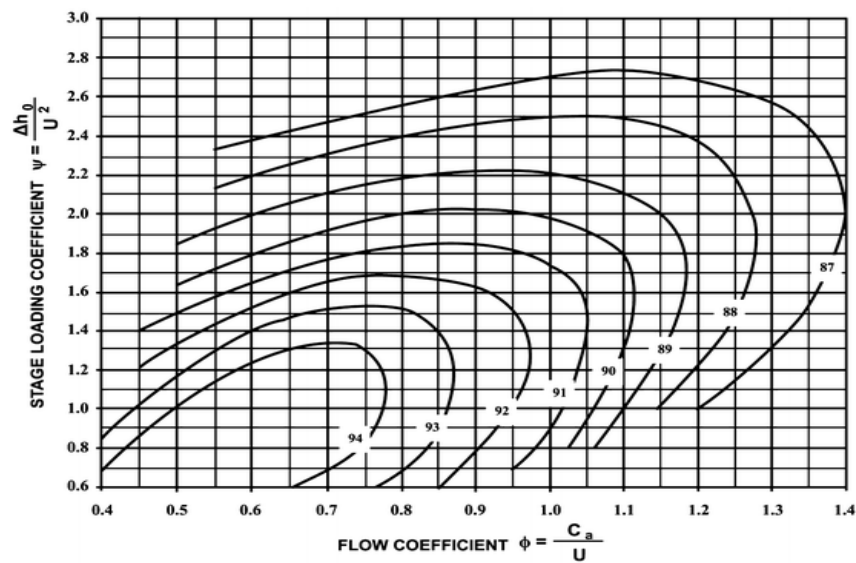


Figure 2-25: The Smith chart provided the correlation between the load coefficient, flow coefficient and efficiency [187, 189]

### 2.7.10 Degree of reaction

The degree of reaction ( $DoR$ ) is the ratio of the stagnation enthalpy drop across the moving blades to the enthalpy drop across the entire stage. It determines the distribution of expansion between the stator and the rotor. As the static enthalpy is simpler to calculate, preliminary studies typically restrict themselves to static enthalpy instead of stagnation enthalpy [203]. It is defined in equation 2.13. with  $P_1$  as the pressure before the stator,  $P_2$  as the pressure between the stator and rotor and  $P_3$  as the pressure after rotor. Based on the degree of reaction, turbines are classified as impulse stages, with a degree of reaction 0, where all the pressure drop is done in stationary blades and reaction stages with a degree of reaction of 0.5, where enthalpy drop is equally distributed between the stationary and moving blades, as shown in Figure 2-26. Real turbines are neither pure impulse or pure reaction, considering each profile contains some degree of frictional loss and associated entropy generation [178].

$$DoR = \frac{P_2 - P_3}{P_1 - P_3}$$

2.13

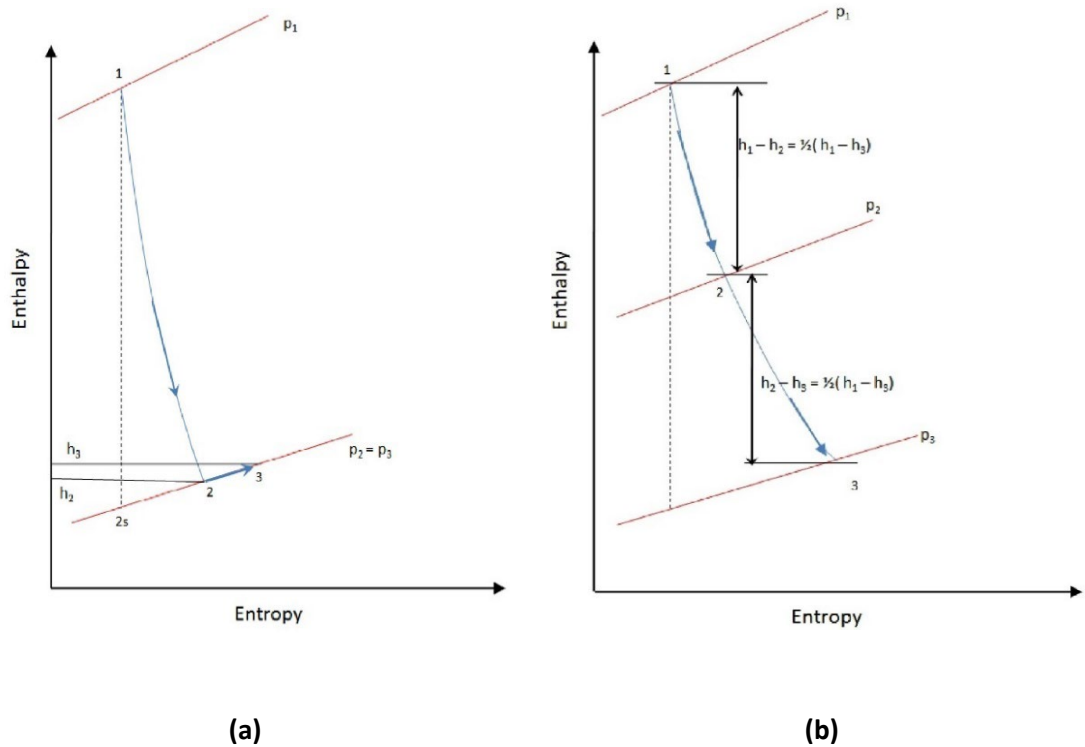


Figure 2-26: Isentropic enthalpy drop for (a) a pure impulse turbine with DoR 0% and (b) a high-reaction turbine with DoR 50%

Pure impulse machines have the benefit of a minimum pressure drop across the rotor, and lower axial thrust [197]. The first stage of large machines usually employs a highly impulse-biased stage for a large pressure drop, which reduces the casing internal pressure, rotor tip leakage mass flow and casing thermal expansion. Low reaction machines place higher importance on the design and manufacturing of the stationary blades.

As impulse turbines operate at higher velocities, they generally produced slightly lower efficiencies [178]. Typical impulse-biased stages have a degree of reaction between 5 and 15%. Reaction-biased turbines are highly sensitive to radial clearance due to flow leakage. To compensate the flow leakage across the rotor, reaction turbines are usually equipped with a rotor tip sealing mechanism with clearances lower than half a millimetre. This mandates greater importance to maintain fluid quality and avoiding the build-up of scale, rust or residue within the turbine [198]. Shrouding of the moving blade passages also helps to reduce the leakage flow and limits the secondary flow losses at the tip [199]. Additionally, reaction turbines do not support partial admission, limiting their flexibility for lower volumetric flow rates [178].

### 2.7.11 Zweifel loading coefficient

Zweifel coefficient is the ratio between the actual to ideal tangential forces acting on the blade as shown in equation 2.14; where  $chord_{axial\ length}$  is the axial chord length,  $s$  is the pitch,  $\alpha_2$  and  $\alpha_3$  are the absolute fluid flow angles at the entry and exit of the moving blades. It is used to determine the number of profiles used, and therefore the blade pitch [200]. Higher values lead to reducing spacing and increasing the number of blades. The reduced work done per blade reduces individual blade stresses and helps avoid resonant excitation modes. However, it leads to an increase in the surface area and induced frictional losses. Zweifel suggested a coefficient value within the range of 0.8 and 1.0; but values greater than 1 are normally used for modern Industrial machines. The reduced blade count associated with higher coefficient values is possible as the use of modern materials and three-dimensional profiles incorporating carefully controlled loading across all sections of the blade provide the ability to withstand higher individual blade stresses, while fewer blades result in reduced manufacturing costs [200-202].

$$Z = 2 \left( \frac{s}{chord_{axial\ length}} \right) * (tan\alpha_2 + tan\alpha_3) * cos^2\alpha_3 \quad 2.14$$

### 2.7.12 Solidity

Solidity is the ratio of axial chord length ( $chord_{axial\ length}$ ) to the mean pitch ( $s$ ), as stated in equation 2.15. It is prioritised above the Zweifel coefficient for preliminary design studies, as it does not require flow deviations from velocity triangles, due to its simple nature [210].

$$Solidity = \frac{chord_{axial\ length}}{s} \quad 2.15$$

### 2.7.13 Aspect ratio

The aspect ratio correlates between the blade height ( $ht_B$ ) and chord length ( $chord_{length}$ ), as stated in equation 2.16. Lower aspect ratios tend towards greater prominence of secondary flows. It is uncommon to change the chord length for a given profile; changes to optimise aspect ratio are undertaken by varying blade height. For impulse turbines, blade height is also varied for a given passage exit area by varying the degree of partial admission [211]. Maintaining the aspect ratios greater than 1 helps to ensure that the flow is attached to the profile and hence, limits the secondary losses [212]. Previous studies have observed that aspect ratio played a critical role in small turbines with lower blade heights [197].

$$Aspect\ Ratio = \frac{ht_B}{chord_{length}} \quad 2.16$$

### 2.7.14 Mach number

Mach number is the ratio of the local velocity of the fluid ( $c_{fluid}$ ) to the local in the given medium ( $SS$ ), as shown in equation 2.17 [213]. The speed of sound is a function of the specific heat ratio ( $\gamma$ ), universal gas constant ( $R$ ) and absolute temperature ( $T$ ). The fluid velocity increases proportionally with the enthalpy drop across the stage. Craig and Cox demonstrated a considerable efficiency drop for a profile operating in the transonic regime, where Mach numbers lie between 0.8 and 1.2 (see Figure 2-27). Turbine profiles operate at their best efficiency in subsonic conditions but operation at transonic or supersonic conditions is common for ORC machines due to the low speed of sound of ORC fluids.

A compromise is required between turbine efficiency and an increasing number of turbine stages. Impulse turbines operating in the supersonic regime typically require two or three rows of moving blades to capture the kinetic energy of the fluid. Supersonic flow is also considered to be more sensitive to off-design operation. While operating in the supersonic regime, beyond a certain point, volumetric flow increases and the Mach number remains constant; this is known as the choked flow condition [203]. White and Sayma remarked that small-scale single-stage ORC systems employ high expansion ratios relative to their blades heights, which usually leads to fluid flows in the supersonic regime at the moving blades [81].

$$M = \frac{c_{fluid}}{SS} = \frac{c_{fluid}}{\sqrt{\gamma RT}} \quad 2.17$$

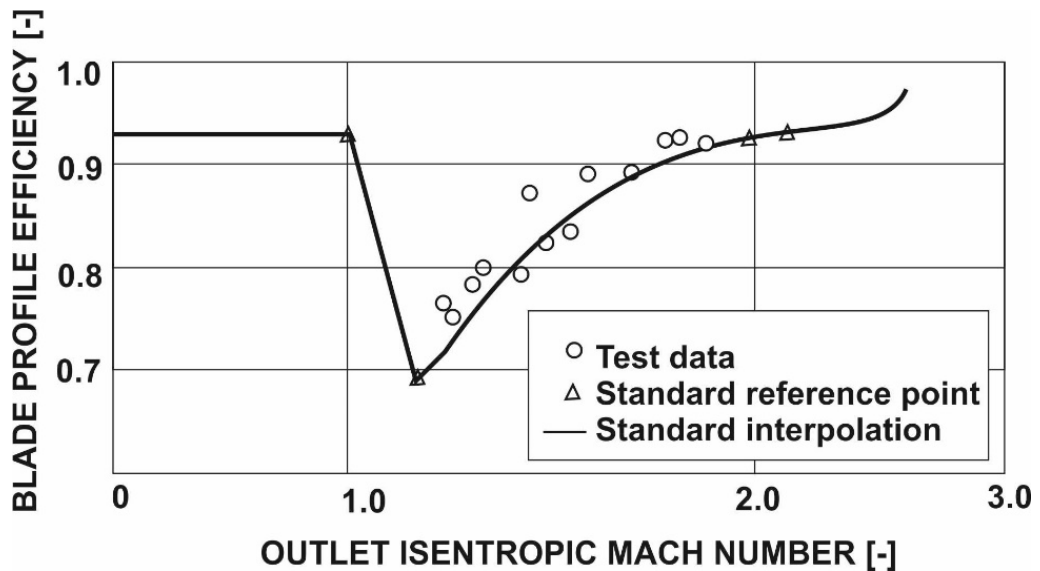


Figure 2-27: Correlation of Mach number with profile efficiency [181]

## 2.8 Turbine efficiency

Most previous studies assumed a fixed value of turbine isentropic efficiency, usually between 60% and 90%, due to the complex process of determining turbine losses and the lack of supporting literature [204]. Song et al. concluded that turbine efficiency has a significant impact on the selection of the working fluid and the cycle's overall performance [131]. Yamamoto et al. remarked that ORC performance is a strong function of the expander's operation [205].

White and Sayma observed significant differences in cycle efficiency when off design-point turbine efficiency was considered, particularly for heat source temperatures above 150°C, where an increase in the heat source temperature led to a 13% reduction in power outputs for thermodynamically optimum cycle configurations, this due to the large amount of superheating required for ideal subcritical cycles [81]. When turbine efficiency was considered as fixed, the optimal thermodynamic cycles produced the best results at conditions where real world turbine performance was worse due to high volumetric expansion ratios. A single-stage expander was concluded as the optimal configuration for small-scale applications with low heat source temperatures and low volumetric flow rates, despite intermittency in turbine efficiency due to high fluid velocity [81].

### 2.8.1 Design point loss models

There are two main approaches to predict design point turbine efficiency: direct and indirect. The direct approach consists of a group of individual losses collated into a loss model [192], while the indirect approach employs non-dimensional parameters. Soderberg's model, developed in 1949 and still widely accepted, was one of the first to use the direct approach [206].

The Craig and Cox direct loss model, developed in 1971 and validated by previous researchers, is still considered a reliable and accurate method for designing modern impulse-bladed axial flow turbines [207-210]. Macchi and Perdichizzi developed correlations between non-dimensional parameters and axial ORC turbine efficiency based on the Craig and Cox loss model [211]. Lazzaretto et al. employed an indirect approach to optimise the turbine efficiency, considering the volumetric expansion ratio and size parameter as performance predictors [212].

White and Sayma optimised a radial ORC turbine using similitude theory, wherein the size parameter, isentropic enthalpy drop, mass flow rate and volumetric expansion ratio were considered as non-dimensional parameters to maintain uniform fluid velocity [81]. Latimer observed that the validity of estimations based on empirical correlations was limited to a family

of scaled-up profiles and needed to be revised with the passage of time to consider improvements due to developments in CFD [213].

## 2.8.2 Off-design point loss models

For turbines operating with a transient heat source, it is also important to consider off-design losses, the importance of which depends on the fraction of unsteady flow. Advanced loss models factored the off-design correlation by studying the incidence losses. The Ainley-Mathieson loss model was the first to consider a wide range of profiles. It factored in the off-design loss by the ratio of the profile pitch to leading edge radius [214].

However, the loss model did not consider the leading-edge geometry and incidence-induced secondary losses, which overestimated off-design losses at high incidence angles up to a magnitude of 4 [215]. The off-design component of this loss model is considered unsatisfactory as it did not consider the shape, wedge and diameter of the leading edge [215].

Craig and Cox evolved the off-design losses to consider the loss factor independently for positive and negative stalling incidence, as shown in Figure 2-28 [192]. However, Ning Wei [216] concluded that the Craig and Cox off-design profile loss model overestimated the loss at large incidence angles as well as produced a sharp decrease in efficiency at the point of maximum positive incidence [124].

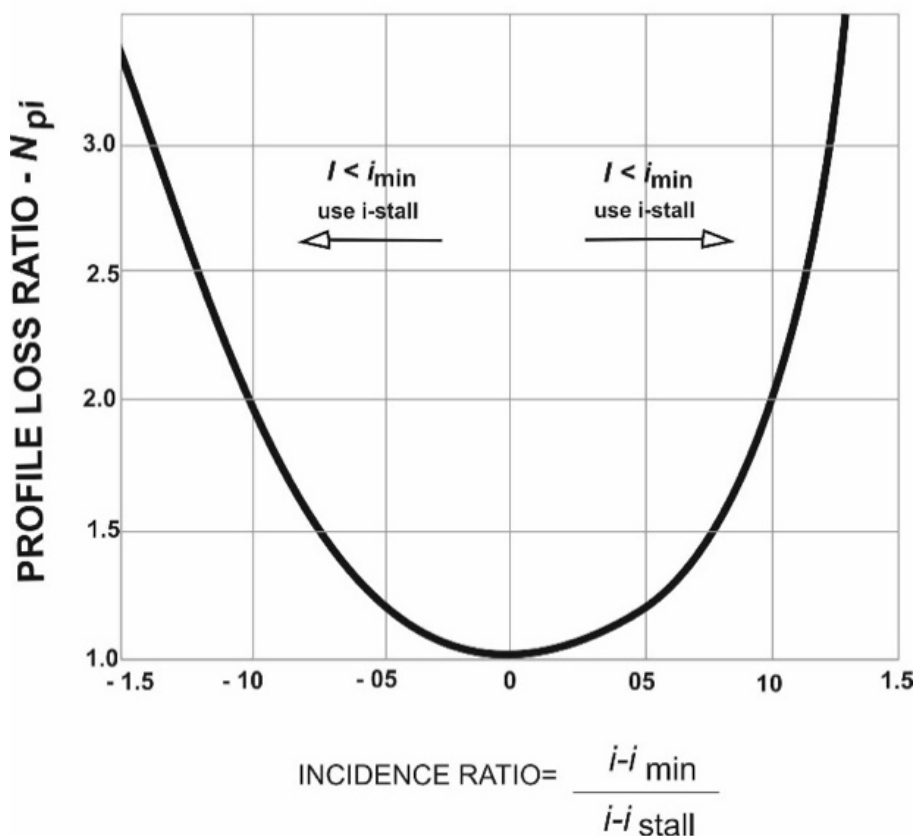


Figure 2-28: Craig and Cox calculated the positive and negative incidence loss independently [181]

Mukhtarov and Krichakin [217] were the first to consider the effect of the diameter of the leading edge and the secondary losses induced by the incidence loss. They determined the incidence loss as a function of incidence angle, convergence ratio, leading edge thickness and compressibility factor, but independent of incidence direction. However, the loss function was independent of the stalling direction and the results were limited to subsonic and transonic flow patterns with cascade geometry similar to those tested during their experiment.

Moustapha et al. observed that Mukhtarov and Krichakin had overpredicted the profile incidence losses [215, 217]. Whereas Moustapha et al. maintained the same influencing factors, they considered the convergence ratio using the metal angle of the blades instead of the gas angle. Moustapha et al. also concluded that the leading-edge's diameter significantly influenced the incidence losses as it determined the size of the horseshoe vortex developed at the leading edge.

### 2.8.2.1 Primary incidence loss

Along with the incidence angle, Moustapha et al.'s loss model also considered the ratio of the leading-edge radius to the pitch, which was deemed significant for the moving blade entry [215]. . Ning Wei observed that the Moustapha et al.'s off-design loss model was the only one that did not suffer from an erratic increase in loss estimation in the negative incidence region [216]. It provided an individual breakup of primary and secondary off-design losses. The improved primary loss prediction of Moustapha's loss model, compared to the Ainley-Mathieson and Mukhtarov-Krichakin models is shown in Figure 2-29.

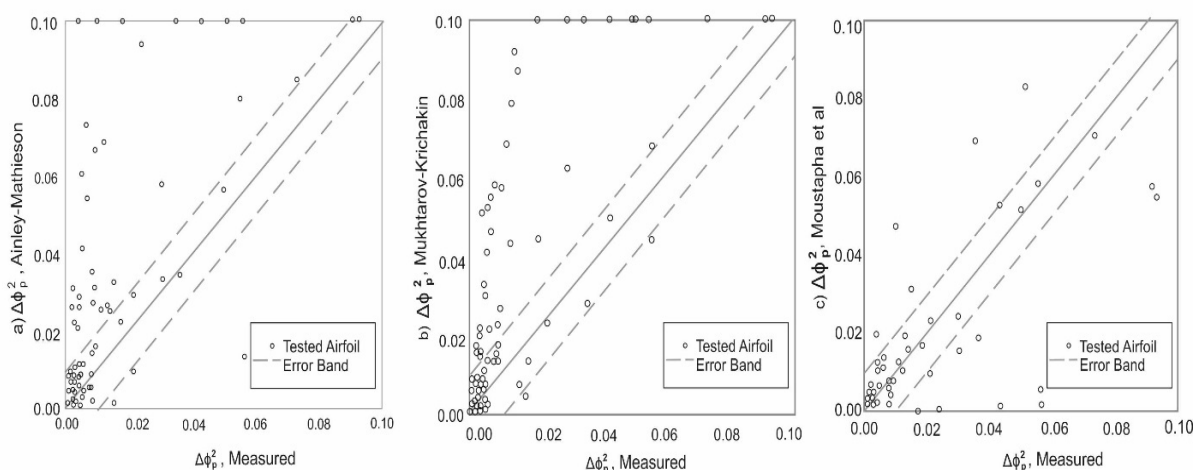


Figure 2-29: The primary loss correlation provided by Ainley-Mathieson [209] (a), and Mukhtarov-Krichakin [212] (b) was improved upon by Moustapha et al. [210] (c)

### 2.8.2.2 Secondary incidence loss

The secondary incidence loss predicted by Moustapha was based on the Mukhtarov-Krichakin loss model with the addition of the profile's leading-edge radius effect, similar to the primary incidence loss [215, 217]. Moustapha's secondary loss factor addressed the Ainley-Mathieson loss model's underprediction of profile losses for low-aspect ratio profiles operating with a large value of positive incidence [214]. Experimental validation undertaken is shown in Figure 2-30 [215].

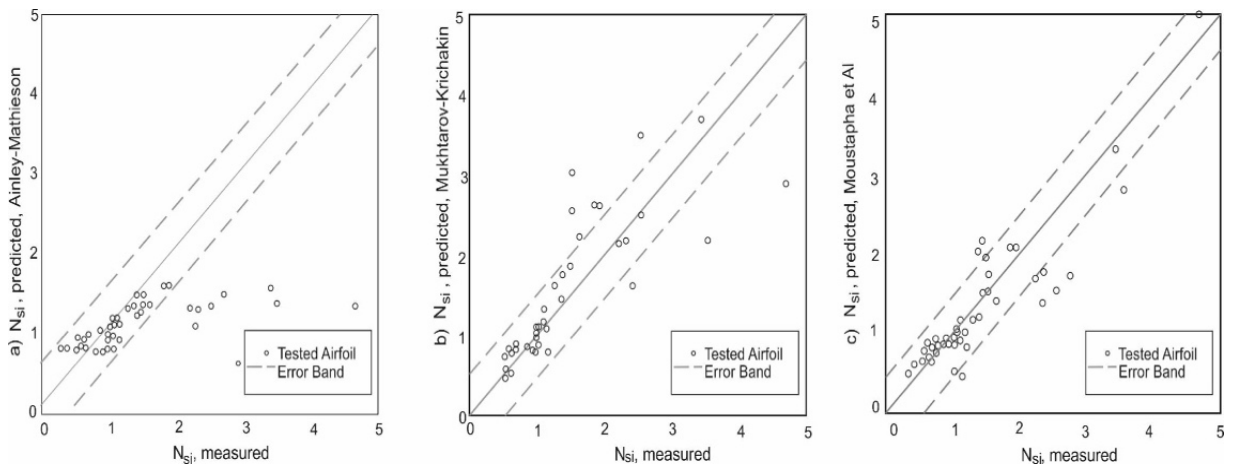


Figure 2-30: The secondary loss correlation provided by Ainley-Mathieson (a) [209], and Mukhtarov-Krichakin [212] (b) loss was improved upon by Moustapha et al. [210] in (c)

## 2.9 Cycle configuration based on operating conditions

Operating conditions such as the degree of superheating and pressure ratio significantly influence the turbine performance, and hence, the overall cycle operation of ORC. The admission of a working fluid at a high degree of superheating to the expander increases the thermodynamic potential across it for a given pressure ratio, thus providing theoretically economical solutions to improve expander power output [218]. However, extracting the additional thermodynamic potential of a superheated fluid depends on the fluid flow passage's losses [219].

Most previous theoretical studies proposed expanding the working fluid directly from the saturated condition at the highest possible pressure to maximise the power output, without considering variable turbine efficiency. Weiß et al. reported that the isentropic efficiency for small axial ORC turbines increased by almost 2% when the pressure ratio was changed from 16 to 22; equally, operating at pressure ratios below 14 marked a decrease in the isentropic efficiency up to 8% [220]. The steeper change in the isentropic efficiency at a low-pressure ratio was attributed to compression shocks in the convergent-divergent nozzle section. Multiple cycle configurations incorporate recuperation to improve cycle efficiency and reduce the effective thermal load on the boiler [221]. Recuperation extracts thermal energy from the

working fluid at the outlet of the expander to preheat it before entering the boiler [90]. As ORC fluids have high heat transfer coefficients due to low Prandtl numbers, commercial ORCs utilise direct recuperation to a large extent. Guo et al. considered recuperated and superheated ORCs using zeotropic mixtures as working fluids to match the gradient of the heat source and sink [222]. The results demonstrated the benefits of using a recuperator in all cases, but the benefit was not linear, as the slope first increased, then decreased with change in the degree of recuperation. This signified the non-linear influence of superheating the working fluid. However, the study assumed fixed turbine efficiency (80%) as an important factor for superheated ORC systems [81].

Whereas recuperation involves indirect heat transfer between spent and preheated working fluid, regeneration involves direct heat transfer by mixing intermediary pressure working fluid to preheat pressurised condensate, leading to a direct increase in working fluid consumption. This leads to an increase in the HP turbine mass flow rate and reduction in heat rejected to the condenser, which improves cycle efficiency. Whereas recuperation requires additional heat exchangers, regeneration is cost-effective and regularly used in steam-based systems to improve cycle efficiency and remove dissolved oxygen [223, 224].

Xi et al. optimised conventional, single regenerative and double regenerative ORC cycles using the genetic algorithm (GA) [70]. They concluded that regenerative cycles had a lower power output, but reduced boiler heat load, higher exergetic efficiency and could provide superior thermodynamic performance at optimal operating conditions. Mago et al. observed that the regenerative ORC cycle offered better second law efficiency and reduced irreversibility, compared to a conventional ORC cycle [225]. Battista et al. suggested the optimum regenerative flow rate was ~ 20% of the rated flow [52].

## **2.10 Economics**

Whereas ORCs have been widely investigated for WHR applications, most previous studies were limited to thermodynamic analysis and dissimilar results were obtained after factoring in techno-economic optimisation due to intermittent heat transfer from sources, heat sources temperature levels, plant scale, working fluid cost and electricity prices [226]. Although higher heat source temperature leads to higher cycle efficiency, it increases capital expenditure [227].

Quoilin et al. stated that higher evaporating pressures were better suited for WHR ORCs as they reduce expander and evaporator expenditure [62]. Expander selection, efficiency prediction models and part load operation are seen as paramount to evaluate the economic feasibility of ORCs [228].

Pili et al. evaluated the economic feasibility of WHR from industrial heat sources using ORCs with sensible heat storage, reporting that the use of thermal storage did not justify additional

capital expenditure [229]. The thermo-economic optimisation of recuperative ORCs was noted as a function of pinch point and recuperator effectiveness, limited by additional heat exchanger cost despite higher thermodynamic efficiency [226].

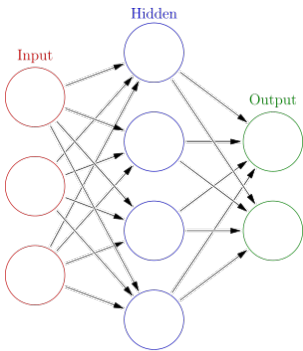
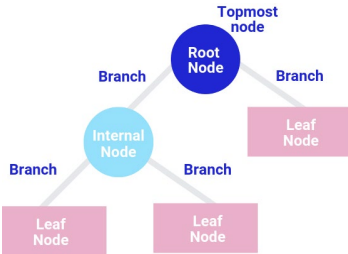
## **2.11 Machine learning for turbine design**

Using conventional modelling approaches to optimise the turbine design and minimise internal losses under a wide range of operating conditions is computationally intensive if one is using CFD-based analysis. Machine learning can be considered as a computationally effective and reliable solution to recognise the interrelated parameters that are strongly correlated to the turbine design such as aerodynamic losses, pressure ratio, flow coefficient, stage loading coefficient, blade velocity, exit angles across the flow path, enthalpy drops across the turbine and Mach numbers, specifically when coupled with global optimisation algorithms.

Machine learning was first used for pattern classification in the 1960s, but advanced computational capabilities and greater interest in the field of artificial intelligence have ensured that the field has garnered significant interest in recent years [230]. Machine learning algorithms are now limited solely by hardware capability to process large data sets, which leads to more reliable prediction models. Their accuracy is undergoing continuous improvement, as data collection has significantly increased in the past twenty years. With the advent of advanced computational capabilities, the field of machine learning has proven these models' suitability for a wide variety of applications, particularly highly non-linear models [231].

Limited machine learning models have been developed for turbomachinery in the past for the purpose of single parameter optimisation. For example, to optimise either profile geometry or cycle efficiency [232, 233]. Oyama et al. employed artificial neural networks (ANN) to optimise the design of a axial compressor operating with transonic flow, which was computationally intensive and time-consuming if CFD was employed [234]. Rashidi et al. successfully optimised the efficiency of an ORC cycle with regenerative feed water heaters using an ANN integrated with the swarm of bees optimisation [235]. This highlights the great potential of using machine learning coupled with global optimisation as an alternative computationally efficient tools for ORC expanders and cycle designs. Table 2.4 presents the commonly used machine learning algorithms, and their advantages and disadvantages.

Table 2.4: Comparison of machine learning algorithms

Algorithm	Figure	Principle	Advantages	Disadvantages
ANN		<p>A set of interconnected nodes based on the neurons simulating the human brain. The arrows represent the synapses in the brain. Each circle represents a neuron, which receives information from the preceding neuron's row, where it undergoes processing and is then passed on as a signal to the subsequent row of neurons, as shown in Figure 2-31. As the learning progresses, the weight of the arrows is adjusted by the algorithm.</p>	<p>It can undertake unsupervised learning as it does not require any constraints or needs to be provided with rules to learn the network.</p>	<p>Neural networks required larger data sets in comparison to other machine learning algorithms.</p>
Decision tree		<p>The algorithms develop a predictive model involving stepwise decision-making represented by the branches of a tree, as in Figure 2-32. The end results are observed in the leaves of the tree.</p>	<p>A decision trees is better suited to multivariable optimisation, when used in conjunction with the weighted attribute approach [236].</p> <p>Compared to neural networks, a decision tree enables easy human interpretation to understand the underlying reasons for algorithm behaviour.</p>	<p>A decision trees is not suitable to depict non-linear relationships. Small changes in data, or inaccurate datasets can lead to drastic changes in the end results.</p> <p>It demonstrates the greedy algorithm effect, which could get trapped at local optimum [237].</p>

Regression analysis

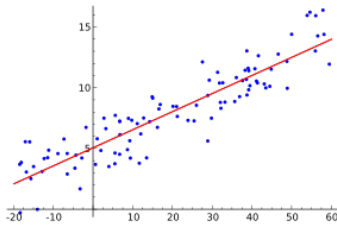


Figure 2-33: Linear regression on a typical data set

Regression analysis combines the use of multiple statistical methods to associate input and output variables. A mathematical criterion is used to generate the best fit for a set of data points, as shown in Figure 2-33.

It provides a well-established statistical approach to linking linear relationships.

It is not suitable for understanding complex relationships.

The polynomial order can be varied to suit the complexity of the problem.

It is inflexible, as it is limited by statistical measures.

Bayesian regularisation

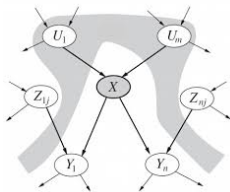


Figure 2-34: Typical Bayesian network

Bayesian networks develop statistic-based graphical models to represent the correlations along with criterion-specific dependencies, as shown in Figure 2-34, using a directed acyclic graph, similar to Figure 2-35.

It is suitable for understanding occurrences along with deducing their cause. This aids operator interpretation and is why it is extensively used for probabilistic studies.

The construction of a Bayesian network is computationally expensive [238].

There is no universally accepted method to generate the Bayesian network from existing data [239].

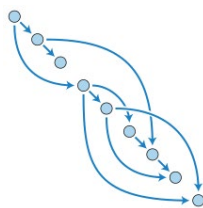


Figure 2-35: Directed acyclic graph

This limits the Bayesian network's ability to the statistical programming experience of the operator.

Acyclic graphs provide freedom from directed cycles and avoid limitations being placed on the origin points of a vertex.

## 2.12 Optimisation

In combination with machine learning algorithms, optimisers based on mathematical techniques and metaheuristic functions were considered in this study to mould the appropriate input variables for maximising the objective functions based on the relationship between the interrelated parameters. Mathematical techniques are notable for their clarity of approach and the metaheuristic optimiser is recommended due to its ability to handle diverse problems. An overview of the optimiser classification undertaken is presented in Figure 2-36. The general objective for all optimisers is to minimise or maximise the objective function defined by Arora in equation 2.18 [248].

$$\text{minimize } f_1(x), \dots, f_i(x), \dots, f_I(x), \quad x = (x_1, \dots, x_d), \quad 2.4$$

Subject to

$$h_j(x) = 0, (j = 1, 2, \dots, J)$$

$$g_k(x) \leq 0, (k = 1, 2, \dots, K)$$

Where  $f_i$  are the non-linear objective functions, and  $h_j$  and  $g_k$  are the equality and inequality constraints, respectively. The value of  $I$  is determined by the number of objectives. Its value for single objective functions is 1.

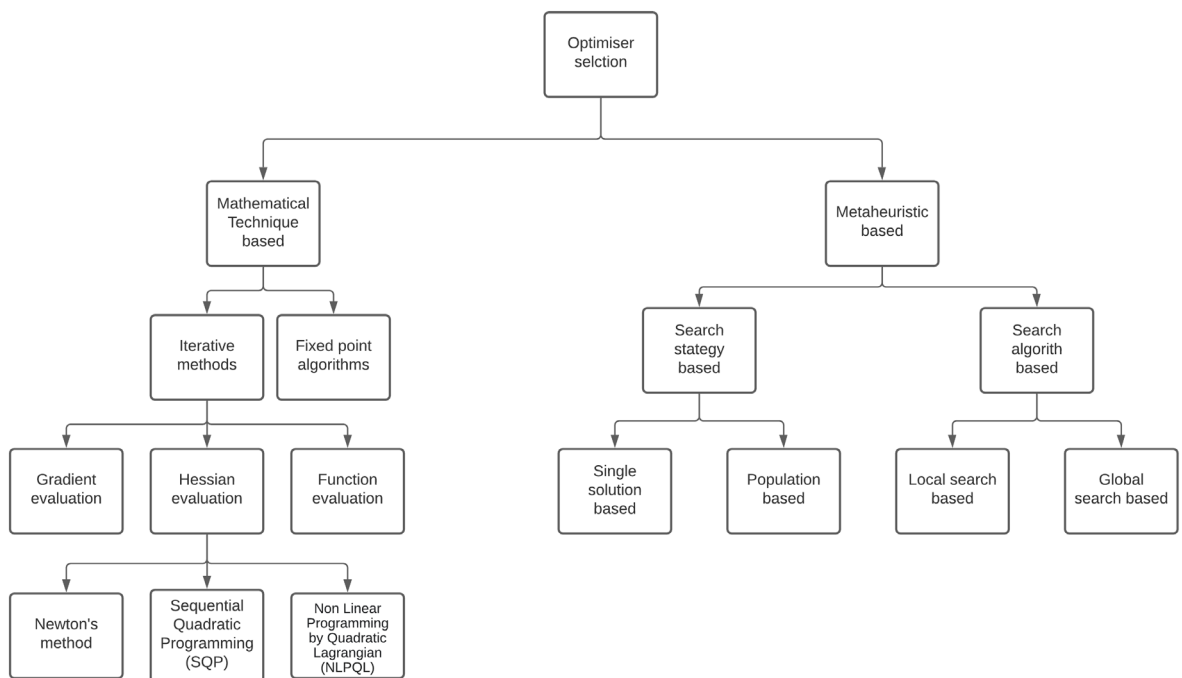


Figure 2-36: Classification of mathematical technique and metaheuristic-based optimisers

Recently, there has been an increasing interest in optimising ORCs [70, 232, 240-247]. Limited studies on optimising ORCs with variable turbine efficiency were undertaken, presenting an optimum solution with fewer details on the influence of individual ORC parameters, specifically for axial flow turbines [133, 207]. Meroni et al. optimised ORC cycle efficiency while considering variable turbine efficiency by integrating a one-dimensional turbine model with a steady-state thermodynamic cycle model [248]. The mass flow rate, pressure ratio and turbine parameters were considered as independent variables. They concluded that the pressure ratio was more impactful on the overall cycle efficiency [248].

### 2.12.1 Mathematical techniques

Mathematical techniques based on iterative methods are better suited than fixed-point algorithms for achieving global convergence [249, 250]. Iterative method operations are based on their evaluation of gradient, Hessians or functions. While solving non-linear problems, Hessian- and gradient-based solvers demonstrate an improved rate of convergence compared to function-based solvers as the latter require a high computational cost for undertaking non-linear problems [251]. Gradient-based solvers observe the information provided by the change of slope to conduct their task whereas Hessian-based solvers used Hessians to determine the optimisation trajectory. As the former relies solely on the gradient, their performance is not comparable to the latter [252]. Furthermore, it requires experienced developers to fine-tune the learning rate to achieve optimal trajectory for a given problem's error surface. A larger learning rate leads to drastic changes after every iteration, which fails to locate the minima, whereas a lower learning rate results in a drastic increase in the number of iterations and computation expense required to optimise the solution [253]. Additionally, gradient-based solvers do not perform well for solutions with multiple peaks and saddle points [252]. Hessian-based solvers also consider the information of the change in curvature. This allows them to vary the length of the step and therefore, the rate of change [252].

Hessian-based solvers include Newton's method and sequential quadratic programming, and operate by minimising the root of a twice differentiable function. Previous studies compared the high computational cost of Newton's method to store Hessian matrix data and to compute the inverse Hessian for each iteration [254]. They also observed its limitation to achieve convergence only if the search area is near the optimum solution. Sequential quadratic programming (SQP) methods solve the problem as a sequence of individual quadratic subproblems. Compared to Newton's method, SQP is better suited to handle larger dimensional as well as non-linear problems [254].

The non-linear programming by quadratic Lagrangian (NLPQL) algorithm stems from SQP using FORTRAN language that was developed by Schittkowski. He employed a smooth and continuously differentiable objective function to solve non-linear problems with well-scaled

gradients, similar to those undertaken by this study [255]. Whereas the NLPQL algorithm was widely used for single objective optimisation, mixed results were reported for its effectiveness and computational efficiency while undertaking multi-objective optimisation [256]. Song et al. applied the NLPQL algorithm to the blade design optimisation of a centrifugal ORC turbine [257]. A good agreement within 1% for shaft power and turbine efficiency was observed between the NLPQL optimised model and CFD simulations. Previous studies for Internal combustion (IC) engine single objective optimisation demonstrated significantly lower computational requirements but a narrower spectrum of solutions for the NLPQL algorithm compared to the GA [258].

### 2.12.2 Metaheuristic optimisers

Metaheuristics are high-level algorithmic structures used to provide guidelines and strategies to develop optimisation algorithms [259]. Compared to traditional optimisation algorithms and iterative methods, metaheuristics do not guarantee a global optima, but are more computationally affordable for complex problems [260]. They operate by performing tests on a subset of solutions where the entire solution space is too large to be explored. Metaheuristic algorithms can be classified based on their search strategy and search algorithm.

Search strategy-based optimisers are further classified as single solution-based and population-based solvers. Notable algorithms of this type include simulated annealing, guided local search and repeated local search [261, 262]. Population-based metaheuristic algorithms focus on improving the characteristics of the entire population. They offer a better result to computational cost ratio for complex problems and a higher probability of a globally optimised solution. Commonly used examples are genetic algorithms, ant colony optimisation and swarm of bees optimisation [261]. Based on a search algorithm, optimisers are classified as local or global search-based solvers. Local search-based metaheuristics include hill climbing, Tabu search and variable neighbourhood search [262]. Notable global search metaheuristics include evolutionary algorithms like genetic algorithms, swarm of bees optimisation and rider optimisation algorithms [246].

Nature-inspired evolutionary algorithms are classified as population-based and global search-based approaches. They included genetic algorithms, genetic programming, evolutionary programming, particle swarm optimisation, evolution strategy, ant colony optimisation, estimation of distribution algorithm and differential evolution [263]. While the use of evolutionary algorithms for ORC turbines has been demonstrated previously, these were used for optimising networks developed with the help of CFD simulations, rather than loss models [264, 265].

### 2.12.3 Multi-objective optimisation

As multi-objective optimisation (MOO) involves the optimisation of more than one objective function, usually involving a trade-off between multiple objectives, it is significantly more computationally extensive [266]. Any commercial ORC should be optimised both thermodynamically and economically.

To the best of the author's knowledge, the NLPQL algorithm was not previously used for the multi-objective turbine design or ORC optimisation, although previous engineering applications include diesel engine optimisation [267, 268]. Chen et al. used the NLPQL algorithm to simultaneously reduce the soot and NO<sub>x</sub> emissions from the combustion chamber of a direct injection diesel engine by 71% [256]. Jones et al. recommended metaheuristic algorithms for multi-objective optimisation studies [269]. Over 70% of studies using the metaheuristic technique relied on the evolutionary algorithms, followed by simulated annealing and Tabu search-based algorithms [270]. Wang et al. used the non-dominated sorting genetic algorithm-II (NSGA-II) for thermo-economic optimisation of dual loop ORCs operating on engine waste heat, with exergetic efficiency and payback period as objective functions [271]. They achieved exergetic efficiency of 39% and a payback period of 1.24 years for the optimal working fluid pairing of Toluene and R124. Roumpedakis et al. conducted an exergo-economic optimisation for an indirect loop small-scale ORC driven by a solar thermal collector with the help of a multi-objective genetic algorithm (MOGA) to optimise the components' integration [272]. Their optimal integration demonstrated a minimum payback period of 11.9 years, which highlighted the importance of a combined thermo-economic evaluation of waste heat recovery ORCs, achieved using MOOs.

Hu et al. compared the NLPQL and genetic algorithm for seven parameter marine speed diesel engine optimisations [258]. NLPQL had faster convergence and was more effective with fewer optimisation parameters, but it was dependent on a well-defined starting point to avoid entrapment within the local optima. Conversely, the MOGA was immune to starting point definition. It required a greater number of iterations but offered a broader Pareto front spread and finer solutions. The additional iterations also provided a better design for each sub-objective.

## 2.13 Aim and objectives of the study

Given the current literature, this thesis aims to enhance and optimise the use of waste heat recovery ORCs to utilise stack waste heat from bio-heat-driven industrial steam boiler plants. To achieve this aim, the specific objectives are as below.

- Compare the axial ORC turbine's loss models and their suitability for cycle-level studies.
- Investigate the effect of fluid parameter changes on the turbine's isentropic efficiency.
- Use artificial intelligence coupled with evolutionary algorithms to optimise the ORC turbine design, aiming at maximum power generation.
- Incorporate mathematical technique and metaheuristic optimisers to undertake thermodynamic and thermo-economic optimisation of ORC cycle configuration based on transient steam boiler flue gas stacks, while considering variable turbine efficiency.
- Assess the numerical and metaheuristic optimisers for single- and multi-objective optimisation employing a case study analysing maximum power output and composite thermo-economic objective function.

## 2.14 Research gap and contribution to the field

ORC cycle-level efficiency optimisation was widely studied by previous researchers for small improvements in power output. Although the efficiency of the turbine was one of the most important determiners for cycle efficiency, previous studies were usually restricted to a fixed expander efficiency due to the complexity involved in the evaluation of the internal losses, which required an advanced knowledge of flow path geometry [31, 53, 60]. A few studies have studied either the turbine efficiency or cycle efficiency, but not both simultaneously [232, 233].

A parametric analysis for the change in turbine efficiency employing an objective, computationally efficient predictive model has not been undertaken in detail. Most previous publications suggested the use of dry ORC fluids at a saturated turbine inlet. Whereas Kang carried out an experimental study to investigate the benefits of superheat for radial turbines, but no similar study has been conducted for axial turbines [130]. As the turbine is a multifaceted component, the design of the system and turbine are inter-dependent. Multiple parametric variations considered here explain the relationship between turbine efficiency and working fluid parameters, using a direct-loss approach, rather than conventionally used indirect loss correlations [211, 273]. The primitive and simple Soderberg loss model was evaluated against the widely accepted Craig and Cox loss model to simplify the evaluation of turbine efficiency for cycle-level studies. The original work by Craig & Cox [192] was limited to graphical correlations. The detailed description of Craig & Cox model and the developed numerical correlations are provided in Appendix 1. The use of loss models considered the impact of basic thermodynamic working fluid parameters like speed of sound, isentropic enthalpy drop and molar mass.

Mean-line simulations and CFD modelling are widely used for axial turbine flow path optimisation. However, mean-line simulations are limited to the secondary loss creation by boundary layer behaviour. The combination of machine learning and evolutionary algorithms has not been performed previously in this field and presented a novel approach towards globally optimising the problem of turbine design optimisation. The use of ANNs trained by a direct loss model also demonstrated the loss compromise of less significant moving blade efficiency to improve the more significant nozzle efficiency, hence improving the overall turbine isentropic efficiency. The integrated direct loss model-ANN-GA approach for turbine optimisation allows a new methodology for cycle-level analysis.

Although organic Rankine cycles were commercially used for waste heat applications since the 1970s, limited studies considered their use for capturing waste heat from process steam boiler flue gas stacks [168]. Historically, process steam boilers have presented a challenge due to their intermittent steam demand, whereas ORCs present a novel way to utilise this fluctuating low-grade heat, while simultaneously reducing their stack losses and consequential global warming. Even though turbine efficiency is reduced at part load conditions, limited studies were undertaken incorporating the off-design behaviour of turbines at part load conditions and their impact on the overall cyclic performance.

The estimation of losses at operating and reduced loads required the use of a design point and off-design loss model. This study considered the use of the Craig and Cox loss model for design point losses along with Moustapha's off-design point loss calculation. Thermodynamic cycle-level optimisation was undertaken for multiple cycle configurations, including novel combinations of capturing turbine exhaust energy. These include the use of recuperation, regeneration, thermal storage and steam boiler air preheating. The suitability of the computationally efficient parametrically pre-optimised NLPQL algorithm to handle a complex thermodynamic problem against the widely used genetic algorithm was evaluated, noting the absence of a similar comparison for ORCs.

As the configurations studied developed different amounts of electrical and thermal energy, an economic analysis was considered for further assessment. Thermodynamically superior cycles were thermo-economically optimised by a weighted multi-objective study to reduce specific investment cost and maximise power generation using the multi-objective NLPQL and MOGA optimisers. The NLPQL algorithm was not previously considered for turbomachinery-related multi-objective optimisation. It is interesting to note that the most thermodynamically efficient cycle was not the most suitable thermo-economically, and the results could vary based on monetary factors outside the focus of this thesis [227].

## 2.15 General outline and structure of thesis

This thesis consists of seven chapters that are briefly introduced below.

**Chapter 1** introduces the change in the global energy scenario, capturing the ever-increasing electricity demand along with the history of ORCs and their contribution to the future global energy mix.

**Chapter 2** is a comprehensive literature review that classified the types of ORC fluids based on their thermodynamic and environmental aspects. The varied applications of steam and organic fluids are concluded, wherein organic fluids are preferred for low-grade waste heat streams such as steam boiler flue gas stacks. Expander selection is flagged as critical to maximise energy recovery. Following a review of existing expanders, the axial turbine is selected as best suited for the application. This study details the influence of non-dimensional parameters on turbine performance. A comparison of design and off-design loss models is undertaken, comparing preliminary and advanced approaches. Finally, a comparison of machine learning and optimisation algorithms is undertaken to identify their suitability for turbine and cycle-level modelling.

**Chapter 3** investigation and selection of the tools used in the thesis. The Soderberg design point loss model, Craig and Cox design point loss model and Moustapha's off-design point loss model are detailed, along with the functioning of NLPQL and GA Optimisers.

**Chapter 4** undertakes a component-level study of turbine design. The previously considered loss models are benchmarked against an existing steam turbine and then used for the parametric studies to investigate the influence of pressure ratio and working fluid temperature on turbine efficiency for multiple working refrigerants, within the engineering equation solver (EES) environment. Furthermore, the use of neural networks and genetic algorithms for optimising turbine efficiency is evaluated. The use of the NLPQL algorithm is not considered for turbine optimisation due to the complexity of the larger number of input variables involved.

**Chapter 5** applies the loss model optimised turbine to observe a cycle-level comparison of the impact of turbine efficiency on cycle characteristics. A case study is undertaken using medium-sized industrial steam boiler flue gas stacks. The core components for the conventional ORC are parametrically optimised. Ten different cycle configurations have been suggested and compared. The component sizing for all cycles further optimised for maximum power generation, while undertaking a comparison of the parametrically pre-optimised numerical NLPQL algorithm and evolutionary genetic algorithm.

**Chapter 6** undertakes a multi-objective economic optimisation for thermodynamically superior cycle configurations with the help of the multi-objective NLPQL and MOGA optimisers.

**Chapter 7** concludes the thesis, including the key research outcomes with respect to the original objectives. The main contribution of the thesis, the potential for further research work and commercial prospects are also outlined.

## **2.16 Summary of literature review**

There is immense potential of ORCs for steam boiler flue gas stacks as an untapped medium-grade waste heat source. The limitations of steam-based cycles and turbines for such a low heat source temperature and mass flow rate were reported. The low boiling temperature and wide choice of refrigerants provided a selection of working fluids with good thermodynamic, environmental and safety factors. The Peng Robinson EoS was noted for its simpler generalisation and the QUADBACKONE EoS was suggested for its superior phase change prediction, being better suited for cycle-level simulation.

The axial flow turbine was deduced as the most suitable expander for this application, mainly due to its reliability, scalability and flexibility in the part load operation. Non-dimensional parameters and loss models relevant for their scaling and efficiency prediction were considered. A comparative study of machine learning algorithms deduced artificial neural networks as the most advanced solution for complex interlinked parameters. Suitable expanders based on mathematical techniques and metaheuristics were observed, for both single- and multi-objective optimisation

# Chapter 3 Methodology

## 3.1 Introduction

As the design of a turbine is a complex task, requiring aerodynamic, thermodynamic, material and economic analysis, its design is an iterative process. Loss models are an integral part of any well-established turbine design philosophy; however, most of them are known to be too complicated for preliminary-level studies, as they require an extensive knowledge about flow path and solid geometry [206]. Parameters such as the stage inlet stagnation pressure and temperature, mass flow rate, profile geometric parameters and machine speed emerge as constraints [216]. To understand the influence of the working fluid parameters in this study, two different loss model approaches have been benchmarked: the Soderberg model and the Craig & Cox model. Soderberg's loss model is considered as a relevant example of a simple loss model and widely accepted as an effective method to determine turbine efficiency [216]. Multiple studies described the Craig and Cox model as the most comprehensive one for impulse machines [210, 211, 274]. Considering the iterative approach required to optimise turbine design while minimising the losses, machine learning coupled with global optimisation algorithms were considered by this study for turbine efficiency improvement. Machine learning is a computationally inexpensive approach used to study highly non-linear correlated parameters. The artificial neural network (ANN) is a black-box modelling technique that uses machine learning to computationally correlate multiple input geometry and output flow parameters. In this study, optimisers based on mathematical techniques and metaheuristics were preferred to the parametric studies due to the large number of input variables. While the use of metaheuristic optimisers, particularly evolutionary algorithms, has been validated by previous studies [51, 70, 271], the use of mathematical techniques has not been validated for turbomachinery applications previously. The non-linear programming by quadratic Lagrangian (NLPQL) algorithm and genetic algorithm (GA) were employed as the mathematical technique-based and metaheuristic optimisers of choice, respectively.

This chapter aims to develop a method for investigating and optimising turbine efficiency and cycle performance by accomplishing the following objectives:

- Comparing the approach of primitive and detailed three-dimensional design-point turbine loss models for the number of input variables, validation, determination of individual losses and accuracy.
- Evaluating the loss model of Moustapha et al. for off-design point losses [215].
- Investigating the varied approach of mathematical technique and evolutionary algorithm -based optimisers.

## 3.2 Loss models

As the flow pattern of a working fluid through a turbine is complex and three-dimensional, multiple analytical and non-dimensional loss models were developed to simplify the optimisation process. These were usually two-dimensional mean line empirical correlations, which provided performance predictions at the mean blade height. Although creating the mean line design was only a preliminary design step, its accuracy ensured its suitability for cycle-level turbine efficiency predictions. Macchi stated that the efficiency of a well-designed axial flow ORC turbine can be predicted within 2% accuracy with the use of mean line loss models [196]. Losses have been categorised as profile losses, end wall losses and leakage losses. Profile losses are considered as the loss generated by the profile at the mean line section, wherein flow is assumed as two dimensional. This loss included the inherent aerodynamic loss as well as the trailing edge loss [275]. Endwall losses arise primarily due to the secondary flows generated by boundary layers created at the hub and tip diameters. The losses were modelled using the EES platform due to its large database of ORC working fluids [170]. Leakage losses include flow passing through pressure balancing holes, shaft end seals, interstage diaphragm glands and over the rotor tips.

### 3.2.1 Soderberg loss model

Soderberg's model (1949) was developed from a large number of tests performed on steam turbines with low aspect ratio blading, similar to those required for a small ORC turbine [206]. The model required only a few parameters as it was limited to the measurement of flow deviation, while accounting for Reynolds number [216]. Lewis and Sayers have noted its suitability for a wide range of Reynolds number and aspect ratios [276, 277]. Soderberg stated that the use of the model was limited to reasonable Zweifel coefficients and well-designed profiles, which restricted its use to an efficiency predictor, rather than a design tool [200]. The enthalpy drop incurred was distributed across the stator and the rotor to determine the degree of reaction across the stage. The parameters employed in Soderberg model are listed in Table 3.1

Table 3.1: Parameters required for Soderberg's loss model

Term	Symbol	Unit
Inlet fluid pressure	$P_1$	kg/cm <sup>2</sup> a
Inlet fluid temperature	$T_1$	°C
Outlet pressure	$P_3$	kg/cm <sup>2</sup> a
Degree of reaction	$DoR$	-
Rotational speed	$N$	rpm
Rotor diameter	$D_{hub}$	m
Nozzle pitch	$s_N$	m
Nozzle height	$ht_N$	m
Nozzle throat width	$thr_N$	m
Blade pitch	$b_N$	m
Blade height	$ht_B$	m
Blade throat width	$thr_B$	m
Mass flow rate of fluid	$MFR$	kg/sec
Nozzle exit angle	$\alpha_2$	°

Soderberg's model considers four basic factors: deflection, pitch, blade heights and Reynolds number. The deflection of the nozzle  $\varepsilon$  is provided as a function of nozzle exit angle  $\alpha_2$  by the equation 3.1. Soderberg determined the basic loss coefficient for fixed nozzles  $G_N^*$  by equation 3.2, which is suitable for deflection up to 120°. The relation between the deflection and the basic loss coefficient for different ratios of maximum profile thickness to overall profile length is shown in Figure 3-1 [206].

$$\varepsilon = 90^\circ - \alpha_2 \quad 3.1$$

$$G_N^* = 0.04 + 0.06 \left( \frac{\varepsilon}{100} \right)^2 \quad 3.2$$

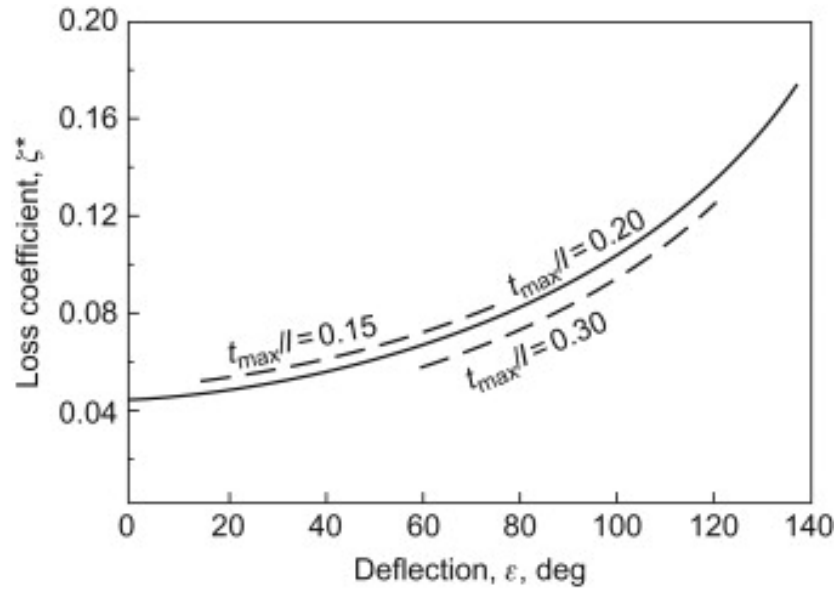


Figure 3-1: Variation of basic loss coefficient with increase in deflection angle for various ratios of maximum profile thickness to overall profile length [206]

The basic loss coefficient  $G_N^*$  was corrected for the pitch  $s_N$  and nozzle height  $Ht_N$  determined from the equation considering the change in height, as shown in equation 3.3.

$$1 + G_{1N} = (1 + G_N^*) \times \left( 0.993 + 0.021 \times \frac{s_N}{Ht_N} \right) \quad 3.3$$

The hydraulic diameter  $D_h$ , density  $\rho_2$ , dynamic viscosity  $\mu_2$  and mean exit velocity  $c_2$  were considered at the nozzle throat section to determine the Reynolds number  $Re$  in equation 3.4.

$$Re = \frac{\rho_2 c_2 D_h}{\mu_2} \quad 3.4$$

Where the hydraulic diameter  $D_h$  was determined using the nozzle height  $Ht_n$  and throat width  $thr_n$  as per equation 3.5.

$$D_h = \frac{4 \times \text{Flow Area}}{\text{Perimeter}} = \frac{4 \times (Ht_n \times thr_n)}{2(Ht_n + thr_n)} \quad 3.5$$

The value of the loss coefficient  $G_N$  was then corrected for the Reynolds number in equation 3.6.

$$G_N = G_{1N} \times ReCF \quad 3.6$$

Where  $ReCF$  was the Reynolds Number correction factor, determined using equation 3.7.

$$ReCF = \left( \frac{100000}{Re} \right)^{0.25} \quad 3.7$$

Based on the isentropic velocity  $C_{2s}$  and loss coefficient  $G_N$ , the actual velocity  $C_2$  was determined using equation 3.8.

$$C_2 = \frac{C_{2s}}{\sqrt{1 + G_N}} \quad 3.8$$

The Soderberg loss model determined the nozzle loss coefficient by considering the amount of deflection, height correction and Reynolds number correction factor to deduce the steam velocity  $C_2$  after the nozzle. This was further used to determine the axial absolute velocity ( $C_{2a}$ ) and relative velocity ( $C_{w2}$ ) components as well as the radial relative velocity component ( $V_{w2}$ ) using equations 3.9 and 3.10. The velocity triangles for fluid flow and moving blade velocity  $u$  are illustrated in Figure 3-2.

$$C_{a2} = C_2 \sin \alpha_2 = V_{a2} \quad 3.9$$

$$V_{w2} = C_2 \cos \alpha_2 - u \quad 3.10$$

For the moving blades, the relative blade inlet angle  $\beta_2$  and exit angle  $\beta_3$  were used to evaluate the deflection of the rotor  $\epsilon_R$  using the equation 3.11. Soderberg considered a similar loss correlation  $G_B^*$  for the moving blades mentioned in equation 3.12.

$$\epsilon_R = 180^\circ - \beta_2 - \beta_3 \quad 3.11$$

$$G_B^* = 0.04 + 0.06 \times \left(\frac{\epsilon_R}{100}\right)^2 \quad 3.12$$

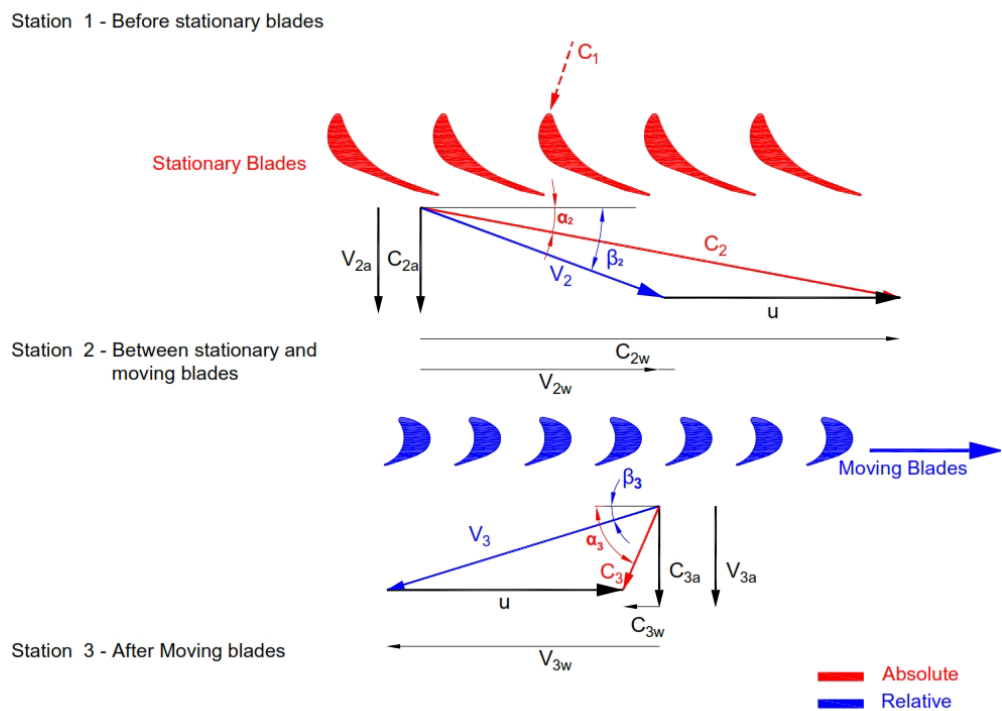


Figure 3-2: Velocity triangles of the flow across blades

The rotor profile loss coefficient  $G_B^*$  was corrected for the pitch  $s_B$  and nozzle height  $Ht_B$ , as shown in equation 3.13.

$$1 + G_{1B} = (1 + G_B^*) \times (0.975 + 0.075 \times \frac{s_B}{Ht_B}) \quad 3.13$$

The final value of loss coefficient  $G_{1B}$  was corrected for the Reynold's number  $ReCF$  by equation 3.14.

$$G_B = G_{1B} \times ReCF \quad 3.14$$

The final loss coefficient  $G_B$  was used to determine the relative velocity of the fluid  $V_3$  after the blade from the isentropic enthalpy drop  $H_3 - H_{3s}$  in equation 3.15.

$$H_3 - H_{3s} = \frac{1}{2} \times V_3^2 G_B \quad 3.15$$

The axial ( $V_{a3}$ ) and radial ( $V_{w3}$ ) components of the relative velocity ( $V_3$ ) of the fluid after the moving blade  $V_3$  were evaluated in equations 3.16 and 3.17 to determine the absolute velocity after stage  $C_3$ , as shown in equation 3.18.

$$V_{w3} = V_3 \cos\beta_3 \quad 3.16$$

$$V_{a3} = V_3 \sin\beta_3 \quad 3.17$$

$$C_3 = \sqrt{(V_{w3} - u)^2 + V_{a3}^2} \quad 3.18$$

The specific work done was denoted by the change in angular momentum in the radial direction, which was used to determine the power output  $P$ , as in equation 3.19.

$$P = \frac{m \times u \times (V_{w2} + V_{w3})}{1000} \quad 3.19$$

The leaving loss was calculated as a function of working fluid velocity  $C_3$  leaving the turbine, as in equation 3.20, to determine the increase in exhaust entropy.

$$Leaving Loss = \frac{C_3^2}{2 \times 1000} \quad 3.20$$

The Soderberg model was limited to profile and secondary losses. Losses due to tip clearance, inlet boundary layer, detailed blade geometry, partial admission and disc friction were not considered [130, 287]. Moreover, Soderberg's model did not consider incidence losses for off-design conditions. Dixon and Hall stated that Soderberg's method was suitable for rapid estimates of turbine efficiency within  $\pm 3\%$  accuracy, which was validated by Horlock [198, 288].

### 3.2.2 Craig and Cox loss model

The Craig and Cox loss model was previously validated by Angelino et al. along with various studies as the most comprehensive loss model for ORC turbines (Table 3.2) [207-209, 211]. Lozza compared the Craig and Cox model with the relatively modern loss model by Kacker-Okapuu and reported that the Craig and Cox loss model was better suited for predicting flow with low aspect ratios, impulse turbines and moving blades with large flow angles [192, 210, 278]. Wei reported that the Craig and Cox loss model provided results closest to the experimental data at the design point [216].

Table 3.2: Parameters required for Craig and Cox loss model

Term	Symbol	Unit
Inlet fluid pressure	$P_1$	kg/cm <sup>2</sup> a
Inlet fluid temperature	$T_1$	°C
Outlet pressure	$P_3$	kg/cm <sup>2</sup> a
Degree of reaction	$DoR$	-
Rotational speed	$N$	rpm
Rotor diameter	$D_{hub}$	m
Nozzle chord length	$b_N$	m
Nozzle height	$ht_N$	m
Nozzle throat width	$thr_N$	m
Nozzle pitch	$s_N$	m
Nozzle backbone length (camber length)	$b_{BN}$	m
Nozzle trailing edge thickness	$te_N$	m
Blade chord length	$b_B$	m
Blade height	$ht_B$	m
Blade throat width	$thr_B$	m
Blade pitch	$s_B$	m
Blade backbone length (camber length)	$b_{BB}$	m
Blade trailing edge thickness	$te_B$	m
Blade overlap	$overlap$	m
Mass flow rate of fluid	$MFR$	kg/sec
Nozzle exit angle	$\alpha_2$	°
Shroud thickness	$thr_{shr}$	m
Shroud to casing clearance	$clearance_{shr}$	m
Axial gap between nozzle and blade	$E_{nb}$	m
Equivalent sand grain roughness of profile	$ks$	m

The Craig and Cox model determined two groups of losses: Group 1, which included nozzle primary loss, nozzle secondary loss, nozzle annulus loss, blade primary loss, blade secondary loss and blade annulus loss; and Group 2, which include nozzle gland leakage loss, balance hole loss, rotor tip leakage loss, lacing wire loss, wetness loss, disc windage loss and partial admission loss. The current

study concerns itself with Group 1 losses (as shown in Figure 3-3), which determine the aerodynamic efficiency associated with the flow path design, whereas the Group 2 losses depended more on the manufacturing precision of the turbine. Equations 3.21 - 3.25 present the breakdown of the nozzle and blade individual primary, secondary and annulus losses based on curve fitting in Craig and Cox maps.

Group 1 losses for the nozzle and blade were the summation of  $G_{Group1Nozzle}$  and  $G_{Group1Blade}$ . Incidence losses  $N_{piN}$  and  $N_{piB}$  were considered using Moustapha's off design loss model.

$$G_{pN} = X_{pbN} \times N_{prN} \times N_{piN} \times N_{ptN} + lossincr_N + \Delta X_{PseN} + \Delta X_{pmN} \quad 3.21$$

$$G_{sN} = N_{prN} \times N_{SaspectratN} \times X_{sbN} \times N_{siN} \quad 3.22$$

$$G_{pB} = X_{pbB} \times N_{prB} \times N_{piB} \times N_{ptB} + lossincr_B + \Delta X_{PseB} + \Delta X_{pmB} \quad 3.23$$

$$G_{sB} = N_{prB} \times N_{SaspectratB} \times X_{sbB} \times N_{siB} \quad 3.24$$

$$G_a = X_{a1} \quad 3.25$$

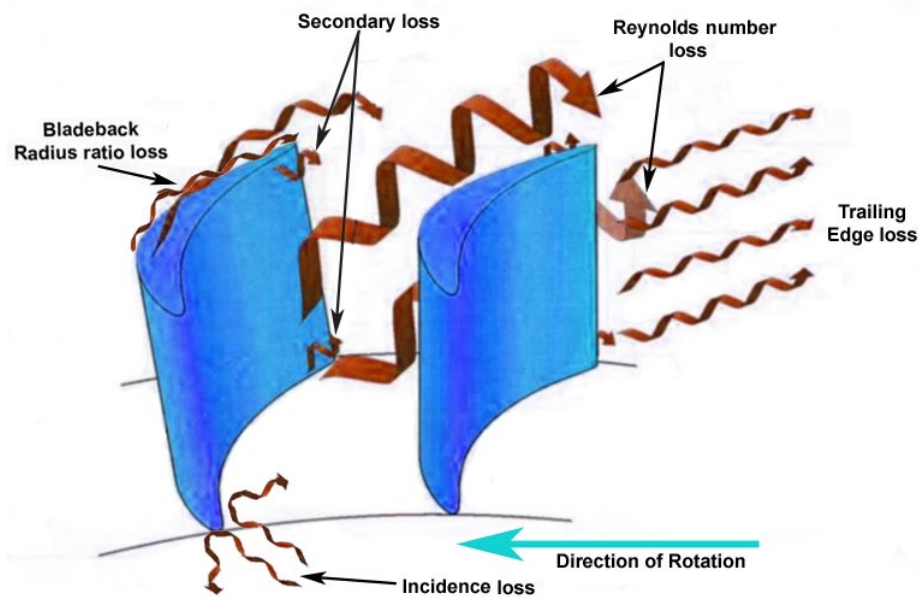


Figure 3-3: Blading loss distribution as per Craig & Cox [24]

The profile losses due to the flow deviation ( $\Delta X_{PseN}$ ,  $\Delta X_{PseB}$ ), Reynolds number losses accounting for wall friction ( $N_{prN}$ ,  $N_{prB}$ ), incidence loss ( $N_{piN}$ ,  $N_{piB}$ ) and trailing edge thickness loss for the nozzle and blade ( $N_{ptN}$ ,  $N_{ptB}$ ) were combined to evaluate the nozzle and blade primary losses expressed by  $G_{pN}$  and  $G_{pB}$ . The additional loss increment due to trailing loss for the nozzle and blade was defined by  $lossincr_N$  and  $lossincr_B$ . Additional losses for supersonic flow with convergent blading were factored in by  $\Delta X_{pmN}$  and  $\Delta X_{pmB}$ . The combined secondary loss factor, defined by  $G_{sN}$  and  $G_{sB}$ , was a function of the basic secondary loss factor stated as  $X_{sbN}$  and  $X_{sbB}$  and secondary loss due to aspect ratio  $N_{SaspectratN}$  and  $N_{SaspectratB}$ . The total auxiliary loss  $G_a$  was a function of annulus loss  $X_{a1}$ . The blade losses were determined using equations 3.26 to 3.28.

$$G_{Group1Nozzle} = \frac{G_{pN} + G_{sN} + G_a}{200} \quad 3.26$$

$$G_{Group1Blade} = \frac{G_{pB} + G_{sB} + G_a \times \left(\frac{C_3^2}{V_3^2}\right)}{200} \quad 3.27$$

$$G_{total} = G_{Group1Nozzle} + G_{Group1Blade} \quad 3.28$$

Like Soderberg's loss model, Craig and Cox loss model utilised the mean exit velocity  $C_3$  and equivalent hydraulic diameter  $D_h$  at the throat section to determine the Reynolds number, as shown in equation 3.29.

$$Re_N = \frac{\rho_2 C_2 D_{hN}}{\mu_2} \quad 3.29$$

Where  $D_{hN}$  was the nozzle equivalent hydraulic diameter determined from the equation 3.30.

$$D_{hN} = \frac{4 * Flow Area}{Perimeter} = \frac{4 * (Ht_N * thr_N)}{2(Ht_N + thr_N)} \quad 3.30$$

The loss model also considered the surface finish of the profiles with the help of the equivalent sand grain roughness to evaluate the profile loss ratio [290, 291]. For axial turbines, Reynolds numbers between  $2 \times 10^4$  and  $2 \times 10^5$  were estimated. Craig and Cox varied the blade opening, instead of varying the chord length or axial width to optimise the correlation. Figure 3-4 governs the relation between the surface finish, Reynold's number and profile loss ratio. The surface friction coefficient had greater significance at higher Reynolds number.

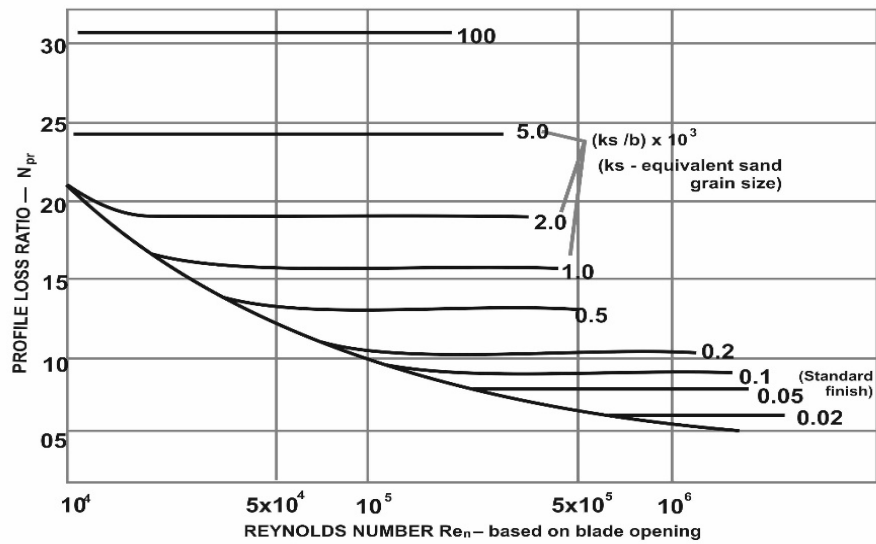


Figure 3-4: Impact of blade surface finish and Reynolds number on profile loss ratio observed by Craig and Cox [23]

$$LC_{mN} = \frac{F_{LN} \times S_N}{b_{BN}} \quad 3.31$$

$$LC_{mB} = \frac{F_{LB} \times S_B}{b_{BB}} \quad 3.32$$

Lift parameter  $F_L$ , presented in Figure 3-5 represented the deflection of the working fluid between the inlet and outlet angles. Correcting the lift parameter for the pitch  $s$  and backbone length  $b_B$  produced the modified lift coefficient  $LC_m$ , described by equations 3.31 and 3.32. The modified lift coefficient was then used to determine the basic profile loss  $X_p$  using Figure 3-6.

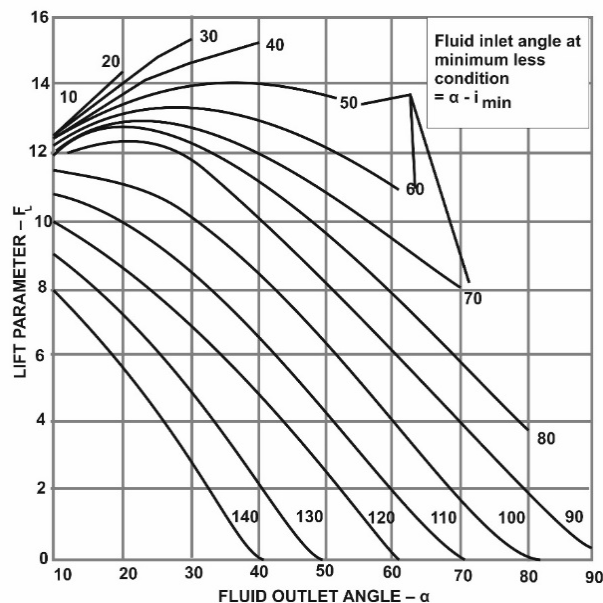


Figure 3-5: Lift parameter determined deviation as a function of fluid inlet and outlet angle [23]

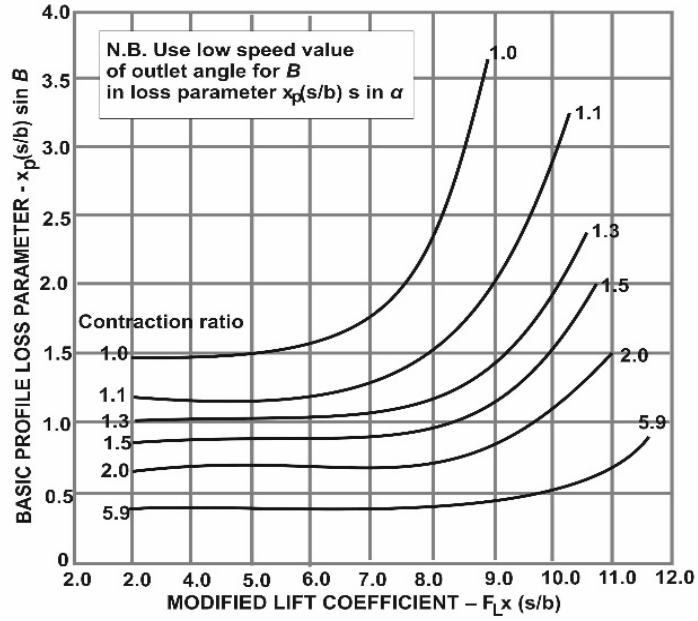


Figure 3-6: The basic profile loss was determined as a function of the modified profile loss, pitch, backbone length and contraction ratio [23]

The profile loss  $X_p$  considered incompressible flow conditions. It accounted for variations in blade angles, passage geometry and pitch to backbone length ratio. The trailing edge loss  $N_{pt}$  was determined using the trailing edge to pitch ratio and fluid outlet angle with an additional increment factored. The contraction ratio is the ratio of the passage area at the inlet and throat sections. The Mach number loss increment  $\Delta X_{pm}$  was determined using the Mach determiner and relative outlet isentropic Mach number  $RelMachW_{outisenB}$ , determined by equations 3.33 to 3.36.

$$Machdeterminer_N = \frac{\arcsin(thr_N + te_N)}{s_N} \quad 3.33$$

$$Machdeterminer_B = \frac{\arcsin(thr_B + te_B)}{s_B} \quad 3.34$$

$$Mach_{outisenN} = \frac{C_{2s}}{SS_{outN}} \quad 3.35$$

$$RelMachW_{outisenB} = \frac{V_{3s}}{SS_{outB}} \quad 3.36$$

Blade back radius was determined by the pitch to blade back radius ratio, profile loss increment  $\Delta X_{pse}$  and outlet isentropic Mach number  $Mach_{outisen}$ . The secondary loss aspect ratio factor  $N_{Saspectrat}$  was determined by the camber length and height. Secondary loss  $G_s$  was inversely proportional to the aspect ratio. Basic secondary loss  $X_s$  factored in the lift parameter, pitch,

camber and square of the relative mean velocity across blading. Uncontrolled expansion loss depended on the profile height and axial distance between subsequent rows of blading. The annulus wall loss  $X_{a1}$ , as shown in Figure 3-7 was determined by the ratio of the nozzle–blade gap to nozzle height or by the half cone angle created by the overlap in blading. The loss coefficient determined by the cumulative of the above losses was used to determine the actual velocity after the profile, as shown in equation 3.37.

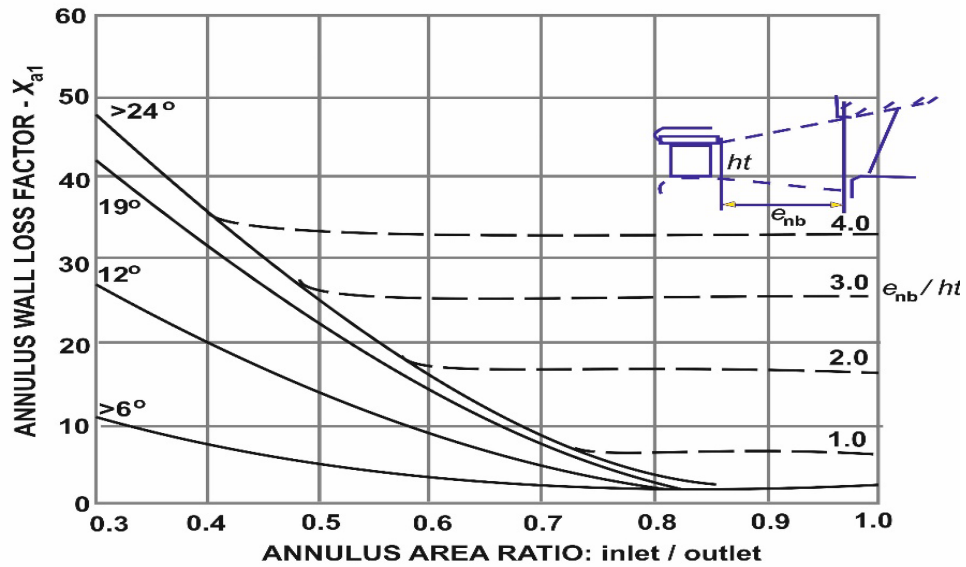


Figure 3-7: Annulus wall loss was a function of the profile height and gap between the fixed and moving blades [23]

$$C_2 = \frac{C_{2s}}{\sqrt{1 + G_{Group1Nozzle}}} \quad 3.37$$

This thesis utilised a surface fitting function to digitize the curves used by the Craig and Cox loss model. The function was selected from the curve fitting toolbox in the MATLAB programming environment [292]. The Craig and Cox loss model contained multidimensional plots. The data points provided by the loss model were converted to a set of polynomial equations with orders between 2 to 5 depending on the complexity of the curve. The absolute deviation of the predicted parameter using the developed equation values was within  $\pm 2\%$ .

For certain data sets, it was not possible to generate analogous polynomial equations within the expected constraints due to the complexity of the curves, despite the use of higher-order polynomial equations. The values between nearby data points were interpolated by using a weighted mean approach. The weighted mean approach was used to determine the modified lift coefficient used in the basic profile loss for the stationary and moving blades. Off-design losses  $N_{piN}$ ,  $N_{piB}$ ,  $N_{SiN}$  and  $N_{SiB}$  were considered using Moustapha’s loss model [223].

### 3.2.3 Off-design loss model

Alongside design point losses, this study investigated the utilisation of an actual transient heat source, which resulted in the turbine operating at off-design conditions. Moustapha et al.'s loss model was selected to conduct the off-design analysis owing to its reliability [195, 222, 223, 225]. It exclusively considered the incidence-induced secondary losses, an individual breakup of primary ( $N_{pi}$ ) and secondary ( $N_{si}$ ) off-design losses, the loss factor independently for positive and negative stalling incidence, leading edge shape, wedge angle and diameter, the ratio of the leading-edge radius to the pitch and lastly, the convergence ratio using the fluid angle rather than the metal angle of the blades [223]. Equation 3.38 shows the conversion of the pressure loss coefficient to a kinetic energy loss coefficient; where  $\gamma$  is the ratio of specific heats,  $\phi^2$  is the off-design kinetic energy loss coefficient (ratio of actual to ideal gas exit velocity) and  $M$  is the Mach number. Moustapha et al.'s primary loss correlation has been expressed in equations 3.39 and 3.40, where  $\Delta\phi_p^2$  is the primary off-design kinetic energy loss coefficient,  $d_{le}$  is the leading-edge diameter,  $s$  is the profile pitch,  $\beta_{M1}$  is the metal inlet angle,  $\beta_{M2}$  is the metal outlet angle and  $[\alpha_1 - \alpha_{1design}]$  is the incidence angle.

$$N_{pi} = \frac{\left[1 - \frac{(\gamma - 1)}{2} M_2^2 \left(\frac{1}{\phi^2} - 1\right)\right]^{\frac{-\gamma}{\gamma - 1}} - 1}{1 - \left(1 + \frac{(\gamma - 1)}{2} M_2^2\right)^{\frac{-\gamma}{\gamma - 1}}} \quad 3.38$$

$$\begin{aligned} \Delta\phi_p^2 &= 0.778 \times 10^{-5} \times x' + 0.56 \times 10^{-7} \times (x')^2 + 0.4 \times 10^{-10} \times (x')^3 \\ &\quad + 2.0544 \times 10^{-19} \times (x')^6 \\ &\text{if } 0 \leq (x') \leq 800 \end{aligned} \quad 3.39$$

And

$$\begin{aligned} \Delta\phi_p^2 &= -5.1734 \times 10^{-6} \times x' + 7.6902 \times 10^{-9} \times (x')^2 \\ &\text{if } -800 \leq (x') \leq 0 \end{aligned} \quad 3.40$$

$$x' = \left(\frac{d_{le}}{s}\right)^{-1.6} \left(\frac{\cos\beta_{M1}}{\cos\beta_{M2}}\right)^{-2} [\alpha_1 - \alpha_{1design}]$$

Moustapha et al.'s loss model defined the secondary incidence loss ( $N_{si}$ ) function as per equation 3.41. Chord length, inlet gas angle and outlet gas angle were denoted by  $chord_{length}$ ,  $\alpha_1$  and  $\alpha_2$ .

$$\begin{aligned} N_{si} &= \exp(0.9 x'') + 13(x'')^2 + 400(x'')^4 \\ &\text{if } 0 \leq x'' \leq 0.3 \end{aligned} \quad 3.41$$

and

$$\text{if } -0.4 \leq x'' \leq 0$$

Where

$$x'' = \frac{(\alpha_1 - \beta_{M1}) * (\cos\beta_{M1})^{-1.5}}{(\beta_{M1} + \beta_{M2}) (\cos\beta_{M2})} \left(\frac{d_{le}}{chord_{length}}\right)^{-0.3}$$

### 3.3 Machine learning

Given that the Craig and Cox loss model includes many interdependent parameters, machine learning was considered as an approach with lower computational cost to simulate the loss model with a high level of accuracy. The ANN uses machine learning to develop a black-box model that correlates between multiple input geometry and output flow parameters. ANNs are well suited to understand non-linear relationships and provide better scalability with parallel processing. ANNs have demonstrated the highest suitability for understanding mathematical data involving the complex velocity field within a turbine [279].

### 3.4 Optimisation approach

After machine learning was correlated to the turbine's parameters, optimisers were required to mould the appropriate input variables to minimise the flow path losses. Local and global optimisation are the two main optimisation techniques. Global optimisation guarantees the global optimal combination of parameters to achieve the objective function, whereas local optimisation most likely converges towards local optima. Optimisers based on mathematical techniques and metaheuristics were preferred to parametric studies due to the large number of input variables. Whereas the use of metaheuristic optimisers, particularly evolutionary algorithms, was validated by previous studies [51, 70, 271], the use of mathematical techniques for the ORC cycle optimisation was not considered previously. This study observed mathematical techniques that were noted for their clarity of approach while metaheuristic optimisers were noted for their ability to handle diverse problems.

Chapter 4 utilised the genetic algorithm (GA) to maximise steady state turbine power output by varying the turbine's geometric configuration. The evolutionary approach of the genetic algorithm made it suitable for optimising a problem with a large number of independent variables [29]. Chapter 5 utilised this optimum turbine configuration to maximise mean turbine power for the considered transient waste heat source, while expanding the horizon of numerical optimisation approaches by considering NLPQL alongside the genetic algorithm. Chapter 6 optimised a composite function consisting of the specific investment cost (SIC) and maximum mean power using NLPQL and genetic algorithms. The cycle-level variables optimised included the pump displacement, boiler heat exchanger area, turbine displacement, condenser heat exchanger area, mass of thermal storage, recuperator heat exchanger area and APH heat exchanger area. Whereas the multi-objective genetic algorithm (MOGA) was already proven by previous studies, the use of the NLPQL algorithm for turbomachinery-based multiple-objective studies had not been undertaken previously [271, 280].

Previous studies signposted the NLPQL algorithm as less computationally intensive as compared to the widely used GA, which stood out in tasks with a small number of independent variables [25]. The evaluation of the abilities of the mathematical technique-based solver to handle thermodynamic and thermo-economic cycle level-problems against the well-established metaheuristic optimiser is one of the aims of Chapters 5 and 6.

### 3.4.1 Mathematical-technique-based optimiser

Based on the literature review, an optimiser incorporating an iterative approach rather than a fixed point approach was selected due to the higher probability of global convergence [250]. Within this category, Hessian-based solvers were preferred over gradient or functions-based solvers, as they were limited by entering local optima due to the trajectory of the gradient and computational expense, respectively [251]. Hessian-based solvers consider the slope of the function as noted by gradient-based solvers, as well as the change in the trajectory of the slope, which allows them to adapt the step size and optimise with minimum supervision [252].

Three Hessian-based solvers were considered—Newton’s method, sequential quadratic programming (SQP) and non-linear programming by quadratic Lagrangian (NLPQL). The SQP and NLPQL algorithms undertook optimisation within multiple parameter bands to avoid the local optima issue faced by Newton’s method [244]. The NLPQL algorithm is a variation of the SQP algorithm which utilises a smooth and continuously differentiable objective function to optimise solutions. Additionally, the quadratic approximation of the Lagrangian function allows for computational efficiency while solving larger dimensional problems, particularly those with non-linear relationships, such as ORC cycles. The function is defined by user-specified constraints, that are linearised by the algorithm. Each objective function provides a direction to the optimisation process. The quadratic problem is generated, solved and iterated to generate a direction towards the optimum solution using the finite difference method [255]. Figure 3-8 explains the optimisation procedure adopted by the NLPQL algorithm.

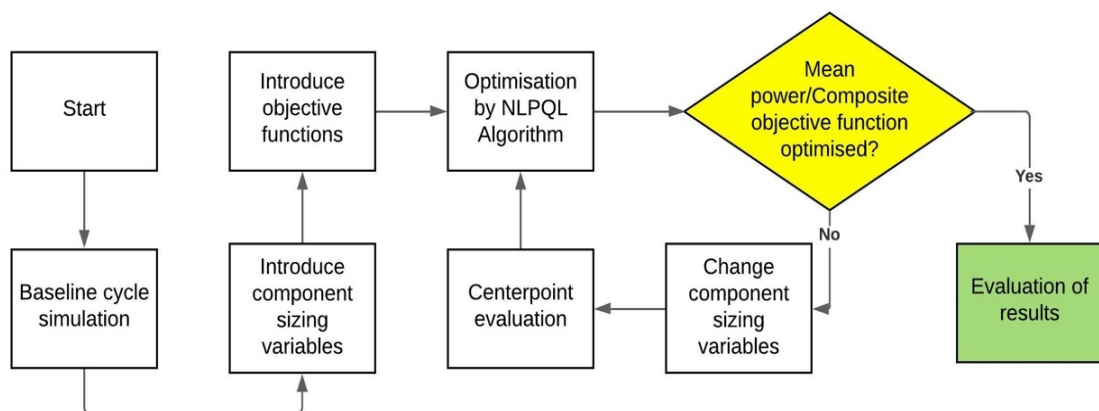


Figure 3-8 :Flowchart of cycle-level optimisation using the NLPQL algorithm

### 3.4.2 Metaheuristic optimisers

Based on the literature review undertaken, this study considered population-based and global search-based approaches suitable for the problem of flow path optimisation. Nature-based metaheuristics is an active research field satisfying both the above criteria. Ezugwu et al. [260] concluded that genetic algorithms, particle swarm optimisation and differential evolution were the most global and robust nature-based evolutionary algorithms. This study further noted the ability of GAs to handle non-differentiable, stochastic and non-linear objective functions as well as discontinuous constraints with the help of simple operators, thereby requiring reduced computational energy [281]. Additionally, they had a low risk of premature convergence [260]. Figure 3-9 demonstrates the scheme used by the genetic algorithm.

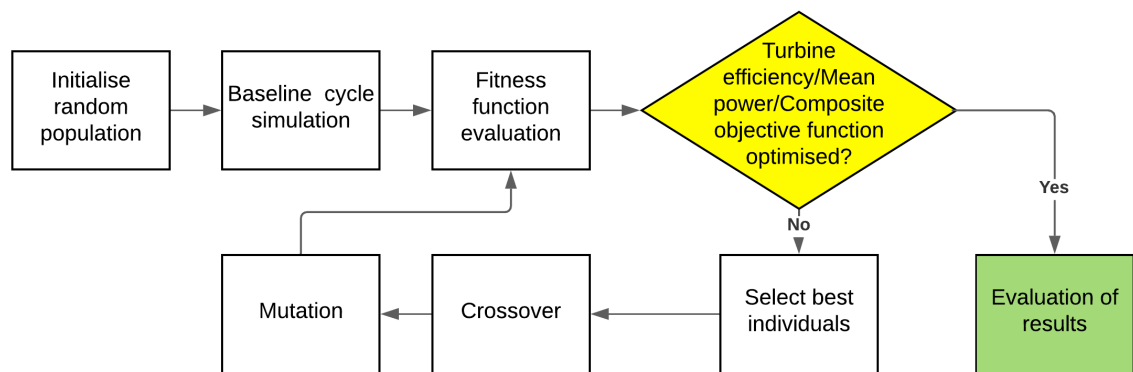


Figure 3-9: The basic structure of the genetic algorithm

## 3.5 Conclusion

This chapter aimed to establish a method for investigating and optimising turbine efficiency and cycle performance. The Craig and Cox loss model was employed owing to its wide acceptance that best suited to axial ORC turbines; however, it requires an advanced knowledge of flow path geometrical parameters.

Comparatively, the Soderberg loss model has a simpler approach and relies primarily on the Reynolds number and flow path deviation to estimate profile efficiency. Whereas the Soderberg loss model simply provides a loss factor, the Craig and Cox loss model provides details on the breakup of losses which were required for detailed studies.

The Moustapha off-design loss model was preferred by this study for cycle level off-design research due to its differentiation of primary and secondary off-design losses as well as its consideration of positive and negative incidence values. In addition, other loss models overestimated incidence losses, particularly in the case of positive incidences.

Machine learning techniques represent a novel approach towards understanding the behaviour of complex relationships, including ORC turbine flow paths and ORC cycles. Artificial neural networks were considered as best suited for turbine performance estimation due to their ability to handle complex data sets, despite the limited transparency they offered. Mathematical technique and metaheuristic optimisers were noted for their clarity of approach and versatility with complex problems, respectively.

The NLPQL algorithm represents the most advanced mathematical technique-based solving, due to its quadratic approximation of the function to be optimised. Genetic algorithms have been widely accepted as the most robust optimisers for global optimisation and provide an ideal benchmark for comparing the NLPQL optimiser.

# Chapter 4 Artificial Neural Network-based Turbine Optimisation

## 4.1 Introduction

The use of direct loss models is the best approach for determining turbine efficiency, as highlighted by the methodology. This chapter aims to envisage the cause of turbine efficiency losses in small-scale axial flow turbines, and their consequent impact on the performance of the organic Rankine cycle (ORC). Experimental data from an axial steam turbine was used to evaluate the established Soderberg loss model and benchmark it against the more complex Craig & Cox loss model. The use of these loss models allowed for a breakdown-based investigation of the factors contributing to the loss coefficient, which explained changes to turbine and cycle behaviour caused by changing the degree of turbine inlet superheat and pressure ratios across the turbine. Genetic algorithm (GA) as a global optimisation tool integrated with artificial neural networks (ANNs) was employed to optimise the design of a single-stage axial flow turbine to maximise its internal efficiency and the overall organic Rankine cycle (ORC) efficiency, whereby the turbine's internal losses were incorporated.

The objectives of this chapter are to:

- Employ loss models to imitate a small-scale axial flow turbine and integrate it with a one-dimensional (1-D) model of an organic Rankine cycle.
- Understand the influence of turbine inlet flow conditions such as superheating and total-to-static stage pressure ratio on the turbine and cyclic performance, utilising low-, medium- and high-temperature organic fluids.
- Undertake a loss comparison between the primitive Soderberg and advanced Craig and Cox loss models.
- Investigate the turbine's aerothermal losses by observing the contributory factors
- Employ ANN deep learning modelling coupled with generic algorithm (GA)-based global optimisation to optimise the turbine flow path as well as study the path's influence on the ORC performance.

The range of parametric analyses and employing an objective, computationally efficient predictive model coupled with a global optimiser are the critical contributions of this chapter. The multiple perspectives considered explain the relationship between turbine efficiency and working fluid parameters, using a direct-loss approach, rather than the conventionally used indirectly loss correlations [211, 273].

This approach enabled studying the impact of basic thermodynamic working fluid parameters like speed of sound, isentropic enthalpy drop and molar mass. The use of ANNs trained by a direct loss model also demonstrates the compromise of less significant moving blade efficiency

to improve the more significant nozzle efficiency, thus improving overall turbine isentropic efficiency. This ANN-integrated approach for turbine optimisation is considered a new methodology for cycle-level analysis.

## 4.2 Working fluids

Compared to traditional steam-based cycles, ORCs offer a high degree of freedom in terms of the choice of working fluid [129]; this is crucial choice as the working fluid influences the exergetic efficiency and irreversibility of the cycles [282]. There is a proven relationship between the working fluid properties and the turbine's architecture and performance [129]. Thus, given the strong relationship of the working fluids with the cyclic and component performance, six working fluids were investigated, each with its own merit: Pentafluoropropane (R245fa), Isobutane (R600), trans-1-chloro-3,3,3-trifluoropropene R1233zd(E), 1,3,3,3-Tetrafluoropropene isomers (R1234ze(E), R1234ze(Z) and 2,3,3,3-Tetrafluoropropene (R1234yf), [129, 282].

Previous studies have confirmed R245fa as the working fluid exhibiting the highest power output with a heat source in the range of 160–200°C and highest specific work output [42, 57]. The low saturation pressure of R245fa and the high specific enthalpy of R600 have ensured the fluids are regularly used for low- to-medium-grade heat recovery [34, 204, 283]; they were considered in the study as baseline fluids. R1234yf and both the R1234ze isomers have emerged as alternatives to alleviate the environmental impacts of the existing organic fluids [167]. R1233zd(E) is a drop-in replacement for R245fa with lower global warming potential (GWP) [41].

A mixture of thermodynamic fluid “type” was chosen, with R245fa and R600 exhibiting dry fluid behaviour, R1234yf and R1234ze(E) exhibiting isentropic behaviour and R1234ze(Z) exhibiting a wet slope. Wet fluids were of interest because they require less sensible heat dissipation in the condenser, reducing cooling tower losses. The working fluid temperature at the turbine inlet was maintained between 110 to 160°C, which ensured that the fluids were not operating in a wet or supercritical regime. The Peng–Robinson equation of state was selected for its simpler generalisation and good prediction of properties, which exhibited a mixture of constituents as well as fluids in a two-phase state of matter [79, 81].

## 4.3 Loss models

### 4.3.1 Soderberg Loss model

Soderberg's loss model, originally formulated in 1922 was chosen for this study due to its relative simplicity [22]. The limited flow path geometrical parameters required by this loss model enables its utility for researchers and engineers with limited turbomachinery proficiency, while providing the advantages of direct loss correlation. The model determines primary and secondary loss coefficients based on the deflection, pitch, blade height and Reynolds number. An additional correction for blade height induced secondary losses is provided using the aspect ratio [206].

### 4.3.2 Craig and Cox loss model

Compared to the Soderberg loss model, the Craig and Cox loss model provided a break-up of twenty-three individual loss factors. Craig and Cox developed a graphical correlation based on primary and secondary losses obtained from linear cascade tests, mainly derived from testing with compressed air. This was supplemented by loss correlations from previous efforts focused on specific annulus losses [214, 284-286]. Despite the added complexity, this model allows operators to undertake a detailed investigation of contributory losses. As this optimisation was limited to Group 1's theoretical aerothermodynamic performance, Group 2's losses were discarded.

The regression for Craig and Cox model was developed by MATLAB curve fitting toolbox. The surface fit function was used to produce a series of polynomial equations. To minimise deviation and optimise calculation time, equations between the 2<sup>nd</sup> to 5<sup>th</sup> order were used as required. The absolute deviation between the values predicted by the polynomial equation from the actual values was less than 2%. A robust fit was chosen as it provided equal weightage to the upper and lower bounds. The least absolute residual (LAR) method develops a curve that minimises the absolute difference of the residuals, rather than the squared differences, as dictated by the commonly utilised Bi-square approach [287]. This leads to an equal importance being placed on all datapoints, including extreme values, and offers overall adaptability to the overall plot. As the loss model did not suffer from outliers and anomalies, the LAR method was selected. Although incidence losses were considered by Craig and Cox in their loss model, they were not considered within this chapter as the design optimisation was considered under steady state condition. A detailed description of the Craig and Cox model and the developed numerical correlations are provided in Appendix 1.

### 4.3.3 Cycle thermodynamic modelling

To study the influence of the inlet temperature on the turbine and cycle performances, the loss models were incorporated into a one-dimensional (1-D) model for a superheated ORC cycle, as shown in Figure 4-1(a). The T-s diagram for the cycle, as in the case of R1234ze(Z), is presented in Figure 4-1(b). An industrial boiler's flue gas stack was considered as the heat source. A temperature of 170°C was considered for the heat source stack [288].

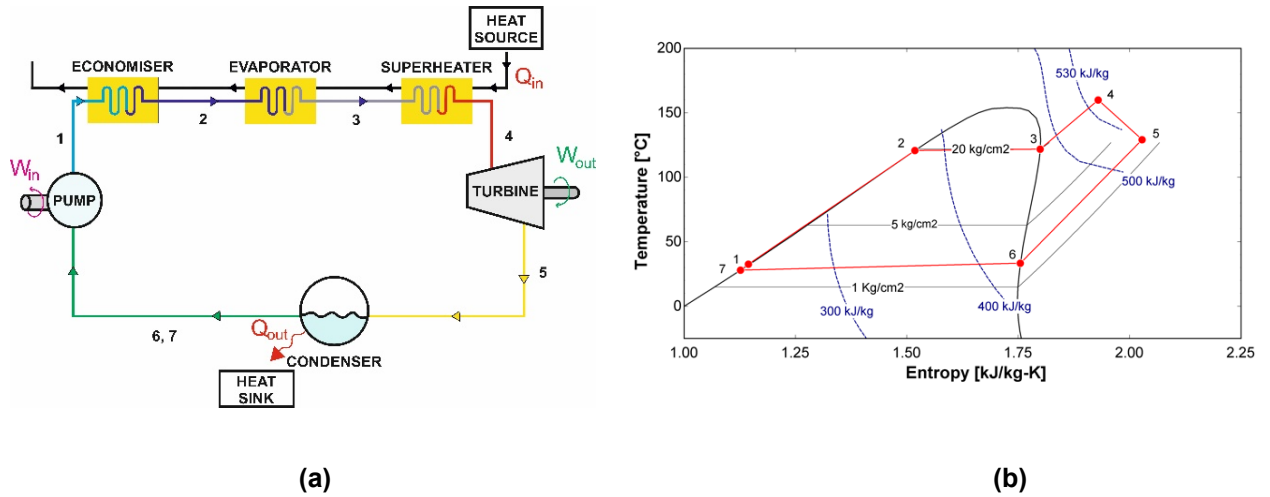


Figure 4-1: (a) Components of a superheated ORC; (b) T-s diagram of superheated ORC for dry fluid R245fa

The heat input to the ORC boiler is stated in equation 4.2, whereas the heat rejection from the water-cooled surface condenser, operated at a mean temperature of 30°C, is calculated using equation 4.4. Work done ( $W_{In}$ ) and efficiency ( $\eta_T$ ) of the turbine were quantified using equations 4.1 and 4.3. Cycle efficiency was quantified as in equation 4.6. The thermodynamic properties at each point in the cycle were determined by using mass and energy balance equations.

$$W_{In} = \frac{\dot{m} \times (P_1 - P_7)}{\eta_P} \quad 4.1$$

$$Q_{In} = -\dot{m}(h_4 - h_1) \quad 4.2$$

$$\eta_T = (1 - (G_{Group1N} + G_{Group1B})) \quad 4.3$$

$$Q_{Out} = \dot{m}(h_5 - h_7) \quad 4.4$$

$$\eta_{cycle} = \frac{W_T - W_P}{Q_{In}} = \frac{\dot{m} \times ((h_4 - h_5) - (h_1 - h_7))}{Q_{In}} \quad 4.5$$

#### 4.3.4 Neural network and optimisation approach

A black-box model based on an ANN was considered as a computationally inexpensive method to improve the turbine design parameters. In the current study, 210 trials were generated from the developed 3D flow path model and employed to develop the neural network; 70% of the data points were used to train the neural network, 15% were used to internally validate the neural network evolution and halt the training when generalisation stopped improving, while the remaining 15% were used to verify the developed neural network and its independency. A dropout rate of 0.8 was utilised, which provided a good balance between refining the existing population and allowing for new variants. The network comprised 70 neurons in the hidden layer, exceeding the number of individual non-linear terms in the loss model, to avoid underfitting of the function, as shown in Figure 4-2. While previous studies used a trial and error method to determine the number of neurons, which was time-consuming and relied on operator experience [289], this study considered a large number of neurons, as neural networks did not suffer from over-fitting the problem. As a result, the number of neurons considered were greater than twice the number of independent variables. The performance of the ANN for training and testing data was evaluated by comparing the root-mean-squared error (RMSE) between the target values and output values. The setup parameters are furnished in Table 4.1.

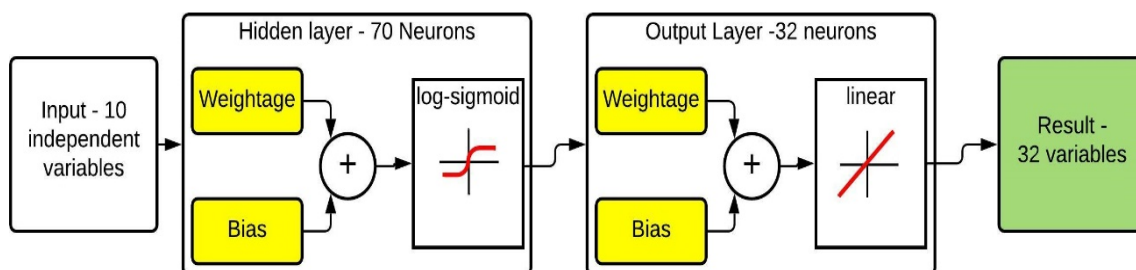


Figure 4-2: Architecture of the ANN used

Table 4.1: Artificial neural network and genetic algorithm setup parameters

Parameter	Description	
Artificial neural network model	Deep neural network (Regression)	
Number of epochs	1000	
Input layers	Number of nodes	10
	Input variables	Turbine speed, hub diameter, degree of reaction, nozzle exit angle, nozzle throat, blade throat, nozzle pitch, blade pitch, nozzle backbone radius, blade backbone radius
Hidden layers	Number of nodes	70
	Number of layers	1
Number of output layer	Number of nodes	32
	Number of variables	22
	Output variables	Nozzle exit velocity, total to total efficiency, total to static efficiency, cycle efficiency, power, volume ratio, flow coefficient, load coefficient, nozzle primary loss, blade primary loss, nozzle secondary loss, blade secondary loss, total loss, heat loss to condenser, Mach determiner for nozzle, Mach determiner for blade, exhaust superheat, inlet total enthalpy, outlet total enthalpy
Optimisation		
Optimizer function	Genetic algorithm	
Population Type	Double vector	
Creation type	Tournament	
Learning rate	0.001	

A unipolar log-sigmoid activation function (equation 4.6) was chosen for the hidden layer owing to its robustness when used in neural networks being trained by back-propagation [307]. The function assigned a weight between 0 and 1 for each neuron. A linear function was chosen for

Y. C. Engineer, PhD Thesis, Aston University, 2022 100

the output layer which comprised of 32 outputs. The Bayesian regularisation algorithm was employed to train the network owing to its robustness for quantitative studies and for previously demonstrating the highest correlation coefficient between predicted and actual data sets [308]. Genetic algorithms were employed to determine the optimal design parameters of the axial flow turbine within the predefined constraints as furnished in Table 4.2, aiming to maximise the turbine power generation. The summary of the learning and optimisation procedure undertaken is presented in Figure 4-3.

$$S(x) = \frac{1}{1+e^{-x}} = \frac{e^x}{e^x+1} \quad [290] \quad 4.6$$

Table 4.2: Turbine optimisation constraints for the genetic algorithm

<b>Parameter</b>	<b>Lower constraint</b>	<b>Upper constraint</b>
Speed (in rpm) [195]	2000	7000
Hub diameter [195]	0.1	0.7
Degree of reaction [291]	0.0	0.5
Nozzle exit angle [292]	12	20
Nozzle throat [187]	0.003	0.01
Blade throat [187]	0.002	0.01
Nozzle pitch [293]	0.01	0.04
Blade pitch [293]	0.015	0.04
Nozzle backbone length [192]	0.02	0.1
Blade backbone length [192]	0.02	0.1

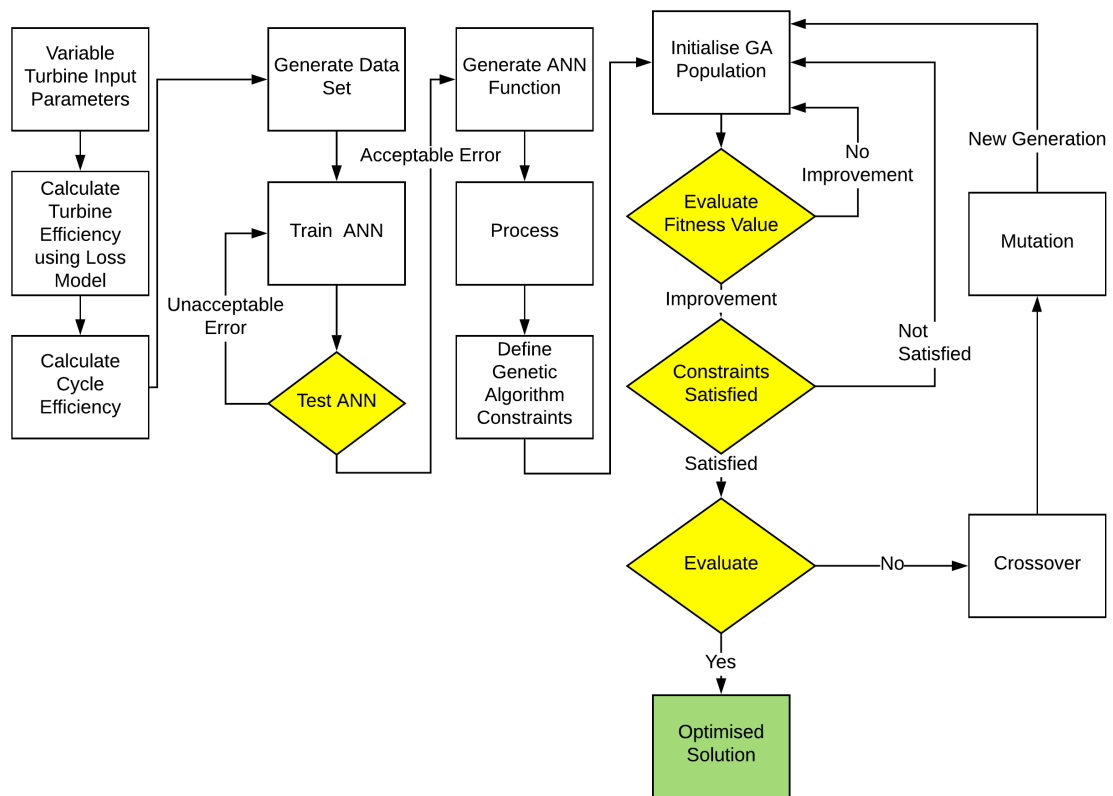


Figure 4-3: Layout of the optimisation procedure

#### 4.4 Assumptions

The study was limited to subcritical cycles. Pressure losses from heat exchangers and piping were ignored. The pinch point for the heat source was considered as 10°C [302, 303]. The heat source and sink temperatures were assumed as constant. The pinch point for the heat sink was considered as 5°C [304]. As the turbine was assumed to operate at the design point, off-design losses were ignored. Profile trailing edge thickness was maintained at 0.3mm, taking into consideration limitations within the manufacturing process. Gearbox and generator losses were ignored [305]. Although the feed pump efficiency was assumed as 70%, the work done by the pump was minor (below 10% of the overall power generated) and ignored during determining cycle efficiency, as it was negligible compared to the turbine work [59]. The thermodynamic model was executed using the EES platform that considered the effect of the operating conditions on the thermophysical properties of the working substance [83, 169].

#### 4.5 Validation

The results predicted by numerical Soderberg, Craig and Cox and ANN black-box models were benchmarked against their analogous actual values measured during the steady operation of a 450-kW axial-flow impulse back-pressure steam turbine manufactured by IB Turbo-India, depicted in Figure 4-4.

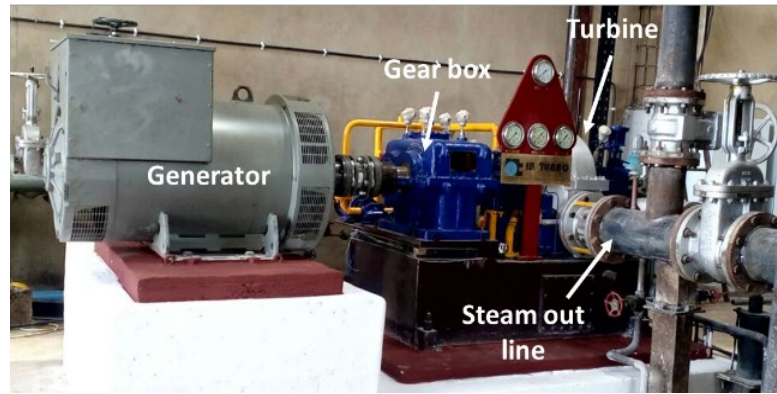


Figure 4-4: Pictorial view of the simulated steam turbine operating in a rice mill firm at Karnal, India (permission granted for image)

The turbine consisted of forty stationary nozzles along with 221 moving blades. The nozzle exit metal angle was maintained as  $20^\circ$ . The moving blade metal inlet and exit angles was machined at  $22.5^\circ$  and  $19^\circ$  to the tangential axis. The nozzles had mean pitch, height, throat width and exit area of 12.4 mm, 42.7 mm, 40.6 mm and  $64.1 \text{ mm}^2$ , respectively. The turbine mean diameter was 336.55 mm, operated at 9000 rpm and integrated with a speed reduction gearbox to couple with a 15000 RPM alternator. Steam inlet conditions were  $10.53 \text{ kg/cm}^2(\text{a})$  and  $296^\circ\text{C}$ , while steam exhaust pressure was  $7.86 \text{ kg/cm}^2(\text{a})$ . The predicted values showed an agreement within 3% of the actual values as multiple load points, as measured and shown in Table 4.3.

Both loss models along with the trained ANN demonstrated a good prediction of fluid behaviour across the stationary blades. Critical thermodynamic parameters like total-to-static efficiency, steam exit temperature and exit static enthalpy showed a variation within  $\pm 4\%$  band. This was in agreement with previous studies [294]. Considering the low degree of reaction, the fluid velocity at the stationary blade exit  $C_2$  reflected the primary nozzle's conversion effectiveness. Comparison between the loss models demonstrated a deviation within  $\pm 1\%$  from the value of the existing machine. Relative velocity at the moving blade exit  $V_3$  and fluid relative exit angle  $\beta_3$  reflected the moving blade efficiency wherein larger deviations were observed as incidence losses were not considered.

Table 4.3: A comparison of the results of the validation

Thermodynamic parameters		Experimental data			Soderberg loss model			Craig and Cox loss model			ANN black-box model		
		Load 1	Load 2	Load 3	Load 1	Load 2	Load 3	Load 1	Load 2	Load 3	Load 1	Load 2	Load 3
Input	Inlet pressure (kg/cm <sup>2</sup> )	10.5	14.4	9.44	10.5	14.4	9.44	10.5	14.4	9.44	10.5	14.4	9.44
	Inlet temperature (°C)	296	311	295	296	311	295	296	311	295	296	311	295
	Outlet pressure (kg/cm <sup>2</sup> )	7.8	8.7	6.6	7.8	8.7	6.6	7.8	8.7	6.6	7.8	8.7	6.6
	Mass flow rate (kg/cm <sup>2</sup> )	6.11	3.32	5.36	6.11	3.32	5.36	6.11	3.32	5.36	6.11	3.32	5.36
Output	Total-to-static stage efficiency (%)	89.76	90.12	86.44	90.73	92.9	89.7	92.46	92.68	89.38	88.5	89.41	87.17
	Static enthalpy after nozzle (kJ/kg)	2981	2957	2980	2971	2948	2965	2971	2950	2967	2972	2952	2967
	Pressure after nozzle (kg/cm <sup>2</sup> )	8.12	9.1	6.88	8.10	9.0	6.6	8.101	9.1	6.87	7.86	8.7	6.6
	Stagnation enthalpy after stage (kJ/kg)	2979	2951	2965	2967	2946	2961	2968	2947	2962	2975	2952	2964
	Exit temperature (°C)	263.25	252	258.1	260.4	256	253.1	252.9	253.5	253.8	261.7	252.4	254.8
	Power output corrected for gearbox and generator efficiency (kW)	396	372	407	401	383	423	408.4	381	419	391	368	410

## 4.6 Results and discussion

### 4.6.1 Effect of turbine inlet temperature

The turbine inlet temperature range in this investigation was 110–160°C to ensure the investigated fluids were superheated. As shown in Figure 4-5(a), both loss models demonstrated total-to-static turbine efficiency improvement in the case of all fluids except for R600. Whereas the Craig and Cox model demonstrated an increase in turbine efficiency for R245fa, R1234ze(Z), R1233zd(E), R1234ze(E) and R1234yf by 11%, 11.7%, 8%, 4.5% and 3.8%, respectively, the Soderberg model demonstrated an improvement by 11%, 11.5%, 9.7%, 5.5% and 4.5%, respectively.

Despite similar trends for all fluids, the Soderberg model observed 2% lower turbine efficiencies on average compared to the Craig and Cox loss model for R1234yf, R1234ze(E) and R1234ze(Z). Whereas the Craig and Cox model attributed this to the higher secondary losses for the moving blade, it was not possible to identify the loss component as the Soderberg model did not provide a break-up of individual secondary losses. The combined effect of the increased inlet fluid enthalpy and variable turbine efficiency increases the power output by up to 36% for both models in Figure 4-5(b). R245fa, R1233zd(E) and R1234ze(Z) working fluids demonstrated an improvement in cycle efficiency, whereas R1234yf, R1234ze(E), and R600 demonstrated a reduction in cycle efficiency with increased superheat (Figure 4-5(c)). R245fa, R1233zd(E) and R1234ze(Z) experienced the least drop in internal energy across the turbine, which was noted by their lowest power output (Figure 4-5(b)); The low outlet isentropic Mach numbers (up to 8% for these fluids), pointed to a lower isentropic heat drop, as shown in Figure 4-5(d). Additionally, the U/C<sub>2</sub> ratios observed for R245fa, R1233zd(E) and R1234ze(Z) were on average 18% higher than those for other fluids (Figure 4-5(e)). The flow coefficients were lowest for these three fluids (Figure 4-5(f)), which aligned well with the Smith chart [195]. The Soderberg model observed higher flow coefficients than the Craig and Cos loss model, pointing towards the additional efficiency losses due to the higher meridional fluid velocity [195]. From the results, it can be concluded that using a multistage, higher rotational speed, or a larger diameter turbine is highly recommended for R600 to maximise turbine efficiency for such fluids.

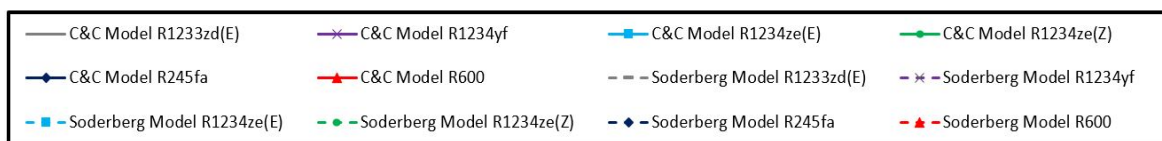
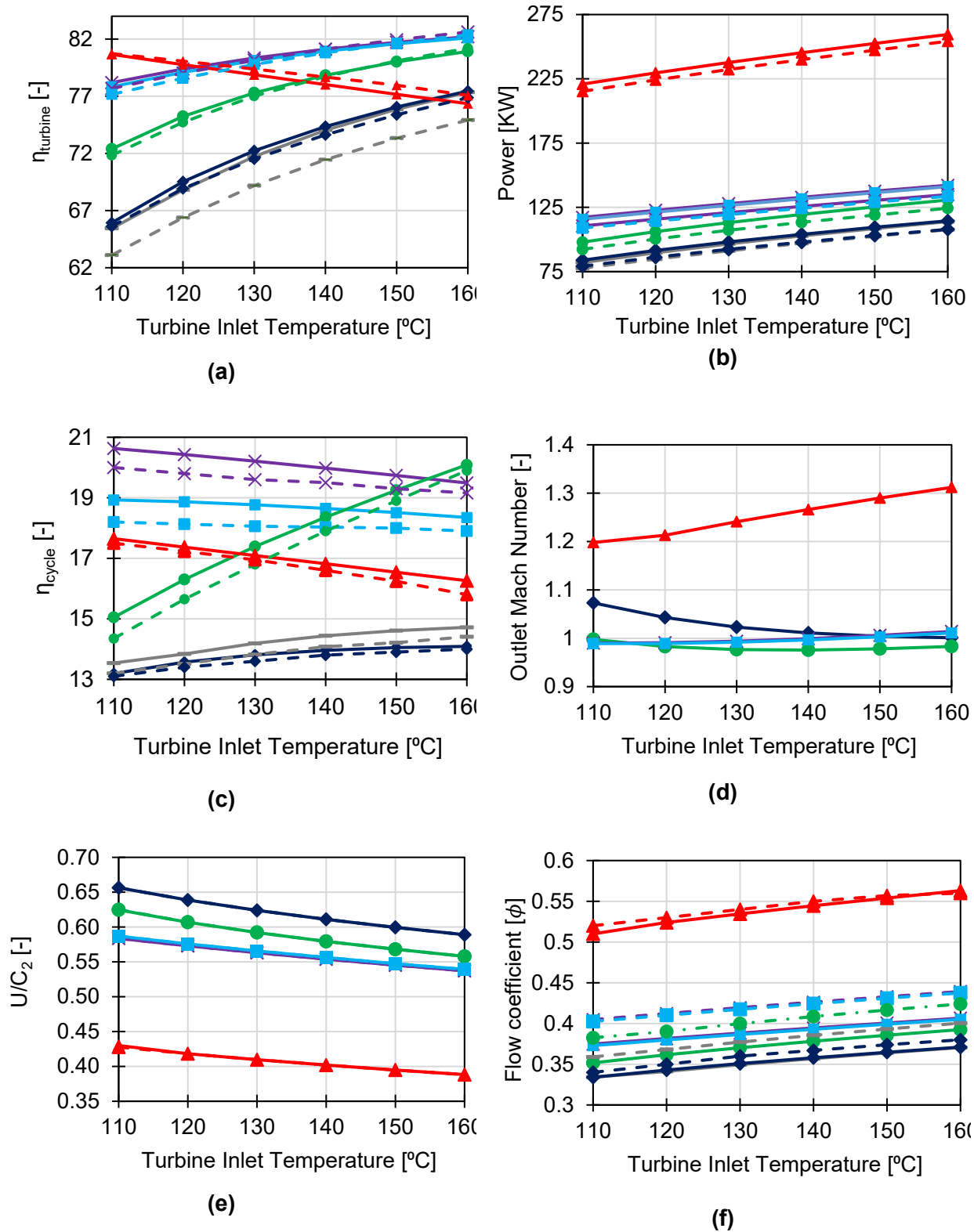


Figure 4-5: The influence of turbine inlet temperature on (a) total-to-static efficiency, (b) power, (c) cycle efficiency, (d) relative stage outlet isentropic Mach number, (e)  $U/C_2$  ratio and (f) flow coefficient

To understand the contradicting trend of turbine efficiency in the case of R600 fluid, the breakdown of individual losses was studied. This was done using the Craig and Cox loss model as the Soderberg model did not provide any analysis of the loss function. The overall turbine loss consists of the primary and secondary losses for the nozzles and blades. Figure 4-7 shows the distribution of the loss factors for all working fluids in the turbine stage between turbine inlet temperature range from 110 to 160°C. The primary blade loss in the case of R600 over the investigated range of superheat increased by 6.1%, compared to 1.7%, 1.48%, 2.62%, 2.59% and 2.6% for R245fa, R1233zd(E), R1234ze(Z), R1234yf and R1234ze(E), respectively. This was attributed to four factors: the moving blade profile, the fluid velocity, the higher enthalpy drop and lower molar mass.

The moving blade had a converging flow path across its length which limits the velocity drop across the profile, as shown Figure 4-6. Based on Bernoulli's equation, at supersonic velocity, the fluid behaviour is reversed, wherein a converging fluid path results in a further increase in velocity. Whereas all other fluids operated at subsonic or transonic conditions, R600 operated at supersonic conditions, where the fluid velocity was compounded by the convergent flow path. A convergent-divergent nozzle would be better suited in this case.

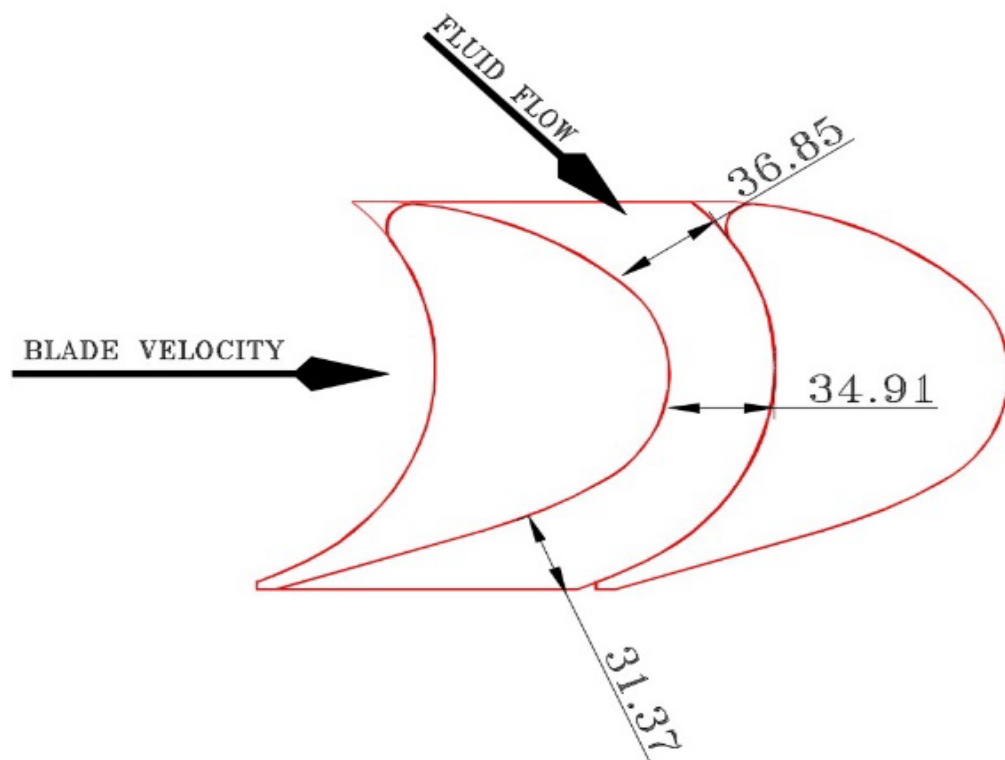


Figure 4-6: Converging area of the moving blade section

As fluid velocity was higher in the case of R600, the fluid experienced higher localised velocities at the suction surface. The incremental profile loss generated was applicable for Mach numbers higher than 0.7 and pitch-to-suction surface ratios lower than 0.7 [192]. The enthalpy drop across the turbine, a function of the internal energy, was relatively higher in the case of R600. The drop in internal energy across the investigated turbine was 77.6 Joules for R600, while in the case of R245fa, R1233zd(E), R1234ze(E), R1234ze(Z) and R1234yf, the mean internal energy drop was 33.4, 33.5, 39.7, 37.2 and 38.9 Joules, respectively. The significantly higher drop in internal energy maintained the fluid at supersonic velocity, which resulted in a greater Mach number loss.

Considering the low speed of sound of organic fluids, it was not uncommon for them to operate in the supersonic regime. This was more significant in the case of R600, due to its relatively lower molar mass of 58.12 g/mol, while those for R245fa, R1233zd(E), R1234ze(E), R1234ze(Z) and R1234yf were 134.04, 130.5, 114.04, 114.04, and 114.0 g/mol, respectively. The correlation of these factors is shown in equations 4.7 and 4.8; where  $R$  and  $MM$  denoted the universal gas constant and the molar mass of the fluid.

$$M = \frac{u}{c} \quad 4.7$$

$$c = \sqrt{\gamma T \frac{R}{MM}} \quad 4.8$$

Contradicting the consensus that superheating causing a loss in cycle efficiency [47, 119, 131, 215, 313, 314], it was observed that superheating of the working fluid could lead to improved cycle efficiency when used with high molecular mass fluids, converging blade profiles and subsonic fluid velocities. Compared to the traditional approach, where a fixed turbine efficiency was considered, this study noted that the turbine efficiency varied between 66 and 83%, as shown in Figure 4-5(a), across the investigated range of superheat considered for both loss models. This revealed that the working fluid's properties and the turbine's design configuration were interrelated. Thus, this finding emphasised the importance of considering the loss model at the component and cycle levels.

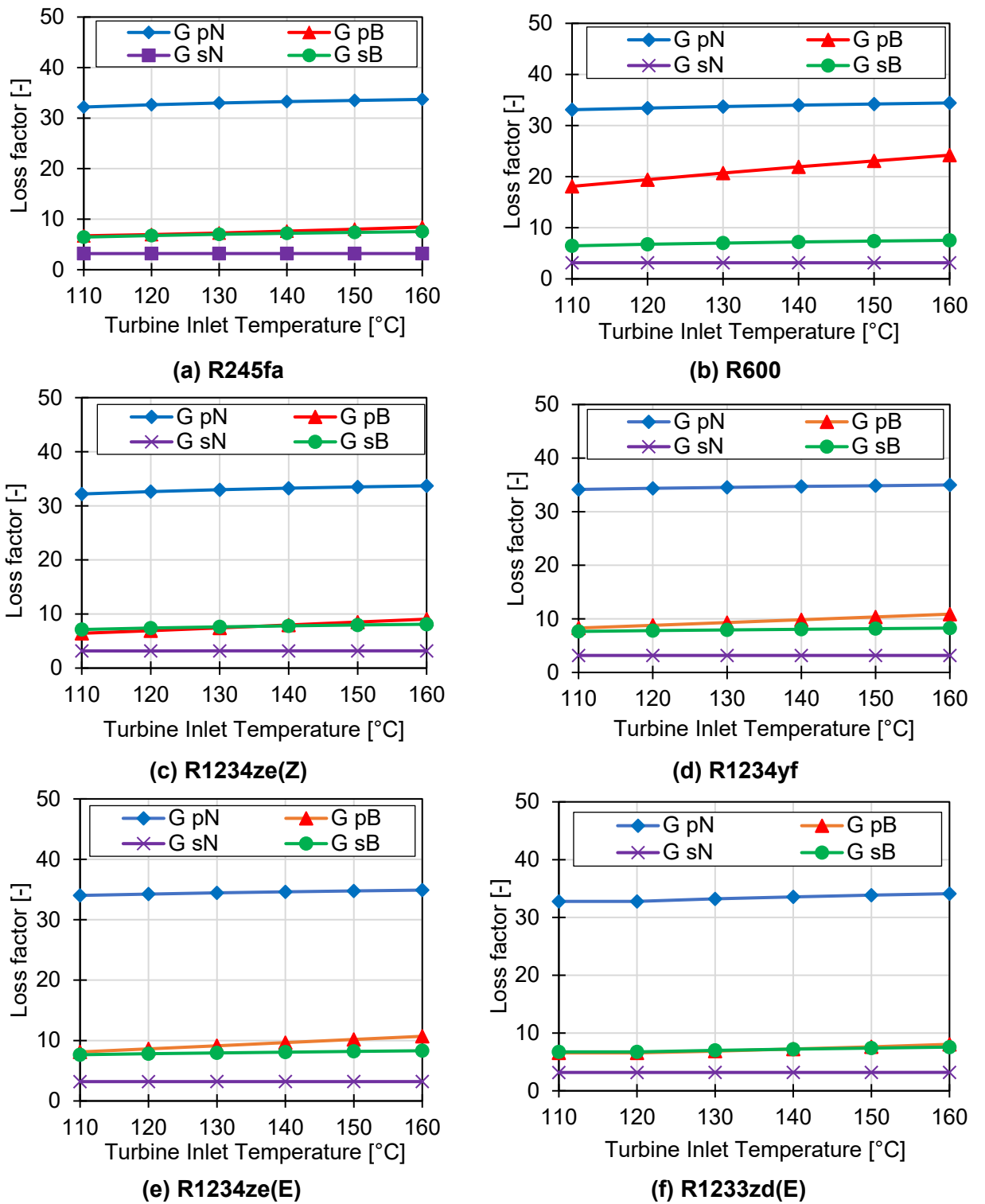


Figure 4-7: The influence of turbine inlet temperature on the loss coefficients for all six working fluids

#### 4.6.2 Effect of pressure ratio on the turbine's efficiency

The effect of varying the pressure ratio on turbine efficiency was investigated by varying the turbine inlet pressure. Pressure ratios between 3 and 10 were considered while all other geometric parameters were considered as fixed. The turbine's inlet temperature was maintained at a constant 140°C. The additional enthalpy drop across the turbine led to a more effective temperature drop, which manifested in the form of reduced turbine exhaust temperature, as seen in Figure 4-8 (a). There was a significant improvement in turbine efficiency up to a pressure ratio of 6; the benefits were less significant beyond that, as shown in Figure 4-8 (b). The power generated at pressure ratios above 6 was at limited efficiency; see Figure 4-8 (c). Both loss models demonstrated similar efficiency contours, despite the underestimation of efficiency by the Soderberg loss model by 6% and up to 21% (as in the case of R600, which has been discussed later). Although limited by the marginal improvements to expander efficiency beyond a pressure ratio of 5, the increased pressure ratios led to an increase in work done (Figure 4-8 (c)) and cycle efficiency (Figure 4-8 (d)).

The Craig and Cox loss model was used to investigate the breakdown of the losses. The model showed a significant increase in total losses beyond the pressure ratio of 6, as noted in Figure 4-9. Whereas a proportional increase of loss coefficient of about 4.5 was observed per unit increase in pressure ratio for the nozzle primary losses (as noted in Figure 4-10), the blade primary losses demonstrated an exponential two-fold increase beyond a pressure ratio of 6, as shown in Figure 4-11. The secondary losses remained relatively constant, irrespective of the pressure ratio, as observed in Figure 4-12 and Figure 4-13. Detailed investigation of the primary losses demonstrated a direct relation between the fluid velocity and primary loss coefficients, as shown in Figure 4-14 and Figure 4-15. The Mach number loss was identified as the largest contributor to the variable turbine efficiency.

The nozzle primary loss coefficient for all fluids increased by up to 275% for a corresponding 44% increase in the nozzle outlet isentropic Mach numbers, with conventional profiles having difficulty in undertaking a high expansion ratio [211]; therefore, multistage turbines could be considered for higher pressure ratios, as suggested by Meroni et al. [133]. The additional profile increment loss was a component of the nozzle primary loss, which occurred for values of blade exit isentropic Mach numbers beyond 1.2 [192]. For R600, increasing the pressure ratio reduced the turbine efficiency, as the energy losses in the form of heat are relatively higher when compared to other fluids. Such heat losses are primarily due to the high flow speed of the turbine blades, which is the work-producing element in the turbine due to its low molar mass, leading to supersonic flow.

In the case of all the investigated fluids, except R600, the moving blade outlet isentropic Mach number demonstrated subsonic fluid velocities up to the pressure ratio of 6.

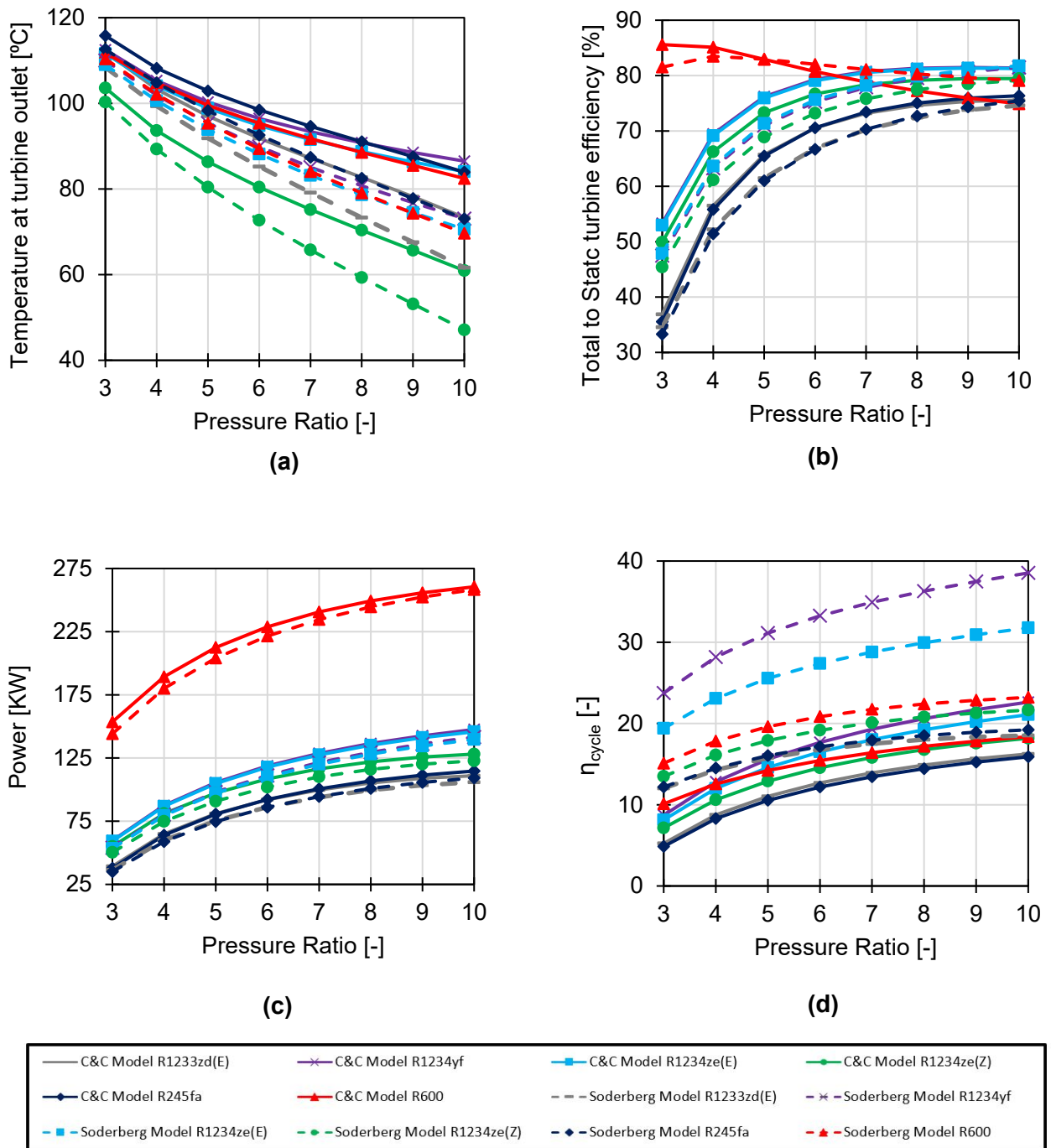


Figure 4-8: The influence of pressure ratio on: (a) Exhaust temperature; (b) Total-to-static efficiency; (c) Power output; (d) Cycle efficiency

A further increase in pressure ratio led to the operation in the transonic regime. It was observed that increasing the pressure ratio from 3 to 6 led to an average increase of the blade primary loss coefficient by 172% (3.8 units). Increasing the pressure ratio from 6 to 9 increased the blade primary loss coefficient by 191% (11.5 units). Pressure ratios between 3 and 5 demonstrated a reduction in fluid velocity, indicating that the given turbine was best configured for a pressure ratio of 5 for these fluids.

In contrast, R600 demonstrated an increase in total loss coefficient across the entire range of pressure ratios; this was due to the higher moving blade primary and secondary losses, which resulted from the higher working fluid velocity at the moving blades, as shown in Figure 4-15. Similar to the effect of superheating, both loss models demonstrated similar trends, although the Soderberg model was noted to underestimate the drop in efficiency caused by these high values of Mach number, exceeding 1.2 in the case of R600 (Figure 4-5 (b)).

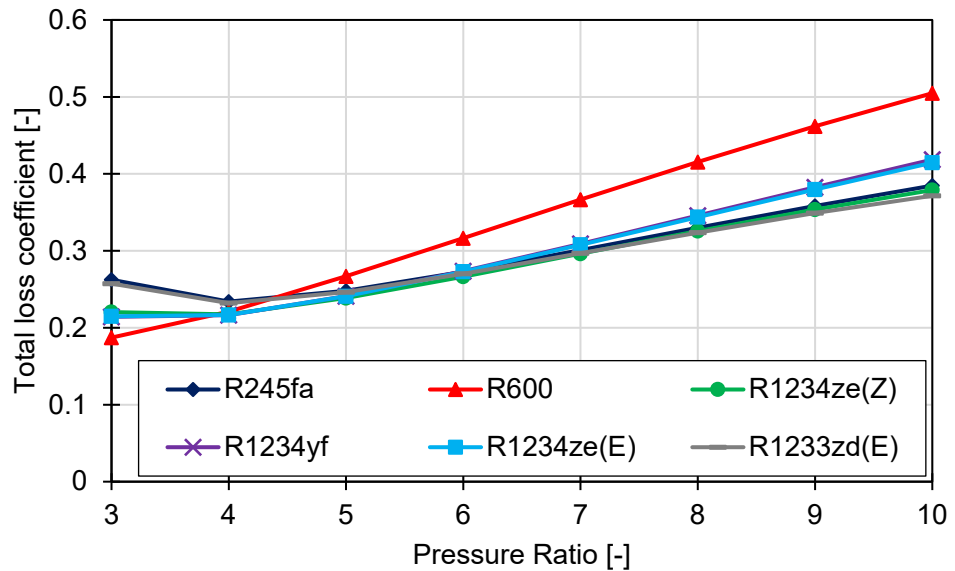


Figure 4-9: Variation of total loss coefficient with change in pressure ratio

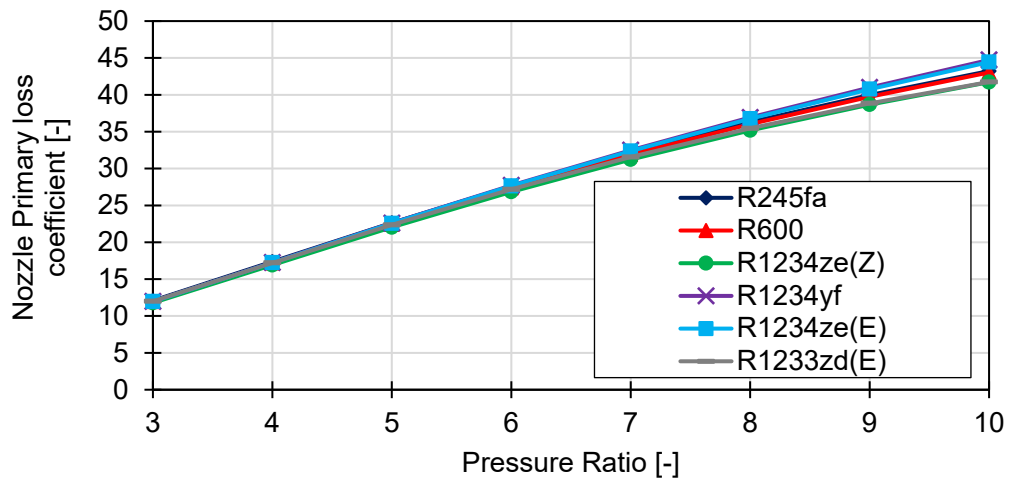


Figure 4-10: Variation of nozzle primary loss coefficient with change in pressure ratio

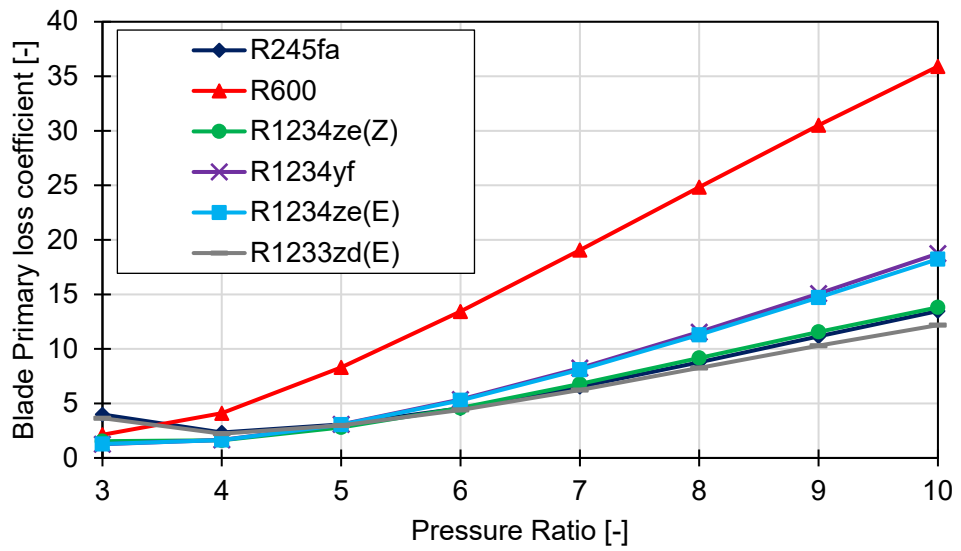


Figure 4-11: Variations in blade primary loss coefficients with change in pressure ratio

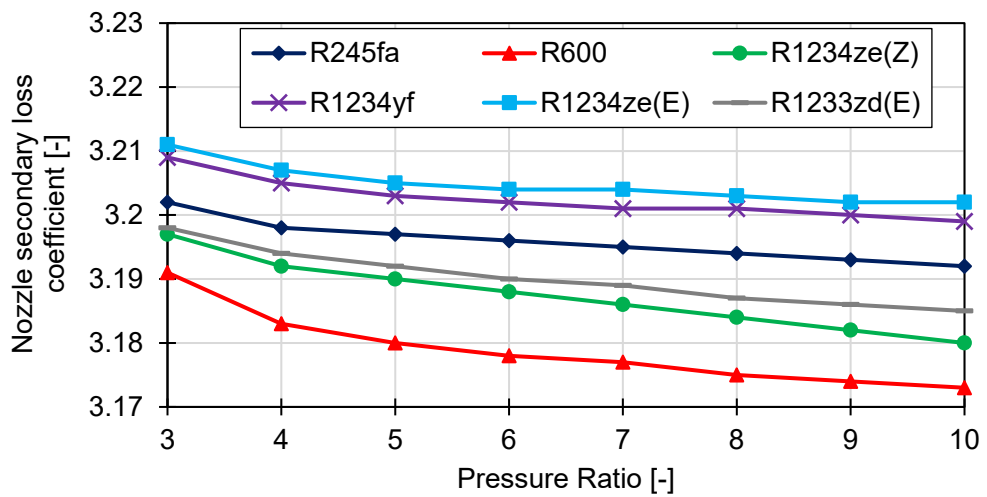


Figure 4-12: Variations in nozzle secondary loss coefficients with change in pressure ratio

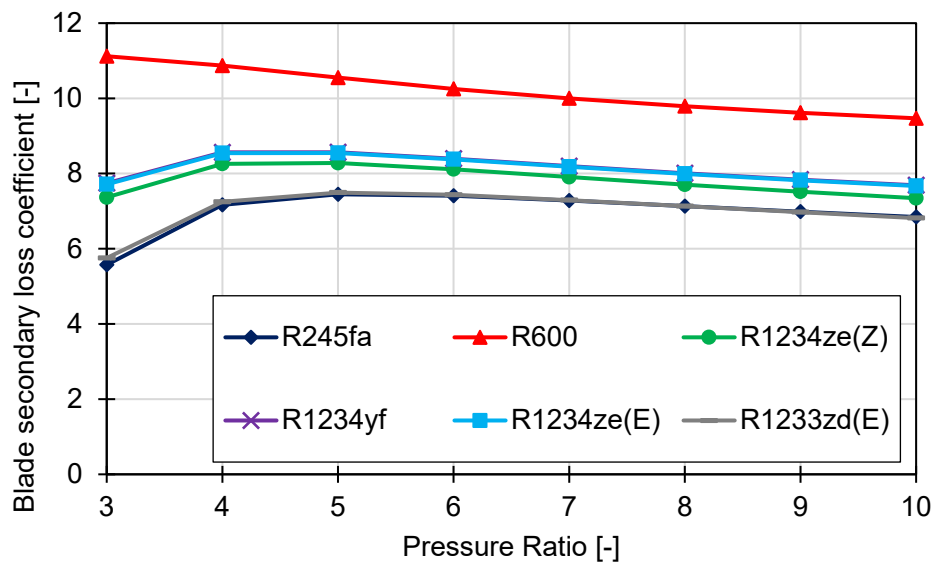


Figure 4-13: Variations in blade secondary loss coefficients with change in pressure ratio

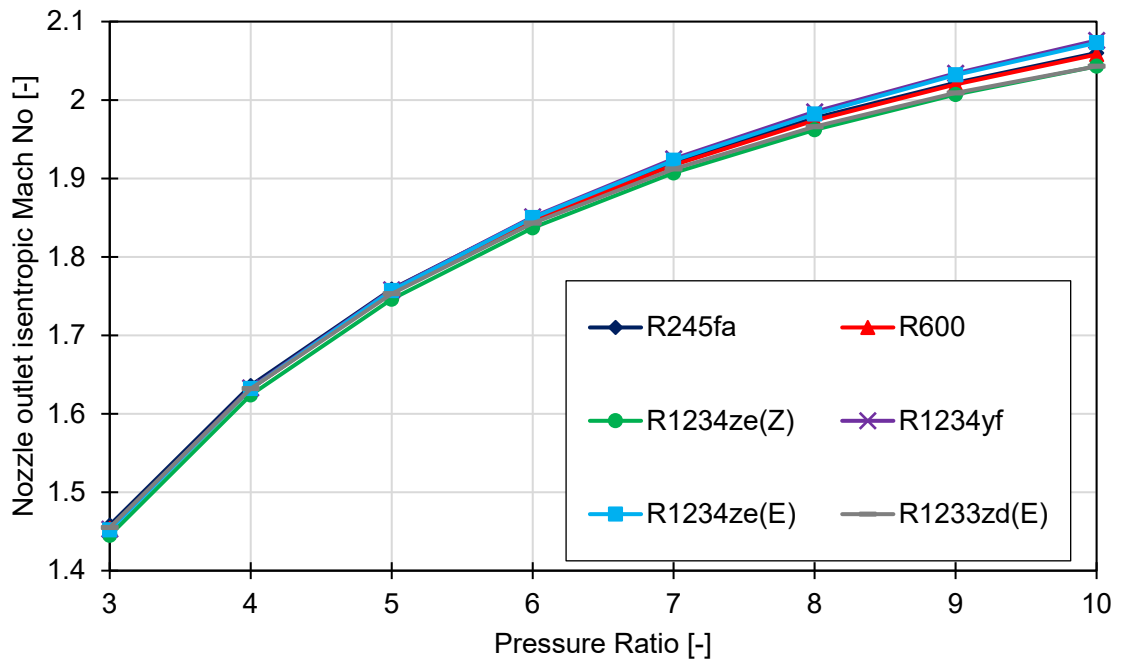


Figure 4-14: Variations in nozzle outlet isentropic Mach number with change in pressure ratio

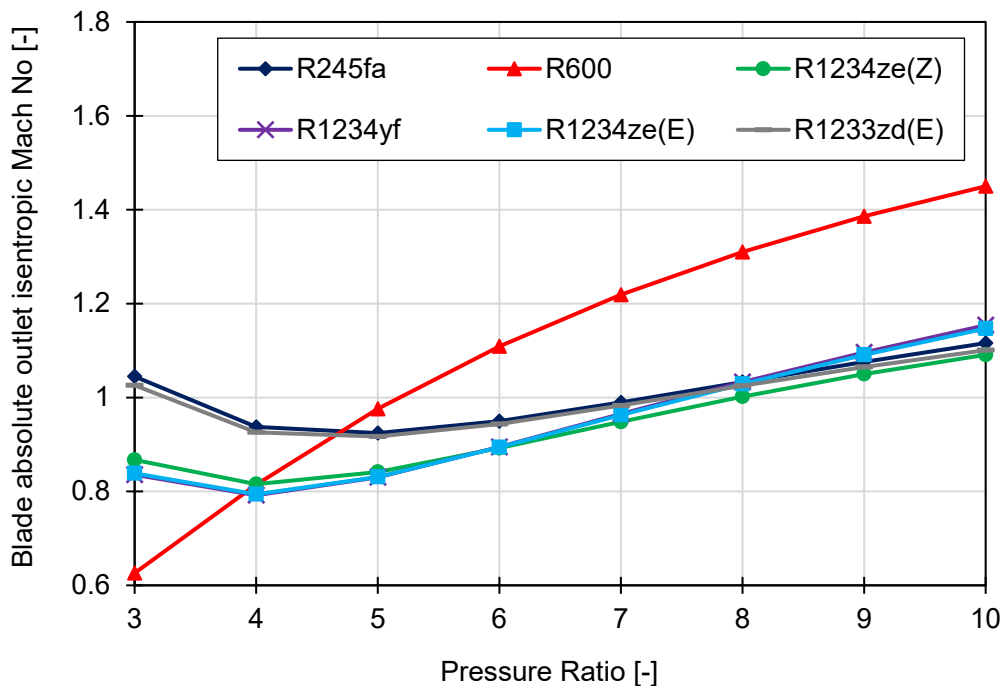


Figure 4-15: Variations in blade outlet isentropic Mach numbers with change in pressure ratio

### 4.6.3 Turbine optimisation

The GA was coupled with the ANN turbine model to optimise the profile geometry, aiming the maximum turbine's total-to-static efficiency. Given that R1234ze(Z) demonstrated high levels of total-to-static efficiency for both boundary condition changes (Figure 4-5(a), Figure 4-8(a)), it was considered for optimisation. The optimised flow geometrical parameters were verified against the Craig and Cox loss model, as shown in Table 4.4, it was observed that the

optimised profile improved the nozzle efficiency by 13.7% at the expense of 18.9% drop in blade efficiency. As the flow path developed was that of a highly impulse-loaded machine, the algorithm achieved 5.14% higher stage efficiency by compromising blade efficiency for nozzle efficiency. The algorithm increased the degree of reaction, which led to a more evenly distributed enthalpy drop across the nozzle and moving blade that led to a 2.6% reduction in nozzle exit velocity ( $C_2$ ). This, in turn, resulted in additional performance gains due to the lower flow coefficient ( $\phi$ ) and an optimised  $\frac{u}{C_2}$  coefficient.

The backbone radius ratio loss was a function of the pitch to back bone radius ratio. Decreasing the pitch and increasing the backbone length achieved an 8.6% improvement in backbone radius ratio loss. Reduced trailing edge thickness led to a 66% and 28% reduction in the trailing edge thickness increment loss, respectively ( $loss_{incr_N}$ ,  $loss_{incr_B}$ ). The nozzle exit angle ( $\alpha_2$ ) was optimised to reduce the axial component of velocity ( $C_{a2}$ ) and the associated losses. The backbone radius ratio loss ( $\Delta X_{pse}$ ), trailing edge thickness increment loss ( $loss_{incr_N}$ ,  $loss_{incr_B}$ ) and axial component nozzle exit velocity ( $C_{a2}$ ) were factors of the primary loss ( $G_{pN}$ ,  $G_{pB}$ ). The selection of a larger throat width ( $thr_N$ ) resulted in lower profile losses for the nozzle due to the reduced boundary layer developed. Reducing the nozzle exit angle led to a reduction in the axial velocity component, that did not carry out useful work. The optimised blade profile led to a 1% improvement in cycle efficiency (Table 4.4). The RMS error value and training charts shown in Figure 4-16 demonstrate the convergence achieved by the ANN.

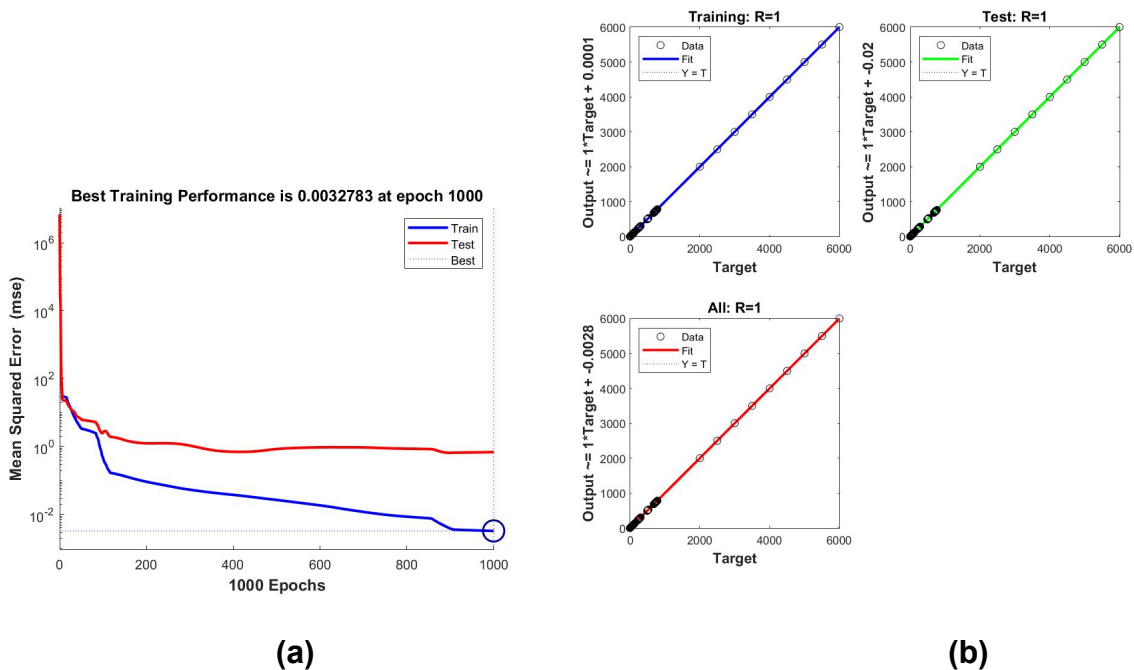


Figure 4-16: (a) RMS error after 1000 iterations; (b) ANN training performance

Table 4.4: Genetic algorithm (GA)-optimised parameters and test results

Variable type	Parameter	Original value from loss model	GA-optimised values	GA-optimised values verified by Loss model
Independent Variable	Speed (rpm)	5000	4715.31	4715.31
	Hub diameter	0.660	0.630	0.630
	Degree of reaction	0	0.07	0.07
	Nozzle exit angle ( $\alpha_2$ )	14	12.23	12.23
	Nozzle throat ( $thr_N$ )	0.00497	0.0065	0.0065
	Blade throat ( $thr_B$ )	0.0035	0.0061	0.0061
	Nozzle pitch	0.029	0.023	0.023
	Blade pitch	0.011	0.025	0.025
	Nozzle backbone length	0.0736	0.0792	0.0792
	Blade backbone length	0.0217	0.0792	0.0792
Dependent Variable	u	172.7	162.8	162.8
	$C_2$	281.6	281.8	274.4
	$u/C_2$	0.61	0.57	0.59
	$C_{a2}$	68.11	59.87	58.21
	Total to static efficiency	0.788	0.81	0.84
	Total to total efficiency	0.89	0.93	0.92
	Cycle efficiency	8.78	9.75	9.53
	Power	119.5	141.8	123.1
	Volume ratio	7.45	7.34	7.5
	Flow coefficient ( $\phi$ )	0.37	0.20	0.35
	Load coefficient ( $\Psi$ )	1.32	2.06	1.62
	$G_{pN}$	33.2	30.56	28.84
	$G_{pB}$	7.95	6.40	8.34
	$G_{sN}$	3.16	2.15	2.55
	$G_{sB}$	7.79	8.08	10.38
	$G_{total}$	0.31	0.33	0.30
	$lossincr_N$	0.0099	0.0034	0.0037
	$lossincr_B$	0.0077	0.0057	0.0058
	$M_{detN}$	10.34	31.83	16.6
	$M_{detB}$	19.95	24.52	14.48
$\Delta X_{pseN}$	17.48	9.39	10.3	
$\Delta X_{pseB}$	5.785	5.294	5.414	

The optimised solutions and original solution mentioned in Table 4.5, were in good agreement with the Smith chart, which correlates the turbine efficiency to the flow coefficient ( $\phi$ ) and load coefficient ( $\Psi$ ) [316]. The optimiser achieved 5.2% improvement in total-to-static efficiency. The research noted that the optimiser reduced the flow coefficient ( $\phi$ ) to maximise efficiency. The GA-optimised profiles were verified with the Craig & Cox loss model. Table 4.6 presents the range of independent variables demonstrating the 98<sup>th</sup> percentile results for best total-to-static efficiency.

Table 4.5: A comparison of losses optimised by ANN and GA

Losses	Original	Optimised	Loss reduction in %
Total losses	0.311	0.2951	5.14%
Total nozzle group 1 loss	0.218	0.193	11.5%
Total blade group 1 loss	0.093	0.102	-9.67%
Nozzle primary loss $G_{pN}$	33.22	28.84	13.18%
Nozzle secondary loss $G_{sN}$	3.16	2.55	19.3%
$lossincr_N$	0.0099	0.00375	62%
Nozzle Profile loss $X_{pN}$	17.48	9.397	46.24%

Table 4.6: The range of parameter variations provided by optimised solutions

Parameter	Unit	Lower value	Upper value
Turbine speed	rpm	4500	5200
Degree of reaction	--	0.05	0.1
Hub diameter	m	0.5	0.6
Nozzle exit angle	°	12.5	14
Nozzle throat	mm	6.490	6.511
Blade throat	mm	6.089	6.177
Nozzle pitch	mm	22.807	23.779
Blade pitch	mm	25.211	26.007
Nozzle backbone length	mm	71.439	90.471
Blade backbone length	mm	71.439	90.471

## 4.7 Conclusion

This chapter aimed to envisage the cause of the turbine efficiency losses in the small-scale axial flow turbines and their impact on ORC performance. The Soderberg and Craig and Cox loss models were employed to imitate a small-scale axial flow turbine and integrated it with a one-dimensional (1-D) model of an ORC. The ANN coupled with GA was utilised to optimise the turbine flow path and study its influence on the ORC performance and to understand the influence of turbine inlet flow conditions on the turbine and cyclic performance utilising a range of organic fluids. The main findings of the current study are summarised below.

- The results obtained highlight the importance of considering turbine efficiency as a part of the cycle-level study. Direct loss models are preferred as they are independent of working fluids. Although the Soderberg loss model typically demonstrated a maximum deviation of 5% in isentropic efficiency, the mean deviation was less than 2%.

Additionally, it demonstrated similar trends to the Craig and Cox loss model in most cases, which highlighted its suitability for preliminary cycle-level studies. However, it had limited values as a turbine design and optimisation tool as it did not provide a detailed loss breakdown.

- Considering variations in superheat and pressure ratios, the choice of working fluid has a significant impact on cycle design. Higher temperature working fluids, with a higher isentropic drop and lower molar mass are less suitable for conventional single-stage turbine designs, as they lead to approximately 30% higher fluid velocities, as observed in the case of R600.
- Although superheating led to an increase in Mach number loss and blade back radius ratio loss, turbine efficiency improved for most of the investigated organic fluids, with a maximum 12.4% improvement in turbine efficiency in the case of R245fa, R1233zd(E) and R1234ze(Z). Cycle efficiency demonstrated an improvement in the case of R245fa, R1233zd(E) and R1234ze(Z), which implied that superheated ORC cycles could be beneficial but need to account for variations in turbine efficiency.
- Increasing pressure ratios led to an average 38% increase in turbine efficiency for R245fa, R1234ze(Z), R1234yf and R1234ze(E). The Mach number of the working fluid, which reached 2.1 at the moving blade, was noted as the most influential on the primary losses.
- Moving blade relative velocity above 1.6 led to a drastic increase in primary loss which nullified improvement in the turbine efficiency achieved by higher pressure ratios.
- Using deep learning for profile optimisation offered a simple and computationally efficient approach for optimising the flow path's design. The optimised flow path showed a 5.2% improvement in turbine total-to-static efficiency and a 0.24% improvement in cycle efficiency. High percentile results generated by ANNs can be used as a good starting point for advanced blade design.

# Chapter 5 Single Objective Thermodynamic Cycle Optimisation

## 5.1 Introduction

The previous chapter was centred around investigating the variations in ORC turbine's isentropic efficiency with changes in boundary conditions and providing a recommendation of an optimised turbine geometry. This chapter details how the optimised turbine geometry was employed to investigate the impact of utilising transient heat sources. Considering the variations in turbine efficiency for any cycle configuration studies with heat source temperatures above 150°C is an indispensable strategy [81]; nevertheless, most cycle optimisation studies have been restricted to a fixed turbine efficiency [51, 226] or similitude theory [81]. In reality, scaling the turbine using similitude influences the Reynolds number, a significant factor for primary profile losses that can cause major variations in turbine efficiency [273, 295].

Although previous studies were undertaken to establish the feasibility of ORCs for utilising low-grade heat sources, limited studies based on flue gas stacks, widely used for industrial process steam boilers, were previously considered [119]. One of the few studies for flue gas-based waste heat recovery (WHR) using ORCs was undertaken by Wang et al. [296]. Although the study considered heat source temperatures between 150°C to 250°C, it was limited to steady state heat source conditions, zero pressure drop across heat exchangers and a fixed turbine isentropic efficiency of 80%. Additionally, the operation of the working fluid was restricted to the saturation phase.

Previous studies have provided controversial results about the benefits of using a recuperator to improve cycle efficiency. Whereas some previous theoretical studies showed an improved cycle efficiency, others 'that adding recuperators was not advisable in the case of an unconstrained waste heat source stream due to the additional pressure drop and increased capital expenditure [58]. This was more relevant for low- and medium-grade heat sources and wet type fluids that provided limited potential for sensible heat recovery [280].

Building on the extensive literature review undertaken, no single study exists that investigated the impact of utilising a quantified waste heat source under transient conditions. Investigating ORCs utilising Transient heat sources require is computationally intensive process, which are best undertaken with the help of an efficient optimiser. Previously, the use of the genetic algorithm (GA) has been well proven for organic Rankine cycles (ORC) optimisation, but operate under steady heat source [70]. This thesis notes that the gradient-based non-linear programming by the quadratic Lagrangian (NLPQL) algorithm had significantly lower

computational requirements compared to the GA, but has not previously validated with a similar application [258].

Therefore, this chapter aims to optimise the component sizes for a range of various ORC configurations, targeting the highest power output for a finite transient waste heat source, considering the variations in turbine efficiency. The objectives are as follows.

- Developing a one-dimensional (1-D) thermodynamic model coupled with the Crag and Cox turbine model to assess the thermodynamic feasibility of an ORC driven with an actual transient heat source wasted from an existing micro co-generation steam power plant considering the variation in the turbine efficiency.
- Optimising the component sizes for a range of ORCs' configuration by considering variable turbine efficiency. The study concerned integrated various heat recovery components to enhance the energy conversion efficiency and minimise the steam power plant's fuel consumption. Two optimisation algorithms were utilised and compared: NLPQL and GA.
- Benchmarking the improvements in the power output and computational efficiency achieved by the parametrically pre-optimised NLPQL and GA in comparison to a conventional parametric optimisation.

In the author's opinion, the optimisation study on an ORC for the given configurations with variable turbine efficiency based on actual transient waste heat source and its comparison using different optimisation techniques is the critical contribution of this chapter.

### 5.1.1 Heat source

This study considered an actual transient waste heat source from a steam boiler operating at a textile plant at Ghaziabad in India. Steam was utilised in the process for conducting dyeing operations over colourless white fabric, commonly known as 'grey fabric' [297]. As the textile plant had over 150 machines including jiggers, calenders, mercerisers, jet dyeing and loop dyeing machines, a reasonably constant steam flow was maintained by the steam boiler, shown in Figure 5-1(a). Such an integrated system smooths the fluctuations in flue gas temperature.

The boiler undertook combustion of crushed Indonesian sub-bituminous coal with a gross calorific value of 23 MJ/kg, using a screw feeder as shown Figure 5-1(b) [298]. The steam boiler along with its superheater was rated to produce 4.44 kg/sec of steam at an operating pressure of 19 kg/cm<sup>2</sup> and 240°C, from feed water at 100°C. The steam first passed through an incidental co-generation micro steam turbine, manufactured by IB Turbo, India, as shown in Figure 5-1(c), which reduced the steam pressure to 4 kg/cm<sup>2</sup>, which was then utilised during

the process. The electricity generation from the steam turbine varied between 240 and 300 kWe hourly.

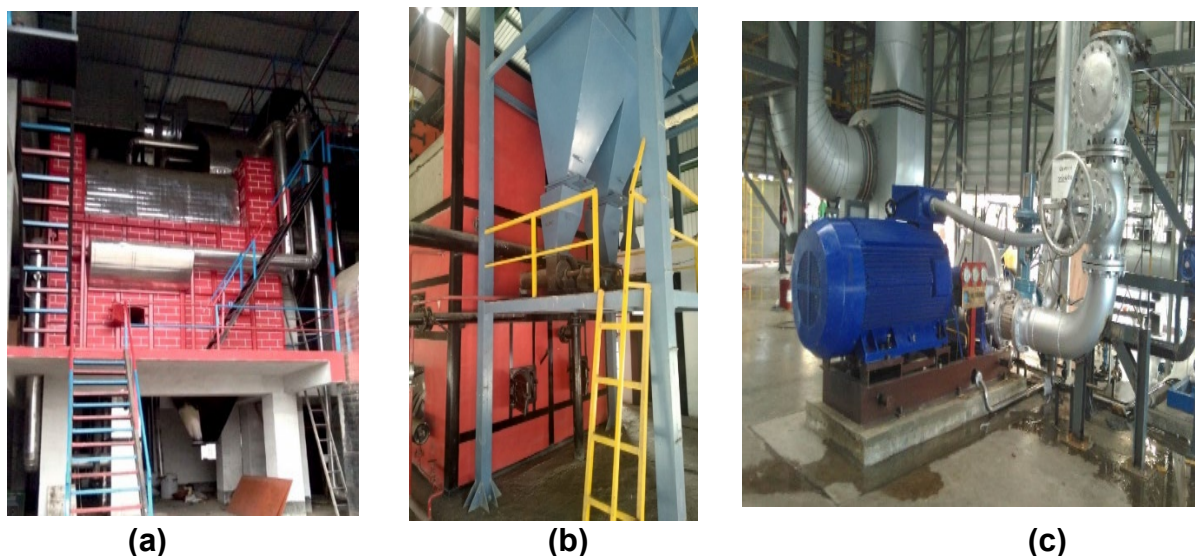


Figure 5-1: (a) Steam boiler considered for study; (b) Boiler coal feeding mechanism; (c) Micro co-generation steam turbine

The boiler used a forced and induced draft fans to maintain the flow of air and flue gas, as shown in Figure 5-2. Ambient air was first directed to the furnace where an atmospheric fluidised bed combustion system facilitated the mixing of fuel and air. The combustion products then passed through the pressurised superheater, evaporator, economiser and a non-pressurised water pre-heater, all using a counter-current design. Consideration of the pinch point required the use of multiple heat exchangers, highlighting the importance of recovering lower-grade heat. The flue gas was passed through an electrostatic precipitator that captured part of the suspended particulate matter and a wet scrubber for desulphurisation, which removed dissolved gases by washing the by-products of combustion, particularly sulphur dioxide (SO<sub>2</sub>) and nitrogen oxide (NO<sub>x</sub>).

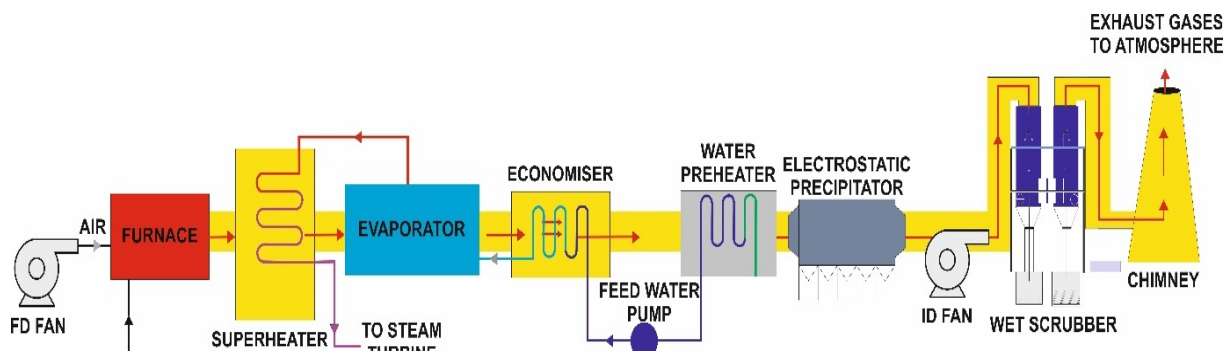


Figure 5-2: Flue gas path of the micro co-generation steam boiler

The hourly mass flow rate of the steam is determined based on the stoichiometric air to fuel ratio from the fuel sample, as detailed by Widodo et al. [299]. Excess air quantity was considered as 35%, as specified by the steam boiler manufacturer and validated using the Y. C. Engineer, PhD Thesis, Aston University, 2022

findings of Mastral et al. [300] for atmospheric fluidised bed combustion boilers. This was used to determine the mass flow rate of flue gas, presented as Figure 5-3(a). Noting that the ash content of Indonesian coal was lower than 1.7%, its contribution to the mass flow rate was ignored [301].

The dry flue gas heat loss is a greater contributor to steam boiler inefficiency [302], which is quantified by measuring the flue gas temperature after the water preheater impeded into the steam boiler. Accordingly, the use of an organic Rankine cycle operating with a medium temperature working fluid was a feasible heat recovery technology to boost the plant energy conversion efficiency. Table 5.1 shows exemplar readings for the operating conditions in the plant. Figure 5-3(b) shows the typical variation in total input thermal energy within an operating shift.

Table 5.1: Flue gas parameters

Reading no.	Time of day	Steam flow	Steam boiler fuel consumption	Steam boiler fuel input energy	Stoichiometric air	Total flue gas	Total feed air	Flue gas Temperature	Power from steam turbine
	hhmm	kg/sec	kg/sec	kJ/sec	kg/sec	kg/sec	kg/sec	°C	kW
1	0730	3.58	0.597	11947.8	4.61	6.23	5.62 <sub>9</sub>	181	284
2	0830	3.05	0.509	10174.6	3.93	5.30	4.79 <sub>3</sub>	177	264
3	0930	3.48	0.581	11610.0	4.48	6.05	5.46 <sub>9</sub>	176	278
4	1030	3.09	0.515	10301.2	3.98	5.37	4.85 <sub>3</sub>	178	264
5	1130	3.65	0.608	12158.8	4.69	6.34	5.72 <sub>8</sub>	179	296
6	1230	2.59	0.433	8654.7	3.34	4.51	4.07 <sub>7</sub>	164	242
7	1330	2.87	0.479	9575.8	3.70	4.99	4.51 <sub>1</sub>	172	259
8	1430	2.63	0.438	8769.9	3.39	4.57	4.13 <sub>2</sub>	173	242
9	1530	3.60	0.599	12010.0	4.63	6.26	5.66	181	273

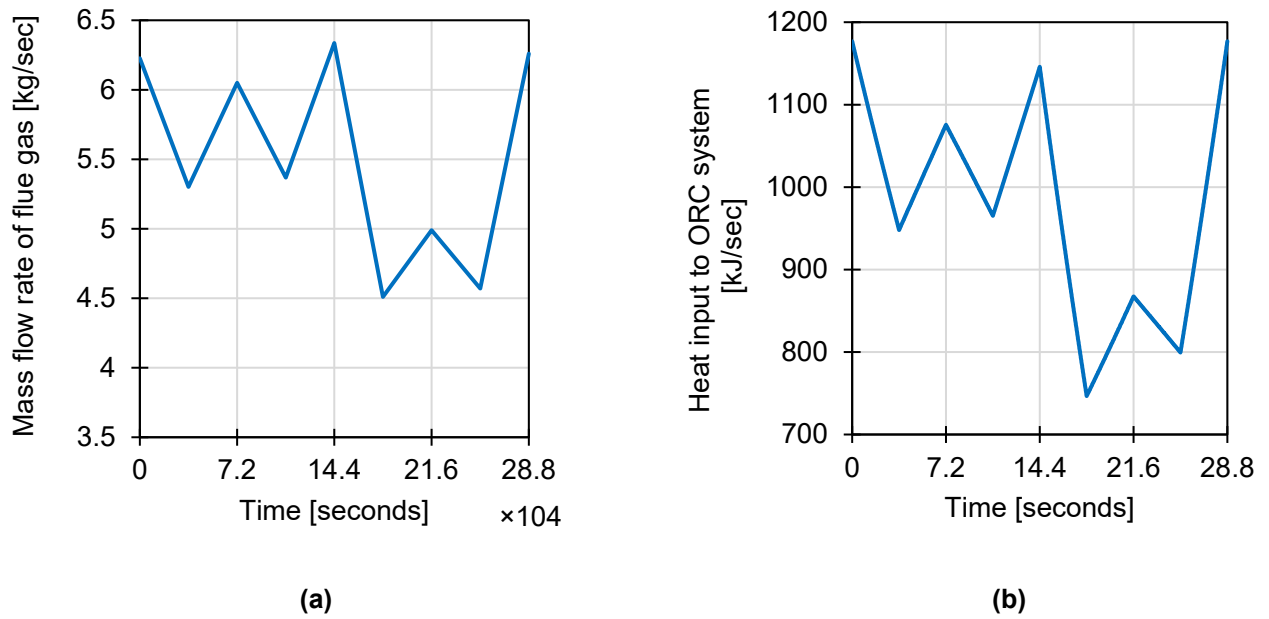


Figure 5-3: (a) Mass flow rate of the flue gas; (b) Input energy to system from the flue gas

### 5.1.2 Assumptions

As the average annual temperature recorded for the city of Ghaziabad, India, was observed as 25.7°C for the year 2020, this was considered as the ambient temperature for the study [303]. This was considerably greater than the global average annual temperature of 13.9°C [12]. The ambient temperature is one of great interests, as previous studies determined an up to 30% drop in power output of ORC systems at elevated temperatures [304]. Altun et al. observed a 1.4% (from 11.23% to 8.05%) drop in cycle energy efficiency and 10% (49.31% to 44.98%) drop in cycle exergetic efficiency for a 10°C increase in the condensation temperature (noted from 0°C to 30°C) [305].

The volumetric efficiency of the pump was considered 50%. As the pump power consumption was less than 10% that of turbine power generation, it was ignored for determining cycle efficiency [63, 306]. Pump sealing losses, turbine sealing losses, turbine bearing losses, gearbox and generator efficiency of the turbine were ignored for the sake of simplicity. Pressure drop across the boiler air preheater (APH) for fresh air was overlooked as this could be reduced using a heat exchanger with reduced gas velocity [307]. Ash content of the fuel was discarded for flue gas mass flow calculations.

## 5.2 Methods and materials

### 5.2.1 Cycle architecture

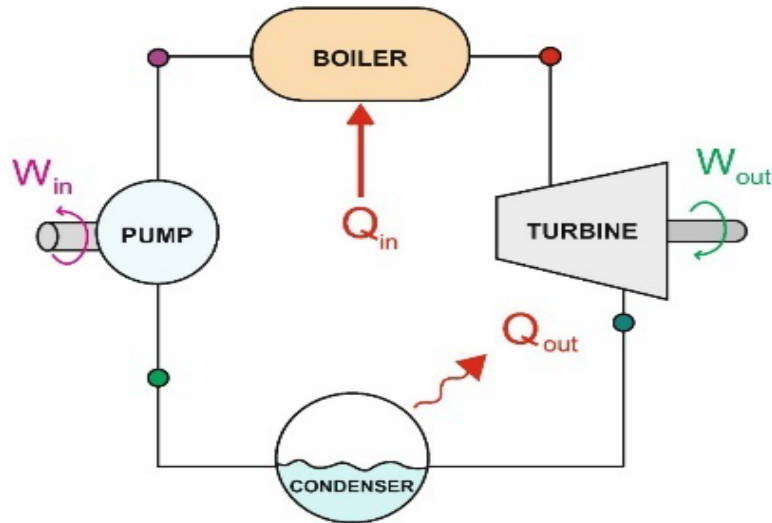


Figure 5-4: Conventional ORC

The conventional ORC consists of four components: boiler, expander, condenser and circulating pump, as shown in Figure 5-4. Ten different configurations of the ORC were investigated. These configurations involved the use of regeneration, thermal energy storage, direct recuperation and regeneration. Recuperators are indirect heat exchangers that are often used to enhance the process energy conversion efficiency. Continuous regeneration involves direct contact between two different streams; the absence of a heat exchanger led to a lower investment in capital expenditure as compared to recuperation and greater flexibility to control the degree of heat recovery during operation. An air preheater is a gas-to-gas recuperator typically utilised in steam boilers to increase the temperature of the feed air. The heat transfer effectiveness between two gaseous mediums in conventional air preheaters is relatively low that limits the process energy conversion efficiency. As organic fluids have high values of latent heat, the air preheater converted of the low-grade ORC exhaust fluid from saturated vapour to liquid phase, where heat transfer coefficients were an average of 2.4 times higher than the gaseous state. [308]. The previous chapter concluded that superheating working fluids led to an improvement in cycle efficiency. In this chapter, the addition of a thermal mass is used to understand the impact of maintaining the superheat at system-level ORC studies.

The dedicated one-dimensional (1-D) simulation package Simcenter Amesim was used to recreate the variations of the ORC cycle. The superheated ORC cycle is shown in Figure 5-5(a), the simulation model of which is shown in Figure 5-5(b). The thermal storage with cycle addition of three masses of GS 53 cast iron of 104 kg each to buffer the variation in thermal energy into the system is shown in Figure 5-6. Figure 5-7 features the addition of an air preheater as an integrated heat energy recovery device to optimise the steam boiler's feed air

Y. C. Engineer, PhD Thesis, Aston University, 2022

temperature, while the modelling of the five stage heat exchangers is demonstrated in Figure 5-7 (b). Figure 5-8 shows a recuperative cycle, then combined with thermal storage in Figure 5-9. In Figure 5-10, high temperature exhaust fluid first passes through the recuperator and then an air preheater as this order maximises the ORC's internal cycle efficiency. A regenerative cycle is presented in Figure 5-11, where intermediate pressure working fluid is extracted to increase the temperature of the ORC fluid to the economiser. The combination of the regenerative cycle along with thermal energy storage was investigated as in Figure 5-12. The regenerative cycle is also combined with the air preheater, as in Figure 5-13. Lastly, an ORC that features a combined recuperation and regeneration is proposed in Figure 5-14.

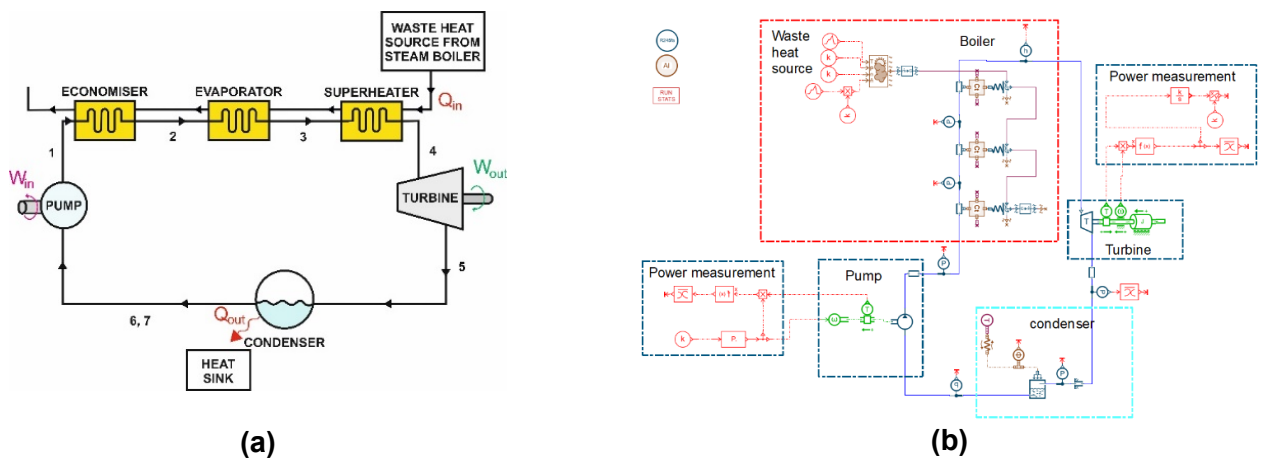


Figure 5-5: Superheated ORC: (a) Schematic; (b) Simcenter AMESIM cycle block diagram

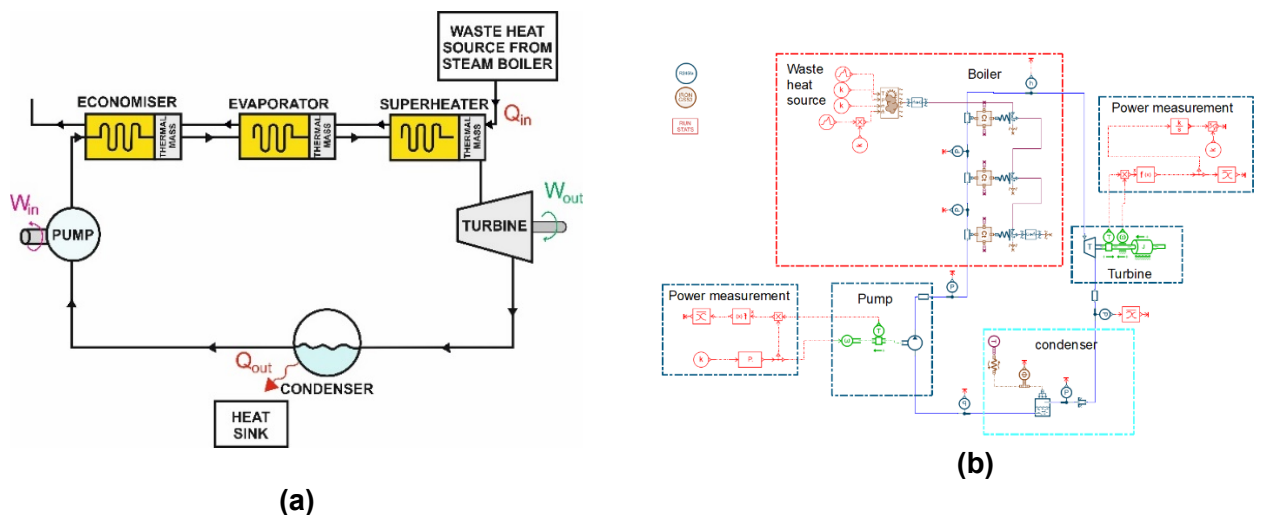
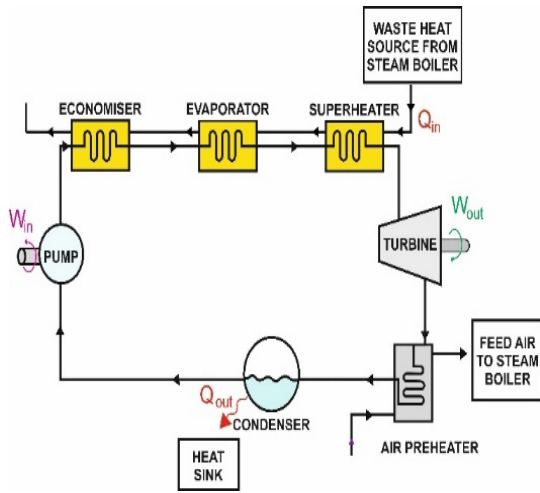
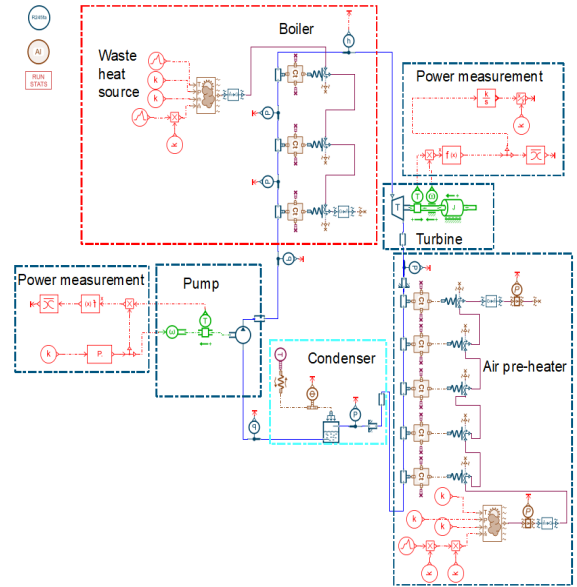


Figure 5-6: Superheated ORC with thermal storage: (a) Schematic; (b) Modelled using Simcenter AMESIM

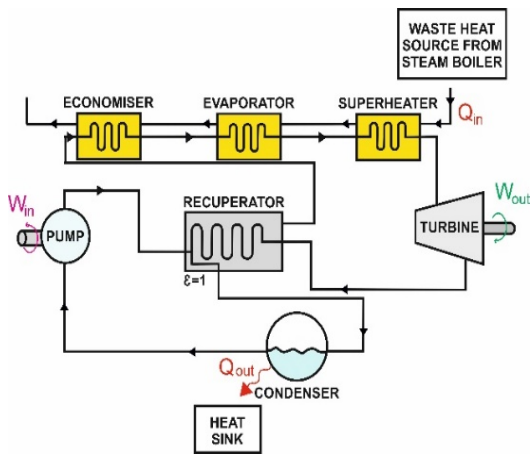


(a)

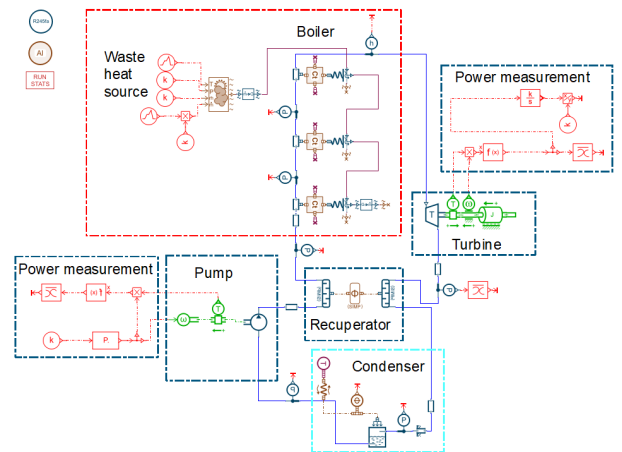


(b)

Figure 5-7: Superheated ORC with air preheating: (a) Schematic; (b) Modelled using Simcenter AMESIM

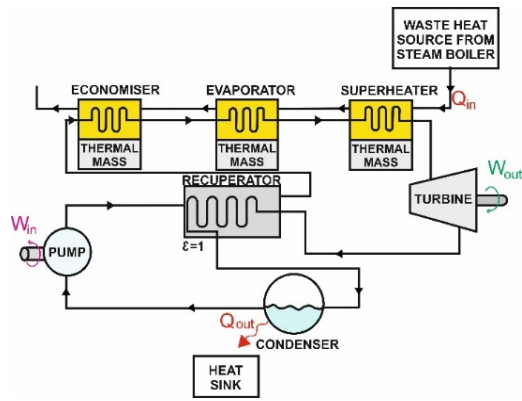


(a)

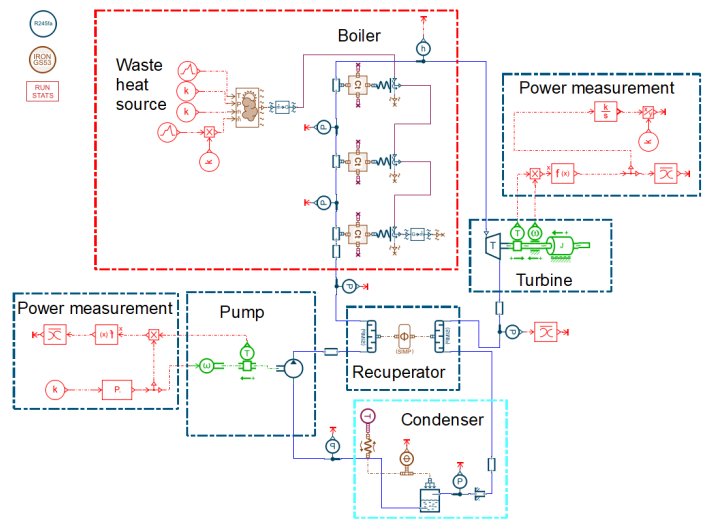


(b)

Figure 5-8: Superheated ORC with recuperation: (a) Schematic; (b) Modelled using Simcenter AMESIM

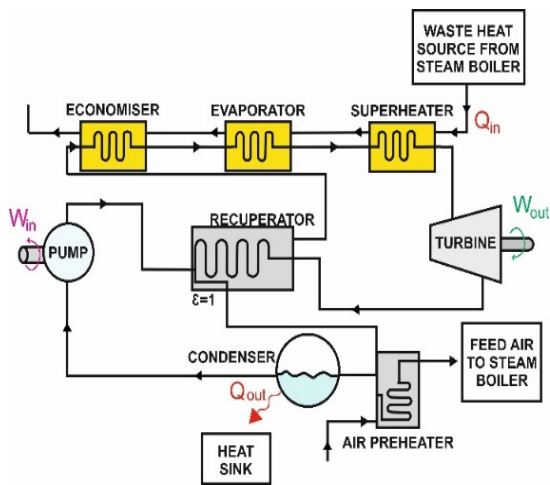


(a)

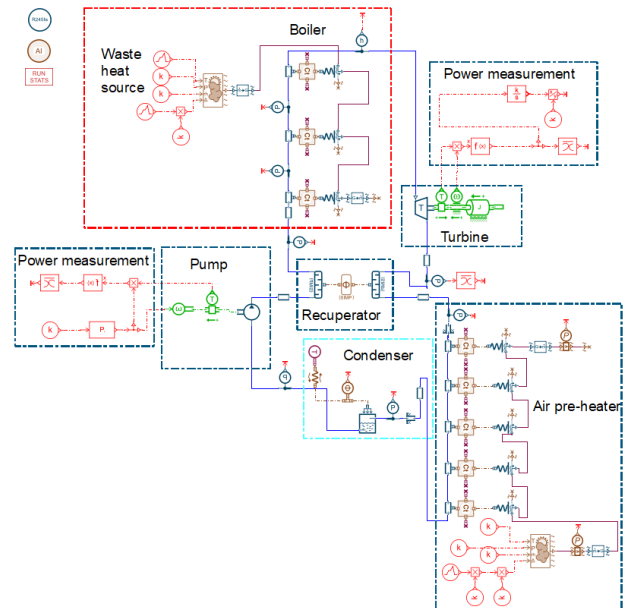


(b)

Figure 5-9: Superheated ORC with thermal storage and recuperation: (a) Schematic; (b) Modelled using Simcenter AMESIM



(a)



(b)

Figure 5-10: Superheated ORC with air pre-heating and recuperation: (a) Schematic; (b) Modelled using Simcenter AMESIM

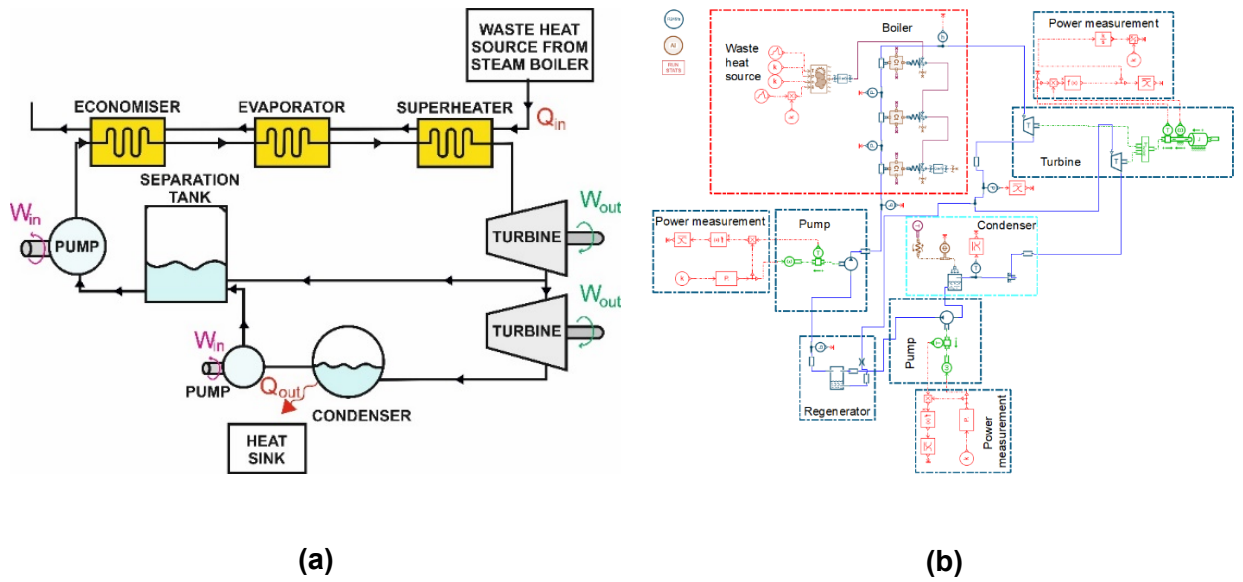


Figure 5-11: Superheated ORC with regeneration (a) schematic (b) modelled using Simcenter AMESIM

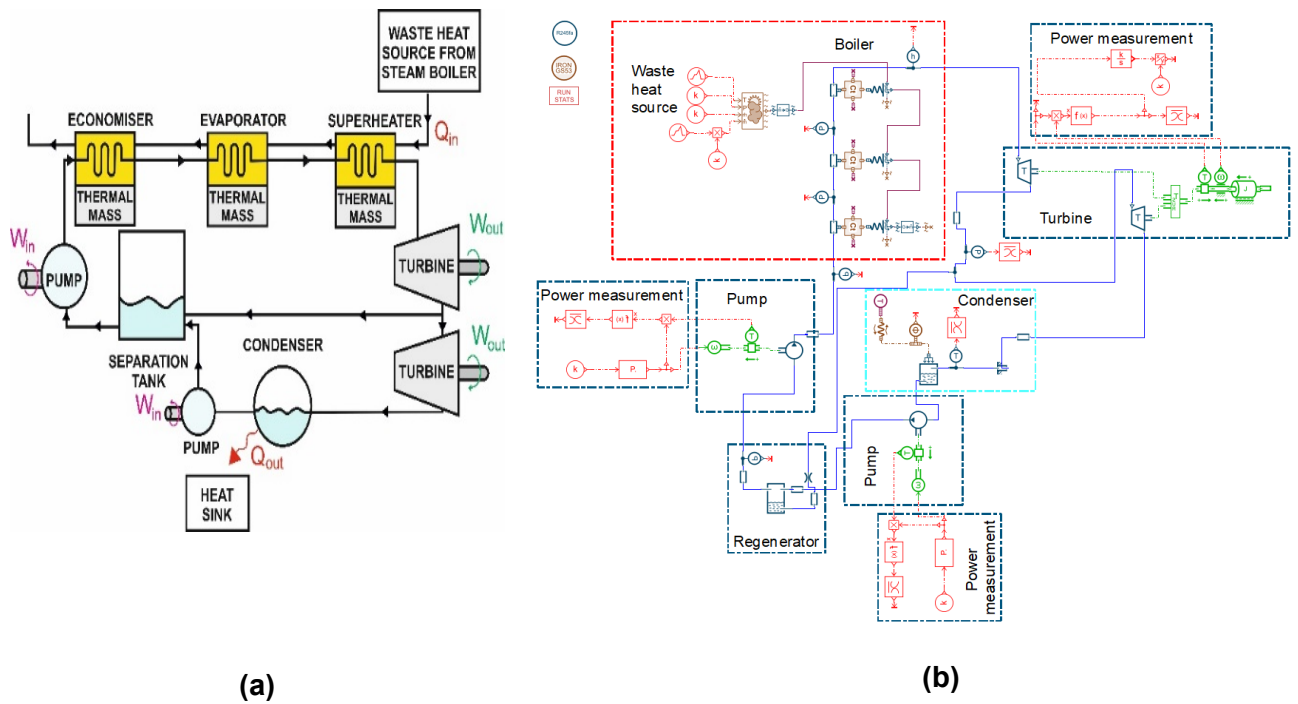
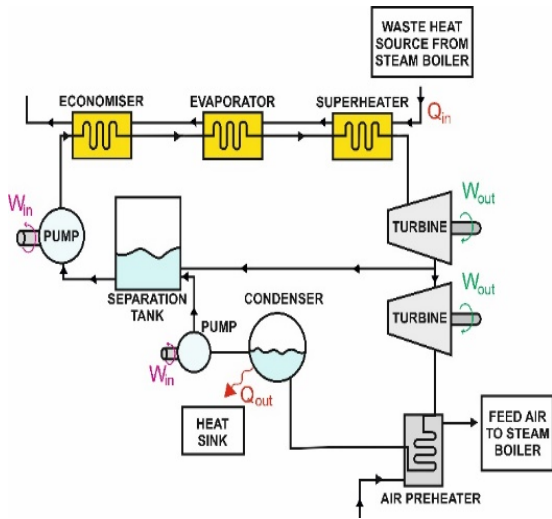
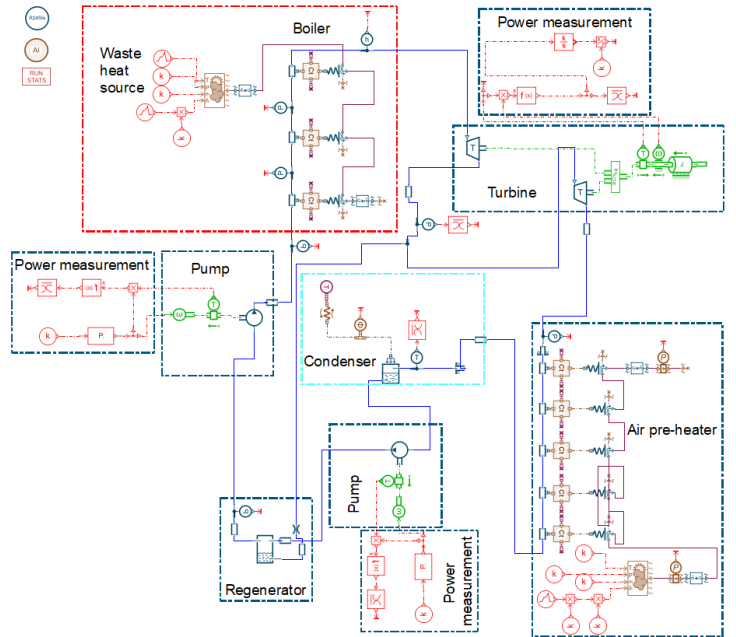


Figure 5-12: Superheated ORC with thermal storage and regeneration: (a) Schematic; (b) Modelled using Simcenter AMESIM

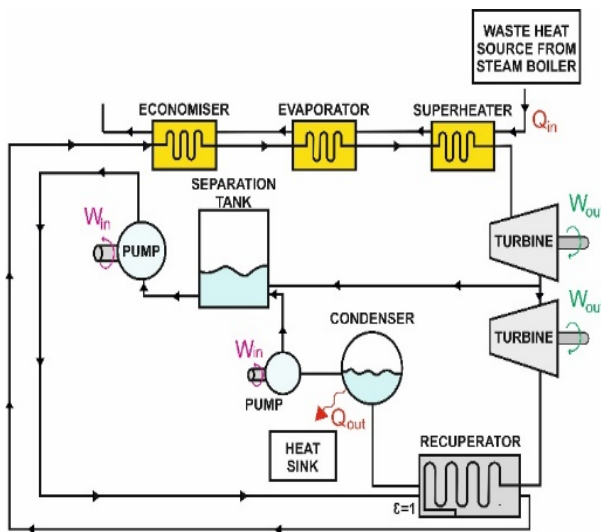


(a)

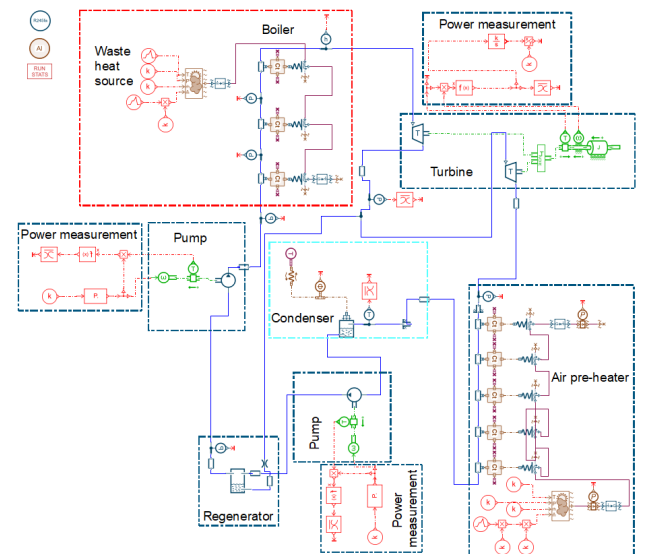


(b)

Figure 5-13: Superheated ORC with air preheating and regeneration: (a) Schematic (b) Modelled using Simcenter AMESIM



(a)



(b)

Figure 5-14: Superheated ORC with recuperation and regeneration: (a) Schematic (b) Modelled using Simcenter AMESIM

## 5.2.2 Thermodynamics

Whereas the Peng-Robinson equation was used in the previous chapter for component-level analysis, it was not suitable for a detailed cycle-level study as it did not consider the effects of viscosity variation [77]. The Helmholtz rule of internal energy was better suited to consider the change of working fluid's thermodynamic energy across multiple phases [329], defined as the sum of the internal energy as well as flow energy. Equation 5.1 stated the loss of Helmholtz free energy was equal to the maximum amount of theoretical work that the system could perform in an isochoric thermodynamic process [329].

$$F = U - T S \quad 5.1$$

Where,  $F$  is the Helmholtz free energy,  $U$  is the internal energy of the system,  $T$  is the absolute temperature of the environment and  $S$  is the entropy of the system.

The industrial steam boiler used coal as the fuel for its combustion. The mass balance equation for the boiler's air circuit, stated in equation 5.2, was used to determine the heat input in the ORC.

$$m_{flue\ gas} + m_{ash} = m_{stoichiometric\ air} + m_{excess\ air} + m_{fuel} \quad 5.2$$

Where,  $m_{flue\ gas}$  is the total flue gas discharged,  $m_{ash}$  is the quantity of ash produced,  $m_{stoichiometric\ air}$  is the ideal quantity of air required for stoichiometric combustion,  $m_{excess\ air}$  is the additional air considered for superior combustion and  $m_{fuel}$  is the quantity of coal.

The heat loss fraction due to dry flue gases were modelled to calculate the fuel savings achieved by the APH, as shown in equation 5.3.

$$LF_{flue\ gas} = m_{flue\ gas} \times C_{p\ flue\ gas} \times \frac{(T_{flue\ gas} - T_{feed\ air})}{GCV_{coal}} \quad 5.3$$

Where,  $LF_{flue\ gas}$  is the dry flue gas loss fraction,  $C_{p\ flue\ gas}$  is the specific heat of the flue gas,  $T_{flue\ gas}$  is the exhaust temperature of the flue gases,  $T_{feed\ air}$  is temperature of the air provided to boiler after the APH and  $GCV_{coal}$  is the gross calorific value of the coal.

Utilising the first law of thermodynamics, the thermal-energy balance for the ORC is determined using equation 5.4.

$$Q = \sum (m_{flue\ gas} \times h_{Flue\ in}) - \sum (m_{flue\ gas} \times h_{Flue\ out}) \quad 5.4$$

Where,  $Q$  is the total heat energy provided to the ORC system,  $h_{Flue_{in}}$  is the specific enthalpy of the flue gas before the ORC heat exchangers and  $h_{Flue_{out}}$  is the specific enthalpy of the flue gas after the ORC heat exchangers.

Based on the instantaneous power generation, the mean power,  $Mean\ Power_{Turb}$  is calculated by integrating the work done by the turbine  $W_{Turb}$  for the entire duration of the operation, shown in equation 5.5.

$$Mean\ Power_{Turb} = \frac{\int_{t=0}^{t=max} W_{Turb}}{t} \quad 5.5$$

The turbine efficiency  $\eta_{Turb}$  was determined using the Craig and Cox and Moustapha loss models as a function of the mass flow rate ( $\dot{m}$ ), turbine speed ( $N$ ), pressure ratio ( $P_R$ ), turbine inlet temperature ( $T_1$ ), nozzle primary loss ( $G_{PN}$ ), blade primary loss ( $G_{BN}$ ), nozzle secondary loss ( $G_{SN}$ ) and blade secondary loss ( $G_{SB}$ ), using equation 5.6.

$$\eta_{Turb} = f(\dot{m}, N, P_{TurbIn}, P_R, T_1, G_{PN}, G_{PB}, G_{SN}, G_{SB}) \quad 5.6$$

Quoilin et al. [85] previously reported pump power consumption lower than 10% of power generation for low temperature ORCs. Due to the insignificance of this value, the pump power requirement was ignored, and the cycle efficiency ( $\eta_{cycle}$ ) was determined using equation 5.7.

$$\eta_{cycle} = \frac{W_{Turb}}{\sum(m_{flue} \times h_{Flue_{in}})} \quad 5.7$$

The heat transfer area of the heat exchangers ( $A_{HX}$ ) for a given quantity of heat ( $Q_{transfer}$ ) was determined using equation 5.8.

$$A_{HX} = \frac{Q_{transfer}}{U_0 F \Delta T_{lm}} \quad 5.8$$

Where,  $\Delta T_{lm}$  is the logarithmic mean temperature difference across the heat exchanger,  $F$  is the logarithmic mean temperature difference (LMTD) correction factor, provided by Fettaka et al. [330].  $U_0$  was the convective heat transfer coefficient, determined by considering the convective heat transfer resistances across both the fluids, as in equation 5.9.

$$\frac{1}{U_0} = \frac{1}{htr_{flue}} + \frac{1}{htr_{ORC}} \quad 5.9$$

Where,  $htr_{flue}$  is the heat transfer resistance of flue gas and  $htr_{ORC}$  is the heat transfer resistance of the ORC fluid.

The log mean temperature difference for the economiser ( $\Delta T_{econo}$ ), evaporator ( $\Delta T_{evap}$ ), superheater ( $\Delta T_{superheater}$ ), recuperator ( $\Delta T_{recuperator}$ ) and APH ( $\Delta T_{APH}$ ) were determined using equations 5.10–5.12.

$$\Delta T_{econo}, \Delta T_{evap}, \Delta T_{superheater} = \frac{((T_{FlueIn} - T_{ORCOut}) - (T_{FlueOut} - T_{ORCIn}))}{\ln\left(\frac{T_{FlueIn} - T_{ORCOut}}{T_{FlueOut} - T_{ORCIn}}\right)} \quad 5.10$$

$$\Delta T_{recuperator} = \frac{((T_{TurbExh} - T_{EconoIn}) - (T_{CondIn} - T_{PumpOut}))}{\ln\left(\frac{T_{TurbExh} - T_{EconoIn}}{T_{CondIn} - T_{PumpOut}}\right)} \quad 5.11$$

$$\Delta T_{APH} = \frac{((T_{ORCAPHIn} - T_{AirFeedOut}) - (T_{ORCAPHOut} - T_{AirFeedIn}))}{\ln\left(\frac{T_{ORCAPHIn} - T_{AirFeedOut}}{T_{ORCAPHOut} - T_{AirFeedIn}}\right)} \quad 5.12$$

Where,  $T_{FlueIn}$  is the temperature of the flue gas entering the heat exchanger,  $T_{FlueOut}$  is the temperature of the flue gas leaving the heat exchanger,  $T_{ORCIn}$  is the temperature of the working fluid entering the heat exchanger,  $T_{ORCOut}$  is the temperature of the working fluid leaving the heat exchanger,  $T_{TurbExh}$  is the temperature of the working fluid from the turbine to the recuperator,  $T_{CondIn}$  is the temperature of the working fluid from the recuperator to the condenser,  $T_{PumpOut}$  is the temperature of the working fluid from the pump to recuperator,  $T_{EconoIn}$  is the temperature of the working fluid from the recuperator to the economiser,  $T_{AirFeedIn}$  is the temperature of the feed air at ambient temperature,  $T_{AirFeedOut}$  is the temperature of the feed air after APH recovery,  $T_{ORCAPHIn}$  is the temperature of the working fluid from the turbine to APH and  $T_{ORCAPHOut}$  is the temperature of the working fluid from the APH to the condenser.

The effectiveness ( $\varepsilon$ ) and energy balance for the recuperator were determined using equations 5.13 and 5.14, where,  $h_{econoIn}$  is the specific enthalpy of the working fluid from the recuperator to the economiser,  $h_{pumpOut}$  is the specific enthalpy of the working fluid from the pump to the recuperator,  $h_{TurbExh}$  is the specific enthalpy of the working fluid from the turbine to the recuperator and  $h_{condIn}$  is the specific enthalpy of the working fluid from the recuperator to the condenser.

$$\varepsilon = \frac{h_{econoIn} - h_{PumpOut}}{h_{TurbExh} - h_{condIn}} \quad 5.13$$

$$m(h_{econoIn} - h_{PumpOut}) = m(h_{TurbExh} - h_{condIn}) \quad 5.14$$

The mass and energy balance equation for the regenerator followed was stated in equations 5.15 and 5.16, respectively, where,  $MFR_{bleed}$  is the fraction of mass used for regeneration,  $m_{bleed}$  is the mass of bleed fluid,  $h_{bleed}$  is the specific enthalpy of bleed fluid,  $m_{CEPD}$  is the mass of condensate extraction pump fluid discharge,  $h_{CEPD}$  is the specific enthalpy of condensate extraction pump fluid discharge,  $h_{LPTOut}$  is the specific enthalpy of the low pressure turbine discharge,  $m_{RGOt}$  is the mass of the regenerator discharge and  $h_{RGOt}$  is the specific enthalpy of the regenerator discharge.

$$MFR_{bleed} = \frac{h_{RGOt} - h_{CEPD}}{h_{LPTOut} - h_{bleed}} \quad 5.15$$

$$m_{bleed}h_{bleed} + m_{CEPD}h_{CEPD} = m_{RGOt}h_{RGOt} \quad 5.16$$

The mass flow rate across the regenerator orifice was calculated by equation 5.17, where  $k$  is the pressure drop coefficient,  $\Psi$  is the discharge coefficient and  $k_{dp}$  is the pressure drop, calculated from the Reynolds number.

$$\dot{m}_{orifice} = \frac{1}{\sqrt{k}} \times area_{orifice} \times \Psi \times \sqrt{\frac{2 \times Pr_{upstream} \times Pr_{downstream}}{k_{dp}}} \quad 5.17$$

Equation 5.18 determines the heat rejection from the condenser, Where,  $Q_{cond}$  is the heat rejected by the condenser,  $h_{CondIn}$  is the enthalpy of the working fluid entering the condenser,  $h_{CondOut}$  is the enthalpy of the working fluid leaving the condenser,  $U_0$  is the heat transfer coefficient for the condenser tubes,  $area_{condenser}$  is the total heat transfer area for the condenser,  $T_{sink}$  is the heat sink temperature and  $T_{fluid}$  is the temperature of the working fluid entering the condenser.

$$Q_{cond} = m(h_{CondIn} - h_{CondOut}) = U_0 \times area_{condenser} \times (T_{sink} - T_{fluid}) \quad 5.18$$

### 5.2.3 NLPQL optimisation

The NLPQL Algorithm search matrix is defined in equation 5.19. [267]

$$\begin{aligned} \text{Objective function} &= \min f(x) \\ g_j &= 0, \quad j = 1, \dots, m_e \\ x \in R^n : g_j(x) &\geq 0, j = m_e + 1, \dots, m \\ x_{min} &\leq x \leq x_{max} \end{aligned} \tag{5.19}$$

Where,  $x$  is the non-dimensional parameter vector to be optimised and  $f(x)$  is the objective function to be minimised. The constraints of the input parameters were provided by  $g_j(x)$ , and  $x_{min}$  and  $x_{max}$  are the input constraints applied for the individual components.

Equation 5.20 is the optimisation's objective function, constrained by waste heat source, turbine's isentropic efficiency, heat transfer coefficients, working fluid thermophysical properties, pump displacement, boiler heat exchange area, turbine displacement, condenser heat exchange area.

$$\text{Objective : Max (Mean Power)} \tag{5.20}$$

Where, mean power is a function of cycle configuration, fluid enthalpy, fluid superheat, degree of recuperation, degree of regeneration, thermal mass and APH heat transfer.

### 5.2.4 Materials and components

#### 5.2.4.1 Working fluid

The suitability of working fluids was investigated in the second and fourth chapters. Accordingly, R245fa was selected, owing to its high exergetic efficiency, low vapour expansion ratio and work output for heat source temperature greater than 160°C, which was mainly due to the optimal evaporator pressure achieved for the range of temperatures considered [38, 53, 158]. Additionally, the low value of vapour expansion ratio led to minimal number of stages (i.e., single stage) to avoid supersonic flow-induced turbine flow path losses. Besides, it was widely studied and has proven popular for commercial ORC plants [58, 68, 129, 137, 215, 233, 331-334]. Thermodynamically, the fluid was suitable for ORC cycles exploiting low- to medium-grade heat [58] [129, 132, 215, 296]. R245fa exhibits a dry working fluid slope, which eliminates the chances of moisture build-up at the turbine exhaust. This provided an increase in superheat across the turbine, even in the case where the turbine received a saturated working fluid at its inlet, which improved the reliability of a turbine operating with a fluctuating waste heat source. As this study involved superheating the working fluid, it was confirmed that the autoignition temperature of 412°C [130] and thermal stability limit of 250°C were above the expected

Y. C. Engineer, PhD Thesis, Aston University, 2022

working fluid temperature [60]. An above atmospheric condensing pressure for this fluid at typical ambient temperatures eliminated the requirement of a vacuum system and ejector assembly, greatly simplifying the pressure vessel, as well as turbomachinery shaft sealing. The critical pressure of 36.4 kg/cm<sup>2</sup> ensured the operation was limited to the subcritical regime [42]. The relatively high density and low saturation pressure of the fluid align with the actual operating conditions Ecologically, R 245fa is non-toxic, and has zero ozone-depleting and acceptable global-warming indices of 0 and 930, respectively, in alignment with the Montreal Protocol of 1987 [40, 162].

#### 5.2.4.2 Feed tank

In the analysed ORC, the feed tank was placed between the condenser and feed pump at a height of 10 m, to maintain a net pressure suction head (NPSH) by gravity feed at the pump inlet. This reduces the possibility of cavitation [139], while avoiding the requirement of an additional condensate extraction pump. Non-condensable gases accumulated near the condenser, reducing its ability to absorb heat [309]. The feed tank was maintained in the liquid phase at the atmospheric pressure, which allowed for isolation from the rest of the system and the venting of non-condensable gases of R245fa [86].

#### 5.2.4.3 Feed pump

The chosen centrifugal feed pump had a nominal speed of 1500 rpm and a displacement of 0.004 m<sup>3</sup>. Figure 5-15 shows the variation in pump displacement and the corresponding change in power consumption and mean boiler inlet pressure. It was observed that peak boiler pressure was maintained with displacement between 80 and 120 cm<sup>3</sup>, where 80 cm<sup>3</sup> was selected, due to its corresponding lower power consumption. Beyond a displacement of 120 cm<sup>3</sup>, the additional working fluid pumped could not be evaporated by the ORC boiler, which, in turn, resulted in a drop in the working pressure of the system, also noted in Figure 5-15. Based on this, 120 cm<sup>3</sup> was restricted as the maximum value for the operating conditions.

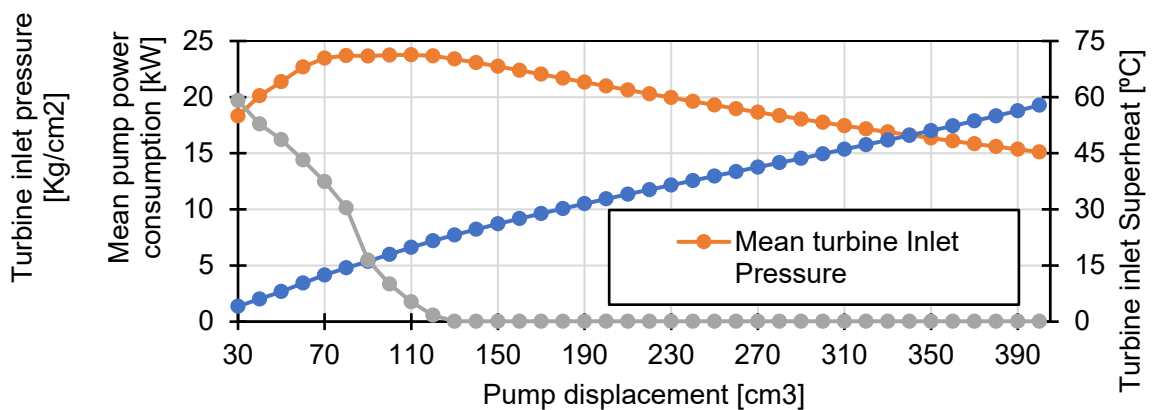


Figure 5-15: Variations in pump outlet pressure with increasing displacement

#### 5.2.4.4 Boiler

ORCs permitted the use of once-through evaporators, without any requirement of steam drums, moisture separators and fluid recirculation. This was possible as ORC fluids with a high molecular mass had limited variations in a specific volume of the working fluid in the liquid and vapour phases [86]. Aluminium was chosen as the heat exchanger material due to its favourable heat transfer properties in both steady and dynamic operations. Conduction and convection heat transfer from the steam boiler flue gas to the ORC fluid was considered. Hollow channels with flue gas on the outside and working fluid on the inside were considered for the counterflow heat exchanger, as shown in Figure 5-16. The use of an intermediary fluid such as thermal oil was not considered to minimise the 2<sup>nd</sup> law deficiencies due to an additional set of pinch points, which are increasingly relevant for a low-medium grade heat source.

To optimise the pinch point, the counterflow heat exchanger was divided into three sections—an economiser, an evaporator and a superheater, as shown in Figure 5-16. Un-finned tubes were employed to avoid the fins coagulating ash particles and degrading the heat transfer area effectiveness [310]. The heat exchangers were modelled using the logarithmic mean temperature difference (LMTD) method for counterflow heat exchangers [175]. The sizing of the heat transfer area was deduced by noting the benefit gained, observed by the parametric study, shown in Figure 5-17.

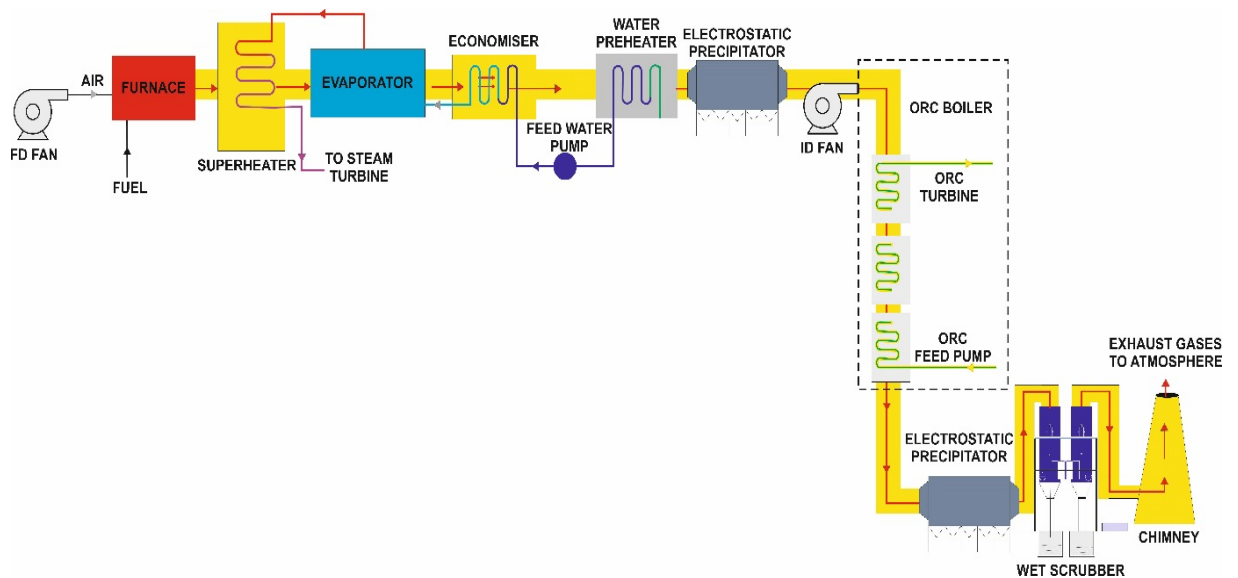


Figure 5-16: Proposed integration of an ORC boiler with an existing boiler flue gas circuit

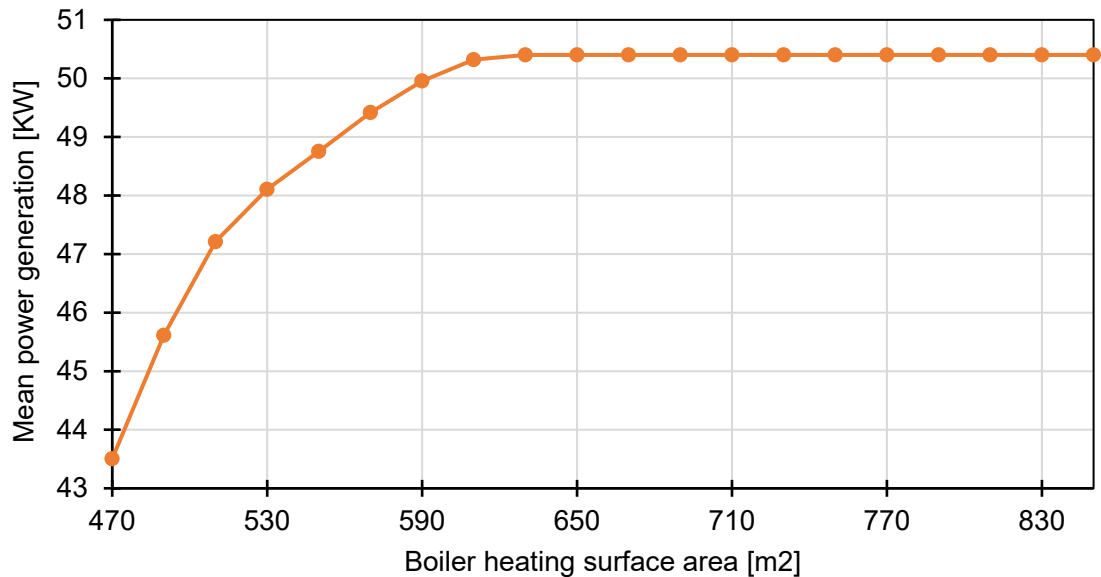


Figure 5-17: Variations in power output with increasing ORC boiler heating surface area

The total heating surface area considered was 550 m<sup>2</sup>, divided as 100 m<sup>2</sup>, 300 m<sup>2</sup> and 150 m<sup>2</sup> for the economiser, evaporator and superheater, respectively. Given the transient operation of the cycle, employing a relatively larger evaporator ensured vaporisation did not occur in the economiser and the superheater received the working fluid in a dry condition. It was critical to avoid pressure variations in the flue gas path of the steam boiler, to avoid changes to its induced and forced draft fan system, subsequently leading to an increase in capital expenditure and power consumption. Accordingly, the Reynolds number of the flue gas flow was maintained below 3000, operating within the Laminar region.

It was important to size the waste heat exchangers to maintain the flue gas exhaust temperature above the acid dew point. Reducing the temperature of flue gas to condensation levels led to the saturation of the flue gas with sulphur trioxide (SO<sub>3</sub>) and carbon dioxide (CO<sub>2</sub>) produced by the combustion of coal, resulting in sulphuric and carbonic acid formation with a pH between 3.5 and 5.0, which, in turn, led to the corrosion of and damage to the aluminium heat exchangers and the low carbon steel flue gas ducts and stack employed in the integrated ORC-steam system [88]. The acid dew point temperature depended on the saturation temperature of the vapour, which varied depending on the composition of the flue gas. Therefore, typical recuperated steam boilers operate with flue gas temperatures between 180°C and 200°C [68, 280, 311, 312]. Considering the acid dew point, it was decided to maintain the minimum flue gas temperature at 90°C higher than the mean local ambient temperature [311]. Given the global average annual temperature 13.9°C, flue gas temperatures between 104°C and 118°C were maintained.

For the ORC boiler, the heat exchangers were designed with a hydraulic diameter of 20 mm along with an overall cross-sectional area of 5024 mm<sup>2</sup>, to maintain the Reynolds number above 14000. This ensured the working fluid operated within the turbulent flow regime of advanced convective heat transfer performance between the tube wall and working fluid [313]. The results obtained an overall heat transfer coefficients  $U_0$  of 28–37.5 W/m<sup>2</sup>/°C for the heat exchangers, in line with previous studies [21].

The variations observed were a function of the heat source temperatures, flue gas mass flow rates and working fluid enthalpy. The Mac Adams correlation was used to model the pressure drop of the working fluid across the boiler, as it was widely validated to determine the pressure drop in case of the two-phase boiling flow [339, 340]. For the evaporation phase, Verein Deutscher Ingenieure (VDI) atlas for horizontal tubes correlation was used as it had been validated for modelling two-phase modern refrigerant flows [341, 342]. For temperature rise across a single phase, the Nusselt number correlation provided by the Gnielinski modification to the original Petukhov–Popov equation for single phase heat transfer across turbulent flow in tubes was used, due to its wide acceptance of Reynolds number values above 4000, as stated in equation 5.21 [343-345], where  $f_{Dff}$  is the Darcy friction factor, described by Petukhov and shown in equation 5.22 [346].

$$Nu = \frac{\left(\frac{f_{Dff}}{8}\right) \times (Re - 1000) \times Pr}{1.00 + 12.7 \sqrt{\left(\frac{f_{Dff}}{8}\right) \times [(Pr)^{\frac{2}{3}} - 1]}} \quad 5.21$$

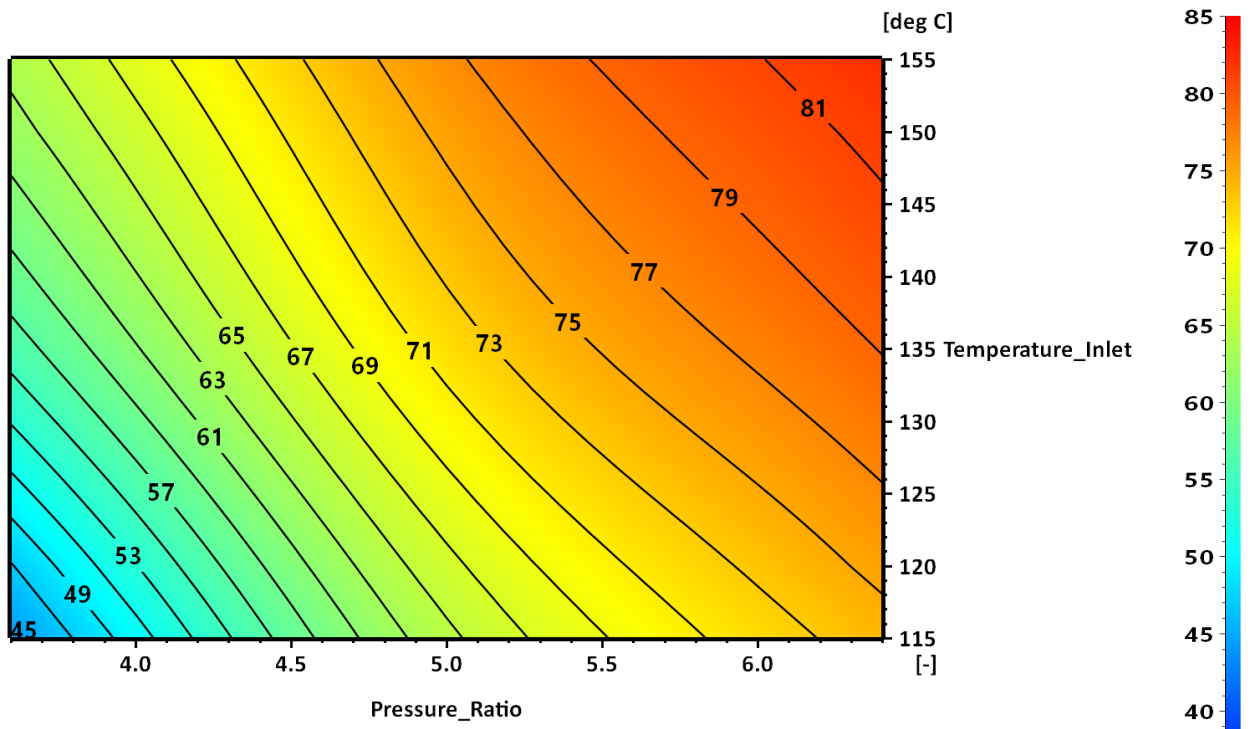
$$f_{Dff} = (0.79 \times \ln(Re_D) - 1.64)^{-2} \quad 5.22$$

#### 5.2.4.5 Turbine

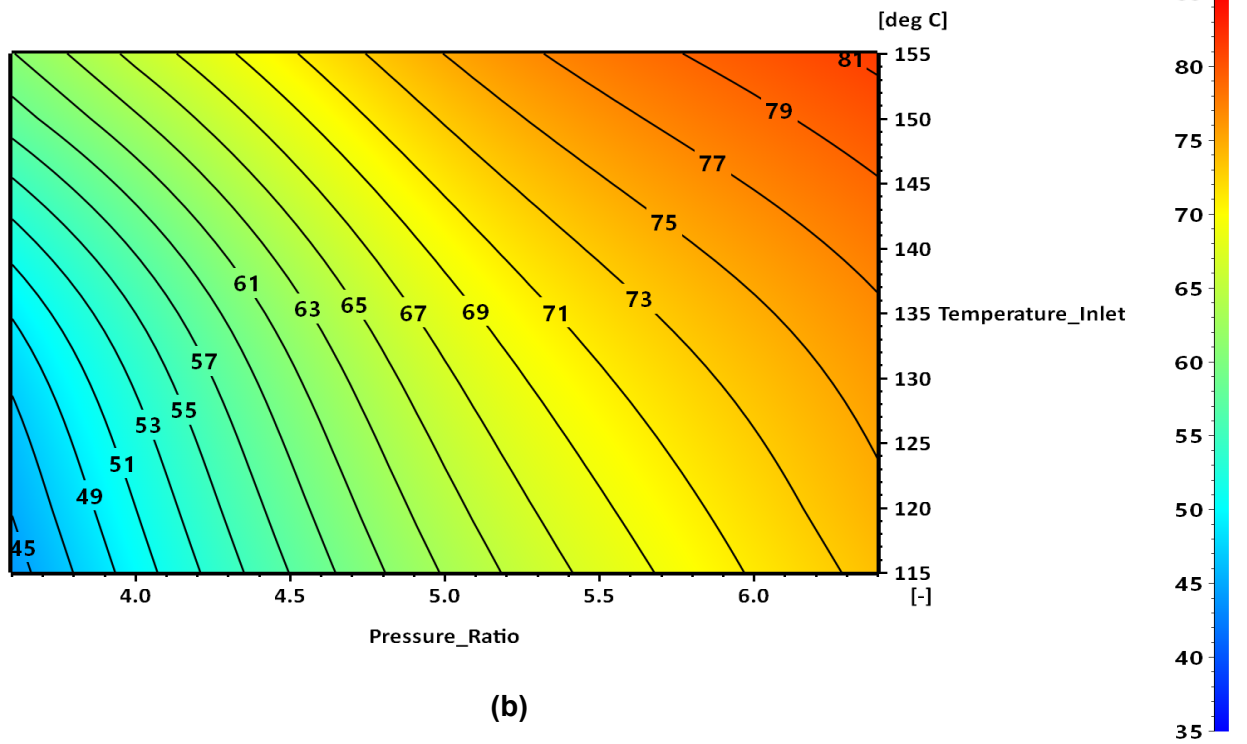
The Craig and Cox loss model [192] was incorporated for modelling design point turbine efficiency using turbine speed, pressure ratio, inlet pressure and inlet temperature. Off-design point losses were calculated using Moustapha et al.'s incidence loss prediction method [215]. Based on these models, efficiency contours for multiple values of turbine inlet temperature were developed and interpolated. Cubic interpolation between data points was used to develop the contours. Extrapolation was not considered to restrict the study to experimental proven data, as shown in Figure 5-18. The contours emphasised the increased turbine efficiency observed for higher pressure ratios and higher inlet temperature (superheat), in line with the findings of the previous chapter. To maintain these parameters, it was essential to minimise pinch point losses and investigate novel cycle configurations such

as those including a thermal storage medium, which could be used to maintain turbine isentropic efficiency during periods with lower heat source temperature. Noting the enthalpy drop across the turbine was below 40 kJ/kg at steady state conditions, an operational speed of 5000 rpm and mean diameter of 0.55 m was considered along with a single row or stationary and moving blades were considered, as per a Rateau wheel configuration, which maintained  $\frac{U}{c_2}$  ratios within the optimum band of 0.4 to 0.5[314]. Considering the compounding employed by regeneration cycles, reducing the operating speed to 3000 RPM was considered to maintain efficient  $\frac{U}{c_2}$  ratios.

A parametric study conducted to decide the turbine displacement noted the highest power output with a turbine displacement of 0.00013 m<sup>3</sup> per cycle, corresponding to an inlet volumetric flow rate 0.0108 m<sup>3</sup>/sec and mass flow rate of 1.32 kg/sec. This has been depicted in Figure 5-19.



(a)



(b)

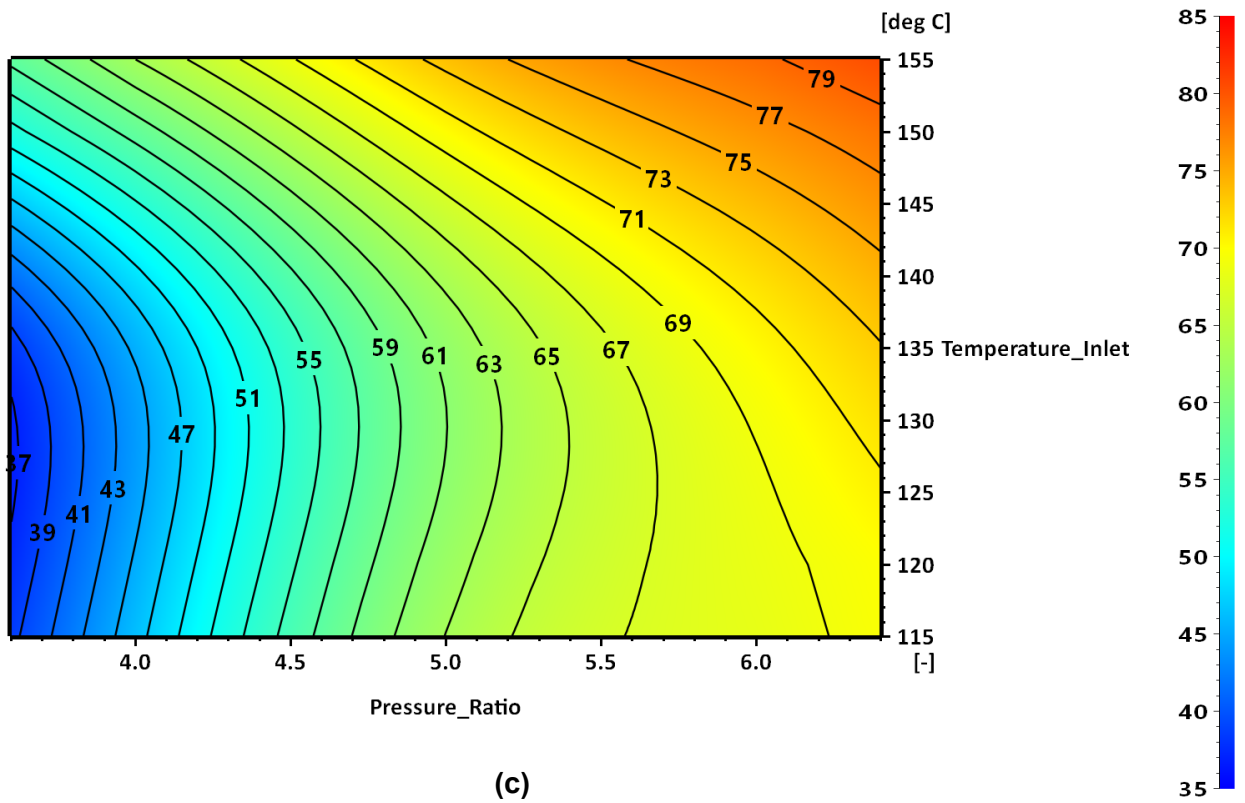


Figure 5-18: Turbine efficiency contours for pressure ratio and turbine inlet temperature plotted for turbine inlet pressure of (a) 16 Bar, (b) 20 Bar and (c) 24 Bar

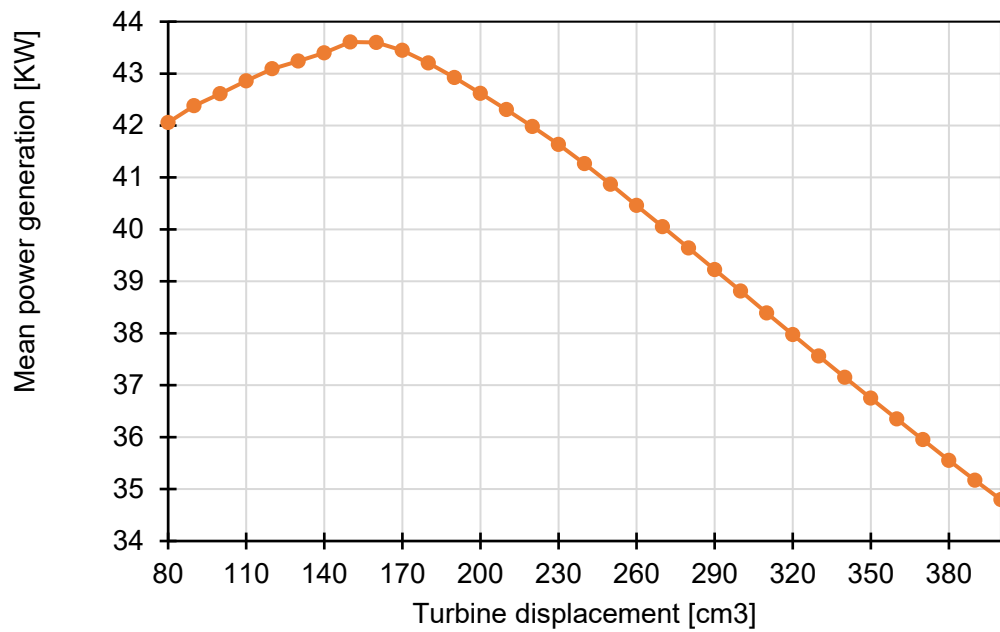


Figure 5-19: Variations in turbine power output with increasing turbine displacement

#### 5.2.4.6 Condenser

A heat sink temperature of 30°C and minimum pinch point between the heat sink and the ORC working fluid of 5°C were considered. Condenser pressure between 2.86 and 3.02 kg/cm<sup>2</sup> was maintained to avoid air ingress into the condenser and pump suction seals, in line with previous commercial efforts [86]. Aluminium was chosen as the heat transfer tube material [315]. Similar to other components, a proportional study for the condenser heat exchanger sizing was conducted. The size of the condenser was increased to 180 m<sup>2</sup>, beyond which the benefit in power output were not proportional to the increase in the heat exchange area, as shown in Figure 5-20. The heat rejection undertaken by the condenser was a significant contributor to a conventional Rankine cycle's electrical power requirement, due to cooling water circulation pumps, condensate extraction pumps and cooling tower draft fans [316]. Ecologically, condenser heat rejection resulted in a significant water evaporation loss [317]. In addition, reduced condenser heat load would lead to smaller equipment sizing, hence lower capital expenditure.

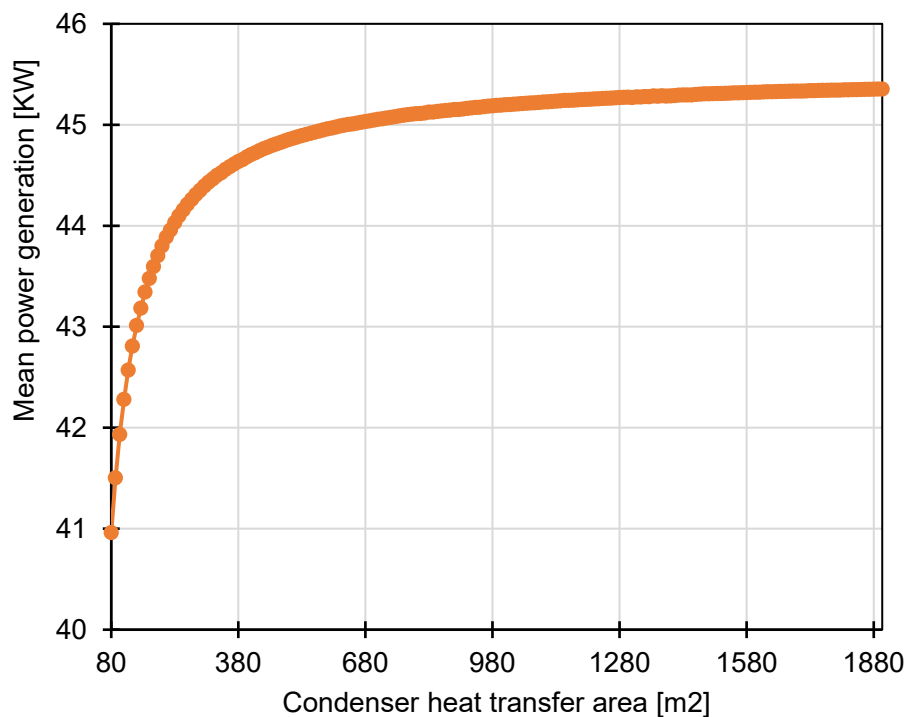


Figure 5-20: Variations in power output with condenser heat transfer area

#### 5.2.4.7 Recuperator

The recuperator operated as a pre-cooler for worked fluid before the condenser, which simultaneously pre-heats the working fluid before the economiser. The LMTD approach was used to model the counterflow heat exchanger. Based on a proportional study, as shown in Figure 5-21, increased power output was observed in a heat transfer area of up to 785 m<sup>2</sup>.

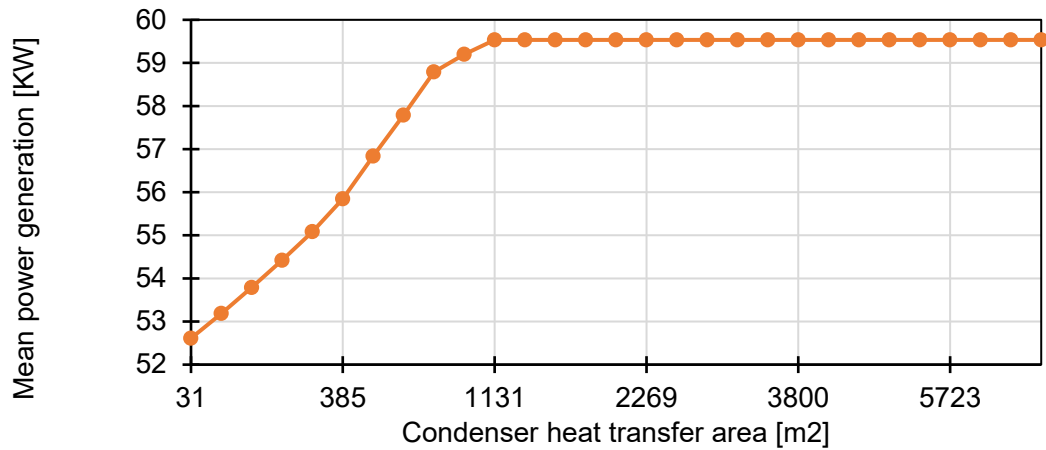


Figure 5-21: Variations in power output with recuperator heat transfer area

#### 5.2.4.8 Thermal mass

Cast iron (sensible heat storage) or customised phase change material (latent heat storage) were initially considered as a 10000 kg thermal mass heat storage medium. Whereas the use of cast iron for thermal energy storage has previously been validated for gas turbine plants, phase change materials have garnered significant interest in recent years due to their superior temperature control and higher thermal efficiency [318]. Considering the transient heat source temperature would vary across the year, sensible heat storage material will provide more flexibility in harnessing high-grade heat from the system. Phase change materials are better suited to heat sources with lower variations in heat storage, as they cannot store thermal energy after the mass is converted to liquid state [319]. The initial temperature for the thermal masses to maintain the total heat input to the system were 88.70°C, 122.86°C and 138.18°C for the economiser, evaporator and superheater, respectively.

#### 5.2.4.9 Regenerator

The degree of regeneration ranged between 22.0% and 26.9%, beyond which evaporation of the working fluid in the separation tank could occur. This limitation was overcome by using a fixed size orifice with a cross-sectional area of 100mm<sup>2</sup>, along with a hydraulic diameter of 8 mm, placed across the intermediate pressure line. This led to an average mass flow rate of 0.21 kg/sec across the orifice and maintained the intermediate pressure between 10.05 and 11.6 kg/cm<sup>2</sup> at the ORC feed heater.

#### 5.2.4.10 Air preheater

To achieve the minimum pinch point, the air preheater was designed as a series of five independent counterflow heat exchangers that utilised ambient air, as summarised in Figure 5-22. The air circuit was designed with a Reynolds number varying between 2100 and 3100, to minimise the flue gas pressure drop; Prandtl numbers between 0.7124 and 0.7126 were observed. The working fluid was maintained at a Reynolds number between 40000 and 90000, operating purely in the turbulent regime, which in turn enabled a heat transfer coefficient

between  $24 \text{ W/ms}^2/\text{°C}$  and  $33 \text{ W/ms}^2/\text{°C}$ . The Prandtl numbers for the flue gas observed remained constant 0.7124 and 0.7126, pointing to good heat transfer by conduction.

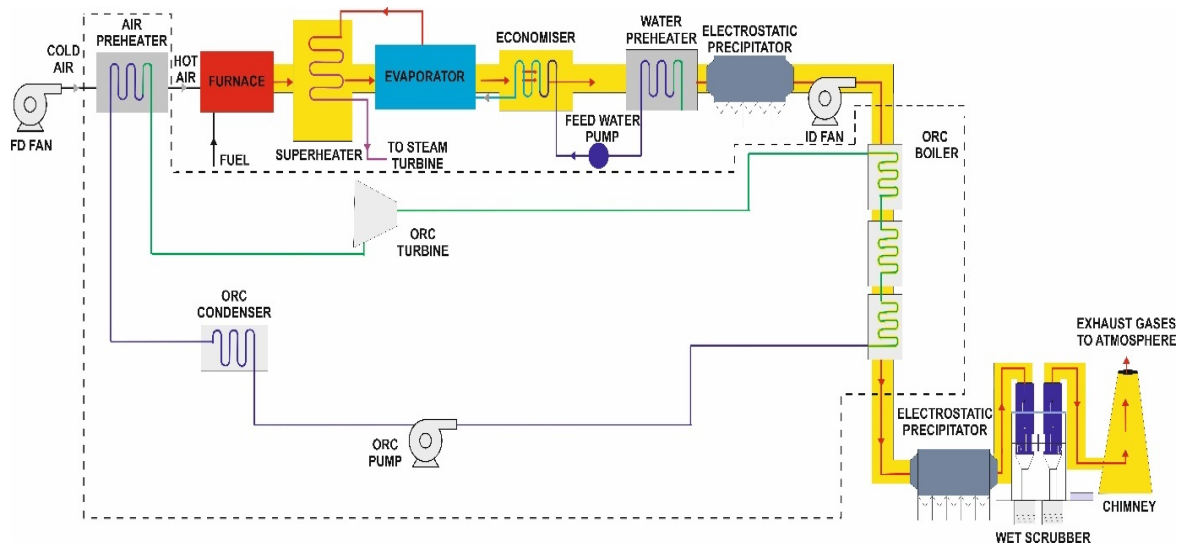


Figure 5-22 Flue gas schematic with integration of ORC and the air preheater

### 5.2.5 Optimisation

As the study was based on waste-heat capturing, maximising power output was defined as the objective function. The sizing of the pump, boiler, turbine and condenser were globally optimised by benchmarking a mathematical technique-based optimisation algorithm known as NLPQL, against the well-established genetic algorithm between the values mentioned in Table 5.2. In the case of the NLPQL Algorithm, the initialization values were decided based on a preliminary parametric study.

Table 5.2: Variation of core component sizing provided to optimiser

S. No.	Component	Parameter	Minimum Value	Initial Value	Maximum Value	Unit
1	Pump	Displacement	64	80	96	$\text{cm}^3$
2	Boiler	Heat Transfer Area	80	100	120	$\text{m}^2$
3	Turbine	Displacement	104	130	156	$\text{cm}^3$
4	Condenser	Heat Transfer Area	144	180	216	$\text{m}^2$
5	Recuperator	Heat Transfer Area	150	120	180	$\text{m}^2$

### 5.2.5.1 Non-linear programming by quadratic Lagrangian (NLPQL) parameters

NLPQL algorithm is a sequential programming method that solves problems with a continuous differentiable objective function by using quadratic approximation of the Lagrangian function and a linearisation of the constraints [255, 258]. The optimiser was designed considering the Karush Kuhn Tucker (KKT) criterion, where a first order derivative test was used to solve non-linear programming equations [352, 353]. Besides, KKT criterion allowed the use of inequality constraints [354]. In this optimisation study, the fitness function to be minimised is the inverse of the mean power output. The relative gradient steps were defined by the finite difference method, stated for two parameters as in equation 5.23, where  $\delta$  is the relative gradient step size. Initial runs were performed using  $x = x_0$  and  $y = y_0$  values to determine the algorithm's starting point  $f(x_0, y_0)$ . Incremental steps of size  $\delta$  were added to compute the combination of parameters  $f(x_0 + \delta x_0, y_0)$  and  $f(x_0, y_0 + \delta y_0)$  for each iteration. Parameters for the NLPQL optimizer are furnished in Table 5.3.

$$\overline{grad(f)}(x_0, y_0) = \begin{pmatrix} \frac{\delta f}{\delta x(x_0, y_0)} \\ \frac{\delta f}{\delta y(x_0, y_0)} \end{pmatrix} = \begin{pmatrix} \frac{f(x_0, y_0) - f(x_0 + \delta x_0, y_0)}{(\delta x_0)} \\ \frac{f(x_0, y_0) - f(x_0, y_0 + \delta y_0)}{(\delta y_0)} \end{pmatrix} \quad 5.23$$

Table 5.3: Setup parameters for the NLPQL algorithm

Parameter	Value
Relative gradient step size for finite difference	0.0001
Desired final accuracy	0.00001
Number of iterations	Not limited

### 5.2.5.2 Genetic algorithm parameters

The genetic algorithm (GA) is a well-known global optimisation approach and is used as a benchmark for NLPQL. The randomly generated initial population size was maintained as greater than 4.5 times the number of independent variables, as recommended by previous studies [243]. The reproductive ratio of 80% was within, the 50% to 85% bounds suggested by previous researchers [320]. An iterative process noted that a minimum of ten generations were required to obtain meaningful results. High values of mutation probability (15%) and mutation amplitude (0.2) allowed for greater design exploration diversity, created space for gradual

variations in each characteristic for subsequent generations and reduced chances of convergence towards the local optimum [355]. The total number of runs is defined in equation 5.24. A summary of the GA setup parameters is shown in Table 5.4.

$$\text{No. of runs} = \text{Population Size} + \frac{\text{Population Size} \times \text{Reproduction Ratio} \times (\text{No. of Generations} - 1)}{100} \quad 5.24$$

Table 5.4: Optimisation setting of GA

Parameter	Value
Population size	50
Number of generations	12
Reproduction ratio	80%
Mutation probability	15%
Mutation amplitude	0.2

### 5.3 Validation

The predicted baseline cycle performance was compared to the experimental/numerical data published by Maraver et al.'s study, which optimised subcritical and transcritical ORCs constrained by technical parameters [280]. Maraver et al. considered a conventional ORC cycle with R245fa working fluid, operating in steady state conditions, without any heat recovery. A heat source temperature slope from 170°C to 90°C was considered, as in Figure 5-23.

The gradient for the heat sink temperature rise was maintained between 10°C and 20°C, along with a condenser temperature of 35°C, shown in Figure 5-23. A minimum pinch point of 10°C was maintained at the heat exchangers (boiler and condenser). Subcooling of the condenser was maintained at 5°C. A minimum superheating of 5°C was observed, which led to working fluid temperature of 115°C at an evaporator pressure of 14.6 kg/cm<sup>2</sup>. Maraver et al. stated the cycle's Carnot efficiency at 34.5%. Variable turbine efficiency was considered using previously defined correlations for size parameter and volume ratio provided by Macchi and Perdichizzi for axial flow ORC turbines [211]. Table 5.5 shows the data yielded from the optimisation study validation.

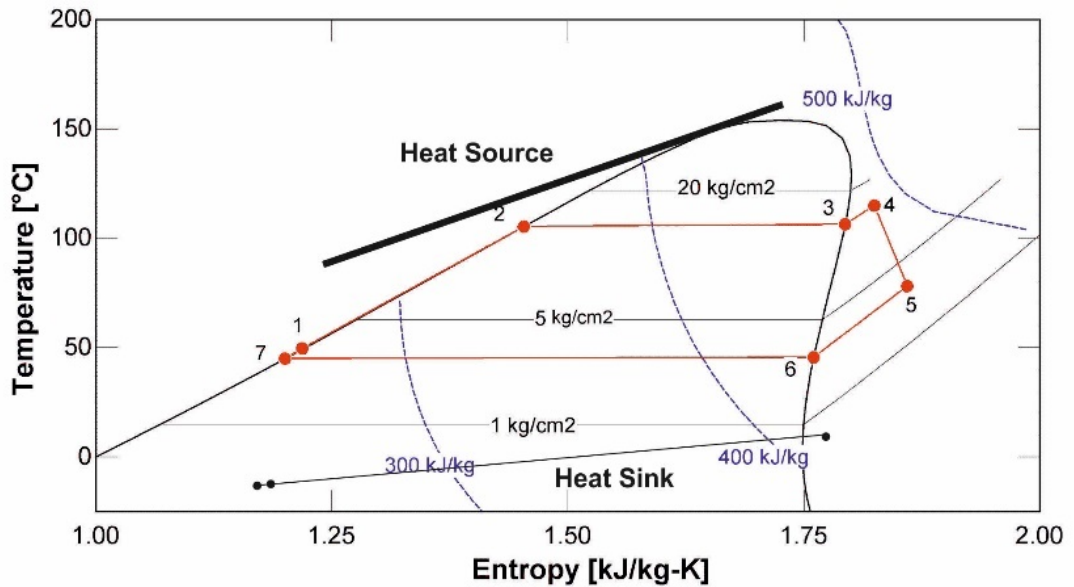


Figure 5-23: T-s diagram of the optimal ORC, validated against the study by Maraver et al. [280]

Table 5.5: Results of conventional ORC validation comparison

Parameter	Maraver et al.	Model	Deviation in %
Cycle efficiency	10.43	10.28	1.43%
Turbine exhaust temperature	73.9	73.5	0.54%
Turbine exhaust specific entropy	1830	1881	2.78%

## 5.4 Results and discussion

### 5.4.1 Parametric cycle evaluation

#### 5.4.1.1 Pump and boiler sizing

The feed pump maintained the mean working pressure of the boiler at 23 kg/cm<sup>2</sup> for the simple cycle configuration. Increasing the pressure further beyond this value increases the wetness of fluid entering the turbine during low thermal energy input, which subsequently leads to mechanical damage due to erosion, as well as working fluid leakage across the turbine's shaft seals [321]. Thermodynamically, wet fluid entering a turbine lowers the turbine isentropic efficiency [192].

Cycles that operated with a reduced working pressure exhibited an increase in the degree of superheat at the turbine inlet, which led to a subsequent increase of superheat at the turbine exhaust, hence increasing the heat load in the condenser or requiring an additional heat recovery device. As the continuous operation of the steam boiler was paramount for the textile plant, the ORC heat exchangers were sized to ensure the flue gas outlet temperatures exceeded 104°C, the acid dew point temperature, as shown in Figure 5-24.

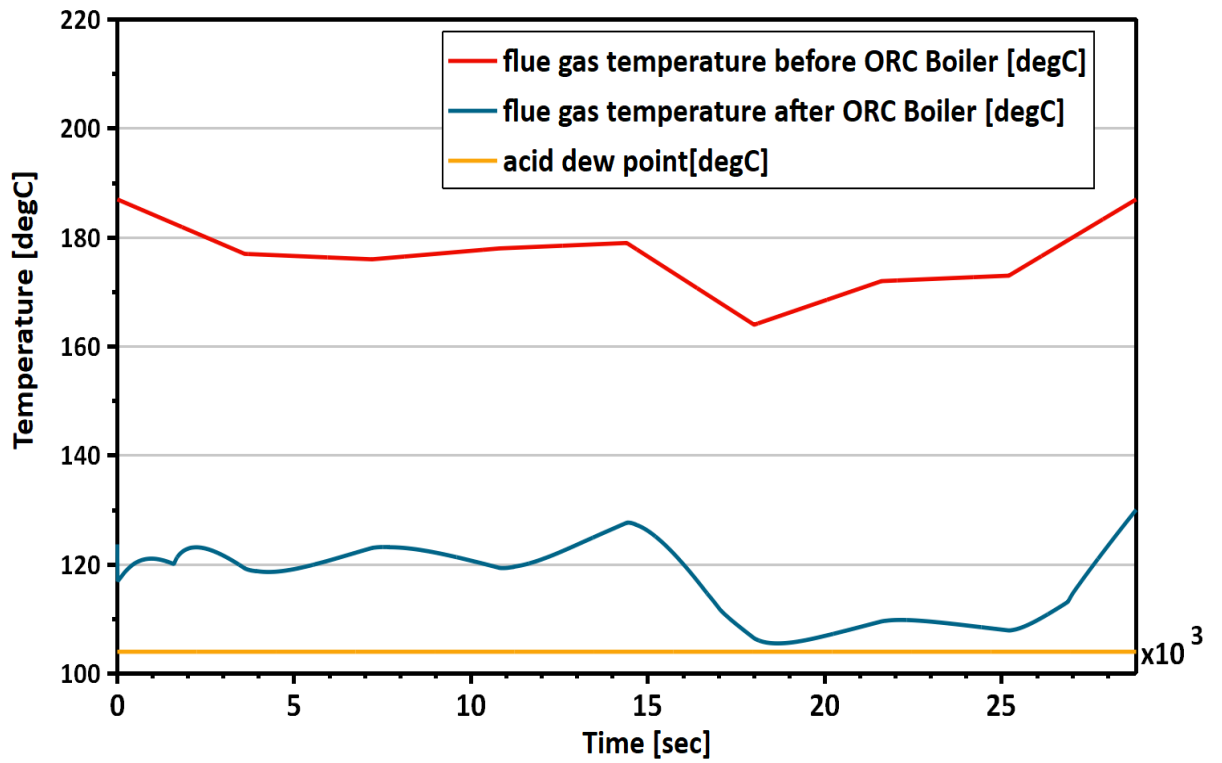
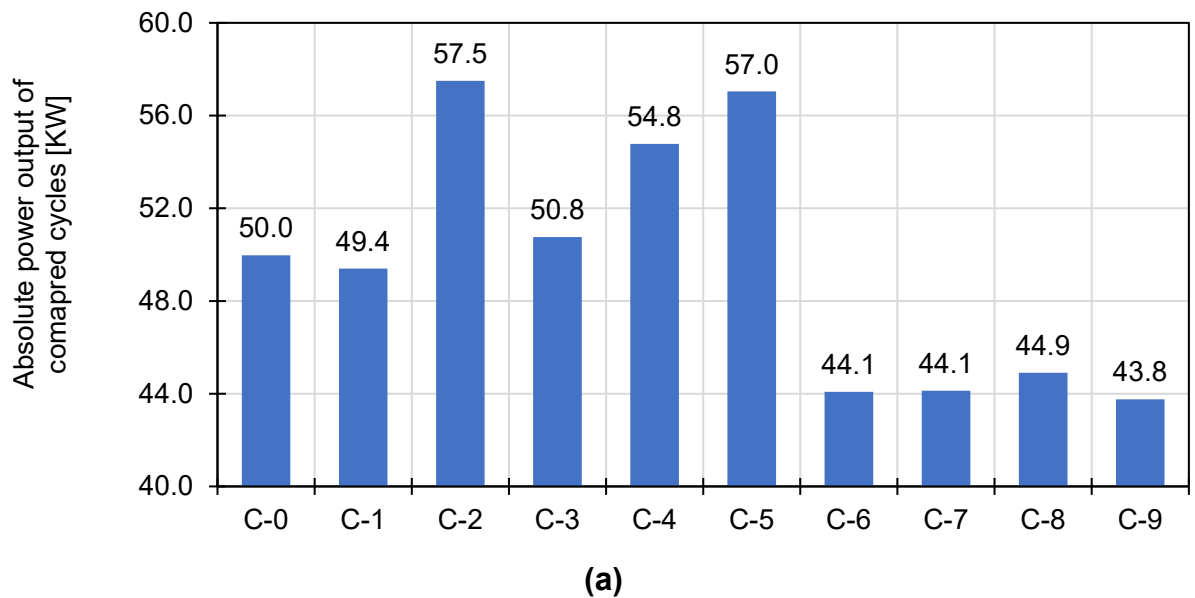
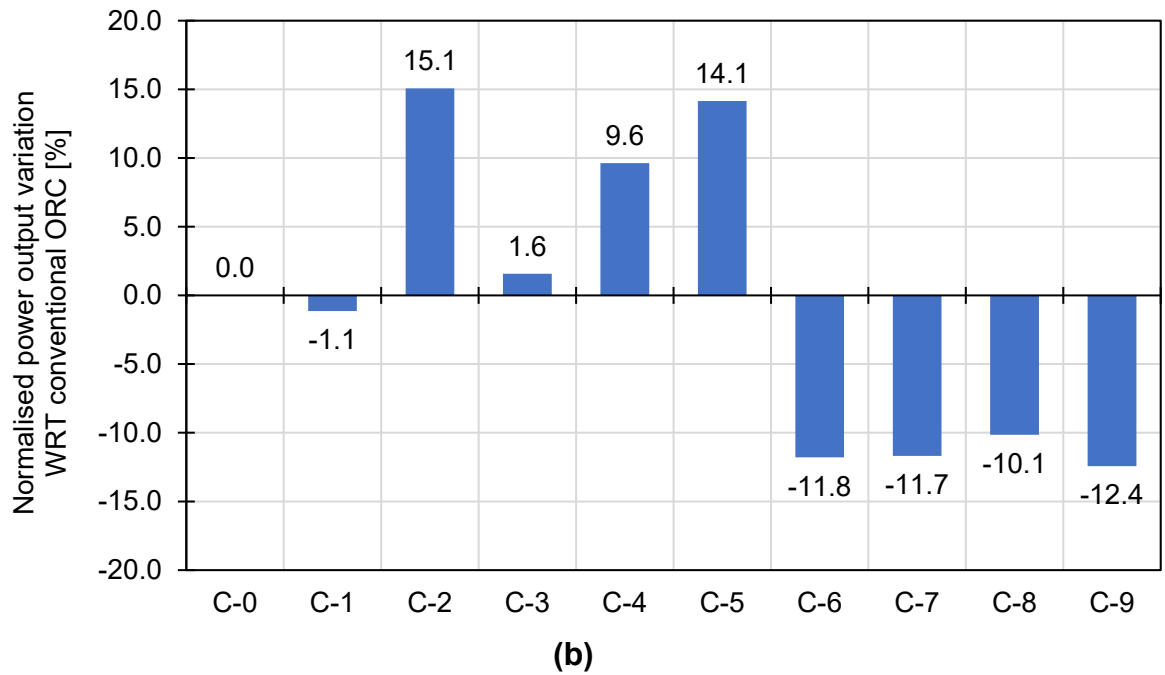


Figure 5-24: Flue gas temperatures observed before and after the use of the ORC boiler

#### 5.4.1.2 Power output



Cycle name	Configuration	Cycle name	Configuration
C-0	Conventional	C-5	Recuperative & Thermal mass
C-1	Thermal mass	C-6	Regenerative & APH
C-2	Recuperative	C-7	Regenerative
C-3	APH	C-8	Regenerative & Recuperative
C-4	Recuperative & APH	C-9	Regenerative & Thermal mass

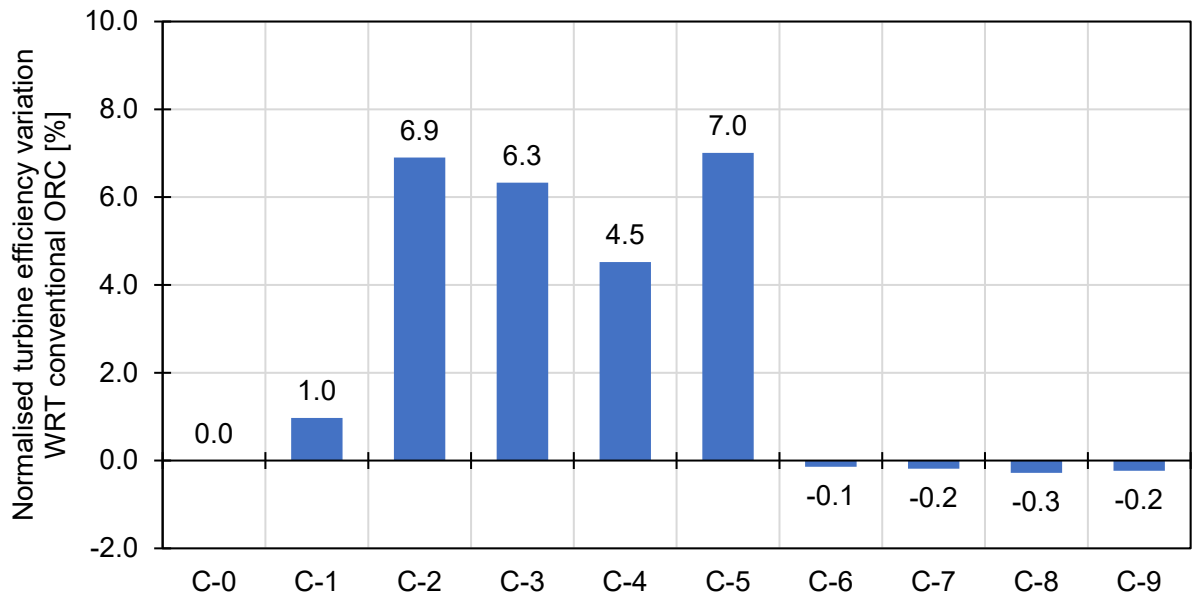


Cycle name	Configuration	Cycle name	Configuration
C-0	Conventional	C-5	Recuperative & Thermal mass
C-1	Thermal mass	C-6	Regenerative & APH
C-2	Recuperative	C-7	Regenerative
C-3	APH	C-8	Regenerative & Recuperative
C-4	Recuperative & APH	C-9	Regenerative & Thermal mass

Figure 5-25: (a) Absolute and (b) nominal power output achieved by various parametrically optimised ORCs

Figure 5-25 shows the absolute and normalised power output of the parametrically optimised cycles along with that of the basic ORC. It can be observed that the use of recuperation demonstrated promising results. It was observed that increasing the recuperation enhanced the overall cycle efficiency from 5.16% to 5.97% and power output from 49.97 kW to 57.50 kW. Although the use of the thermal mass reduced the system's nominal power output by 1.1%, combining it with a high degree of recuperation provided the second-best results of any cycle, with 14.1% enhancement of the system's nominal power output. Incorporating the regeneration showed an adverse impact on power output in agreement with Xi et al. [70]. Recuperative cycles perform indirect heat transfer, wherein the entire working fluid passed through the turbine. In contrast, regenerative cycles used direct heat transfer, wherein a part of the intermediary working fluid was used for preheating and was not available for the low-pressure turbine, thereby reducing its mass flow rate and overall power output; this conclusion was in line with previous findings by Feng et al. [322].

### 5.4.1.3 Turbine efficiency



Cycle name	Configuration	Cycle name	Configuration
C-0	Conventional	C-5	Regenerative & Thermal mass
C-1	Thermal mass	C-6	Regenerative & APH
C-2	Regenerative	C-7	Regenerative
C-3	APH	C-8	Regenerative & Regenerative
C-4	Regenerative & APH	C-9	Regenerative & Thermal mass

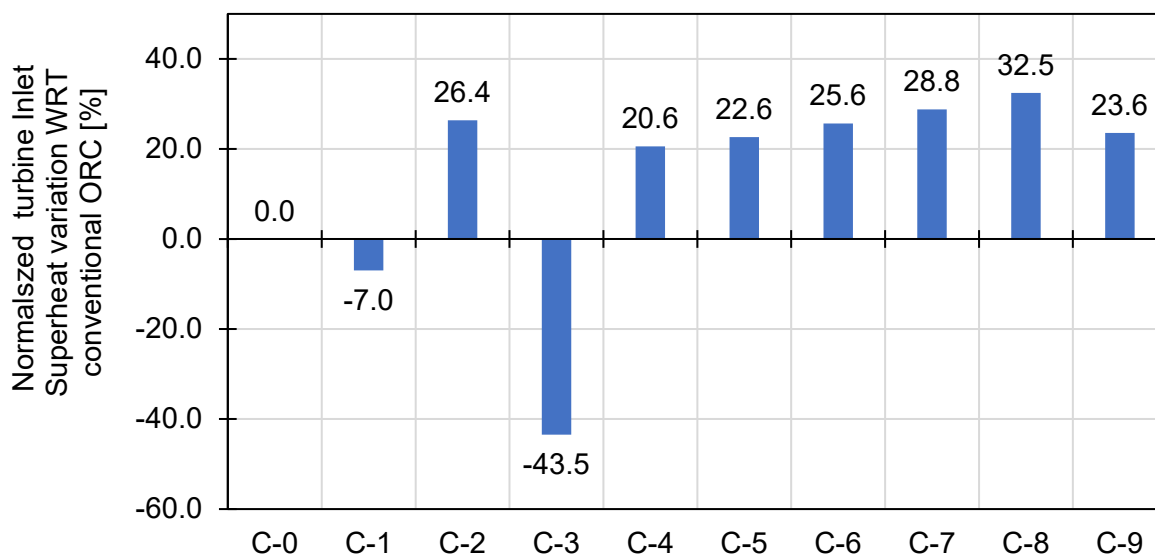
Figure 5-26: Normalised variation in turbine efficiency

Figure 5-26 shows the variation in normalized mean turbine isentropic efficiency for the parametrically optimised ORC configurations. Turbine isentropic efficiency for the conventional ORC was observed as 85.62%. Variations of up to 7% were observed across the investigated cycle configurations, which fosters the importance of considering turbine efficiency for cyclic-level analysis. Regeneration-based cycles demonstrated the lowest isentropic efficiency of 84.5%, in line with the findings by Mago et al. [225]. As the turbine for the regenerative cycle was compounded across two stages, the mean isentropic efficiency for both the turbines was considered. The low isentropic efficiency for the regenerative cycle stemmed from the low  $\frac{U}{c_2}$  ratios in the turbine stage, despite the reduced speed considered for such a configuration. Additionally, the reduced mass flow rate to the LP turbine led to an increase in the fraction of secondary losses. The use of a smaller diameter turbine could address these issues, as it leads to a lower blade pitch velocity ( $U$ ) and reduced secondary losses due to the increased blade heights. In contrast, cycles employing recuperation demonstrated the highest isentropic efficiencies, up to 91%. As observed in the turbine performance mapping (Figure 5-18), the high degree of superheat was observed as a factor contributing to this improved turbine isentropic efficiency.

#### 5.4.1.4 Degree of superheat

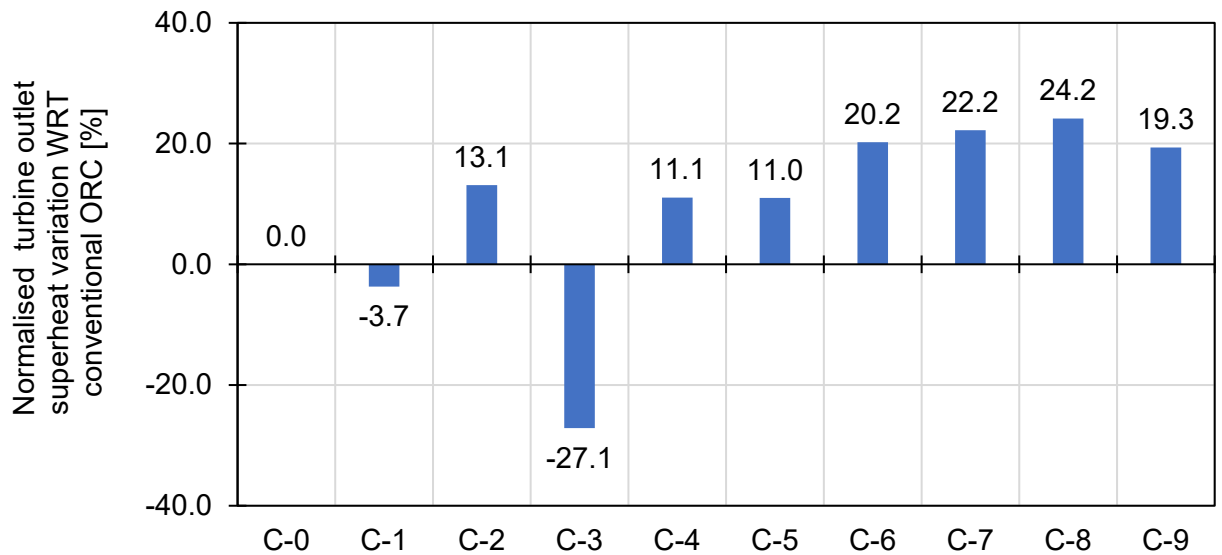
The study of the normalised superheat comparison at the turbine inlet and outlet are shown in Figure 5-27 and Figure 5-28, respectively. The absolute superheat at the turbine inlet was 23.48°C for the conventional cycle and varied between 13.27°C and 31.1°C for other configurations. The absolute superheat at the turbine outlet was 47.76°C for the conventional cycle, and varying between 34.8 and 58.4°C for other cycles. Both the recuperative and regenerative cycles demonstrated high values of inlet superheat temperature due to thermal energy recovery devices.

However, the outlet superheat was highest in the case of regenerative cycles due to the poor isentropic efficiency of the turbines in the regenerative cycle. ORC with APH demonstrated the lowest mean superheat at turbine inlet (23.48°C for the APH cycle and 13.2°C for the conventional cycle) and mean turbine inlet temperature (152.4°C for the APH cycle and 147.1°C for the conventional cycle). It is linked to the removal of heat from the working fluid by the APH for the steam boiler, validated by the increased sub-cooling of working fluid at the pump discharge, noted as 22.6°C for the conventional cycle and 36.8°C for the APH cycle.



Cycle name	Configuration	Cycle name	Configuration
C-0	Conventional	C-5	Recuperative & Thermal mass
C-1	Thermal mass	C-6	Regenerative & APH
C-2	Recuperative	C-7	Regenerative
C-3	APH	C-8	Regenerative & Recuperative
C-4	Recuperative & APH	C-9	Regenerative & Thermal mass

Figure 5-27: Normalised Variations in turbine inlet superheat for multiple cycle configurations with respect to (WRT) conventional ORC

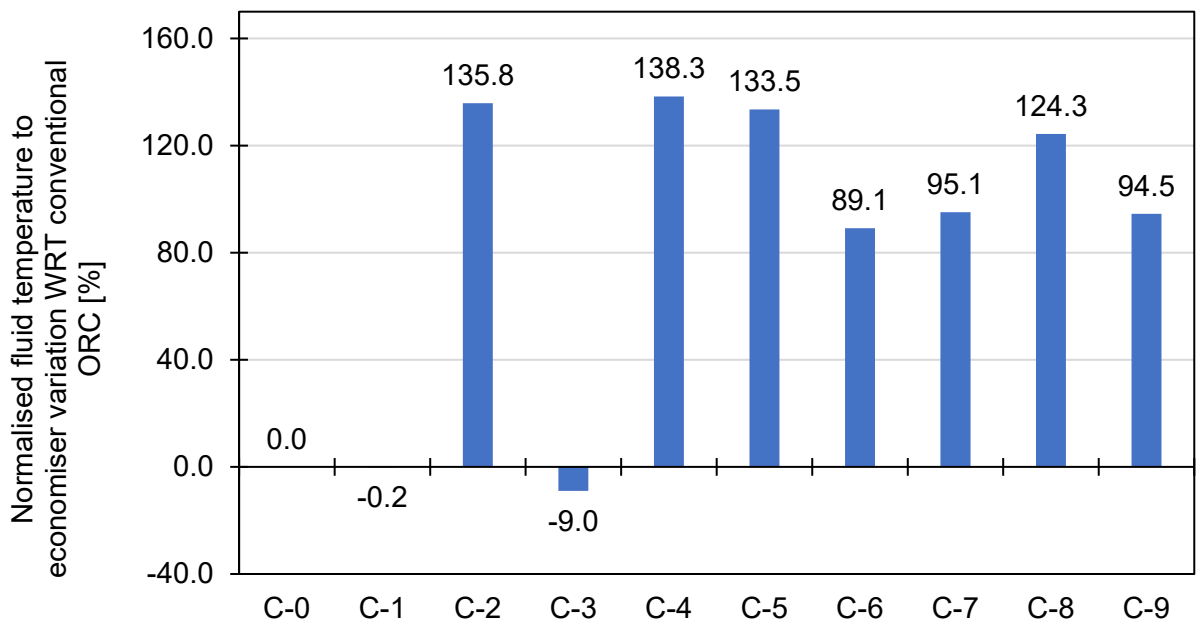


Cycle name	Configuration	Cycle name	Configuration
C-0	Conventional	C-5	Recuperative & Thermal mass
C-1	Thermal mass	C-6	Regenerative & APH
C-2	Recuperative	C-7	Regenerative
C-3	APH	C-8	Regenerative & Recuperative
C-4	Recuperative & APH	C-9	Regenerative & Thermal mass

Figure 5-28: Increases in exhaust superheat temperature noted for all cycles

#### 5.4.1.5 Feedwater temperature

Given the fixed size of the boiler's heater exchangers, the working fluid was preheated to its highest possible value. It is worth mentioning that the conventional cycle did not operate at preheating temperature but at the saturation temperature of 38.6°C. Compared to the traditional cycle, cycles incorporating recuperation and regeneration achieved a significant increase in the working fluid temperature. The improved thermal energy recovery was observed in Figure 5-29, where the inlet temperature of the working fluid to the economiser was noted. The thermal energy transferred by the APH from the ORC system to the steam boiler's air circuit was also recorded. The use of thermal mass did not contribute to fluid temperature.

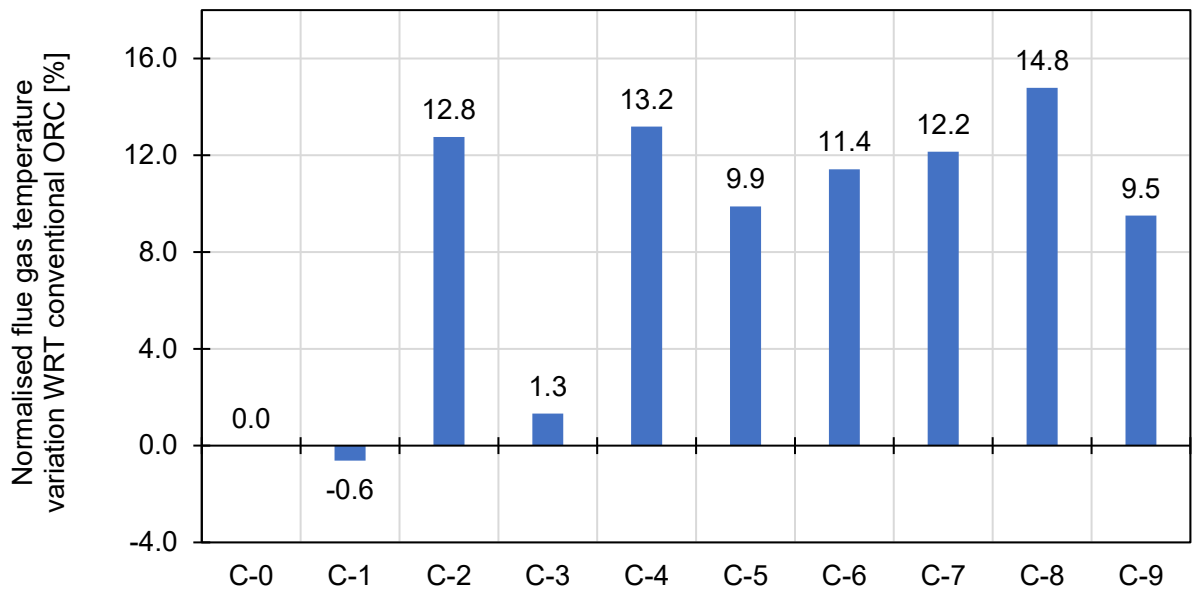


Cycle name	Configuration	Cycle name	Configuration
C-0	Conventional	C-5	Recuperative & Thermal mass
C-1	Thermal mass	C-6	Regenerative & APH
C-2	Recuperative	C-7	Regenerative
C-3	APH	C-8	Regenerative & Recuperative
C-4	Recuperative & APH	C-9	Regenerative & Thermal mass

Figure 5-29: Increases in feedwater temperature achieved when energy recovery was employed

#### 5.4.1.6 Flue gas temperature

It is important to understand the cycle performance with respect to fixed heat exchanger sizing. As the temperature of the working fluid increased, the LMTD and heat across the boiler's heat exchangers were reduced. It resulted in an increase in the flue gas temperature, and penalised cycles with superior thermal energy recovery, as shown in Figure 5-30.



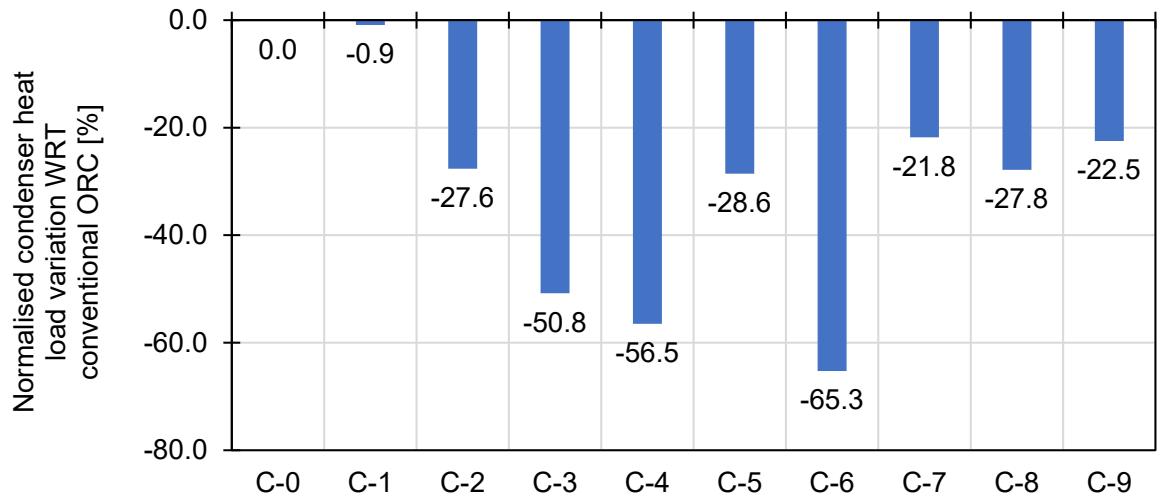
Cycle name	Configuration	Cycle name	Configuration
C-0	Conventional	C-5	Recuperative & Thermal mass
C-1	Thermal mass	C-6	Regenerative & APH
C-2	Recuperative	C-7	Regenerative
C-3	APH	C-8	Regenerative & Recuperative
C-4	Recuperative & APH	C-9	Regenerative & Thermal mass

Figure 5-30: Increases in flue gas temperature noted due to reduced ORC boiler LMTD

#### 5.4.1.7 Condenser heat load

The mean cooling load requirement for the conventional ORC cycle was 308 kWth. To fulfil such a requirement, a cooling water flow of 108 m<sup>3</sup>/hr was used. This led to a substantial evaporation loss of 6.5 m<sup>3</sup>/hr for a wet cooling tower [323]. The condenser heat load, cooling water fluid and evaporation loss mentioned were to be sized in proportion to the condenser's thermal load. As discussed earlier, increased heat rejection to the condenser can lead to an adverse operational, capital expenditure, environmental and thermodynamic impact, as studied in the following chapter.

This study considered three different approaches to reduce the condenser's heat load. The regenerative cycle reduced the total quantity of the mass flow to the condenser [70]. The second approach involved enthalpy reduction with the help of an indirect heat exchange using recuperation. The final method extracted the low-grade heat for preheating air for the steam boiler cycle.



Cycle name	Configuration	Cycle name	Configuration
C-0	Conventional	C-5	Recuperative & Thermal mass
C-1	Thermal mass	C-6	Regenerative & APH
C-2	Recuperative	C-7	Regenerative
C-3	APH	C-8	Regenerative & Recuperative
C-4	Recuperative & APH	C-9	Regenerative & Thermal mass

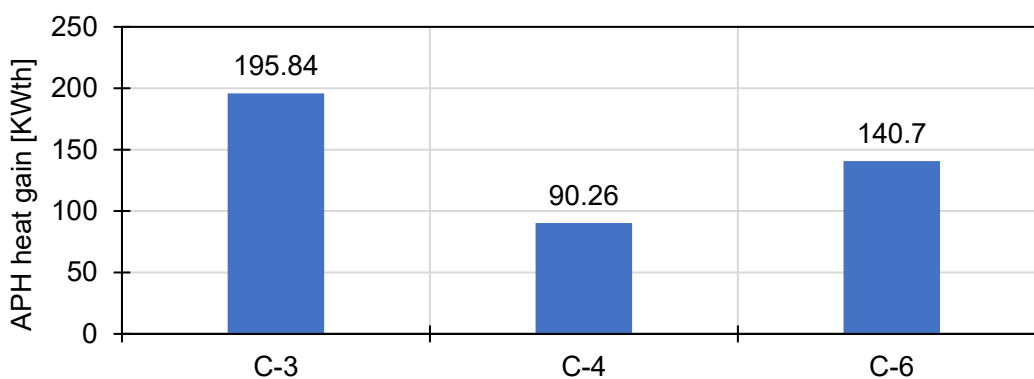
Figure 5-31: Thermal load of condenser compared for all configurations

As the mass flow rate of working fluid to be condensed by the working fluid for the regenerative cycle was approximately 20% lower compared to a conventional cycle, a similar reduction in the condenser heat load for this cycle was demonstrated, as depicted in Figure 5-31. Recuperation demonstrated a direct benefit of up to 28% reduction in condenser heat loss, which was proportional to the degree of recuperation undertaken. All three cycles incorporating air preheating for removal of waste heat from the ORC system to the external boiler cycle demonstrated the lowest condenser heat loads, achieving this by reducing the sensible heat of the working fluid. For the finite-sized condenser, this reduction in heat load allowed achieving a lower mean condenser pressure of 2.01 kg/cm<sup>2</sup>, in comparison to 2.30 kg/cm<sup>2</sup> achieved by the conventional cycle. The condenser heat load for the APH incorporated cycle was 50% of the conventional ORC cycle. The cycles employing the APH along with other variations demonstrated even better results. The regenerative APH cycle along with its reduced mass flow rate and external heat removal provided the maximum benefit of a 65% reduction in condenser heat rejection. The combination of recuperation along with air preheating resulted in a 60% lower condenser heat load.

#### 5.4.1.8 Air preheater heat gain

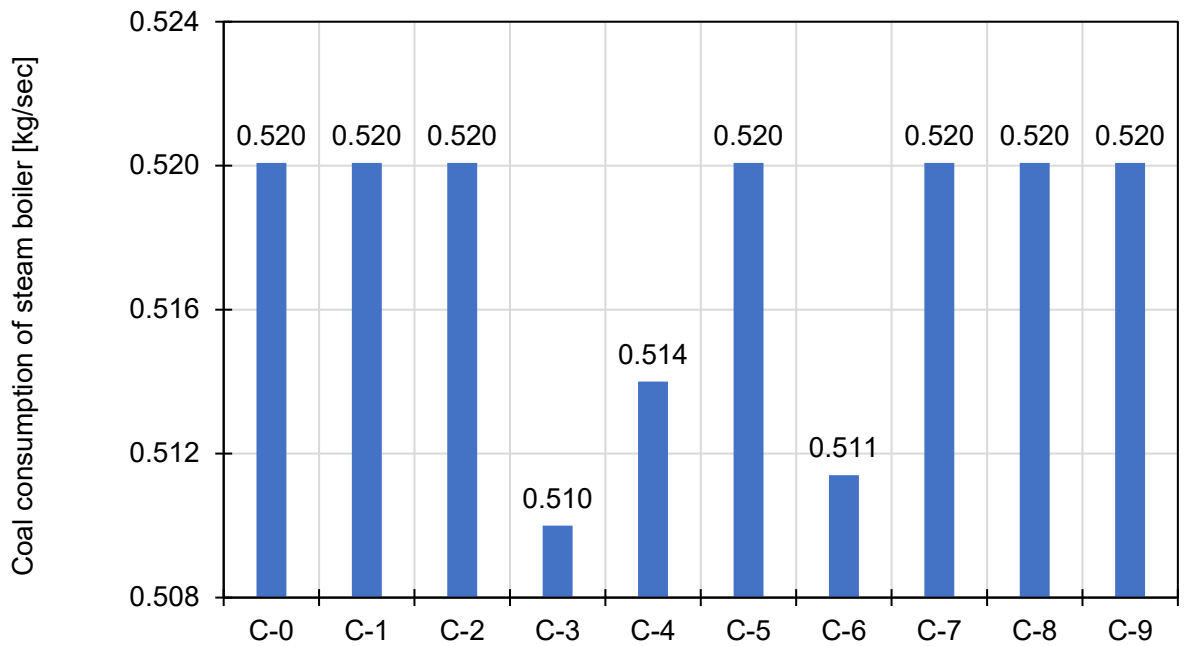
The integration of the APH provided an opportunity to utilise ORC waste heat for an existing industrial process. In addition to the lowest condenser heat loads for all cycles incorporating air preheating, the APH-based ORC cycles demonstrated a considerable reduction of steam boiler fuel consumption of 1.9%, 1.16% and 1.66% for the basic APH, recuperative APH and regenerative cycles, respectively. The results observed were in line with previous studies that observed the influence of input air temperature on steam boiler efficiency [324].

The absolute thermal energy recovered by the APH- based cycles is shown in Figure 5-32. Integrating the APH with the recuperative cycle achieved the maximum thermal energy recovery of 196 kWth. The estimated steam boiler fuel consumption for all cycles has been depicted in Figure 5-33. In addition to the fuel savings, there were proportionate financial benefits in terms of capital equipment sizing, fuel transportation, exhaust gas loss, flue gas treatment, air pollution and de-sulfurization and ash handling. Previous studies have estimated the generation of 2.62 metric tons of CO<sub>2</sub> emissions per metric ton of coal [324]. The recovery of combustion waste heat provides environmental benefits in the form of reduced CO<sub>2</sub> emissions, particulate matter emissions, ash generation and ash discharge which were not quantified by this study [324].



Cycle name	Configuration	Cycle name	Configuration	Cycle name	Configuration
C-3	Recuperative	C-4	APH	C-6	Recuperative & APH

Figure 5-32: Thermal energy gain in APH-based cycles



Cycle name	Configuration	Cycle name	Configuration
C-0	Conventional	C-5	Regenerative & Thermal mass
C-1	Thermal mass	C-6	Regenerative & APH
C-2	Regenerative	C-7	Regenerative
C-3	APH	C-8	Regenerative & Recuperative
C-4	Regenerative & APH	C-9	Regenerative & Thermal mass

Figure 5-33: Fuel consumption estimated for all cycle configurations

#### 5.4.1.9 Thermal storage

Chapter 4 elaborated the benefit of providing superheated steam to ORC turbines. The turbines perform most reliably when the working fluid does not experience a significant variation in inlet temperatures [360]. Uniform operating temperatures reduce cyclic thermal stresses and induced turbine component expansion [361, 362]. The major benefit of the thermal mass ORC was noted in terms of more stable superheat of the working fluid at the turbine inlet, compared to a conventional ORC in Figure 5-34(a). The contours of the turbine isentropic efficiency (Figure 5-34(b)) demonstrated a resemblance to the turbine inlet superheat, that is, high efficiency during periods of high inlet temperature and vice-versa. Overall, the cycle employing thermal mass demonstrated lower fluctuation of the turbine isentropic efficiency.

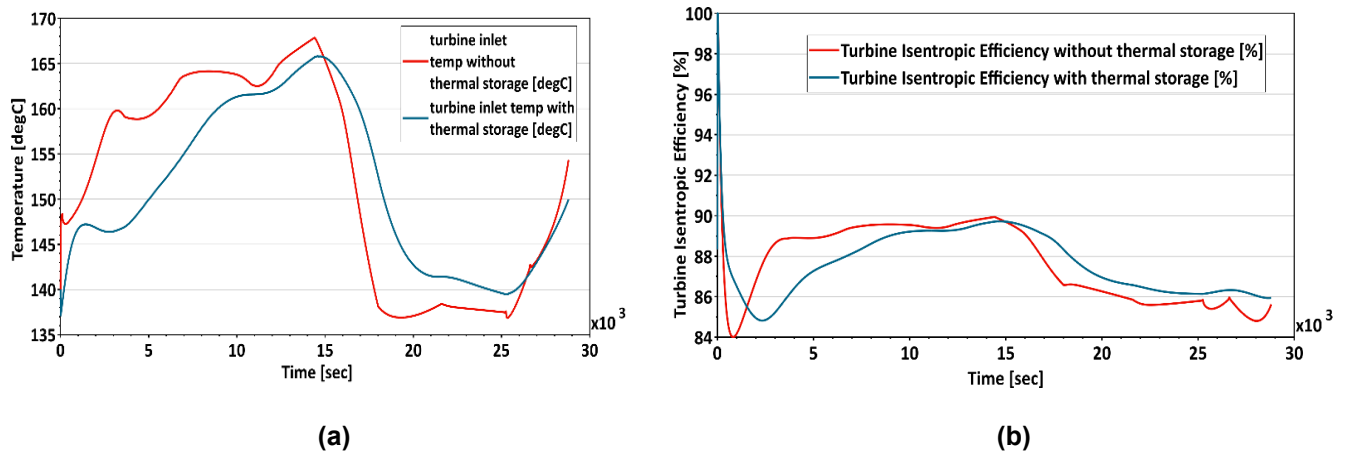


Figure 5-34 (a): Turbine inlet superheat maintained with addition of thermal mass (b): Steady turbine isentropic efficiency achieved with the help of thermal mass

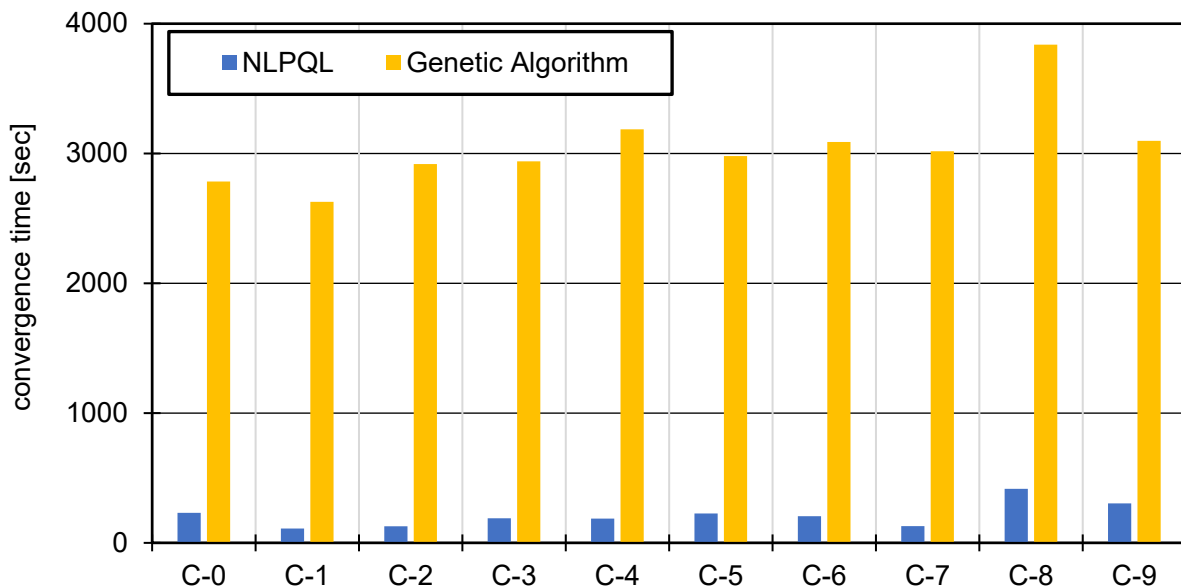
However, while the thermal mass did maintain superheat temperatures for longer ( $14.88 \times 10^3$  -  $26.2 \times 10^3$ s of heat source profile), it also absorbed to consume thermal energy during periods of high heat source temperature ( $0$  to  $14.88 \times 10^3$ ,  $26.2 \times 10^3$  to  $28.8 \times 10^3$ s of heat source profile), neutralising the overall improvement to turbine isentropic efficiency to 1%, as previously observed in Figure 5-17, over the duration of the study.

#### 5.4.2 Optimisation study results

Two global optimisation approaches were used to optimise the component sizes: NLPQL and GA. The NLPQL algorithm was less computationally intensive and in good agreement with GA, as shown in Figure 5-35. On reflection, despite the growing popularity of the genetic algorithm and artificial intelligence, simpler mathematical solvers are capable of optimising ORC problems at similar level of complexity. Considering the case of the conventional ORC, the NLPQL algorithm achieved the desired final accuracy within 50 iterations, whereas the genetic algorithm required 624 iterations. The reduced number of iterations required by the NLPQL was in line with previous studies undertaken for diesel engines [258, 325]. A population size of 50 individuals and 12 generations were required to achieve convergence for the GA. As the genetic algorithm did not consider initialisation values, but was merely restricted by constraints, it explored widely spread characteristics over a larger search area, wherein additional iterations were required for convergence. The improvement of fitness function for the NLPQL and GAs was observed in Figure 5-36 and Figure 5-37, respectively. The Pareto fronts demonstrated negligible improvement of the objective function after 46 and 550 iterations, respectively.

It is noteworthy mentioning that despite the benefits of the NLPQL algorithm for single objective optimisation, mixed results were reported for the effectiveness and computational efficiency for the NLPQL algorithm while undertaking multi-objective optimisation [256, 258]. A few previous studies have used the Latin hypercube algorithm [363] and multi-island genetic algorithm [364] for initial iterations in combination with and prior to the NLPQL algorithm, to

ensure the NLPQL algorithm was not trapped within local optima. A simpler approach based on parametric evaluation was considered by this study (in section 5.4.1: Parametric cycle evaluation), validated by the analogous results achieved in the case of both optimisers.



Cycle name	Configuration	Cycle name	Configuration
C-0	Conventional	C-5	Recuperative & Thermal mass
C-1	Thermal mass	C-6	Regenerative & APH
C-2	Recuperative	C-7	Regenerative
C-3	APH	C-8	Regenerative & Recuperative
C-4	Recuperative & APH	C-9	Regenerative & Thermal mass

Figure 5-35: Comparison of convergence time required for NLPQL and GA optimisers

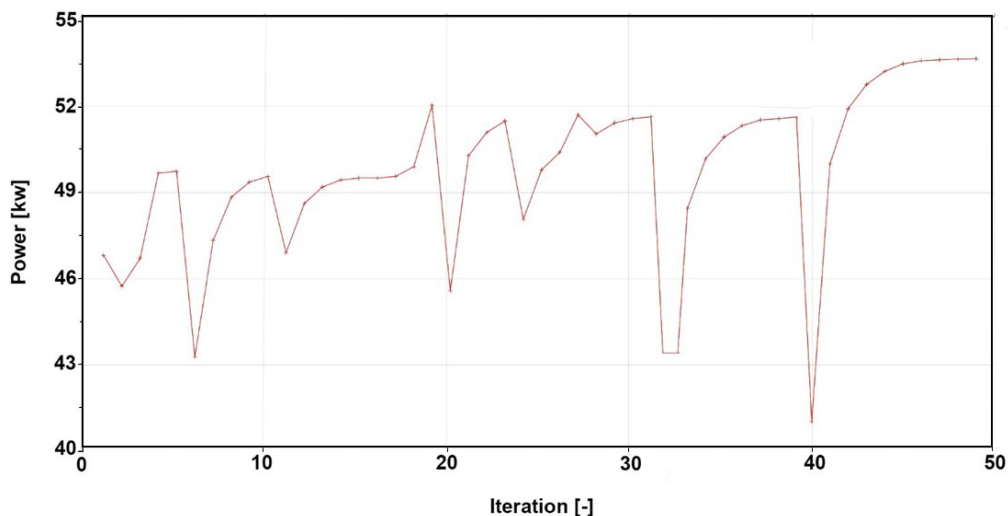


Figure 5-36: NLPQL algorithm achieved convergence within 48 iterations

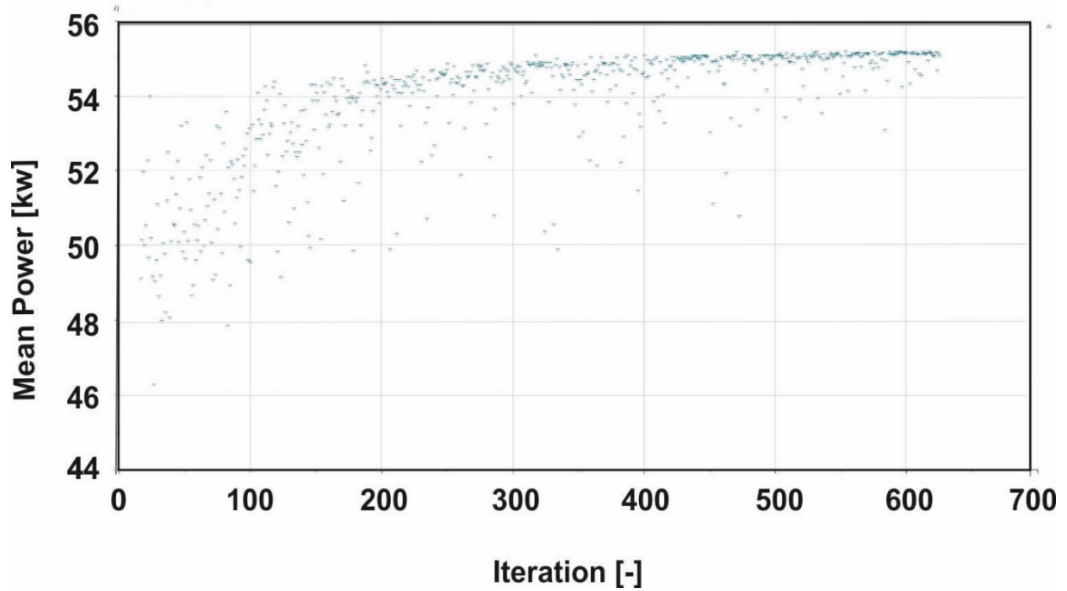
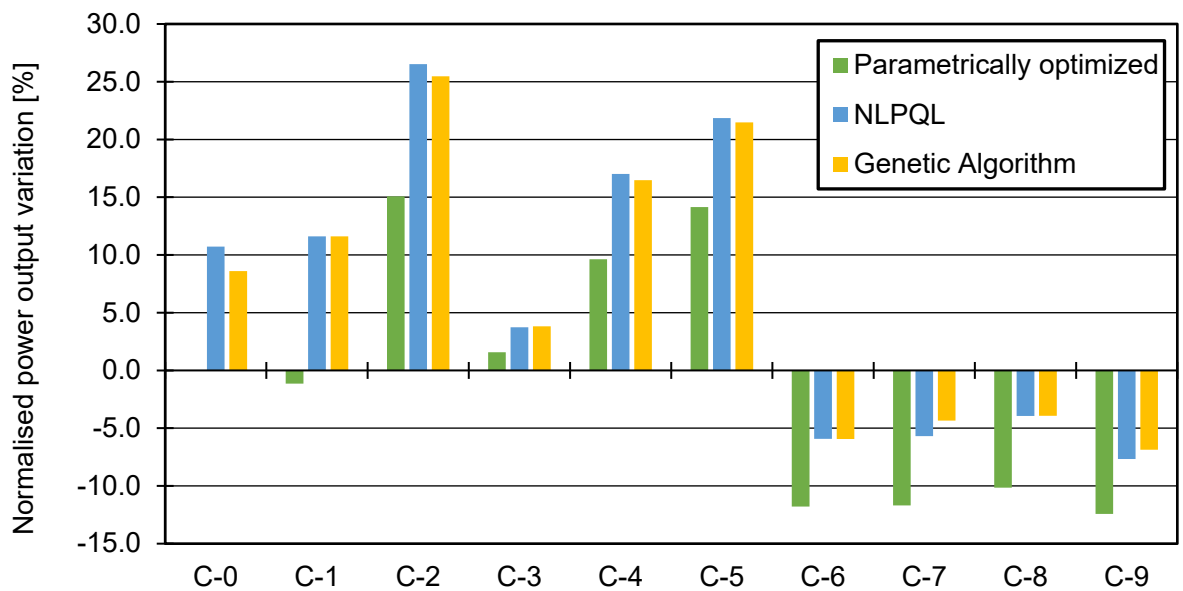
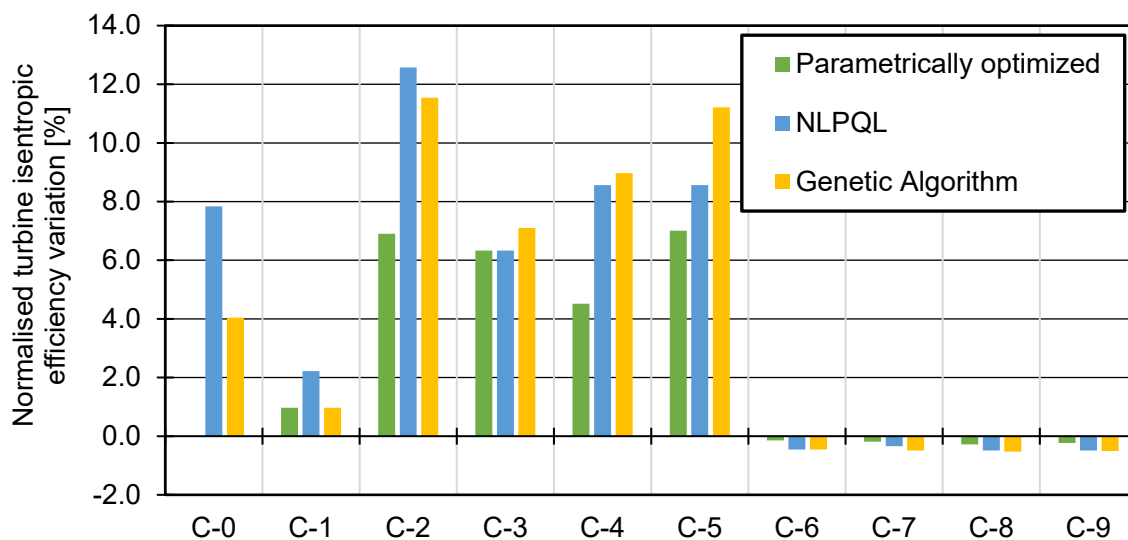


Figure 5-37: Pareto spread of GA population improvement in objective function over 624 iterations



Cycle name	Configuration	Cycle name	Configuration
C-0	Conventional	C-5	Regenerative & Thermal mass
C-1	Thermal mass	C-6	Regenerative & APH
C-2	Regenerative	C-7	Regenerative
C-3	APH	C-8	Regenerative & Recuperative
C-4	Regenerative & APH	C-9	Regenerative & Thermal mass

Figure 5-38: Normalised power output gains of all cycles with optimisers compared



Cycle name	Configuration	Cycle name	Configuration
C-0	Conventional	C-5	Recuperative & Thermal mass
C-1	Thermal mass	C-6	Regenerative & APH
C-2	Recuperative	C-7	Regenerative
C-3	APH	C-8	Regenerative & Recuperative
C-4	Recuperative & APH	C-9	Regenerative & Thermal mass

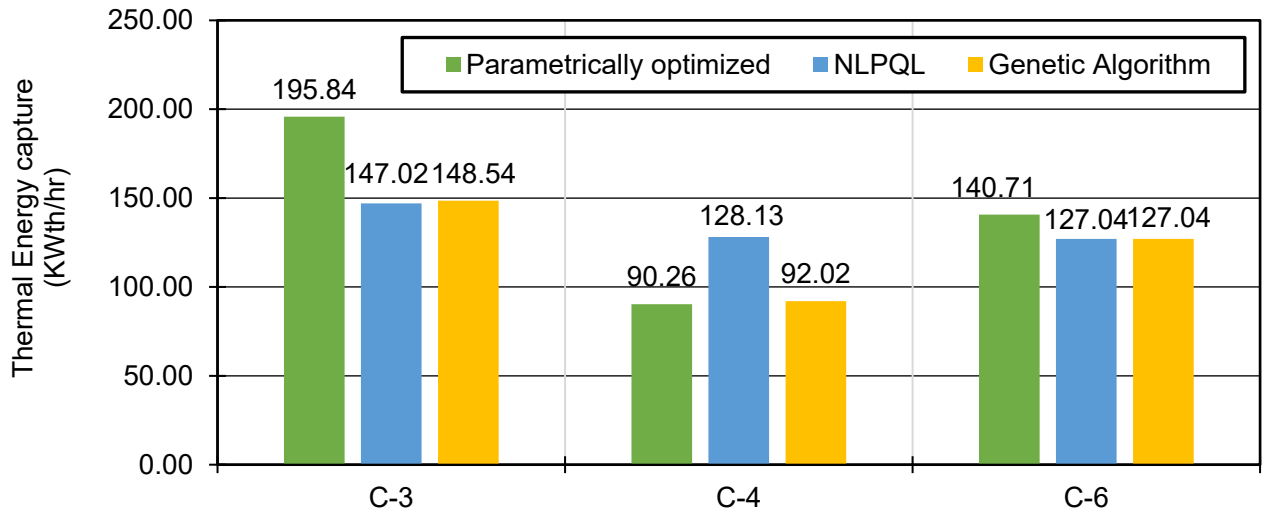
Figure 5-39: Variations in turbine isentropic efficiency noted for all cases

In the case of the conventional ORC, both optimisers improved power output by 5 kWe, equivalent to 10% of the total power generation of the parametrically optimised ORC. Cycle efficiency improvement using optimisers within the given cycle varied from 2% in the case of the APH cycle upto 12% in the case of the recuperative cycle. In the case of NLPQL algorithm, the recuperative cycle produced an overall 26.5% improvement compared to the parametrically optimised conventional ORC cycle. The optimisation improved the efficiency proportionally to the degree of recuperation. A strong correlation between the mean turbine isentropic efficiency and the overall power generation was observed, as shown in Figure 5-39. It confirms the importance of considering the turbine performance towards overall cycle performance optimisation. The analogues optimised component sizes for such cycles are mentioned in Table 5.6. The variation in component sizing was explained by the differing approaches adopted by local and global optimisers.

As the only objective of the optimisation was to increase the electrical power output, the optimised cycles did not improve the thermal energy recovery in the case of the APH-based cycles, as shown in Figure 5-40. Optimising the cycles for power output resulted in an up to 24% reduction in thermal heat recovery. The recuperative APH cycle provided a balanced result for exploiting electrical as well as thermal energy recovery. However, to further understand the compromise between electrical and thermal energy recovery, a techno-economic study encompassing capital expenditure, operation and installation cost, electrical savings and fuel savings have been analysed in Chapter 6.

Table 5.6: Optimised component sizes provided by parametric optimisation, NLPQL and genetic algorithm

Type of Cycle	Unit	Conventional			Thermal Mass			Recuperative			APH			Recuperative & APH		
Component		Param- etric	NLPQL	GA	Param- etric	NLPQL	GA	Param- etric	NLPQL	GA	Param- etric	NLPQL	GA	Param- etric	NLPQL	GA
Pump displacement	cm <sup>3</sup>	80	89	96	80	95	95	80	91	90	80	79	79	80	88	85
Boiler area	m <sup>2</sup>	100	103	120	100	90	117	100	120	117	100	120	120	100	120	111
Turbine displacement	cm <sup>3</sup>	130	104	104	130	104	105	130	104	107	130	104	104	130	104	105
Condenser area	m <sup>2</sup>	180	215	216	180	214	214	180	216	211	180	216	215	180	216	111
Recuperator area	m <sup>2</sup>							180	180	174				150	143	161
Type of Cycle	unit	Recuperative & Thermal mass			Regenerative & APH			Regenerative			Regenerative & Recuperative			Regenerative & Thermal Mass		
Component		Param- etric	NLPQL	GA	Param- etric	NLPQL	GA	Param- etric	NLPQL	GA	Param- etric	NLPQL	GA	Param- etric	NLPQL	GA
Pump displacement	cm <sup>3</sup>	80	88	87	80	94	94	80	96	93	80	93	93	80	91	93
Boiler area	m <sup>2</sup>	100	119	113	100	119	119	100	112	119	100	118	120	100	100	111
Turbine displacement	cm <sup>3</sup>	130	111	111	130	105	105	130	128	114	130	113	112	130	124	123
Condenser area	m <sup>2</sup>	180	216	215	180	213	213	180	199	211	180	216	215	180	204	215
Recuperator area	m <sup>2</sup>	150	161	159							150	150	151			



Cycle name	Configuration	Cycle name	Configuration	Cycle name	Configuration
C-3	Recuperative	C-4	APH	C-6	Recuperative & APH

Figure 5-40: Thermal energy captured by APH-based cycles

## 5.5 Conclusion

This chapter aimed to optimise the component sizes for a range of ORC configurations targeting the highest power output for a finite transient waste heat source and considering the variation of turbine efficiency. Ten different cycle configurations were studied, including novel combinations of recuperators, regenerators, thermal storage mediums and steam boiler air pre-heaters.

A parametric optimisation was initially undertaken for a conventional Rankine cycle to estimate a baseline for equipment sizing, which was later considered as the initialisation for the NLPQL algorithm. The main findings of the parametric study were:

- The recuperative cycle generated the highest power, 15% greater than the conventional cycle, whereas regeneration-based cycles did not demonstrate any improvement in terms of electrical power generation.
- Turbine isentropic efficiency varied by up to 7% across multiple cycle configurations, which foster the importance of considering a loss model rather than assuming a fixed isentropic efficiency. The regenerative cycles suffered from poor isentropic efficiency as well as a loss of mass flow of working fluid to the low-pressure turbine stage.
- The heat rejection of the cycle was an additional factor, often overlooked by previous studies, which required additional energy. The addition of the APH significantly reduced the condenser heat load, while simultaneously providing the steam boiler with over 195

kWth of usable low-grade heat recovery, which led to a reduction in fossil fuel consumption and environmental benefits of up to 1.9%. The combination of the APH, recuperator and regenerator as thermal energy recovery devices led to a condenser heat load reduction upto 65%.

- Although the use of thermal mass did not provide significant benefits in terms of power generation for this study, its buffering properties were evident and could be of benefit to future studies with a higher transience of heat sources.
- The combination of the regenerative and recuperative cycle led to a 32% increase in degree of superheat and could be considered for the operation of cycles with wet ORC fluids and dealing with a high degree of intermittency.

A comparative study between the mathematical technique based NLPQL algorithm and genetic algorithm was undertaken in this chapter. The NLPQL algorithm demonstrated comparable results with significantly reduced computational cost which led to faster convergence, proving its effectiveness for single objective ORC cycle thermodynamic optimisation. The NLPQL- optimised recuperative cycle was noted as the optimal cycle, with a 26.5% increase in mean power generation compared to the 49.9 kW generated by the parametrically optimised conventional cycle. The optimised cycle also improved turbine isentropic efficiency by 12.57%, the highest of any cycle, yet again highlighting the importance of turbine efficiency.

The recommendation of this chapter is to consider organic recuperative cycle configurations for utilising finite transient heat sources. Variable turbine isentropic efficiency was deemed integral to any ORC and recommended to be considered for any detailed studies at cycle level.

The success of the NLPQL optimiser depended on the initialisation midpoint. When combined with a parametric pre-optimiser, the use of the NLPQL algorithm could be explored for multi-objective optimisation studies. Alternatively, a GA could be used to determine the preliminary design point, aided by its wider search area, followed by NLPQL for a final localised study.

A multi-objective optimisation study could be undertaken to apportion the value of electrical energy and thermal energy recovered, then used to determine the most economical overall solution. This study is undertaken in Chapter 6, encompassing equipment cost, operation cost, fuel savings and electrical cost.

# Chapter 6 Thermo-Economic Optimisation

## 6.1 Introduction

Organic Rankine cycles (ORCs) have been widely studied previously for the conversion of low-to-medium-grade heat into power. However, high investment costs and the lack of suitable components for small-sized ORCs have limited their widespread adoption [77]. The thermodynamic study conducted in Chapter 5 concluded that cycles incorporating recuperation, air preheating, a combination of recuperation and thermal storage, a combination of recuperation and air preheating and a combination of regeneration and air preheating boosted the thermodynamic performance of the conventional ORC. Whereas the recuperative cycle demonstrated the highest cycle efficiency, it is not necessary that it is the most commercially viable configuration, due to variable component costs as well as the multiple combinations of electrical and thermal outputs produced by the varied configurations. Optimising for cycle efficiency leads to larger heat exchanger sizing despite diminishing gains, due to the absence of consideration of the economic aspects. A combined thermo-economic assessment was thus noted as an essential criterion for commercial ORC evaluation as it assessed the additional cost and complexity implied versus benefits brought in by these subsystems [318]. Whereas the previous chapter validated the use of the non-linear programming by quadratic Lagrangian (NLPQL) algorithm for single objective optimisation for cycle-level thermodynamic studies, the NLPQL algorithm was not previously used for multi-objective ORC-related optimisation to the best of the researcher's knowledge.

Therefore, the aim of this chapter is to thermo-economically evaluate and optimise cycle configurations for the waste heat recovery ORC, which will be achieved through achieving the following objectives:

- Benchmark the thermo-economic viability of the thermodynamically superior cycle configurations against conventional ORC.
- Evaluate the suitability of the NLPQL and genetic algorithms for multi-objective ORC optimisation.
- Assess the most financially viable cycle for combination with the transient steam boiler flue gas stacks and determine the corresponding payback period.

## 6.2 Methodology

### 6.2.1 System description

The waste heat source considered was flue gas from an industrial steam boiler operating in a medium-sized textile plant, as detailed in Chapter 5. Indonesian sub-bituminous coal fuelled the steam boiler. The levelised cost of fuel (LCOF) at the textile plant was  $5.22 \times 10^{-3}$  €/MJ for bituminous coal with a gross calorific value of 23 MJ/kg, as reported by Alameer et al. [365]. These prices included the raw material, transportation, unloading and taxation. The levelised cost of electricity (LCOE) for the textile plant was inferred/deduced as € 0.15 per unit kW, deduced by noting the monthly electricity payment; this value was validated by Rettig et al. in a previous study [91].

Whereas Chapter 5 compared 10 different cycle configurations, this chapter focuses on cycles that demonstrate improved electrical and thermal output with respect to conventional ORC benchmarks, as listed in Table 6.1. R245fa is maintained as the working fluid due to its low evaporation temperature, high thermal efficiency, thermal stability, low cycle-specific investment cost and compatibility with common ORC materials, as noted by Imran et al. [326]. The size of all major components, considered as independent variables, were varied to minimise the specific investment cost (SIC) and maximise the mean power generation, noted in Table 6.2. The variables to be optimised were provided a degree of freedom of 25% from the starting point values. The preliminary investigation revealed that broadening the degree of freedom further leads to convergence issues.

Table 6.1: Cycle configuration and variables

Cycle	Independent Variables
Conventional ORC	Pump displacement, boiler heat exchanger area, turbine displacement, condenser heat exchanger area
Recuperation	Pump displacement, boiler heat exchanger area, turbine displacement, condenser heat exchanger area, recuperator heat exchanger area
Recuperation + APH	Pump displacement, boiler heat exchanger area, turbine displacement, condenser heat exchanger area, APH heat exchanger area, recuperator heat exchanger area
APH	Pump displacement, boiler heat exchanger area, turbine displacement, condenser heat exchanger area, APH heat exchanger area
Recuperation + Thermal Mass	Pump displacement, boiler heat exchanger area, turbine displacement, condenser heat exchanger area, mass of thermal storage, recuperator heat exchanger area
Regeneration + APH	Pump displacement, boiler heat exchanger area, turbine displacement, condenser heat exchanger area, APH heat exchanger area

Table 6.2: Range of variables considered

S. No.	Component	Parameter	Minimum value	Starting value	Maximum value	Unit
1	Pump	Displacement	60	80	100	cm <sup>3</sup>
2	Boiler	Heat transfer area	75	100	125	m <sup>2</sup>
3	Turbine	Displacement	98	130	162	cm <sup>3</sup>
4	Condenser	Heat transfer area	135	180	225	m <sup>2</sup>
5	Recuperator	Heat exchange area	120	150	180	m <sup>2</sup>
6	APH 1- 5	Heat exchange area	225	300	375	m <sup>2</sup>
7	Thermal mass 1–3	Mass	1	10,000	10,000	kg

### 6.2.2 Problem definition

An economic comparison of cycle configurations is the most recommended approach for the combined evaluation of electrical and thermal energy. The variable turbine efficiency was considered as a key parameter for the thermodynamic modelling undertaken, carried over from the previous chapter (Chapter 5). Whereas that chapter considered a single objective function, a composite approach incorporating varied contradicting objectives was adapted for multi-objective optimisation in this chapter.

### 6.2.3 Multi-objective optimisation approach

Two general approaches were previously noted for multi-objective optimisation [327]. The first approach combined the individual objective functions into a single composite function using the weighted sum method. Defining the constraints, weighing and objective functions are iterative processes, even for operators familiar with the problem domain [327]. This method involved the movement of all objective functions simultaneously. The second approach was to develop and examine a Pareto front. It contained a set of solutions that were nondominated with respect to each other; achieved by compromising individual objectives. Each point on the Pareto front represented a set of variables linked to a design point. The band of optimal solutions within the

Pareto front increased in proportion to the number of objectives. The weighted sum was selected in this study as it was better suited to problems with a limited number of objective functions, well-defined constraints and weightage. It enabled assigning weightage to individual objective functions and did not require operator intervention for global optima selection. Equally, the results obtained were visualised on a Pareto front; this to correlate the trade-off between individual objectives.

The weighted sum composite function has been defined in equation 6.1. Eighty percent of the weightage was assigned to minimise the specific investment cost (*SIC*), and 20% weightage was assigned to maximising the power generation (*Mean Power*), to ensure the scale of operations was sufficient to generate meaningful saving in the absolute value, with limited manpower, in line with previous findings [266]. Articulation preference was not considered in the interest of computational efficiency.

$$F_{weighted\ sum} = \sum 0.8 \times F(SIC) + 0.2 \times F\left(\frac{1}{Mean\ Power}\right) \quad 6.1$$

#### 6.2.4 Specific investment cost

The specific Investment cost (*SIC*), mentioned in equation 6.2, factors in the expenses in the form of capital investment and labour cost, against the value of economic benefits provided in terms of electricity generation and thermal energy recovery.  $\text{€}W_T$  is the value of electricity generation by the turbine and  $\text{€}W_p$  is the value of electricity consumption by the pump considering the LCOE.  $\text{€}H_{recovery}$  is the value of thermal energy recovery, considering the LCOF. The air preheater (APH) cycle recovered low-grade thermal energy, for which a good correlation with high-grade electrical energy does not exist; instead, an economic indicator was considered as a suitable appropriation. Input heat costs were not considered, as the application was centred around a waste heat recovery-based source.

The component and labour cost components were determined as in Table 6.3. Indices for the material cost of the cast iron thermal mass were calculated by using the international prices for 2021 [368]. The cost of the working fluid was considered as 34.08 €/kg, based on the findings of Roumpedakis et al., sourced from manufacturer quotes [281]. The total capital expenditure have been summarised in equation 6.3.

$$SIC = \frac{Cost_{Components} + Cost_{Labour}}{\text{€}W_T + \text{€}H_{recovery}} \quad 6.2$$

$$\begin{aligned}
Cost_{Components} = & Cost_{Pump} + Cost_{Economiser} + Cost_{Evaporator} + Cost_{Superheater} \\
& + Cost_{Turbine} + Cost_{Condenser} + Cost_{Piping} + Cost_{Fluid} + Cost_{Recuperator} \\
& + Cost_{Regenerator} + Cost_{APH} + Cost_{ThermalMass}
\end{aligned} \tag{6.3}$$

$\dot{W}_{Pump}$  and  $KW_{ePump}$  denote the specific work done, and power consumed by the pump.  $Vol_{tank}$ ,  $Mass_{fluid}$ ,  $Mass_{Thermal}$  and  $Cost_{capital}$  denote the volume of the working fluid storage tank between the condenser and pump, mass of working fluid required, mass of thermal storage required and total capital expenditure.  $D_{pipe}$  and  $L_{pipe}$  denote the diameter and length of piping, calculated to limit fluid pressure drop to within 0.02 kg/cm<sup>2</sup> per unit metre of length using the Mac Adams correlation for frictional pressure drop [330, 331], as mentioned in Table 6.4. The pipeline length was decided based on observations of previous similar-sized configurations [332, 333].

Table 6.3: Component and labour costs

Component	Equation	Reference
Heat exchangers	$ 190 + 310 \times (Area_{economiser} + Area_{Evaporator} + Area_{Superheater} + Area_{Condenser} + Area_{Recuperator} + Area_{APH}) $	Quoilin and Declaye [62], Roumpedakis et al. [272]
Turbine	$ 1.5 \times (225 + 170 \times \dot{V}_m) $	Quoilin and Declaye [62]
Feed pump	$ 900 \times \left( \frac{\dot{W}_{Pump} \times KW_{ePump}}{300} \right) $	Lecompte and Huisseune [228]
Storage tank	$ 31.5 + 16 \times Vol_{tank} $	Quoilin and Declaye [62]
Working fluid	$ 34.08 \times Mass_{fluid} $	Roumpedakis et al. [272]
Piping	$ (0.89 + 0.28 \times D_{pipe}) \times L_{pipe} $	Lecompte and Huisseune [228]
Thermal mass	$ 0.25 \times Mass_{Thermal} $	Golubev et al. [328]
Miscellaneous	300	Kavvadias and Quoilin [329]
Installation labour	$ 0.3 \times Cost_{capital} $	Quoilin and Declaye [62], Roumpedakis et al. [272]

Table 6.4: Diameter and length of working fluid piping

Section of piping	Diameter (mm)	Length (m)
Pump to economiser	50	3
Superheater to turbine	80	5
Turbine to condenser	800	6
Condenser to pump	50	10
Recuperator piping on liquid side	50	3
Recuperator piping on vapour side	800	3
Regenerator bleed	3	5

$$Cost_{2020} = Cost_{REFyear} \times \frac{CEPCI_{2020}}{CEPCI_{REFyear}} \quad 6.4$$

The chemical engineering plant cost index (CEPCI) was used to adjust the variations of the equipment cost and inflation, as in equation 6.4 [373], where  $Cost_{2020}$  is the inflation adjusted material cost based on year 2020, and  $Cost_{REFyear}$  is the material cost based on the year it is was derived. The  $CEPCI_{2020}$  index was used as a scaling reference for the year 2020, according to the index value of the material-based on the year of publishing ( $CEPCI_{REFyear}$ ). Annual CEPCI indices were noted as 573.9, 567.3, 603.1 and 595 for the years 2011, 2013, 2018 and 2020, respectively.

### 6.2.5 Payback

The payback was determined by the expenditure and annual income, as shown in equation 6.5. The total expenditure is the sum of equipment capital, installation labour, annual operational manpower and annual maintenance costs. The income is the sum of the electrical and thermal energy generation.

$$\text{Payback (years)} = \frac{Cost_{Components} + Cost_{Labour} + Annual\ Cost_{Operation\ manpower} + Annual\ Cost_{Maintenance}}{Annual\ (\text{€}W_T - \text{€}W_P + \text{€}H_{recovery})} \quad 6.5$$

## 6.2.6 Optimisation

The NLPQL algorithm was employed within the specified constraints and the Hessian of the Lagrange functions was used for quadratic approximation. The quadratic subproblem was formed by linearising the Karush-Kuhn-Tucker criterion, by using equation 6.6 [353]. NLPQL was benchmarked against GA, which is a population-based approach and recommended by Konak et al [367].

$$L(x, \lambda, \mu) = f(x) + \lambda g(x) + \mu h(x) \quad [265] \quad 6.6$$

As the optimisation of one objective could lead to a compromise in another, the spread of the Pareto front, as typically shown in Figure 6-1 helps to visually elaborate the distribution and trade between individual objectives.

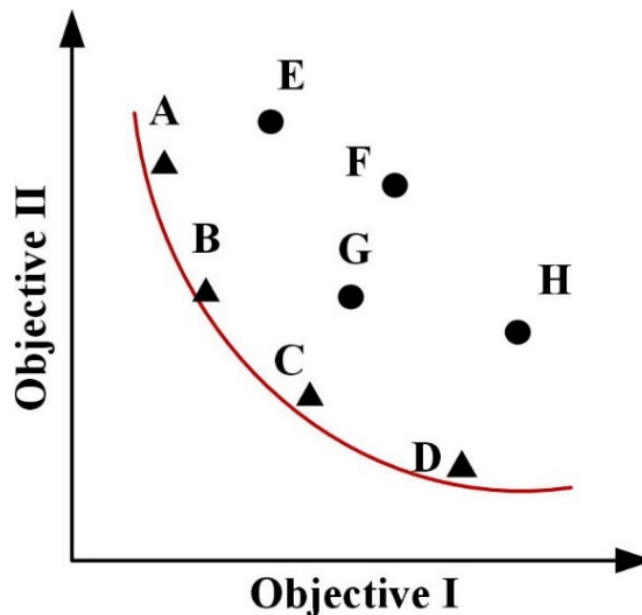


Figure 6-1: Expected Pareto front for two objective optimisations [20]. Cases A–H represent individual iterations, wherein A–D represent Pareto optimal cases

## 6.2.7 Assumptions

The average ambient temperature recorded for the location of the textile plant, at Ghaziabad, in north India was considered as 25.7°C, and the wet bulb temperature was 21.4°C, based on data recorded by the Indian Meteorological Department [303]. The average ambient temperature is considerably higher than the global average annual temperature of 13.9°C [303]. This will ensure better economics for colder locations, as previous studies noted up to 30% reduced payback period for ORC systems with lower heat sink temperatures [12, 38, 305].

The volumetric, isometric and mechanical efficiency of the pumps were considered as 50%, 65% and 70%, respectively; and steam boiler efficiency was considered as 82% [8, 301]. Variable turbine efficiency was considered using the Craig and Cox design point loss model [192] and Moustapha et al.'s off-design loss model [215]. Working fluid gland leakage across the pump and turbine were ignored. Isentropic efficiency of the cooling water pump was considered as 65%. Operation of the ORC cycle was considered as 8000 hours per annum [296].

### 6.3 Results and discussion

The costs for major equipment before optimisation are furnished in Table 6.5. The values agreed with those reported by Shengjun et al. [334], that stated heat exchangers were 80–90% of the conventional ORCs' cost. The specific investment cost before optimisation was 44842 €/kW. In the current study, the cost per unit of installed capacity for the optimised conventional cycle was 2122 €/kW, in line with Astolfi et al.'s predictions of 1800 – 2500 €/kW for techno-economically optimised ORCs [227]. This significant improvement was mainly attributed to reduced heat exchanger sizing, as detailed in section 6.3.2.

Table 6.5: Material cost of equipment before optimisation

S. No	Component	Cost in Euros (€)
1	Pump	317
2	Boiler	17,240
3	Turbine	341
4	Condenser	70,832
5	Piping	6,500
6	Working fluid	10,480
7	Recuperator	24,714
8	APH	46,690
9	Thermal Mass	9,600

### 6.3.1 Individual objective trade-off

For most configurations, the optimisation enhances the value of both objectives towards the prespecified aim, with the multi-objective genetic algorithm (MOGA) providing 1.98% better value of objective function. On average, for a given cycle, both optimisers led to a 26.95% improvement in the value of the composite objective function, 21.72% improvement in the value of the SIC but a 1.1% reduction in power generation, compared to the un-optimised conventional ORC, as shown in Table 6.6. The maximum improvement in mean power was limited to 7.9% for the MOGA-optimised conventional ORC cycle.

Besides, mean power decreased by up to 8.6% while the objective function improved by up to 30.9% in the case of the APH and regenerative APH cycles. The contrasting trends for the individual objectives emphasised the increased weightage for the SIC at the expense of power generation. This was also observed in the Pareto front, as shown in Figure 6-2, which demonstrates a clearly defined trade-off between both objectives. The composite objective function provides a consolidated approach to achieve the best overall configuration.

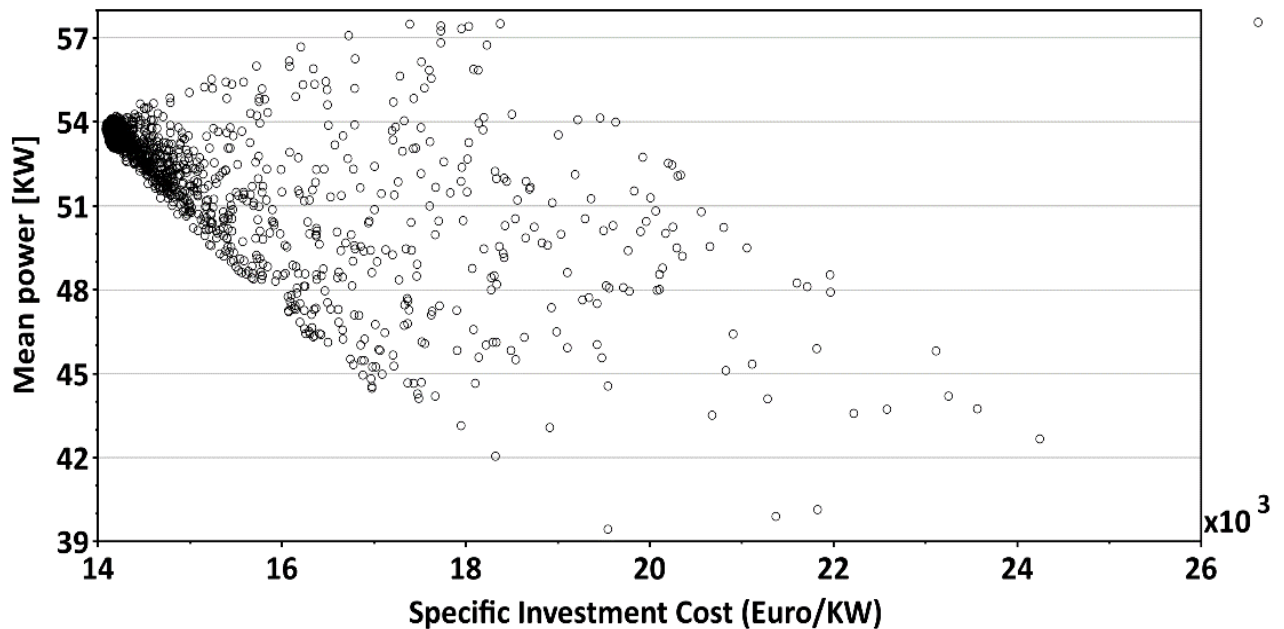


Figure 6-2: Pareto front for conventional ORC cycle with NLPQL optimisation. The considered objectives are mean power and specific investment cost

Table 6.6: Improvement in composite objective Function and SIC values achieved by optimiser

Cycle	Optimiser	Composite objective function [-]	Composite objective function improvement to original [%]	Composite objective function improvement within cycle [%]	SIC [€/kW]	SIC improvement to original [%]	SIC improvement within cycle [%]	Mean power [kW]	Mean power improvement to original [%]	Mean power improvement within cycle [%]
Conventional ORC	Before optimisation	13682			18229			49.97		
	NLPQL	9954.8	27.3	27.3	14774	18.9	18.9	50.83	1.7	1.7
	MOGA	9291.2	32.1	32.1	14197	22.1	22.1	53.91	7.9	7.9
Recuperation	Before optimisation	14349	-4.9		19581	-7.4		57.5	15.1	
	NLPQL	9752.2	28.7	32.0	14789	18.9	24.5	55.35	10.8	-3.7
	MOGA	9610.1	29.8	33.0	14464	20.7	26.1	53.34	6.7	-7.2
Recuperation + APH	Before optimisation	8638	36.9		13623	25.3		54.78	9.6	
	NLPQL	6993.4	48.9	19.0	12063	33.8	11.5	55.71	11.5	1.7
	MOGA	6478.7	52.6	25.0	11487	36.9	15.7	57.52	15.1	5.0
APH	Before optimisation	7075.2	48.3		11445	37.2		48.02	-3.9	
	NLPQL	4892.5	64.2	30.9	9235	49.3	19.3	47.72	-4.5	-0.6
	MOGA	5493.9	59.8	22.3	9649	47.1	15.7	45.66	-8.6	-4.9
Recuperation + Thermal Mass	Before optimisation	11486	-5.9		19769	-8.4		58.05	16.2	
	NLPQL	9780.7	28.5	32.5	15046	17.5	23.9	57.86	15.8	-0.3
	MOGA	9585.6	29.9	33.8	14496	20.5	26.7	53.96	8.0	-7.0
Regeneration + APH	Before optimisation	8386.1	38.7		12886	29.3		49.45	-1.0	
	NLPQL	6976.2	49.0	16.8	11245	38.3	12.7	46.91	-6.1	-5.1
	MOGA	6933.8	49.3	17.3	11219	38.5	12.9	47.09	-5.8	-4.8

Table 6.7 Component size for optimised configuration

Cycle	Component	Pump displacement cm <sup>3</sup>	Boiler area m <sup>2</sup>	Turbine displacement cm <sup>3</sup>	Condenser area m <sup>2</sup>	Recuperator area m <sup>2</sup>	APH area m <sup>2</sup>	Thermal mass kg
conventional ORC	NLPQL	77.8	75.0	98.0	143.1	-	-	-
	MOGA	99.65	97.72	98.07	148.3	-	-	-
Recuperation	NLPQL	94.65	79.2	98.10	135	180	-	-
	MOGA	94.34	80.83	98.46	135.1	180	-	-
Recuperation + APH	NLPQL	78.24	125.0	126.5	135	143	354	-
	MOGA	87.37	122.09	109	137.1	180	249.6	-
APH	NLPQL	77.78	109.0	130.8	135	-	225	-
	MOGA	83.6	110.13	155.2	136.5	-	252.2	-
Recuperation + Thermal Mass	NLPQL	91.59	92.93	98.0	135	144.4	-	31976
	MOGA	92.12	87.79	102.9	135	142.5	-	35762
Regeneration + APH	NLPQL	97.63	117.34	113.6	135	-	296.5	-
	MOGA	98.9	124.4	115.8	135	-	299.2	-

### 6.3.2 Heat exchanger sizing

Compared to the thermodynamic study undertaken in Chapter 5, the inclusion of the economic aspect led to reduced boiler and condenser sizes along with larger recuperator and APH sizing, as seen in Table 6.7. Along with increased capital expenditure, larger condensers led to an increased thermal energy loss. However, larger recuperators and air pre-heaters recovered this thermal energy in the form of electrical and thermal energy, respectively.

Table 6.8 shows that the optimised APH cycle reduces the condenser heat load, thereby reducing the cooling tower's capital expenditure by 62%, and evaporation loss by 1.8 m<sup>3</sup>/hr (62%). The power consumed by the cooling water pump reduced by 5.8 kW (62%), corresponding to an 11% reduction of the ORC's total power generation. The T-s diagrams in Figure 6-3 demonstrate the extent of sensible and latent heat recovery undertaken up to APH 5. The NLPQL optimiser's results showed that the minor benefits achieved with the help of the thermal mass were not thermo-economically justified in line with the previous chapter (Chapter 5).

Table 6.8: Reduced cooling water evaporation loss and pump consumption for ORC with APH

<b>Cooling water pump power consumption</b>		<b>Conventional ORC before optimisation</b>	<b>NLPQL-optimised integrated APH</b>
Working fluid mass flow rate	kg/hr	4,767	4,767
Heat load	kJ/hr	867,594	333,690
Temperature Inlet to condenser	°C	20	20
Temperature outlet of condenser	°C	28	28
Mean WF inlet enthalpy	kJ/kg	431	311
Mean WF outlet enthalpy	kJ/kg	249	241
Cooling water (CW) flow	m <sup>3</sup> /hr	108.4	41.7
Pump power required	kW	9.36	3.60
<b>Cooling Tower</b>			
Flow	m <sup>3</sup> /hr	108.45	41.71
Refrigeration required	TR	286.90	110.35
Evaporation loss	m <sup>3</sup> /hr	2.92	1.12

Cycles incorporating air preheating required a larger ORC boiler size than the initialisation value would suggest, whereas a reduced boiler size was noted for all other configurations. This was because the large area of the air preheater enabled more thermal energy recovery. It is noteworthy that the largest boiler heat exchanger area was noted for the recuperative APH cycle, wherein sequential heat exchangers allowed for the highest thermal energy recovery.

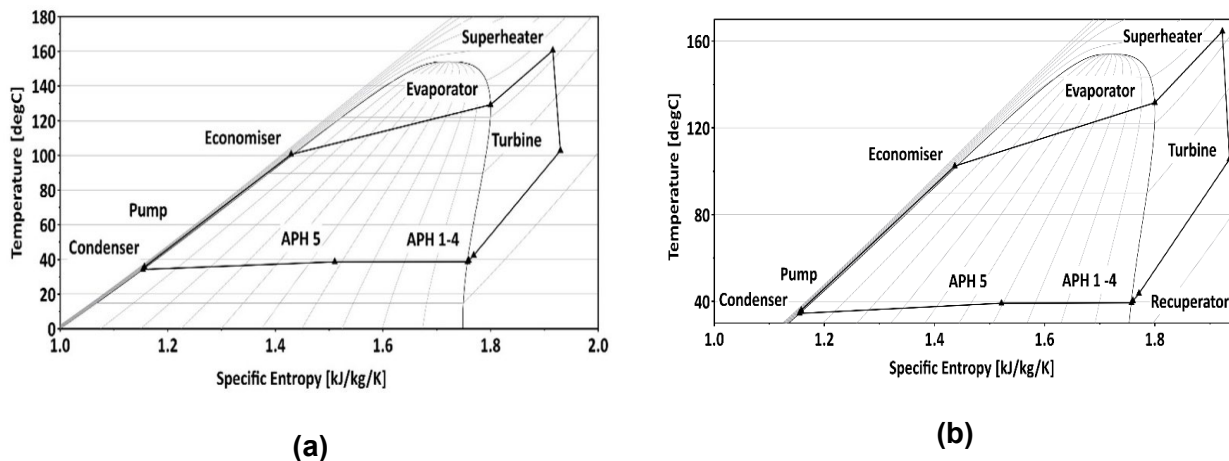


Figure 6-3: T-s Diagram for (a) NLPQL-optimised APH cycle; (b) NLPQL-optimised recuperative APH cycle

### 6.3.3 Thermal energy recovery

Despite the lowest power generation, the APH cycle showed the lowest value of the objective function, optimising it from 7,075 to 4,892 by the NLQPL algorithm that led to a 49% improvement in SIC despite the reduction in the power generation by 4.5%. Whereas the conventional cycle dissipated an average of 324 kW<sub>th</sub> to the condenser, the large size of APH used by this configuration reduced that by 57% to 156.9 kW<sub>th</sub>. The APH reduced the enthalpy of the working fluid from 48°C superheated gas to a saturated vapour with gas mass fraction of 0.61, as shown in Figure 6-4, extracting sensible and latent heat. Further investigation showed that the operational revenue generated by this configuration was € 8.35 for power generation and €8.82 fuel saving. Equipment costs for the NLPQL-optimised APH cycle are populated in Table 6.9.

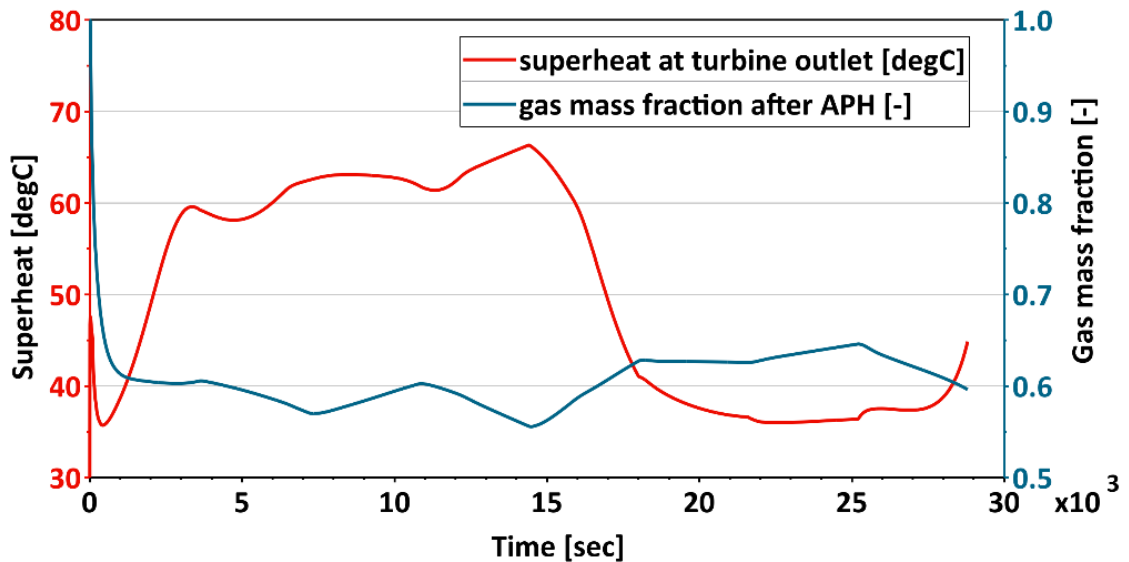


Figure 6-4: High effectiveness of an air pre-heater demonstrated for an APH-based cycle

Table 6.9: Material cost of the APH cycle after optimisation

S. No.	Component	Cost in Euros (€)
1	Pump	316.2
2	Boiler	17,521
3	Turbine	340.7
4	Condenser	53,172.1
5	Piping	6,500
6	Working fluid	10,461
7	APH	35,065

The regenerative APH and recuperative APH cycles showed the second- and third- lowest values of the objective function. Despite similar results, both configurations undertook a different approach. The regenerative APH cycle had a 6.7% lower SIC, as it undertook direct preheating of the working fluid and reduced heat exchanger cost. However, the working fluid used for preheating was not provided to the low-pressure turbine for power generation, the reduced mass flow rate dropping this configuration's power generation by 6.1%. In contrast, the entire mass of working fluid evaporated from the ORC boiler (in the case of the recuperative APH cycle), passed through the turbine, generating higher power output, while incurring additional heat exchanger cost. The total heat exchanger cost for the regenerative APH and recuperative APH cycles are given in Table 6.10.

Table 6.10: The total heat exchanger cost in Euros for the regenerative APH and recuperative APH cycles

S. No.	Heat exchanger	Regenerative APH cost in Euros (€)	Recuperative APH cost in Euros (€)
1	Boiler	17,997	17,925
2	Condenser	53,181	48,705
3	Regenerator	7,800	-
4	Recuperator	-	77,744
5	APH	56,627	41,503
	<b>Total</b>	<b>135,605</b>	<b>185,877</b>

Additionally, for the recuperative APH cycle, the optimal combination of 180 m<sup>2</sup> recuperator and 354m<sup>2</sup> APH was obtained at multiple control variables. Figure 6-5 shows the latent and sensible heat recovery undertaken by the recuperative APH cycle. It was observed that the optimised design of the counterflow recuperator allowed the preheated working fluid to enter the boiler at a mean temperature of 72°C; much higher than the exit temperature of the low-pressure working fluid (mean temperature 48.4°C), which left the recuperator in the saturated phase at 0.88 gas mass fraction. The wet fluid was further reduced to a mean gas mass fraction of 0.54 after the APH, demonstrating the effective recovery of waste heat by 85 kJ/kg, which allowed for a reduction in both the condenser size (from 180 to 137 m<sup>2</sup>) and cost by 24%, as shown in Table 6.10. The recovery of latent heat was possible due to the use of two heat exchangers at different pinch points. The lower condenser area offset the cost of the larger recuperator and APH, maintaining an SIC of 12,013 €/kW.

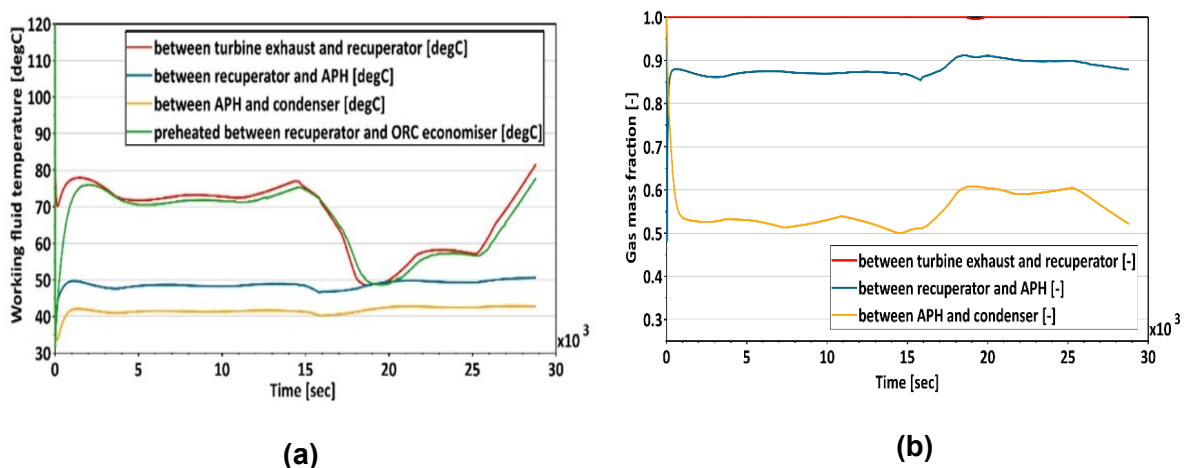


Figure 6-5: (a) Sensible heat recovery by the recuperative APH cycle; (b) Latent heat recovery using multiple pinch points and large heat exchangers

Whereas previous studies proposed the use of a dual-loop bottoming ORC, the direct use of industrial low-grade heat offered a simpler and more effective approach to minimise the irreversibility as reported by Feng et al. [322, 335-339]. In fact, the trade-off between recuperation by the ORC fluid and steam boiler APH is a strong function of the fuel prices and LCOE. Higher fuel prices tended towards greater thermal recuperation by the APH compared to the recuperator and vice-versa.

For the thermal and electrical energy prices considered by the investigated textile plant, recovering the ORC waste heat as thermal energy was more viable than a combination of thermal energy recovery by APH and electrical energy recovery by the recuperator. This raises the question of eliminating the ORC altogether and recovering all the internal energy for an APH. However, it has previously been concluded that increasing the temperature of the primary combustion air beyond 97°C has resulted in poor performance of steam boilers, as shown in Figure 6-6, as any additional thermal energy capture has been lost to flue gas [340].

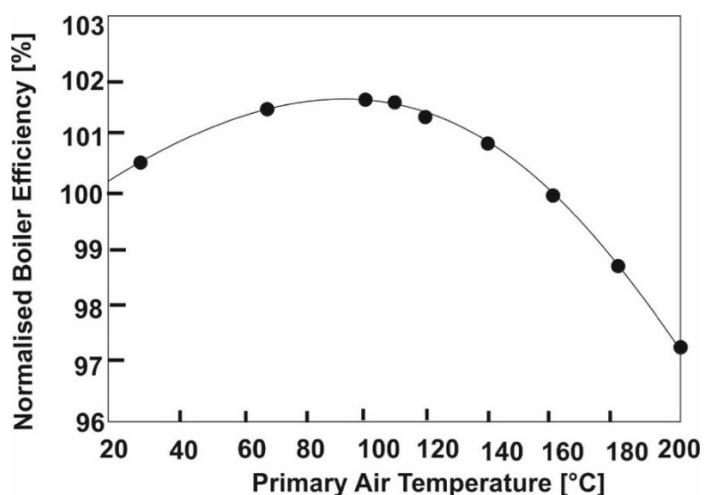


Figure 6-6: Peak boiler performance achieved with an air temperature of 97°C [37]

#### 6.3.4 Pump sizing

The regenerative APH cycle optimisation yielded the largest pump size, to compensate for the low mass flow rate of the LP turbine that led to poor isentropic efficiency due to increased secondary losses. Given that the work done was distributed across two turbines, the individual turbines were operating at mean pressure ratios of 3.2 and 2.61, lower than that of 7.88 in the conventional ORC with a single turbine configuration. In line with the findings in Chapter 4, this led to reduced turbine isentropic efficiency. Increasing the pump size led to an increased mass flow rate and pressure ratio across the turbines, as shown in Figure 6-7.

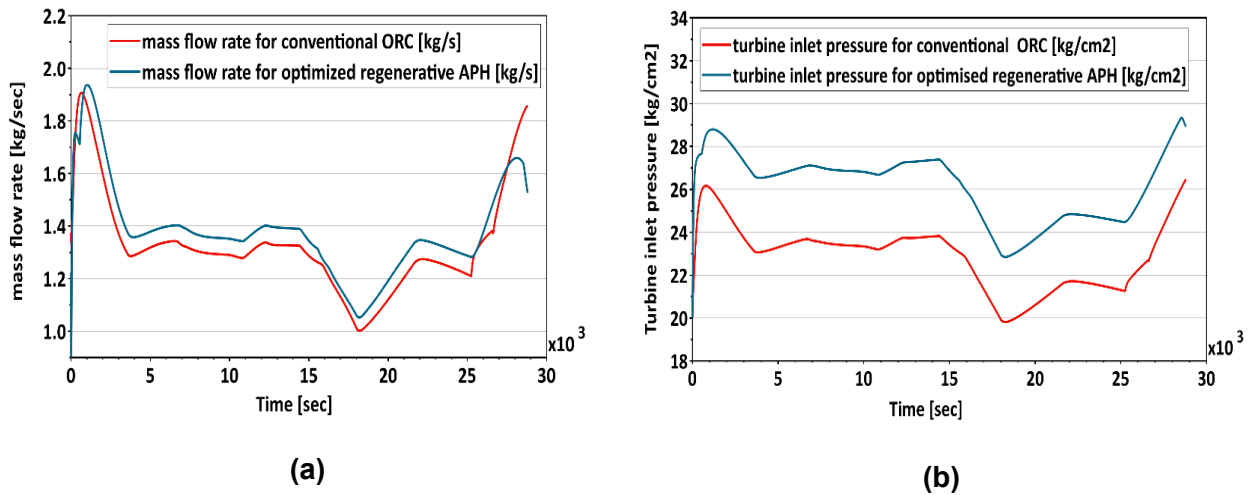


Figure 6-7: (a) Higher mass flow rate; (b) Higher turbine inlet pressure observed for a NLPQL-optimised regenerative APH cycle

### 6.3.5 Payback analysis

Table 6.11 shows payback values resulting from the NLPQL-optimised ORC with APH configuration, considering an interest rate of 8% per annum and annual maintenance cost of 1% of the capital cost [341]. Generally, ORCs do not require diversified manpower from the process industry viewpoint as it operates in a closed loop and is automatically controlled [296]. Five hours of weekly preventive maintenance have been considered, including the supervision and monitoring of the health check of the components equivalent to 30 €/hr for a single operator [49, 342, 343]. The analysis yielded a payback period of 1.72 years.

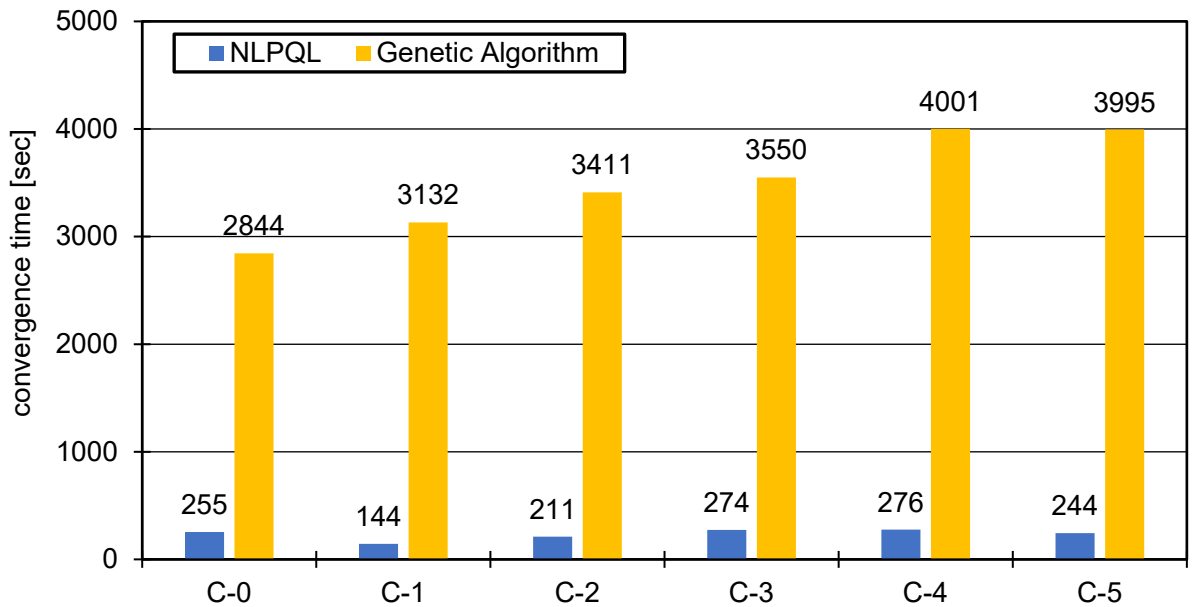
Table 6.11: Payback calculations for the most feasible ORC with APH combination

Expenditure			
Capital Cost			Annual
Pump	€	316	
Boiler	€	17,521	
Turbine	€	341	
Condenser	€	53,172	
APH	€	35,065	
Piping	€	6,500	
Working fluid	€	10,461	
Equipment cost- Total	€	123,376	
Labour cost for installation	€	3,7013	
Total capital cost	€	160,389	

<b>Operational cost</b>			
Manpower cost (260 hours, €30/hour)	€	30	7,800
Pump power consumption	€	6.78	54,240
Maintenance cost	€		1,233
Income			
Electrical	kW <sub>e</sub>	47.72	381,760
	€	8.59	68,717
Thermal	kW <sub>th</sub>	168.3	1,346,400
	€	8.82	70,551
Payback without interest	years	1.22	
Simple interest cost for payback duration @ 8% per annum	€		15,609
Payback with interest	years	1.72	

### 6.3.6 Optimiser comparison

Reflecting on the results, it emerges that using an NLPQL algorithm improved the objective function by up to 64%. Despite the localised approach of the NLPQL algorithm, the variation in the final values of objective function was within 3%, compared to the GA algorithm, which was more globalised, as shown in Table 6.6. This was attributed to the careful selection of initialisation values, building on the knowledge developed in Chapter 5. In line with previous findings, this study identified higher incidence of convergence issues when the NLPQL algorithm was operated with larger variations of independent variables. This was due to the NLPQL algorithm's dependence on the user-specified initialisation centre point and local search region; an issue that was overcome in this study by the use of parametrically pre-optimised data sets [258]. Figure 6-8 shows a comparison of the convergence time of the employed optimisers using the same computational capacity. In agreement with previous studies, the NLPQL algorithm approached optimal configurations with significantly less computational expense by one order of magnitude [258]. The results point towards consideration of this seldom-used optimiser for future studies of ORCs' techno-economic analysis.



Cycle name	Configuration	Cycle name	Configuration
C-0	Conventional	C-3	APH
C-1	Recuperative	C-4	Regenerative & thermal mass
C-2	Recuperative & APH	C-5	Regenerative & APH

Figure 6-8: Convergence time required for multi-objective optimisation

## 6.4 Conclusion

A new method of optimisation which employed a composite objective function that weighed the technical and economic aspects was developed. The composited objective function included contradicting objectives: minimise specific investment cost and maximise mean power generation. The following concludes the key finding of this chapter.

- Two different optimisation techniques were considered: mathematical and metaheuristics techniques. The thermo-economic optimisation study yielded a reduced heat exchanger size, particularly for heat exchangers where heat was rejected into the environment.
- The best cycle configurations were achieved when the low-grade energy rejected by the ORC was utilised, as it offset the additional capital expenditure of ORC itself. This waste heat could be undertaken for preheating ORC fluid or steam-boiler air.
- The optimised APH cycle achieved a 64.2% improvement in the value of the objective function, compared to the conventional ORC before optimisation and achieved a payback period of 1.72 years. The selection criterion pointed towards case-specific investigation that depended on the price of fuel and the levelised cost of electricity (LCOE).
- The NLPQL algorithm provided optimised solutions within 2% of that of the multi-objective genetic algorithm, proving its suitability for multi-objective ORC thermo-economic optimisation considering the computational cost and accuracy aspects, owing to fewer iterations aided by suitable initialisation.

# Chapter 7 Conclusions and Prospects

## 7.1 Introduction

Global warming remains the most pertinent threat for our planet. Despite significant strides in renewable energy, conventional sources form the backbone of the energy sector for most countries today. Biomass and coal-based steam boilers are widely used to meet the thermal energy demands of most industrial process plants for energy deficit developing countries like India. The flue gas stacks of these boilers represent a readily available, yet untapped waste heat source, despite their transient nature. Organic Rankine cycles represent an opportunity to reduce these stack losses, by generating renewable power, simultaneously reducing the heat expelled to the environment.

This thesis aimed to assess the optimum ORC turbine and cycle configurations to integrate this technology with the coal and emerging bioheat-driven steam boilers. The study centred around the inclusion of turbine efficiency, by utilising Craig and Cox and Soderberg loss models. Besides, Moustapha's off-design point loss model was incorporated to model incidence losses. The use of genetic algorithms coupled with artificial neural networks were explored for optimising the turbine's flow path geometry. Moreover, several cycle configurations were studied and optimised from the technical and economic viewpoints, providing varied electrical and thermal output. The study included a comparison between employing mathematical -based optimisers and well-proven metaheuristic optimisers, to evaluate their technical ability to perform computationally affordable multi-objective optimisation for ORC technoeconomic optimisation.

## 7.2 Conclusions

The following are the key objectives achieved and the conclusion of their outcomes:

**Objective 1:** *Comparing the axial ORC turbine's loss models and their suitability for cycle-level studies.*

The variations in turbine efficiency with the change of working fluid choice, pressure and temperature highlighted the importance of considering turbine efficiency as a part of the cycle-level study. Direct loss models were preferred as they are independent of working fluid. The Soderberg and Craig & Cox models were validated for 1-D modelling and simulation of a small-scale axial flow ORC turbine. Despite its simplicity, the Soderberg model demonstrated similar trends and deviation in isentropic efficiency was less than 2%. However, it did not provide a detailed break-up of individual losses, as was the case in Craig and Cox loss model; thus,

limiting its capability to preliminary cycle-level studies and rendering it unsuitable for turbine design and optimisation.

***Objective 2: Investigate the effect of fluid parameter changes on the turbine isentropic efficiency.***

The selection of working fluid provided the single largest flexibility of ORCs, which in turn demonstrated a significant influence on cycle design. Fluids with higher evaporation temperatures like R600 showed higher isentropic enthalpy drop and were characterised by lower molecular mass. The additional isentropic enthalpy drops in these fluids suggested better suitability for ORCs with multi-stage turbines, as the fluid velocities observed were 30% higher than high molecular mass fluids.

Increasing working fluid enthalpy by additional superheating contributed to higher turbine efficiency for most investigated organic fluids, despite increasing the Mach number loss and blade back radius ratio loss. In the case of R245fa, R1233zd(E) and R1234ze(Z), a 12.4% increase in isentropic efficiency was noted, which contributed to improved overall cycle efficiency. This proved that superheated ORC cycles could be more efficient, but need to consider the variations in turbine efficiency.

The impact of variable turbine efficiency was observed when the cycle pressure ratio increased. Higher pressure ratios led to an averaged 38% increase in turbine efficiency for R245fa, R1234ze(Z), R1234yf and R1234ze(E); this despite the significant increase in Mach-number-induced primary losses beyond 1.6 Mach number. The velocity of the working fluid at the moving blade exceeded Mach 2.1.

***Objective 3: Employ artificial intelligence coupled with evolutionary algorithms to optimise the ORC turbine design, aiming at maximum power generation.***

Given the increasing interest in utilising artificial intelligence in different fields, ANN deep learning was coupled with the genetic algorithm optimiser to optimise the turbine design. The ANN considered the variable turbine efficiency modelled by a direct turbine loss model. The optimisation led to 9.7% higher moving blade losses and reduced nozzle losses by 11.5%. Thus, an overall turbine total-to-static efficiency improvement of 5.2%, translating into a 0.24% improvement in cycle efficiency, quantifies the impact of turbine efficiency on the overall cycle performance. The deep learning approach offered a simple yet computationally efficient approach for optimising turbine flow path design, suitable for cycle design users with limited turbomachinery experience. High percentile results generated by ANNs prove its suitability for advanced blade design.

**Objective 4:** *Undertaking thermodynamic and thermo-economic optimisation of an ORC cycle configuration based on transient steam boiler flue gas stacks while considering variable turbine efficiency.*

Various cycle configurations were studied using the transient steam boiler waste heat source, including novel combinations of recuperators, regenerators, thermal storage mediums and steam boiler air preheaters. The recuperative cycle showed the highest mean power output, 15% greater than the conventional ORC.

Differences in turbine efficiency up to 7% was observed across multiple cycle configurations, highlighting the importance of considering a loss model rather than assuming a fixed isentropic efficiency. Regeneration-based ORC configurations suffered poor isentropic efficiency and a loss of mass flow of working fluid to the low-pressure turbine stage, resulting in poor cycle efficiency.

A novel configuration with integrated steam boiler air preheater was developed that recovered 195 kW<sub>th</sub> thermal energy. This configuration reduced the steam boiler's fossil fuel combustion by 1.9% and significantly reduced the ORC condenser heat load. The maximum condenser heat load was reduced by up to 65% for ORC with combined APH, recuperator, and regenerator, leading to lower evaporation loss. In addition, the recuperative-regenerative cycle produced the highest working fluid temperature, quantified by a 32% increase in the degree of superheat at turbine inlet, thus providing this configuration with better suitability to cycles with a high degree of heat source intermittency along with the use of wet fluids.

Thermo-economic optimisation suggested reducing heat exchanger size, particularly those where heat was rejected to the environment. As such, both optimisers concluded the ORC-APH configuration as the most suitable. This configuration achieved a 64.2% improvement of the objective function value over the conventional unoptimised ORC. The resulting payback period of 1.72 years indicated its economic feasibility. Moreover, the evaluation revealed that optimal configuration was a strong function of the local electricity and steam boiler fuel cost.

**Objective 5:** *Assessing the numerical and metaheuristic optimisers for single- and multi-objective optimisation employing a case study targeting maximum thermo-economic benefits.*

A single objective thermodynamic optimisation was undertaken between the mathematical-technique-based NLPQL algorithm and the metaheuristic genetic algorithm. The parametrically pre-optimised NLPQL algorithm demonstrated similar results along with significantly reduced computational cost, leading to faster convergence. The NLPQL-optimised recuperative cycle was noted as the optimal configuration, with a 26.5% increase in mean power generation compared to the 49.9 kW generated by the parametrically optimised conventional cycle. The optimised recuperative cycle also improved turbine isentropic efficiency by 12.57%, the highest of any cycle, yet again highlighting the importance of turbine

efficiency. The NLPQL optimiser's success and optimisation time were noted as a function of the initialisation midpoint. As a result, using a parametric or GA pre-optimiser to determine the preliminary design point within a wider search area, followed by NLPQL for a final localised study, can be recommended.

A multi-objective thermo-economic optimisation study was undertaken in Chapter 6 by applying a composited objective function with contrasting objectives using the parametrically pre-optimised multi-objective NLPQL and multi-objective Genetic Algorithm, to conclude the ORC with APH as the optimum thermos-economic configuration for the given case study. The multi-objective NLPQL algorithm provided optimised solutions within 2% of that of the MOGA, paving the way for its future use in computational economical multi-objective ORC thermo-economic optimisation.

### 7.3 Prospects

The following can be recommended for future work:

- Considering variable turbine efficiency using direct method-based approaches is advisable even for preliminary cycle-level design studies, particularly for superheated ORC cycles, where a simple correlation such as the Soderberg loss model can be used to observe trends. In addition, loss model validation is strongly suggested for profile validation with high-pressure ratio nozzles.
- The suitability of multi-stage turbines for high-pressure ratio cycles with low working fluid molecular mass requires further investigation, as such turbines are better suited to the higher enthalpy drops of such fluids but typically require larger volumetric flow rates. Development of high enthalpy low volumetric flow specific multi-stage ORC turbines incorporating partial admission, higher number of stages, reduced stage diameters and higher rotational speed promise superior isentropic efficiency and reduced windage losses and can lead to improved isentropic efficiency, even for small machines.
- The use of recent artificial intelligence-based techniques provides a user-friendly approach to turbine flow path loss and other technical optimisations. Such techniques can be used to develop a consolidated thermodynamic numerical tool incorporating optimised turbine and cycle efficiency optimised by Artificial intelligence (AI), allowing automated transient cycle optimisation for cycle-level studies. Generally, artificial intelligence in thermal and thermodynamic systems is still nascent and requires more research effort to extend it beyond the use of commercial tools such as ANN. This is timely with the worldwide effort to decarbonise the energy sector based on the huge data generated over the years.
- The air pre-heated ORC was noted as the optimum thermo-economic configuration, wherein the sizing of the heat exchangers was a function of the prevailing levelised cost of fuel and high levelised cost of electricity for the considered case study.

Variations in these indices could lead to changes in the thermal and electrical output for optimised cycles. Therefore, it is recommended to develop a combined fuel and electricity cost index-based algorithm for assessing the ideal boiler and APH sizing.

- Whereas the use of thermal mass did not improve power generation, its buffering properties were evident and could benefit future studies with higher transience of heat sources. They could be added to existing cycles to eliminate the ingress of wet fluid at the turbine inlet. Besides, further evidence-based analysis is needed for analysing the techno-economic feasibility of using low-cost sensible heat storage compared to emerging technologies such as phase change materials and sorption heat storages.

## References

- [1] N. S. Kardashev, "On the inevitability and the possible structures of supercivilizations," 1985, vol. 112: Cambridge University Press, pp. 497-504.
- [2] N. S. Kardashev, "Transmission of Information by Extraterrestrial Civilizations," *Soviet Astronomy*, vol. 8, p. 217, 1964.
- [3] M. Kaku, "The physics of interstellar travel: To one day, reach the stars," ed: Retrieved 2010-08-29, 2010.
- [4] S. Barca, "Energy, property, and the industrial revolution narrative," *Ecological Economics*, vol. 70, no. 7, pp. 1309-1315, 2011.
- [5] D. Anderson, "Energy and economic prosperity," *UNDP, World Energy Assessment. Energy and the Challenge of Sustainability*. New York: UNDP/UNDESA/WEC, pp394-413, 2000.
- [6] C. Sulzberger, "Thomas Edison's 1882 Pearl Street Generating Station," *IEEE Global History Network*, 2010.
- [7] Z. O. U. Caineng *et al.*, "Formation, distribution, potential and prediction of global conventional and unconventional hydrocarbon resources," *Petroleum Exploration and Development*, vol. 42, no. 1, pp. 14-28, 2015.
- [8] C. Zou, Q. Zhao, G. Zhang, and B. Xiong, "Energy revolution: From a fossil energy era to a new energy era," *Natural Gas Industry B*, vol. 3, no. 1, pp. 1-11, 2016/01/01/ 2016, doi: <https://doi.org/10.1016/j.ngib.2016.02.001>.
- [9] H. Khatib, "IEA world energy outlook 2011—A comment," *Energy policy*, vol. 48, pp. 737-743, 2012.
- [10] S. Pirani, *Burning up: A global history of fossil fuel consumption*. Pluto Press, 2018.
- [11] S. Jungcurt, "Global Energy Demand in 2018 Grew at Fastest Pace in a Decade," Retrieved from SDG Knowledge Hub: <https://sdq.iisd.org>, 2019.
- [12] N. Stern and C. Taylor, *What do the Appendices to the Copenhagen Accord tell us about global greenhouse gas emissions and the prospects for avoiding a rise in global average temperature of more than 2 C?* Centre for Climate Change Economics and Policy, 2010.
- [13] M. J. Rodwell *et al.*, "Characteristics of occasional poor medium-range weather forecasts for Europe," *Bulletin of the American Meteorological Society*, vol. 94, no. 9, pp. 1393-1405, 2013.
- [14] ed.
- [15] S. K. Jha, J. Bilalovic, A. Jha, N. Patel, and H. Zhang, "Renewable energy: Present research and future scope of Artificial Intelligence," *Renewable and Sustainable Energy Reviews*, vol. 77, pp. 297-317, 2017/09/01/ 2017, doi: <https://doi.org/10.1016/j.rser.2017.04.018>.
- [16] A. Evans, V. Strezov, and T. J. Evans, "Assessment of sustainability indicators for renewable energy technologies," *Renewable and Sustainable Energy Reviews*, vol. 13, no. 5, pp. 1082-1088, 2009/06/01/ 2009, doi: <https://doi.org/10.1016/j.rser.2008.03.008>.
- [17] N. Armaroli and V. Balzani, "The future of energy supply: challenges and opportunities," *Angewandte Chemie International Edition*, vol. 46, no. 1-2, pp. 52-66, 2007.
- [18] T. Tartière and M. Astolfi, "A world overview of the organic Rankine cycle market," *Energy Procedia*, vol. 129, pp. 2-9, 2017.
- [19] N. Abas, A. Kalair, and N. Khan, "Review of fossil fuels and future energy technologies," *Futures*, vol. 69, pp. 31-49, 2015.
- [20] H. Muraoka, "Geothermal Energy," in *Handbook of Climate Change Mitigation*: Springer, 2012, pp. 1325-1353.

- [21] E. Macchi and M. Astolfi, *Organic rankine cycle (ORC) power systems: Technologies and applications*. Woodhead Publishing, 2016.
- [22] C. M. Invernizzi, "Closed power cycles," *Lecture Notes in Energy*, vol. 11, 2013.
- [23] D. Dragomir-Stanciu and C. Luca, "Solar Power Generation System with Low Temperature Heat Storage," *Procedia Technology*, vol. 22, pp. 848-853, 2016.
- [24] L. Y. Bronicki, "History of Organic Rankine Cycle systems," in *Organic Rankine Cycle (ORC) Power Systems*: Elsevier, 2017, pp. 25-66.
- [25] C. M. Invernizzi, "The Organic Rankine Cycle," in *Closed Power Cycles*: Springer, 2013, pp. 117-175.
- [26] H. Tabor, S. Schweitzer, and S. Sargent, "SOLAR POND RESEARCH AND DEVELOPMENT," in *Energy, Resources and Environment*: Elsevier, 1982, pp. 492-499.
- [27] H. Tabor and L. Bronicki, "Establishing criteria for fluids for small vapor turbines," *SAE Transactions*, pp. 561-575, 1965.
- [28] L. Zanellato, M. Astolfi, A. Serafino, D. Rizzi, and E. Macchi, "Field performance evaluation of geothermal ORC power plants with a focus on radial outflow turbines," *Renewable Energy*, 2018.
- [29] M. Astolfi *et al.*, "Testing of a new supercritical ORC technology for efficient power generation from geothermal low temperature resources," 2013.
- [30] G. Qiu, Y. Shao, J. Li, H. Liu, and S. B. Riffat, "Experimental investigation of a biomass-fired ORC-based micro-CHP for domestic applications," *Fuel*, vol. 96, pp. 374-382, 2012/06/01/ 2012, doi: <https://doi.org/10.1016/j.fuel.2012.01.028>.
- [31] U. Drescher and D. Brüggemann, "Fluid selection for the Organic Rankine Cycle (ORC) in biomass power and heat plants," *Applied Thermal Engineering*, vol. 27, no. 1, pp. 223-228, 2007/01/01/ 2007, doi: <https://doi.org/10.1016/j.applthermaleng.2006.04.024>.
- [32] M. Preißinger, F. Heberle, and D. Brüggemann, "Thermodynamic analysis of double-stage biomass fired Organic Rankine Cycle for micro-cogeneration," *International Journal of Energy Research*, vol. 36, no. 8, pp. 944-952, 2012.
- [33] M. Tańczuk and R. Ulbrich, "Implementation of a biomass-fired co-generation plant supplied with an ORC (Organic Rankine Cycle) as a heat source for small scale heat distribution system – A comparative analysis under Polish and German conditions," *Energy*, vol. 62, pp. 132-141, 2013/12/01/ 2013, doi: <https://doi.org/10.1016/j.energy.2013.09.044>.
- [34] M. A. Al-Weshahi, F. Latrash, A. Anderson, and B. Agnew, "Working fluid selection of low grade heat geothermal Organic Rankine Cycle (ORC)," *International Journal of Thermal Technologies*, vol. 4, no. 1, 2014.
- [35] E. Barbier, "Nature and technology of geothermal energy: A review," *Renewable and Sustainable Energy Reviews*, vol. 1, no. 1, pp. 1-69, 1997/03/01/ 1997, doi: [https://doi.org/10.1016/S1364-0321\(97\)00001-4](https://doi.org/10.1016/S1364-0321(97)00001-4).
- [36] R. DiPippo, *Geothermal power plants: principles, applications, case studies and environmental impact*. Butterworth-Heinemann, 2012.
- [37] F. Heberle, M. Preißinger, and D. Brüggemann, "Zeotropic mixtures as working fluids in Organic Rankine Cycles for low-enthalpy geothermal resources," *Renewable Energy*, vol. 37, no. 1, pp. 364-370, 2012/01/01/ 2012, doi: <https://doi.org/10.1016/j.renene.2011.06.044>.
- [38] H. D. Madhawa Hettiarachchi, M. Golubovic, W. M. Worek, and Y. Ikegami, "Optimum design criteria for an Organic Rankine cycle using low-temperature geothermal heat sources," *Energy*, vol. 32, no. 9, pp. 1698-1706, 2007/09/01/ 2007, doi: <https://doi.org/10.1016/j.energy.2007.01.005>.

- [39] M. Preißinger, F. Heberle, and D. Brüggemann, "Advanced organic rankine cycle for geothermal application," *International Journal of Low-Carbon Technologies*, vol. 8, no. suppl\_1, pp. i62-i68, 2013.
- [40] H. Zhai, L. Shi, and Q. An, "Influence of working fluid properties on system performance and screen evaluation indicators for geothermal ORC (organic Rankine cycle) system," *Energy*, vol. 74, pp. 2-11, 2014/09/01/ 2014, doi: <https://doi.org/10.1016/j.energy.2013.12.030>.
- [41] H. Uehara, C. O. Dilao, and T. Nakaoka, "Conceptual design of ocean thermal energy conversion (OTEC) power plants in the Philippines," *Solar energy*, vol. 41, no. 5, pp. 431-441, 1988.
- [42] R. Rayegan and Y. X. Tao, "A procedure to select working fluids for Solar Organic Rankine Cycles (ORCs)," *Renewable Energy*, vol. 36, no. 2, pp. 659-670, 2011/02/01/ 2011, doi: <https://doi.org/10.1016/j.renene.2010.07.010>.
- [43] B. F. Tchanche, G. Papadakis, G. Lambrinos, and A. Frangoudakis, "Fluid selection for a low-temperature solar organic Rankine cycle," *Applied Thermal Engineering*, vol. 29, no. 11-12, pp. 2468-2476, 2009.
- [44] M. Villarini, E. Bocci, M. Moneti, A. Di Carlo, and A. Micangeli, "State of art of small scale solar powered ORC systems: a review of the different typologies and technology perspectives," *Energy Procedia*, vol. 45, pp. 257-267, 2014.
- [45] V. R. Patil, V. I. Biradar, R. Shreyas, P. Garg, M. S. Orosz, and N. C. Thirumalai, "Techno-economic comparison of solar organic Rankine cycle (ORC) and photovoltaic (PV) systems with energy storage," *Renewable energy*, vol. 113, pp. 1250-1260, 2017.
- [46] L. Tocci, T. Pal, I. Pasmazoglou, and B. Franchetti, "Small scale Organic Rankine Cycle (ORC): A techno-economic review," *Energies*, vol. 10, no. 4, p. 413, 2017.
- [47] F. Alshammari, A. Karvountzis-Kontakiotis, A. Pesiridis, and T. Minton, "Radial expander design for an engine organic Rankine cycle waste heat recovery system," *Energy Procedia*, vol. 129, pp. 285-292, 2017.
- [48] P. S. Bundela and C. Vivek, "Sustainable development through waste heat recovery," *American Journal of Environmental Sciences*, vol. 6, no. 1, pp. 83-89, 2010.
- [49] F. Campana *et al.*, "ORC waste heat recovery in European energy intensive industries: Energy and GHG savings," *Energy Conversion and Management*, vol. 76, pp. 244-252, 2013.
- [50] Y. Chen, P. Lundqvist, A. Johansson, and P. Platell, "A comparative study of the carbon dioxide transcritical power cycle compared with an organic Rankine cycle with R123 as working fluid in waste heat recovery," *Applied thermal engineering*, vol. 26, no. 17-18, pp. 2142-2147, 2006.
- [51] Y. Dai, J. Wang, and L. Gao, "Parametric optimization and comparative study of organic Rankine cycle (ORC) for low grade waste heat recovery," *Energy Conversion and Management*, vol. 50, no. 3, pp. 576-582, 2009/03/01/ 2009, doi: <https://doi.org/10.1016/j.enconman.2008.10.018>.
- [52] D. Di Battista, M. Di Bartolomeo, C. Villante, and R. Cipollone, "On the limiting factors of the waste heat recovery via ORC-based power units for on-the-road transportation sector," *Energy Conversion and Management*, vol. 155, pp. 68-77, 2018/01/01/ 2018, doi: <https://doi.org/10.1016/j.enconman.2017.10.091>.
- [53] T. C. Hung, T. Y. Shai, and S. K. Wang, "A review of organic rankine cycles (ORCs) for the recovery of low-grade waste heat," *Energy*, vol. 22, no. 7, pp. 661-667, 1997/07/01/ 1997, doi: [https://doi.org/10.1016/S0360-5442\(96\)00165-X](https://doi.org/10.1016/S0360-5442(96)00165-X).
- [54] M. Imran, B.-S. Park, H.-J. Kim, D.-H. Lee, and M. Usman, "Economic assessment of greenhouse gas reduction through low-grade waste heat recovery using organic Rankine cycle (ORC)," *Journal of Mechanical Science and Technology*, vol. 29, no. 2, pp. 835-843, 2015.

- [55] M. Imran, M. Usman, B.-S. Park, and D.-H. Lee, "Volumetric expanders for low grade heat and waste heat recovery applications," *Renewable and Sustainable Energy Reviews*, vol. 57, pp. 1090-1109, 2016/05/01/ 2016, doi: <https://doi.org/10.1016/j.rser.2015.12.139>.
- [56] H. Jouhara, N. Khordehgah, S. Almahmoud, B. Delpech, A. Chauhan, and S. A. Tassou, "Waste heat recovery technologies and applications," *Thermal Science and Engineering Progress*, vol. 6, pp. 268-289, 2018/06/01/ 2018, doi: <https://doi.org/10.1016/j.tsep.2018.04.017>.
- [57] A. A. Lakew and O. Bolland, "Working fluids for low-temperature heat source," *Applied Thermal Engineering*, vol. 30, no. 10, pp. 1262-1268, 2010/07/01/ 2010, doi: <https://doi.org/10.1016/j.applthermaleng.2010.02.009>.
- [58] S. Lecompte, H. Huisseune, M. Van Den Broek, B. Vanslambrouck, and M. De Paepe, "Review of organic Rankine cycle (ORC) architectures for waste heat recovery," *Renewable and sustainable energy reviews*, vol. 47, pp. 448-461, 2015.
- [59] S. Lion, C. N. Michos, I. Vlaskos, C. Rouaud, and R. Tacconi, "A review of waste heat recovery and Organic Rankine Cycles (ORC) in on-off highway vehicle Heavy Duty Diesel Engine applications," *Renewable and Sustainable Energy Reviews*, vol. 79, pp. 691-708, 2017.
- [60] V. Maizza and A. Maizza, "Unconventional working fluids in organic Rankine-cycles for waste energy recovery systems," *Applied Thermal Engineering*, vol. 21, no. 3, pp. 381-390, 2001/02/01/ 2001, doi: [https://doi.org/10.1016/S1359-4311\(00\)00044-2](https://doi.org/10.1016/S1359-4311(00)00044-2).
- [61] U. Muhammad, M. Imran, D. H. Lee, and B. S. Park, "Design and experimental investigation of a 1 kW organic Rankine cycle system using R245fa as working fluid for low-grade waste heat recovery from steam," *Energy Conversion and Management*, vol. 103, pp. 1089-1100, 2015.
- [62] S. Quoilin, S. Declaye, B. F. Tchanche, and V. Lemort, "Thermo-economic optimization of waste heat recovery Organic Rankine Cycles," *Applied thermal engineering*, vol. 31, no. 14-15, pp. 2885-2893, 2011.
- [63] J. P. Roy, M. K. Mishra, and A. Misra, "Parametric optimization and performance analysis of a waste heat recovery system using Organic Rankine Cycle," *Energy*, vol. 35, no. 12, pp. 5049-5062, 2010.
- [64] G. Shu, L. Shi, H. Tian, X. Li, G. Huang, and L. Chang, *An improved CO<sub>2</sub>-based transcritical Rankine cycle (CTRC) used for engine waste heat recovery*. 2016, pp. 171-182.
- [65] K. K. Srinivasan, P. J. Mago, and S. R. Krishnan, "Analysis of exhaust waste heat recovery from a dual fuel low temperature combustion engine using an Organic Rankine Cycle," *Energy*, vol. 35, no. 6, pp. 2387-2399, 2010.
- [66] H. Tian, G. Shu, H. Wei, X. Liang, and L. Liu, "Fluids and parameters optimization for the organic Rankine cycles (ORCs) used in exhaust heat recovery of Internal Combustion Engine (ICE)," *Energy*, vol. 47, no. 1, pp. 125-136, 2012/11/01/ 2012, doi: <https://doi.org/10.1016/j.energy.2012.09.021>.
- [67] E. H. Wang, H. G. Zhang, B. Y. Fan, M. G. Ouyang, Y. Zhao, and Q. H. Mu, "Study of working fluid selection of organic Rankine cycle (ORC) for engine waste heat recovery," *Energy*, vol. 36, no. 5, pp. 3406-3418, 2011/05/01/ 2011, doi: <https://doi.org/10.1016/j.energy.2011.03.041>.
- [68] C. Wang *et al.*, "Application of a low pressure economizer for waste heat recovery from the exhaust flue gas in a 600 MW power plant," *Energy*, vol. 48, no. 1, pp. 196-202, 2012.
- [69] M. T. White, O. A. Oyewunmi, A. J. Haslam, and C. N. Markides, "Industrial waste-heat recovery through integrated computer-aided working-fluid and ORC system

- optimisation using SAFT- $\gamma$  Mie," *Energy Conversion and Management*, vol. 150, pp. 851-869, 2017.
- [70] H. Xi, M.-J. Li, C. Xu, and Y.-L. He, "Parametric optimization of regenerative organic Rankine cycle (ORC) for low grade waste heat recovery using genetic algorithm," *Energy*, vol. 58, pp. 473-482, 2013/09/01/ 2013, doi: <https://doi.org/10.1016/j.energy.2013.06.039>.
- [71] P. Ziółkowski, T. Kowalczyk, S. Kornet, and J. Badur, "On low-grade waste heat utilization from a supercritical steam power plant using an ORC-bottoming cycle coupled with two sources of heat," *Energy Conversion and Management*, vol. 146, pp. 158-173, 2017/08/15/ 2017, doi: <https://doi.org/10.1016/j.enconman.2017.05.028>.
- [72] D. Ziviani, R. Dickes, S. Quoilin, V. Lemort, M. De Paepe, and M. van den Broek, "Organic Rankine cycle modelling and the ORCmKit library: analysis of R1234ze (Z) as drop-in replacement of R245fa for low-grade waste heat recovery," 2016, pp. 1-13.
- [73] Y. Zhao, G. Liu, L. Li, Q. Yang, B. Tang, and Y. Liu, "Expansion devices for organic Rankine cycle (ORC) using in low temperature heat recovery: A review," *Energy Conversion and Management*, vol. 199, p. 111944, 2019.
- [74] W. G. Chapman, K. E. Gubbins, G. Jackson, and M. Radosz, "SAFT: Equation-of-state solution model for associating fluids," *Fluid Phase Equilibria*, vol. 52, pp. 31-38, 1989/12/01/ 1989, doi: [https://doi.org/10.1016/0378-3812\(89\)80308-5](https://doi.org/10.1016/0378-3812(89)80308-5).
- [75] P. Perrot, *A to Z of Thermodynamics*. Oxford University Press on Demand, 1998.
- [76] R. Brignoli and J. S. Brown, "Organic Rankine cycle model for well-described and not-so-well-described working fluids," *Energy*, vol. 86, pp. 93-104, 2015.
- [77] J. S. Brown, "Predicting performance of refrigerants using the Peng–Robinson Equation of State," *International Journal of Refrigeration*, vol. 30, no. 8, pp. 1319-1328, 2007.
- [78] W. Su, L. Zhao, and S. Deng, "Developing a performance evaluation model of organic Rankine cycle for working fluids based on the group contribution method," *Energy Conversion and Management*, vol. 132, pp. 307-315, 2017.
- [79] D.-Y. Peng and D. B. Robinson, "A new two-constant equation of state," *Industrial & Engineering Chemistry Fundamentals*, vol. 15, no. 1, pp. 59-64, 1976.
- [80] G. Soave, "Equilibrium constants from a modified Redlich-Kwong equation of state," *Chemical engineering science*, vol. 27, no. 6, pp. 1197-1203, 1972.
- [81] M. T. White and A. I. Sayma, "Simultaneous cycle optimisation and fluid selection for ORC systems accounting for the effect of the operating conditions on turbine efficiency," *Frontiers in Energy Research*, vol. 7, p. 50, 2019.
- [82] P. Donnez, *Essentials of reservoir engineering*. Editions Technip, 2012.
- [83] M. T. White and A. I. Sayma, "A generalised assessment of working fluids and radial turbines for non-recuperated subcritical organic rankine cycles," *Energies*, vol. 11, no. 4, p. 800, 2018.
- [84] E. W. Lemmon, M. L. Huber, and M. O. McLinden, "NIST reference fluid thermodynamic and transport properties–REFPROP," *NIST standard reference database*, vol. 23, p. v7, 2002.
- [85] B.-S. Park, M. Usman, M. Imran, and A. Pesyridis, "Review of Organic Rankine Cycle experimental data trends," *Energy conversion and management*, vol. 173, pp. 679-691, 2018.
- [86] S. Quoilin, M. Van Den Broek, S. Declaye, P. Dewallef, and V. Lemort, "Techno-economic survey of Organic Rankine Cycle (ORC) systems," *Renewable and Sustainable Energy Reviews*, vol. 22, pp. 168-186, 2013.

- [87] L. Liu, Q. Yang, and G. Cui, "Supercritical Carbon Dioxide (s-CO<sub>2</sub>) Power Cycle for Waste Heat Recovery: A Review from Thermodynamic Perspective," *Processes*, vol. 8, no. 11, p. 1461, 2020.
- [88] A. Bahadori, "Estimation of combustion flue gas acid dew point during heat recovery and efficiency gain," *Applied Thermal Engineering*, vol. 31, no. 8-9, pp. 1457-1462, 2011.
- [89] J. Bao and L. Zhao, "A review of working fluid and expander selections for organic Rankine cycle," *Renewable and Sustainable Energy Reviews*, vol. 24, pp. 325-342, 2013/08/01/ 2013, doi: <https://doi.org/10.1016/j.rser.2013.03.040>.
- [90] R. Chacartegui, D. Sánchez, J. M. Muñoz, and T. Sánchez, "Alternative ORC bottoming cycles FOR combined cycle power plants," *Applied Energy*, vol. 86, no. 10, pp. 2162-2170, 2009/10/01/ 2009, doi: <https://doi.org/10.1016/j.apenergy.2009.02.016>.
- [91] A. F. Babatunde and O. O. Sunday, "A Review of Working Fluids for Organic Rankine Cycle (ORC) Applications," *Mater. Sci. Eng.*, vol. 413, p. 012019, 2018.
- [92] O. Boydak, I. Ekmekci, M. Yilmaz, and H. Koten, "Thermodynamic investigation of organic Rankine cycle energy recovery system and recent studies," *Thermal Science*, vol. 22, no. 6 Part A, pp. 2679-2690, 2018.
- [93] A. Rettig *et al.*, "Application of organic Rankine cycles (ORC)," 2011, pp. 1-10.
- [94] Z. Gu and H. Sato, "Performance of supercritical cycles for geothermal binary design," *Energy Conversion and management*, vol. 43, no. 7, pp. 961-971, 2002.
- [95] A. Franco and M. Villani, "Optimal design of binary cycle power plants for water-dominated, medium-temperature geothermal fields," *Geothermics*, vol. 38, no. 4, pp. 379-391, 2009.
- [96] S. Van Loo and J. Koppejan, *The handbook of biomass combustion and co-firing*. Earthscan, 2012.
- [97] S. K. Ray and G. Moss, "Fluorochemicals as working fluids for small rankine cycle power units," *Advanced Energy Conversion*, vol. 6, no. 2, pp. 89-102, 1966/04/01/ 1966, doi: [https://doi.org/10.1016/0365-1789\(66\)90003-8](https://doi.org/10.1016/0365-1789(66)90003-8).
- [98] H. Zhai, Q. An, L. Shi, V. Lemort, and S. Quoilin, "Categorization and analysis of heat sources for organic Rankine cycle systems," *Renewable and Sustainable Energy Reviews*, vol. 64, pp. 790-805, 2016.
- [99] T. Z. Kaczmarczyk, G. Zywica, and E. Ihnatowicz, "Experimental investigation of a radial microturbine in organic Rankine cycle system with HFE7100 as working fluid," 2015, pp. 12-14.
- [100] J. Mascuch, V. Novotny, V. Vodicka, J. Spale, and Z. Zeleny, "Experimental development of a kilowatt-scale biomass fired micro-CHP unit based on ORC with rotary vane expander," *Renewable Energy*, vol. 147, pp. 2882-2895, 2020.
- [101] G. Carraro, V. Bori, A. Lazzaretto, G. Toniato, and P. Danieli, "Experimental investigation of an innovative biomass-fired micro-ORC system for cogeneration applications," *Renewable Energy*, vol. 161, pp. 1226-1243, 2020.
- [102] R. Rayegan and Y. X. Tao, "A critical review on single component working fluids for Organic Rankine Cycles (ORCs)," *ASME Early Career Tech. J.*, vol. 8, no. 1, pp. 20-1, 2009.
- [103] Ž. Jesko, "Classification of solar collectors," *rN*, vol. 1, no. 21, p. 21, 2008.
- [104] S. Loeb and G. D. Mehta, "Solar collection system," ed: Google Patents, 1981.
- [105] S. Lakhani, A. Raul, and S. K. Saha, "Dynamic modelling of ORC-based solar thermal power plant integrated with multitube shell and tube latent heat thermal storage system," *Applied Thermal Engineering*, vol. 123, pp. 458-470, 2017.
- [106] J. C. Bruno, J. López-Villada, E. Letelier, S. Romera, and A. Coronas, "Modelling and optimisation of solar organic rankine cycle engines for reverse osmosis desalination,"

- Applied Thermal Engineering*, vol. 28, no. 17, pp. 2212-2226, 2008/12/01/ 2008, doi: <https://doi.org/10.1016/j.applthermaleng.2007.12.022>.
- [107] D. Manolakos, E. S. Mohamed, I. Karagiannis, and G. Papadakis, "Technical and economic comparison between PV-RO system and RO-Solar Rankine system. Case study: Thirasia island," *Desalination*, vol. 221, no. 1, pp. 37-46, 2008/03/01/ 2008, doi: <https://doi.org/10.1016/j.desal.2007.01.066>.
- [108] C. Forman, I. K. Muritala, R. Pardemann, and B. Meyer, "Estimating the global waste heat potential," *Renewable and Sustainable Energy Reviews*, vol. 57, pp. 1568-1579, 2016/05/01/ 2016, doi: <https://doi.org/10.1016/j.rser.2015.12.192>.
- [109] C. Haddad, C. Périlhon, A. Danlos, M.-X. François, and G. Descombes, "Some Efficient Solutions to Recover Low and Medium Waste Heat: Competitiveness of the Thermoacoustic Technology," *Energy Procedia*, vol. 50, pp. 1056-1069, 2014/01/01/ 2014, doi: <https://doi.org/10.1016/j.egypro.2014.06.125>.
- [110] S. Krishnan and A. Jothibasu, *An Ideal Combined Heat and Power System for the Mitigation of Fossil Fuel for Power Generation*. 2015.
- [111] C. Carcasci, R. Ferraro, and E. Miliotti, "Thermodynamic analysis of an organic Rankine cycle for waste heat recovery from gas turbines," *Energy*, vol. 65, pp. 91-100, 2014/02/01/ 2014, doi: <https://doi.org/10.1016/j.energy.2013.11.080>.
- [112] H. Legmann, "Recovery of industrial heat in the cement industry by means of the ORC process," 2002: IEEE, pp. 29-35.
- [113] S. Lecompte *et al.*, "Case study of an organic Rankine cycle (ORC) for waste heat recovery from an electric arc furnace (EAF)," *Energies*, vol. 10, no. 5, p. 649, 2017.
- [114] M. Mirzaei, M. H. Ahmadi, M. Mobin, M. A. Nazari, and R. Alayi, "Energy, exergy and economics analysis of an ORC working with several fluids and utilizes smelting furnace gases as heat source," *Thermal Science and Engineering Progress*, vol. 5, pp. 230-237, 2018/03/01/ 2018, doi: <https://doi.org/10.1016/j.tsep.2017.11.011>.
- [115] A. Bejan and A. D. Kraus, *Heat transfer handbook*. John Wiley & Sons, 2003.
- [116] C. Ma, X. Chen, J. Wang, S. Zang, and Y. Ji, "An experimental investigation of heat transfer characteristics for steam cooling and air cooling in a rectangular channel roughened with parallel ribs," *Experimental Thermal and Fluid Science*, vol. 64, pp. 142-151, 2015/06/01/ 2015, doi: <https://doi.org/10.1016/j.expthermflusci.2015.02.009>.
- [117] M. Kanoglu and I. Dincer, "Performance assessment of cogeneration plants," *energy conversion and management*, vol. 50, no. 1, pp. 76-81, 2009.
- [118] H. Holmberg, M. Tuomaala, T. Haikonen, and P. Ahtila, "Allocation of fuel costs and CO<sub>2</sub>-emissions to heat and power in an industrial CHP plant: Case integrated pulp and paper mill," *Applied Energy*, vol. 93, pp. 614-623, 2012/05/01/ 2012, doi: <https://doi.org/10.1016/j.apenergy.2011.11.040>.
- [119] T. Bause, F. Campana, L. Filippini, A. Foresti, N. Monti, and T. Pelz, "Cogeneration with ORC at elbe-stahlwerke feralpi EAF shop," 2014, pp. 5-8.
- [120] O. V. Inshakov, L. Y. Bogachkova, and E. G. Popkova, "The transformation of the global energy markets and the problem of ensuring the sustainability of their development," in *Energy Sector: A Systemic Analysis of Economy, Foreign Trade and Legal Regulations*: Springer, 2019, pp. 135-148.
- [121] Z. Gao *et al.*, "The evaluation of developing vehicle technologies on the fuel economy of long-haul trucks," *Energy Conversion and Management*, vol. 106, pp. 766-781, 2015.
- [122] E. Doyle, L. DiNanno, and S. Kramer, "Installation of a diesel-organic Rankine compound engine in a class 8 truck for a single-vehicle test," SAE Technical Paper, 0148-7191, 1979.

- [123] R. Singh and O. Singh, "Comparative study of combined solid oxide fuel cell-gas turbine-Organic Rankine cycle for different working fluid in bottoming cycle," *Energy Conversion and Management*, vol. 171, pp. 659-670, 2018/09/01/ 2018, doi: <https://doi.org/10.1016/j.enconman.2018.06.009>.
- [124] J. Song, X.-s. Li, X.-d. Ren, and C.-w. Gu, "Performance analysis and parametric optimization of supercritical carbon dioxide (S-CO<sub>2</sub>) cycle with bottoming Organic Rankine Cycle (ORC)," *Energy*, vol. 143, pp. 406-416, 2018/01/15/ 2018, doi: <https://doi.org/10.1016/j.energy.2017.10.136>.
- [125] R. Van den Broek, A. Faaij, and A. van Wijk, "Biomass combustion for power generation," *Biomass and Bioenergy*, vol. 11, no. 4, pp. 271-281, 1996.
- [126] B. Matofska, "What is the sharing economy," *The people who share*, 2016.
- [127] W. Rached, "Hydrofluoroolefin compositions," ed: Google Patents, 2011.
- [128] J. A. White and S. Velasco, "Characterizing wet and dry fluids in temperature-entropy diagrams," *Energy*, vol. 154, pp. 269-276, 2018/07/01/ 2018, doi: <https://doi.org/10.1016/j.energy.2018.04.105>.
- [129] E. Macchi, "The choice of working fluid: the most important step for a successful organic Rankine cycle (and an efficient turbine)," 2013, pp. 7-8.
- [130] S. H. Kang, "Design and experimental study of ORC (organic Rankine cycle) and radial turbine using R245fa working fluid," *Energy*, vol. 41, no. 1, pp. 514-524, 2012/05/01/ 2012, doi: <https://doi.org/10.1016/j.energy.2012.02.035>.
- [131] J. Song, C.-w. Gu, and X. Ren, "Influence of the radial-inflow turbine efficiency prediction on the design and analysis of the Organic Rankine Cycle (ORC) system," *Energy Conversion and Management*, vol. 123, pp. 308-316, 2016/09/01/ 2016, doi: <https://doi.org/10.1016/j.enconman.2016.06.037>.
- [132] K. A. Barse and M. D. Mann, "Maximizing ORC performance with optimal match of working fluid with system design," *Applied Thermal Engineering*, vol. 100, pp. 11-19, 2016/05/05/ 2016, doi: <https://doi.org/10.1016/j.applthermaleng.2016.01.167>.
- [133] A. Meroni, J. G. Andreasen, G. Persico, and F. Haglind, "Optimization of organic Rankine cycle power systems considering multistage axial turbine design," *Applied Energy*, vol. 209, pp. 339-354, 2018/01/01/ 2018, doi: <https://doi.org/10.1016/j.apenergy.2017.09.068>.
- [134] S. Quoilin, S. Declaye, A. Legros, L. Guillaume, and V. Lemort, "Working fluid selection and operating maps for Organic Rankine Cycle expansion machines," 2012, p. 10.
- [135] A. I. Papadopoulos, M. Stijepovic, and P. Linke, "On the systematic design and selection of optimal working fluids for Organic Rankine Cycles," *Applied Thermal Engineering*, vol. 30, no. 6, pp. 760-769, 2010/05/01/ 2010, doi: <https://doi.org/10.1016/j.applthermaleng.2009.12.006>.
- [136] V. Lemort, S. Declaye, and S. Quoilin, "Experimental characterization of a hermetic scroll expander for use in a micro-scale Rankine cycle," (in English), *Proceedings of the Institution of Mechanical Engineers Part a-Journal of Power and Energy*, Article vol. 226, no. A1, pp. 126-136, 2012, doi: 10.1177/0957650911413840.
- [137] M. Mohanraj, S. Jayaraj, and C. Muraleedharan, "Environment friendly alternatives to halogenated refrigerants—A review," *International Journal of Greenhouse Gas Control*, vol. 3, no. 1, pp. 108-119, 2009/01/01/ 2009, doi: <https://doi.org/10.1016/j.ijggc.2008.07.003>.
- [138] B. Saleh, G. Koglbauer, M. Wendland, and J. Fischer, "Working fluids for low-temperature organic Rankine cycles," *Energy*, vol. 32, no. 7, pp. 1210-1221, 2007/07/01/ 2007, doi: <https://doi.org/10.1016/j.energy.2006.07.001>.
- [139] M. Santos, J. André, E. Costa, R. Mendes, and J. Ribeiro, "Design strategy for component and working fluid selection in a domestic micro-CHP ORC boiler," *Applied*

*Thermal Engineering*, vol. 169, p. 114945, 2020/03/25/ 2020, doi:

<https://doi.org/10.1016/j.applthermaleng.2020.114945>.

- [140] R. L. McKenzie, P. J. Aucamp, A. F. Bais, L. O. Björn, M. Ilyas, and S. Madronich, "Ozone depletion and climate change: impacts on UV radiation," *Photochemical & Photobiological Sciences*, vol. 10, no. 2, pp. 182-198, 2011.
- [141] G. Qiu, "Selection of working fluids for micro-CHP systems with ORC," *Renewable Energy*, vol. 48, pp. 565-570, 2012.
- [142] A. R. Ravishankara, J. S. Daniel, and R. W. Portmann, "Nitrous oxide (N<sub>2</sub>O): the dominant ozone-depleting substance emitted in the 21st century," *science*, vol. 326, no. 5949, pp. 123-125, 2009.
- [143] B. Xiang *et al.*, "Global emissions of refrigerants HCFC-22 and HFC-134a: Unforeseen seasonal contributions," *Proceedings of the National Academy of Sciences*, vol. 111, no. 49, pp. 17379-17384, 2014.
- [144] W. Goetzler, J. Burgos, and T. Sutherland, "Ultra-Low GWP Refrigerants," *ASHRAE Journal*, vol. 52, no. 10, p. 34, 2010.
- [145] H. M. Pham and K. Monnier, "Interim And Long-Term Low-GWP Refrigerant Solutions For Air Conditioning," 2016.
- [146] E. A. Heath, "Amendment to the Montreal protocol on substances that deplete the ozone layer (Kigali amendment)," *International Legal Materials*, vol. 56, no. 1, pp. 193-205, 2017.
- [147] B. B. Chen, J. S. Costa, P. Bonnet, M. Y. Elsheikh, and B. L. Van Horn, "Blowing agent composition of hydrochlorofluoroolefin and hydrofluoroolefin," ed: Google Patents, 2016.
- [148] A. Ç. Köne and T. Büke, "Forecasting of CO<sub>2</sub> emissions from fuel combustion using trend analysis," *Renewable and Sustainable Energy Reviews*, vol. 14, no. 9, pp. 2906-2915, 2010/12/01/ 2010, doi: <https://doi.org/10.1016/j.rser.2010.06.006>.
- [149] B. K. Bose, "Global Warming: Energy, Environmental Pollution, and the Impact of Power Electronics," *IEEE Industrial Electronics Magazine*, vol. 4, no. 1, pp. 6-17, 2010, doi: 10.1109/MIE.2010.935860.
- [150] G. A. Meehl *et al.*, "How much more global warming and sea level rise?," *science*, vol. 307, no. 5716, pp. 1769-1772, 2005.
- [151] J. Hansen *et al.*, "Ice melt, sea level rise and superstorms: evidence from paleoclimate data, climate modeling, and modern observations that 2 C global warming could be dangerous," *Atmospheric Chemistry and Physics*, vol. 16, no. 6, pp. 3761-3812, 2016.
- [152] A. McCulloch, P. M. Midgley, and P. Ashford, "Releases of refrigerant gases (CFC-12, HCFC-22 and HFC-134a) to the atmosphere," *Atmospheric Environment*, vol. 37, no. 7, pp. 889-902, 2003.
- [153] A. Sekiya and S. Misaki, "The potential of hydrofluoroethers to replace CFCs, HCFCs and PFCs," *Journal of Fluorine Chemistry*, vol. 101, no. 2, pp. 215-221, 2000.
- [154] J. M. Calm, "The toxicity of refrigerants," United States, 1996-07-01 1996, Research Org.: Calm (James M.), Arlington, VA (United States), Sponsor Org.: USDOE Assistant Secretary for Energy Efficiency and Renewable Energy, Washington, DC (United States); Air-Conditioning and Refrigeration Inst., Arlington, VA (United States). [Online]. Available: <https://www.osti.gov/servlets/purl/459965>
- [155] W. A. Affens and G. W. McLaren, "Flammability properties of hydrocarbon solutions in air," *Journal of Chemical and Engineering Data*, vol. 17, no. 4, pp. 482-488, 1972.
- [156] T. A. Albahri, "Flammability characteristics of pure hydrocarbons," *Chemical Engineering Science*, vol. 58, no. 16, pp. 3629-3641, 2003/08/01/ 2003, doi: [https://doi.org/10.1016/S0009-2509\(03\)00251-3](https://doi.org/10.1016/S0009-2509(03)00251-3).
- [157] V. L. Le, M. Feidt, A. Kheiri, and S. Pelloux-Prayer, "Performance optimization of low-temperature power generation by supercritical ORCs (organic Rankine cycles) using

- low GWP (global warming potential) working fluids," *Energy*, vol. 67, pp. 513-526, 2014/04/01/ 2014, doi: <https://doi.org/10.1016/j.energy.2013.12.027>.
- [158] A. Kaya, M. Lazova, H. Huisseune, and M. De Paepe, "Selection of prospective working fluid candidates for subcritical OR evaporators," 2014: International Conference on Heat Transfer, Fluid Mechanics and Thermodynamics.
- [159] J. S. Daniel *et al.*, "Halocarbon scenarios, ozone depletion potentials, and global warming potentials," *Scientific assessment of ozone depletion*, pp. 8-1, 2006.
- [160] D. Luo, A. Mahmoud, and F. Cogswell, "Evaluation of Low-GWP fluids for power generation with Organic Rankine Cycle," *Energy*, vol. 85, pp. 481-488, 2015/06/01/ 2015, doi: <https://doi.org/10.1016/j.energy.2015.03.109>.
- [161] M. W. Spatz and B. H. Minor, "Update on a low GWP refrigerant: fluid H," 2007.
- [162] M. Protocol, "Montreal protocol on substances that deplete the ozone layer," *Washington, DC: US Government Printing Office*, vol. 26, pp. 128-136, 1987.
- [163] B. O. Bolaji, "Experimental study of R152a and R32 to replace R134a in a domestic refrigerator," *Energy*, vol. 35, no. 9, pp. 3793-3798, 2010/09/01/ 2010, doi: <https://doi.org/10.1016/j.energy.2010.05.031>.
- [164] "<https://www.honeywell-refrigerants.com/europe/product/genetron-245fa/>," ed.
- [165] T. Thongtip and S. Aphornratana, "An alternative analysis applied to investigate the ejector performance used in R141b jet-pump refrigeration system," *International Journal of Refrigeration*, vol. 53, pp. 20-33, 2015.
- [166] C. M. Invernizzi, P. Iora, M. Preißinger, and G. Manzolini, "HFOs as substitute for R-134a as working fluids in ORC power plants: A thermodynamic assessment and thermal stability analysis," *Applied Thermal Engineering*, vol. 103, pp. 790-797, 2016.
- [167] P. Petr and G. Raabe, "Evaluation of R-1234ze (Z) as drop-in replacement for R-245fa in Organic Rankine Cycles—From thermophysical properties to cycle performance," *Energy*, vol. 93, pp. 266-274, 2015.
- [168] O. a. M. S. a. A. K. a. R. H. Rowshanaie, "Increasing Electricity generation By Using Organic Rankine Cycle (ORC) Through the Fluegas of Boilers as a Heat Source," *Journal of Multidisciplinary Engineering Science and Technology (JMEST)*, vol. 1, pp. 161-170, 2014.
- [169] D. Mendrinou, E. Kontoleontos, and C. Karytsas, "Geothermal binary plants: water or air cooled," *Centre for Renewable Energy Sources*, vol. 19, pp. 1-10, 2006.
- [170] S. A. Klein and F. L. Alvarado, "EES-Engineering equation solver, F-chart software," ed, 2010.
- [171] B. Zhang, X. Peng, Z. He, Z. Xing, and P. Shu, "Development of a double acting free piston expander for power recovery in transcritical CO<sub>2</sub> cycle," *Applied Thermal Engineering*, vol. 27, no. 8-9, pp. 1629-1636, 2007.
- [172] F. Alshammari, A. Karvountzis-Kontakiotis, and A. Pesyridis, "Effect of radial turbo-expander design on off-highway vehicle organic Rankine cycle system efficiency," *International Journal of Powertrains*, vol. 7, no. 1-3, pp. 72-93, 2018.
- [173] B. Yang, X. Peng, Z. He, B. Guo, and Z. Xing, "Experimental investigation on the internal working process of a CO<sub>2</sub> rotary vane expander," *Applied Thermal Engineering*, vol. 29, no. 11, pp. 2289-2296, 2009/08/01/ 2009, doi: <https://doi.org/10.1016/j.applthermaleng.2008.11.023>.
- [174] H. Wang, R. B. Peterson, and T. Herron, "Experimental performance of a compliant scroll expander for an organic Rankine cycle," *Proceedings of the Institution of Mechanical Engineers, Part A: Journal of Power and Energy*, vol. 223, no. 7, pp. 863-872, 2009, doi: 10.1243/09576509jpe741.
- [175] S. Quoilin, V. Lemort, and J. Lebrun, "Experimental study and modeling of an Organic Rankine Cycle using scroll expander," *Applied energy*, vol. 87, no. 4, pp. 1260-1268, 2010.

- [176] I. Papes, J. Degroote, and J. Vierendeels, "New insights in twin screw expander performance for small scale ORC systems from 3D CFD analysis," *Applied Thermal Engineering*, vol. 91, pp. 535-546, 2015/12/05/ 2015, doi: <https://doi.org/10.1016/j.applthermaleng.2015.08.034>.
- [177] J. S. Baek, E. A. Groll, and P. B. Lawless, "Piston-cylinder work producing expansion device in a transcritical carbon dioxide cycle. Part I: experimental investigation," *International Journal of Refrigeration*, vol. 28, no. 2, pp. 141-151, 2005/03/01/ 2005, doi: <https://doi.org/10.1016/j.ijrefrig.2004.08.006>.
- [178] A. P. Weiß, "Volumetric expander versus turbine—which is the better choice for small ORC plants," 2015, pp. 12-14.
- [179] S. Quoilin, S. Declaye, and V. Lemort, "Expansion machine and fluid selection for the organic Rankine cycle," 2010, pp. 19-21.
- [180] V. Pethurajan, S. Sivan, and G. C. Joy, "Issues, comparisons, turbine selections and applications—An overview in organic Rankine cycle," *Energy Conversion and Management*, vol. 166, pp. 474-488, 2018.
- [181] B. Aoun, "Micro combined heat and power operating on renewable energy for residential building," 2008.
- [182] T. Z. Kaczmarczyk, E. Ichnatowicz, G. Żywica, and J. Kiciński, "Experimental investigation of the ORC system in a cogenerative domestic power plant with a scroll expanders," *Open Engineering*, vol. 5, no. 1, 2015.
- [183] N. P. Halm, "Mathematical modeling of scroll compressors," *Mémoire de DEA, Herrick Lab., School of Mechanical Engineering, Purdue University*, p. 51, 1997.
- [184] R. L. Huffmaster and J. D. Robichaux, "System and method for controlling the transient torque output of a variable displacement internal combustion engine," ed: Google Patents, 1995.
- [185] M. Fukuta, T. Yanagisawa, and R. Radermacher, "Performance prediction of vane type expander for CO<sub>2</sub> cycle," 2003.
- [186] Z. Gnutek and P. Kolasiński, "The application of rotary vane expanders in organic rankine cycle systems—thermodynamic description and experimental results," *Journal of engineering for gas turbines and power*, vol. 135, no. 6, 2013.
- [187] H. Moustapha, M. F. Zelesky, N. C. Baines, and D. Japikse, *Axial and radial turbines*. Concepts NREC White River Junction, VT, 2003.
- [188] D. Ziviani, A. Beyene, and M. Venturini, "Advances and challenges in ORC systems modeling for low grade thermal energy recovery," *Applied Energy*, vol. 121, pp. 79-95, 2014.
- [189] L. Shao, J. Zhu, X. Meng, X. Wei, and X. Ma, "Experimental study of an organic Rankine cycle system with radial inflow turbine and R123," *Applied Thermal Engineering*, vol. 124, pp. 940-947, 2017.
- [190] A. Whitfield and N. C. Baines, "Design of radial turbomachines," 1990.
- [191] J. J. Bao and L. Zhao, "A review of working fluid and expander selections for organic Rankine cycle," *Renewable & Sustainable Energy Reviews*, vol. 24, pp. 325-342, Aug 2013, doi: 10.1016/j.rser.2013.03.040.
- [192] H. R. M. Craig and H. J. A. Cox, "Performance estimation of axial flow turbines," *Proceedings of the Institution of Mechanical Engineers*, vol. 185, no. 1, pp. 407-424, 1970.
- [193] O. E. Balje and R. L. Binsley, "Axial turbine performance evaluation. Part A—Loss-geometry relationships," *Journal of Engineering for Power*, vol. 90, no. 4, pp. 341-348, 1968.
- [194] W. J. Kearton, *Steam turbine theory and practice: a textbook for engineering students*. I. Pitman, 1948.

- [195] S. F. Smith, "A simple correlation of turbine efficiency," *The Aeronautical Journal*, vol. 69, no. 655, pp. 467-470, 1965.
- [196] E. Macchi, "Design limits: Basic parameter selection and optimization methods in turbomachinery design," *Thermodynamics and fluid Mechanics of turbomachinery*, vol. 2, pp. 805-828, 1985.
- [197] T. Efstathiadis, A. I. Kalfas, P. Seferlis, K. G. Kyprianidis, and M. Rivarolo, "Geometry Optimization of Power Production Turbine For A Low Enthalpy ( $\leq 100$  C) ORC System," *Energy Procedia*, vol. 75, pp. 1624-1630, 2015.
- [198] S. Yoon, "The effect of the degree of reaction on the leakage loss in steam turbines," *Journal of Engineering for Gas Turbines and Power*, vol. 135, no. 2, p. 022602, 2013.
- [199] S. Yoon, E. Curtis, J. Denton, and J. Longley, "The effect of clearance on shrouded and unshrouded turbines at two levels of reaction," *Journal of Turbomachinery*, vol. 136, no. 2, p. 021013, 2014.
- [200] O. Zweifel, "The spacing of turbo-machine blading, especially with large angular deflection," *Brown Boveri Rev.*, vol. 32, no. 12, pp. 436-444, 1945.
- [201] I. Popovic, J. Zhu, W. Dai, S. A. Sjolander, T. Praisner, and E. Grover, "Aerodynamics of a Family of Three Highly Loaded Low-Pressure Turbine Airfoils: Measured Effects of Reynolds Number and Turbulence Intensity in Steady Flow," 2006: American Society of Mechanical Engineers, pp. 961-969.
- [202] T. Zoric, I. Popovic, S. A. Sjolander, T. Praisner, and E. Grover, "Comparative Investigation of Three Highly Loaded LP Turbine Airfoils: Part II—Measured Profile and Secondary Losses at Off-Design Incidence," 2007: American Society of Mechanical Engineers, pp. 631-638.
- [203] S. H. Moustapha, U. Okapuu, and R. G. Williamson, "Influence of rotor blade aerodynamic loading on the performance of a highly loaded turbine stage," *Journal of turbomachinery*, vol. 109, no. 2, pp. 155-161, 1987.
- [204] B. V. Datla and J. J. Brasz, "Comparing R1233zd and R245fa for low temperature ORC applications," 2014.
- [205] T. Yamamoto, T. Furuhashi, N. Arai, and K. Mori, "Design and testing of the Organic Rankine Cycle," *Energy*, vol. 26, no. 3, pp. 239-251, 2001/03/01/ 2001, doi: [https://doi.org/10.1016/S0360-5442\(00\)00063-3](https://doi.org/10.1016/S0360-5442(00)00063-3).
- [206] C. Hall and S. L. Dixon, *Fluid mechanics and thermodynamics of turbomachinery*. Butterworth-Heinemann, 2013.
- [207] G. Angelino, M. Gaia, and E. Macchi, "Medium temperature 100 kW ORC engine for total energy systems," in *Energy Conservation in Industry—Combustion, Heat Recovery and Rankine Cycle Machines*: Springer, 1983, pp. 177-189.
- [208] G. Lozza, E. Macchi, and A. Perdichizzi, "On the influence of the number of stages on the efficiency of axial-flow turbines," 1982: American Society of Mechanical Engineers Digital Collection.
- [209] P. Klonowicz, F. Heberle, M. Preißinger, and D. Brüggemann, "Significance of loss correlations in performance prediction of small scale, highly loaded turbine stages working in Organic Rankine Cycles," *Energy*, vol. 72, pp. 322-330, 2014/08/01/ 2014, doi: <https://doi.org/10.1016/j.energy.2014.05.040>.
- [210] G. Lozza, "A comparison between the Craig-Cox and the Kacker-Okapuu methods of turbine performance prediction," *Meccanica*, vol. 17, no. 4, pp. 211-221, 1982.
- [211] E. Macchi and A. Perdichizzi, "Efficiency prediction for axial-flow turbines operating with nonconventional fluids," *Journal of engineering for power*, vol. 103, no. 4, pp. 718-724, 1981.
- [212] A. Lazzaretto and G. Manente, "A new criterion to optimize ORC design performance using efficiency correlations for axial and radial turbines," *International Journal of Thermodynamics*, vol. 17, no. 3, pp. 192-200, 2014.

- [213] R. J. Latimer, "Axial turbine performance prediction," *Von Karman Inst. for Fluid Dyn. Off-Design Performance of Gas Turbines*, vol. 1, 1978.
- [214] D. G. Ainley and G. C. Mathieson, "A method of performance estimation for axial-flow turbines," AERONAUTICAL RESEARCH COUNCIL LONDON (UNITED KINGDOM), 1951.
- [215] S. H. Moustapha, S. C. Kacker, and B. Tremblay, "An improved incidence losses prediction method for turbine airfoils," 1990.
- [216] N. Wei, "Significance of loss models in aerothermodynamic simulation for axial turbines," 2000.
- [217] M. K. Mukhtarov and V. I. Krichakin, "Procedure of estimating flow section losses in axial flow turbines when calculating their characteristics," *Teploenergetika*, vol. 16, no. 7, pp. 76-79, 1969.
- [218] P. I. Onwuamaeze, "Improving Steam Turbine Efficiency: An Appraisal," *PI Onwuamaeze (2018). Research Journal of Mechanical Operations*, vol. 1, no. 1, pp. 24-30, 2018.
- [219] S. P. Malysenko and A. I. Schastlivtsev, "Thermodynamic efficiency of geothermal power stations with hydrogen steam superheating," *Thermal engineering*, vol. 57, no. 11, pp. 931-936, 2010.
- [220] A. P. Weiß, T. Popp, J. Müller, J. Hauer, D. Brüggemann, and M. Preißinger, "Experimental characterization and comparison of an axial and a cantilever micro-turbine for small-scale Organic Rankine Cycle," *Applied Thermal Engineering*, vol. 140, pp. 235-244, 2018.
- [221] C. N. Michos, S. Lion, I. Vlaskos, and R. Taccani, "Analysis of the backpressure effect of an Organic Rankine Cycle (ORC) evaporator on the exhaust line of a turbocharged heavy duty diesel power generator for marine applications," *Energy Conversion and Management*, vol. 132, pp. 347-360, 2017/01/15/ 2017, doi: <https://doi.org/10.1016/j.enconman.2016.11.025>.
- [222] C. Guo, X. Du, L. Yang, and Y. Yang, "Organic Rankine cycle for power recovery of exhaust flue gas," *Applied Thermal Engineering*, vol. 75, pp. 135-144, 2015.
- [223] D. E. Labbe and M. E. Brown Jr, "Attemperator-deaerator condenser," ed: Google Patents, 1983.
- [224] G. Cerri and A. Colage', "Steam Cycle Regeneration Influence on Combined Gas-Steam Power Plant Performance," *Journal of Engineering for Gas Turbines and Power*, vol. 107, no. 3, pp. 574-581, 1985, doi: 10.1115/1.3239775.
- [225] P. J. Mago, L. M. Chamra, K. Srinivasan, and C. Somayaji, "An examination of regenerative organic Rankine cycles using dry fluids," *Applied thermal engineering*, vol. 28, no. 8-9, pp. 998-1007, 2008.
- [226] K. Braimakis and S. Karellas, "Energetic optimization of regenerative Organic Rankine Cycle (ORC) configurations," *Energy Conversion and Management*, vol. 159, pp. 353-370, 2018/03/01/ 2018, doi: <https://doi.org/10.1016/j.enconman.2017.12.093>.
- [227] M. Astolfi, M. C. Romano, P. Bombarda, and E. Macchi, "Binary ORC (Organic Rankine Cycles) power plants for the exploitation of medium–low temperature geothermal sources—Part B: Techno-economic optimization," *Energy*, vol. 66, pp. 435-446, 2014.
- [228] S. Lecompte, H. Huisseune, M. Van den Broek, S. De Schampheleire, and M. De Paepe, "Part load based thermo-economic optimization of the Organic Rankine Cycle (ORC) applied to a combined heat and power (CHP) system," *Applied Energy*, vol. 111, pp. 871-881, 2013.
- [229] R. Pili, A. Romagnoli, H. Spliethoff, and C. Wieland, "Techno-economic analysis of waste heat recovery with ORC from fluctuating industrial sources," *Energy procedia*, vol. 129, pp. 503-510, 2017.
- [230] N. J. Nilsson, "Introduction to machine learning: An early draft of a proposed textbook," ed: USA; Stanford University, 1996.

- [231] E. Alpaydin, *Introduction to machine learning*. MIT press, 2020.
- [232] Ö. Öksüz and İ. S. Akmandor, "Multi-objective aerodynamic optimization of axial turbine blades using a novel multilevel genetic algorithm," *Journal of Turbomachinery*, vol. 132, no. 4, p. 041009, 2010.
- [233] M. A. Trigg, G. R. Tubby, and A. G. Sheard, "Automatic genetic optimization approach to two-dimensional blade profile design for steam turbines," 1999.
- [234] A. Oyama, M.-S. Liou, and S. Obayashi, "Transonic axial-flow blade optimization: Evolutionary algorithms/three-dimensional Navier-Stokes solver," *Journal of Propulsion and Power*, vol. 20, no. 4, pp. 612-619, 2004.
- [235] M. M. Rashidi, N. Galanis, F. Nazari, A. B. Parsa, and L. Shamekhi, "Parametric analysis and optimization of regenerative Clausius and organic Rankine cycles with two feedwater heaters using artificial bees colony and artificial neural network," *Energy*, vol. 36, no. 9, pp. 5728-5740, 2011.
- [236] S. B. Akben, "Optimization Using Decision Trees Method in Multivariable Food Engineering Experiments and Its Sample of Applicability on Experiment Related with the Nisin Production of *Lactococcus lactis* N8," *Eurasian Journal of Food Science and Technology*, vol. 1, no. 1, pp. 50-57.
- [237] G. James, D. Witten, T. Hastie, and R. Tibshirani, *An introduction to statistical learning*. Springer, 2013.
- [238] C. Lacave and F. J. Díez, "A review of explanation methods for Bayesian networks," *The Knowledge Engineering Review*, vol. 17, no. 2, pp. 107-127, 2002.
- [239] G. S. Sandhu and D. S. Salaria, "A Bayesian network model of the particle swarm optimization for software effort estimation," *International Journal of Computer Applications*, vol. 96, no. 4, 2014.
- [240] H. Adeli and N.-T. Cheng, "Augmented Lagrangian genetic algorithm for structural optimization," *Journal of Aerospace Engineering*, vol. 7, no. 1, pp. 104-118, 1994.
- [241] A. B. Ennil, R. Al-Dadah, S. Mahmoud, K. Rahbar, and A. AlJubori, "Minimization of loss in small scale axial air turbine using CFD modeling and evolutionary algorithm optimization," *Applied Thermal Engineering*, vol. 102, pp. 841-848, 2016.
- [242] Y.-C. Wu, W.-P. Lee, and C.-W. Chien, "Modified the performance of differential evolution algorithm with dual evolution strategy," 2011, vol. 3, pp. 57-63.
- [243] P. K. Senecal, E. Pomraning, and K. J. Richards, "Multi-mode genetic algorithm optimization of combustion chamber geometry for low emissions," SAE Technical Paper, 0148-7191, 2002.
- [244] K. Schittkowski, "NLPQLP: A fortran implementation of a sequential quadratic programming algorithm with distributed and non-monotone line search—user's guide," *Report, Department of Computer Science, University of Bayreuth*, 2006.
- [245] A. Jamali, P. Ahmadi, and M. N. M. Jaafar, "Optimization of a novel carbon dioxide cogeneration system using artificial neural network and multi-objective genetic algorithm," *Applied Thermal Engineering*, vol. 64, no. 1-2, pp. 293-306, 2014.
- [246] D. Binu and B. S. Kariyappa, "RideNN: A new rider optimization algorithm-based neural network for fault diagnosis in analog circuits," *IEEE Transactions on Instrumentation and Measurement*, vol. 68, no. 1, pp. 2-26, 2018.
- [247] A. Samad and K.-Y. Kim, "Shape optimization of an axial compressor blade by multi-objective genetic algorithm," *Proceedings of the Institution of Mechanical Engineers, Part A: Journal of Power and Energy*, vol. 222, no. 6, pp. 599-611, 2008.
- [248] A. Meroni, A. La Seta, J. Andreasen, L. Pierobon, G. Persico, and F. Haglind, "Combined Turbine and Cycle Optimization for Organic Rankine Cycle Power Systems—Part A: Turbine Model," *Energies*, vol. 9, no. 5, p. 313, 2016.
- [249] P. K. Subramanian, "Fixed Point Methods for The Complementarity Problem," *Journal of Computational Mathematics*, pp. 121-130, 1988.

- [250] J.-S. Pang and D. Chan, "Iterative methods for variational and complementarity problems," *Mathematical programming*, vol. 24, no. 1, pp. 284-313, 1982.
- [251] K. Taji, M. Fukushima, and T. Ibaraki, "Optimization-Based Iterative Methods for Solving Nonlinear Complementarity Problems (Nonlinear Analysis and Mathematical Economics)," 1993.
- [252] H. H. Tan and K. H. Lim, "Review of second-order optimization techniques in artificial neural networks backpropagation," 2019, vol. 495: IOP Publishing, 1 ed., p. 012003.
- [253] Y. A. LeCun, L. Bottou, G. B. Orr, and K.-R. Müller, "Efficient backprop," in *Neural networks: Tricks of the trade*: Springer, 2012, pp. 9-48.
- [254] J. Nocedal and S. Wright, *Numerical optimization*. Springer Science & Business Media, 2006.
- [255] K. Schittkowski, "Mathematical programming software," in *System Modelling and Optimization*: Springer, 1986, pp. 804-810.
- [256] Y. Chen and L. Lv, "The multi-objective optimization of combustion chamber of DI diesel engine by NLPQL algorithm," *Applied Thermal Engineering*, vol. 73, no. 1, pp. 1332-1339, 2014/12/05/ 2014, doi: <https://doi.org/10.1016/j.applthermaleng.2014.09.028>.
- [257] Y. Song, X. Sun, and D. Huang, "Preliminary design and performance analysis of a centrifugal turbine for Organic Rankine Cycle (ORC) applications," *Energy*, vol. 140, pp. 1239-1251, 2017/12/01/ 2017, doi: <https://doi.org/10.1016/j.energy.2017.08.061>.
- [258] N. Hu, P. Zhou, and J. Yang, "Comparison and combination of NLPQL and MOGA algorithms for a marine medium-speed diesel engine optimisation," *Energy Conversion and Management*, vol. 133, pp. 138-152, 2017/02/01/ 2017, doi: <https://doi.org/10.1016/j.enconman.2016.11.066>.
- [259] K. Sörensen and F. Glover, "Metaheuristics," *Encyclopedia of operations research and management science*, vol. 62, pp. 960-970, 2013.
- [260] A. E. Ezugwu, O. J. Adeleke, A. A. Akinyelu, and S. Viriri, "A conceptual comparison of several metaheuristic algorithms on continuous optimisation problems," *Neural Computing and Applications*, vol. 32, no. 10, pp. 6207-6251, 2020.
- [261] E.-G. Talbi, *Metaheuristics: from design to implementation*. John Wiley & Sons, 2009.
- [262] C. Blum and A. Roli, "Metaheuristics in combinatorial optimization: Overview and conceptual comparison," *ACM computing surveys (CSUR)*, vol. 35, no. 3, pp. 268-308, 2003.
- [263] K. Sörensen, "Metaheuristics—the metaphor exposed," *International Transactions in Operational Research*, vol. 22, no. 1, pp. 3-18, 2015.
- [264] A. M. Al Jubori, R. Al-Dadah, and S. Mahmoud, "Performance enhancement of a small-scale organic Rankine cycle radial-inflow turbine through multi-objective optimization algorithm," *Energy*, vol. 131, pp. 297-311, 2017/07/15/ 2017, doi: <https://doi.org/10.1016/j.energy.2017.05.022>.
- [265] P. Rodriguez-Fernandez and G. Persico, "Automatic design of ORC turbine profiles using evolutionary algorithms."
- [266] R. T. Marler and J. S. Arora, "Survey of multi-objective optimization methods for engineering," *Structural and multidisciplinary optimization*, vol. 26, no. 6, pp. 369-395, 2004.
- [267] H. Taghavifar and S. Anvari, "Optimization of a DI diesel engine to reduce emission and boost power by exergy and NLPQL method," *Environmental Progress & Sustainable Energy*, vol. 39, no. 2, p. e13338, 2020.
- [268] F. Kyriakidis, K. Sørensen, S. Singh, and T. Condra, "Modeling and optimization of integrated exhaust gas recirculation and multi-stage waste heat recovery in marine

- engines," *Energy Conversion and Management*, vol. 151, pp. 286-295, 2017/11/01/ 2017, doi: <https://doi.org/10.1016/j.enconman.2017.09.004>.
- [269] D. F. Jones, S. K. Mirrazavi, and M. Tamiz, "Multi-objective meta-heuristics: An overview of the current state-of-the-art," *European Journal of Operational Research*, vol. 137, no. 1, pp. 1-9, 2002/02/16/ 2002, doi: [https://doi.org/10.1016/S0377-2217\(01\)00123-0](https://doi.org/10.1016/S0377-2217(01)00123-0).
- [270] H. Youssef, S. M. Sait, and H. Adiche, "Evolutionary algorithms, simulated annealing and tabu search: a comparative study," *Engineering Applications of Artificial Intelligence*, vol. 14, no. 2, pp. 167-181, 2001/04/01/ 2001, doi: [https://doi.org/10.1016/S0952-1976\(00\)00065-8](https://doi.org/10.1016/S0952-1976(00)00065-8).
- [271] Z. Wang, Y. Hu, X. Xia, Q. Zuo, B. Zhao, and Z. Li, "Thermo-economic selection criteria of working fluid used in dual-loop ORC for engine waste heat recovery by multi-objective optimization," *Energy*, vol. 197, p. 117053, 2020/04/15/ 2020, doi: <https://doi.org/10.1016/j.energy.2020.117053>.
- [272] T. C. Roumpedakis, G. Loumpardis, E. Monokrousou, K. Braimakis, A. Charalampidis, and S. Karellas, "Exergetic and economic analysis of a solar driven small scale ORC," *Renewable Energy*, vol. 157, pp. 1008-1024, 2020.
- [273] M. White and A. I. Sayma, "The Application of Similitude Theory for the Performance Prediction of Radial Turbines Within Small-Scale Low-Temperature Organic Rankine Cycles," *Journal of Engineering for Gas Turbines and Power*, vol. 137, no. 12, 2015, doi: 10.1115/1.4030836.
- [274] E. Macchi and G. Lozza, "Comparison of partial vs full admission for small turbines at low specific speeds," 1985, vol. 79382: American Society of Mechanical Engineers, p. V001T03A059.
- [275] J. D. Denton, "The 1993 IGTI scholar lecture: Loss mechanisms in turbomachines," 1993.
- [276] R. I. Lewis, *Turbomachinery performance analysis*. Butterworth-Heinemann, 1996.
- [277] A. T. Sayers, *Hydraulic and compressible flow turbomachines*. McGraw-Hill Book Company Limited, 1990.
- [278] S. C. Kacker and U. Okapuu, "A mean line prediction method for axial flow turbine efficiency," 1982.
- [279] J. N. Kutz, "Deep learning in fluid dynamics," *Journal of Fluid Mechanics*, vol. 814, pp. 1-4, 2017.
- [280] D. Maraver, J. Royo, V. Lemort, and S. Quoilin, "Systematic optimization of subcritical and transcritical organic Rankine cycles (ORCs) constrained by technical parameters in multiple applications," *Applied Energy*, vol. 117, pp. 11-29, 2014/03/15/ 2014, doi: <https://doi.org/10.1016/j.apenergy.2013.11.076>.
- [281] J. Carr, "An introduction to genetic algorithms," *Senior Project*, vol. 1, no. 40, p. 7, 2014.
- [282] S. Lecompte, B. Ameel, D. Ziviani, M. van den Broek, and M. De Paepe, "Exergy analysis of zeotropic mixtures as working fluids in Organic Rankine Cycles," *Energy Conversion and Management*, vol. 85, pp. 727-739, 2014.
- [283] J. M. Luján, J. R. Serrano, V. Dolz, and J. Sánchez, "Model of the expansion process for R245fa in an Organic Rankine Cycle (ORC)," *Applied Thermal Engineering*, vol. 40, pp. 248-257, 2012.
- [284] R. M. Yablounik, E. E. Markovich, and L. E. Al'tshuler, "The effect of installing a moisture trap before the moving row on the efficiency of a turbine stage," *Teploénergetika*, vol. 13, no. 3, p. 38, 1966.
- [285] K. Baumann, "Some recent developments in large steam turbine practice," *Journal of the institution of electrical engineers*, vol. 59, no. 302, pp. 565-623, 1921.

- [286] J. W. Daily and R. E. Nece, "Chamber dimension effects on induced flow and frictional resistance of enclosed rotating disks," 1960.
- [287] J.-A. Luo, C.-C. Xue, and D.-L. Peng, "Robust Bearing-Only Localization Using Total Least Absolute Residuals Optimization," *Complexity*, vol. 2020, 2020.
- [288] S. Enkhbayar and J. Tseyen-Oidov, "Compared study of operation regime for FB and CFB steam generators with small and medium capacity," 2013, vol. 2: IEEE, pp. 488-492.
- [289] F. Yılmaz, R. Selbaş, and A. Ş. Şahin, "Efficiency analysis of organic Rankine cycle with internal heat exchanger using neural network," *Heat and Mass Transfer*, vol. 52, no. 2, pp. 351-359, 2016.
- [290] O. Memarian Sorkhabi, "Geoid determination based on log sigmoid function of artificial neural networks:(a case study: Iran)," *Journal of Artificial Intelligence in Electrical Engineering*, vol. 3, no. 12, pp. 18-24, 2015.
- [291] L. Moroz, C.-R. Kuo, O. Guriev, Y.-C. Li, and B. Frolov, "Axial turbine flow path design for an organic Rankine cycle using R-245fa," 2013, vol. 55195: American Society of Mechanical Engineers, p. V05AT23A004.
- [292] A. Rusanov, R. Rusanov, and P. Lampart, "Designing and updating the flow part of axial and radial-axial turbines through mathematical modeling," *Open Engineering*, vol. 5, no. 1, 2015.
- [293] L. Talluri and G. Lombardi, "Simulation and Design Tool for ORC Axial Turbine Stage," *Energy Procedia*, vol. 129, pp. 277-284, 2017/09/01/ 2017, doi: <https://doi.org/10.1016/j.egypro.2017.09.154>.
- [294] J. Jouybari, M. Eftari, H. D. Kaliji, F. Ghadak, and M. Rad, "Analytical modeling of performance characteristics of axial flow two-stage turbine engine using pressure losses models and comparing with experimental results," *World Applied Sciences Journal*, vol. 21, no. 9, pp. 1250-1259, 2013.
- [295] B. Zhou, H. Liang, H. Miao, and C. Zang, "Reduced-Scale Model Design for a High-Speed Rotor System Based on Similitude Theory," 2019. [Online]. Available: <https://doi.org/10.1115/GT2019-91112>.
- [296] X.-Q. Wang, X.-P. Li, Y.-R. Li, and C.-M. Wu, "Payback period estimation and parameter optimization of subcritical organic Rankine cycle system for waste heat recovery," *Energy*, vol. 88, pp. 734-745, 2015/08/01/ 2015, doi: <https://doi.org/10.1016/j.energy.2015.05.095>.
- [297] P. Verma, "Shahi Exports Pvt. Ltd," 2019.
- [298] D. F. Umar, H. Usui, and B. Daulay, "Effects of processing temperature of hot water drying on the properties and combustion characteristics of an Indonesian low rank coal," *Coal Preparation*, vol. 25, no. 4, pp. 313-322, 2005.
- [299] S. Widodo, S. Sufriadin, A. Imai, and K. Anggayana, "Characterization of Some Coal Deposits Quality by Use of Proximate and Sulfur Analysis in The Southern Arm Sulawesi, Indonesia," *International Journal of Engineering and Science Applications*, vol. 3, no. 2, pp. 137-143, 2017.
- [300] A. M. Mastral, M. Callén, R. Murillo, and T. García, "Assessment of PAH emissions as a function of coal combustion variables in fluidised bed. 2. Air excess percentage," *Fuel*, vol. 77, no. 13, pp. 1513-1516, 1998/10/01/ 1998, doi: [https://doi.org/10.1016/S0016-2361\(98\)00069-6](https://doi.org/10.1016/S0016-2361(98)00069-6).
- [301] M. Muthuraman, T. Namioka, and K. Yoshikawa, "A comparative study on co-combustion performance of municipal solid waste and Indonesian coal with high ash Indian coal: A thermogravimetric analysis," *Fuel Processing Technology*, vol. 91, no. 5, pp. 550-558, 2010.
- [302] R. Pachaiyappan and J. Dasa Prakash, "Improving the boiler efficiency by optimizing the combustion air," 2015, vol. 787: Trans Tech Publ, pp. 238-242.

- [303] "Indian Meteorological Department (Ministry of Earth Sciences), Government of India. [https://mausam.imd.gov.in/imd\\_latest/contents/index\\_smart\\_cities1.php](https://mausam.imd.gov.in/imd_latest/contents/index_smart_cities1.php) (Accessed 2021)," ed.
- [304] H. D. M. Hettiarachchi, M. Golubovic, W. M. Worek, and Y. Ikegami, "Optimum design criteria for an organic Rankine cycle using low-temperature geothermal heat sources," *Energy*, vol. 32, no. 9, pp. 1698-1706, 2007.
- [305] A. F. Altun and M. Kilic, "Thermodynamic performance evaluation of a geothermal ORC power plant," *Renewable Energy*, vol. 148, pp. 261-274, 2020.
- [306] V. Minea, "Power generation with ORC machines using low-grade waste heat or renewable energy," *Applied Thermal Engineering*, vol. 69, no. 1-2, pp. 143-154, 2014.
- [307] M. Zeng *et al.*, "Investigation on pressure drop and heat transfer performances of plate-fin iron air preheater unit with experimental and Genetic Algorithm methods," *Applied energy*, vol. 92, pp. 725-732, 2012.
- [308] Y. A. Cengel and A. J. Ghajar, "Heat and mass transfer," *A practical approach*, 2007.
- [309] J. Li *et al.*, "Experimental study of organic Rankine cycle in the presence of non-condensable gases," *Energy*, vol. 142, pp. 739-753, 2018.
- [310] P. M. Walsh, A. F. Sarofim, and J. M. Beer, "Fouling of convection heat exchangers by lignitic coal ash," *Energy & fuels*, vol. 6, no. 6, pp. 709-715, 1992.
- [311] Y. V. Shatskikh, A. I. Sharapov, and I. G. Byankin, "Analysis of Deep Heat Recovery From Flue Gases," 2017, vol. 891: IOP Publishing, 1 ed., p. 012188.
- [312] D. Meinel, C. Wieland, and H. Spliethoff, "Effect and comparison of different working fluids on a two-stage organic rankine cycle (ORC) concept," *Applied Thermal Engineering*, vol. 63, no. 1, pp. 246-253, 2014.
- [313] M. Pranit, A. P. Yadav, and P. Patil, "Comparative study between heat transfer through laminar flow and turbulent flow," *International Journal of Innovative Research in Science*, vol. 4, no. 4, pp. 2223-2226, 2015.
- [314] S. M. Yahya, *Turbines compressors and fans*. Tata McGraw-Hill Education, 1987.
- [315] R. W. Powell and Y. S. Touloukian, "Thermal conductivities of the elements," *Science*, vol. 181, no. 4104, pp. 999-1008, 1973.
- [316] S. A. Leeper, "Wet cooling towers: rule-of-thumb design and simulation," EG and G Idaho, Inc., Idaho Falls, ID (United States), 1981.
- [317] R. J. Stewart *et al.*, "Horizontal cooling towers: riverine ecosystem services and the fate of thermoelectric heat in the contemporary Northeast US," *Environmental Research Letters*, vol. 8, no. 2, p. 025010, 2013.
- [318] P. V. Gilli, G. Beckmann, and F. E. Schilling, "Thermal energy storage using Prestressed Cast Iron Vessels (PCIV). Final report," Gilli (PV), Graz (Austria); Beckmann (G.), Consultant, Vienna (Austria ...), 1977.
- [319] S. Landini *et al.*, "Effect of geometry and thermal mass of Direct-Metal-Laser-Sintered aluminium heat exchangers filled with Phase Change Materials on Lithium-Ion cells' passive cooling," *Applied Thermal Engineering*, p. 117151, 2021.
- [320] A. Hassanat, K. Almohammadi, E. Alkafaween, E. Abunawas, A. Hammouri, and V. B. Prasath, "Choosing mutation and crossover ratios for genetic algorithms—a review with a new dynamic approach," *Information*, vol. 10, no. 12, p. 390, 2019.
- [321] J. A. Hesketh and P. J. Walker, "Effects of wetness in steam turbines," *Proceedings of the Institution of Mechanical Engineers, Part C: Journal of Mechanical Engineering Science*, vol. 219, no. 12, pp. 1301-1314, 2005.
- [322] Y. Feng, Y. Zhang, B. Li, J. Yang, and Y. Shi, "Comparison between regenerative organic Rankine cycle (RORC) and basic organic Rankine cycle (BORC) based on thermoeconomic multi-objective optimization considering exergy efficiency and

- levelized energy cost (LEC)," *Energy Conversion and Management*, vol. 96, pp. 58-71, 2015/05/15/ 2015, doi: <https://doi.org/10.1016/j.enconman.2015.02.045>.
- [323] B. A. Qureshi and S. M. Zubair, "Prediction of evaporation losses in wet cooling towers," *Heat transfer engineering*, vol. 27, no. 9, pp. 86-92, 2006.
- [324] L. Chao, L. Ke, W. Yongzhen, M. Zhitong, and G. Yulie, "The effect analysis of thermal efficiency and optimal design for boiler system," *Energy Procedia*, vol. 105, pp. 3045-3050, 2017.
- [325] N. Hu, J. Yang, and P. Zhou, "Optimisation of injection-related parameters by using the NLPQL algorithm for a marine medium-speed diesel engine," *International Journal of Engine Research*, pp. 1-14, 2017.
- [326] M. Imran, B. S. Park, H. J. Kim, D. H. Lee, M. Usman, and M. Heo, "Thermo-economic optimization of Regenerative Organic Rankine Cycle for waste heat recovery applications," *Energy Conversion and Management*, vol. 87, pp. 107-118, 2014/11/01/ 2014, doi: <https://doi.org/10.1016/j.enconman.2014.06.091>.
- [327] A. Konak, D. W. Coit, and A. E. Smith, "Multi-objective optimization using genetic algorithms: A tutorial," *Reliability Engineering & System Safety*, vol. 91, no. 9, pp. 992-1007, 2006/09/01/ 2006, doi: <https://doi.org/10.1016/j.ress.2005.11.018>.
- [328] S. S. Golubev, V. D. Sekerin, A. E. Gorokhova, G. V. Komlatskiy, and Y. I. Arutyunyan, "Analysis of the Current State and Forecast of Cast Iron Production in Russia," *Archives of Foundry Engineering*, vol. 21, no. 2, p. 70, 2021.
- [329] K. C. Kavvadias and S. Quoilin, "Exploiting waste heat potential by long distance heat transmission: Design considerations and techno-economic assessment," *Applied Energy*, vol. 216, pp. 452-465, 2018.
- [330] J. Yue, G. Chen, and Q. Yuan, "Pressure drops of single and two-phase flows through T-type microchannel mixers," *Chemical Engineering Journal*, vol. 102, no. 1, pp. 11-24, 2004.
- [331] G. B. Wallis, *One-dimensional two-phase flow*. Courier Dover Publications, 2020.
- [332] A. Uusitalo, T. Turunen-Saaresti, J. Honkatukia, and R. Dhanasegaran, "Experimental study of small scale and high expansion ratio ORC for recovering high temperature waste heat," *Energy*, vol. 208, p. 118321, 2020/10/01/ 2020, doi: <https://doi.org/10.1016/j.energy.2020.118321>.
- [333] V. K. Avadhanula, C.-S. Lin, and T. Johnson, "Testing a 50kW ORC at different heating and cooling source conditions to map the performance characteristics," SAE Technical Paper, 0148-7191, 2013.
- [334] Z. Shengjun, W. Huaixin, and G. Tao, "Performance comparison and parametric optimization of subcritical Organic Rankine Cycle (ORC) and transcritical power cycle system for low-temperature geothermal power generation," *Applied energy*, vol. 88, no. 8, pp. 2740-2754, 2011.
- [335] N. Shokati, F. Ranjbar, and M. Yari, "Exergoeconomic analysis and optimization of basic, dual-pressure and dual-fluid ORCs and Kalina geothermal power plants: A comparative study," *Renewable Energy*, vol. 83, pp. 527-542, 2015.
- [336] T. Li, Z. Zhang, J. Lu, J. Yang, and Y. Hu, "Two-stage evaporation strategy to improve system performance for organic Rankine cycle," *Applied energy*, vol. 150, pp. 323-334, 2015.
- [337] H. Huang, J. Zhu, and B. Yan, "Comparison of the performance of two different Dual-loop organic Rankine cycles (DORC) with nanofluid for engine waste heat recovery," *Energy Conversion and Management*, vol. 126, pp. 99-109, 2016.
- [338] D. M. Thierry, A. Flores-Tlacuahuac, and I. E. Grossmann, "Simultaneous optimal design of multi-stage organic Rankine cycles and working fluid mixtures for low-temperature heat sources," *Computers & Chemical Engineering*, vol. 89, pp. 106-126, 2016.

- [339] G. Manente, A. Lazzaretto, and E. Bonamico, "Design guidelines for the choice between single and dual pressure layouts in organic Rankine cycle (ORC) systems," *Energy*, vol. 123, pp. 413-431, 2017.
- [340] J. De Greef, H. Van Belle, K. Villani, S. Bram, and F. Contino, "Impact of Operation Mode and Design on the Energy Efficiency of Waste Combustion Plants," 2013, pp. 1-11.
- [341] V. Bhatt and A. Virmani, "Global integration of India's money market: Interest rate parity in India," Working Paper, 2005.
- [342] A. Kagel, *A handbook on the externalities, employment, and economics of geothermal energy*. Geothermal Energy Association, 2006.
- [343] T. Müller and T. Schulten, "The European minimum wage on the doorstep," *ETUI Research Paper-Policy Brief*, vol. 1, 2020.
- [344] H. U. Qing-Wan, "Curve fitting by curve fitting toolbox of Matlab," *Computer Knowledge and Technology*, vol. 21, p. 068, 2010.
- [345] T. Adams, C. Grant, and H. Watson, "A simple algorithm to relate measured surface roughness to equivalent sand-grain roughness," *International Journal of Mechanical Engineering and Mechatronics*, vol. 1, no. 2, pp. 66-71, 2012.
- [346] D. G. Bogard, D. L. Schmidt, and M. Tabbita, "Characterization and laboratory simulation of turbine airfoil surface roughness and associated heat transfer," 1996, vol. 78750: American Society of Mechanical Engineers, p. V004T09A044.
- [347] W. L. Stewart, W. J. Whitney, and R. Y. Wong, "A study of boundary-layer characteristics of turbomachine blade rows and their relation to over-all blade loss," 1960.

# Appendices

## APPENDIX 1

### Polynomial Equations of the Craig and Cox Loss Model

This thesis utilised a surface fitting function to digitise the curves used by the Craig and Cox loss model. The function was selected from the curve fitting toolbox in the MATLAB programming environment [344]. The Craig and Cox loss model contained two or three-dimensional plots. The data points provided by the loss model were converted to a set of polynomial equations with orders between 2 to 5 depending on the complexity of the curve. The absolute deviation of the predicted parameter using the developed equation values was within 2%. For the basic profile loss coefficient, it was not possible to generate analogous polynomial equations within the expected constraints due to the complexity of the gradient, despite the use of higher-order polynomial equations. The values between nearby data points were interpolated by using a weighted mean approach.

Profile loss ratio due to Reynolds number  $N_{prN}$  was defined as in equation 1 and Figure 1.

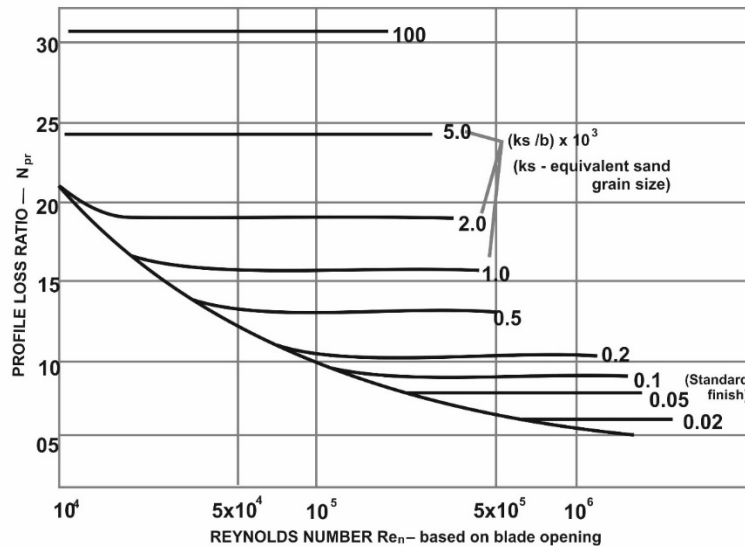


Figure 1 – profile loss due to Reynold's number

$$\begin{aligned}
 N_{prN} = & 0.9135 - 4.299 \times 10^{-8} \times Re_N + 0.7864 \times \left(\frac{ks}{b}\right) \times 10^3 & 1 \\
 & + 2.158 \times 10^{-15} \times Re_N^2 + 1.255 \times 10^{-8} \times Re_N \times \left(\frac{ks}{b}\right) \times 10^3 \\
 & - 0.136 \times \left(\left(\frac{ks}{b}\right) \times 10^3\right)^2 + 1.333 \times 10^{-14} \times Re_N^2 \times \left(\frac{ks}{b}\right) \times 10^3 \\
 & - 1.092 \times 10^{-9} \times Re_N \times \left(\left(\frac{ks}{b}\right) \times 10^3\right)^2 + 0.00787 \times \left(\left(\frac{ks}{b}\right) \times 10^3\right)^3
 \end{aligned}$$

where

$k_s$  is the surface finish measured by equivalent sand grain size [345, 346]. Craig and Cox observed that the surface friction coefficient had greater significance at higher Reynold's number values.  $b$  is the backbone length,  $Re_N$  is the Reynold's number, determined in equation 2, wherein  $D_{hN}$  was the nozzle equivalent hydraulic diameter at the throat section, determined in equation 3.

$$Re_N = \frac{Q_2 C_2 D_{hN}}{\mu_2} \quad 2$$

$$D_{hN} = \frac{4 \cdot \text{Flow Area}}{\text{Perimeter}} = \frac{4 \cdot (Ht_N \cdot thr_N)}{2(Ht_N + thr_N)} \quad 3$$

The lift parameter  $F_L$ , represented the deflection of the working fluid by measuring the deviation of the fluid between the inlet and outlet angles, as given in equation 4 and Figure 2. Correcting the lift parameter for the pitch  $s$  and backbone length  $b$  produced the modified lift coefficient  $LC_m$ , described by equation 5, which was a primary loss contributor.

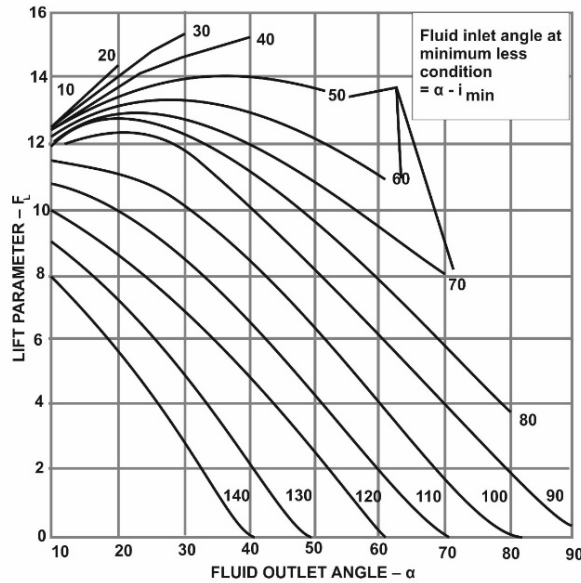


Figure 2 – Determining the lift parameter using deviation of flow

$$F_{LN} = 9.807 + 0.2042 \times \alpha_{Nin} + 0.1345 \times \alpha_2 + 0.004977 \times \alpha_{Nin}^2 \quad 4$$

$$- 0.004855 \times \alpha_{Nin} \times \alpha_2 - 0.005104 \times \alpha_2^2 + 3.081 \times 10^{-5} \times \alpha_{Nin}^3$$

$$- 0.0002772 \times \alpha_{Nin}^2 \times \alpha_2 + 0.0001862 \times \alpha_{Nin} \times \alpha_2^2$$

$$+ 7.86 \times 10^{-5} \times \alpha_2^3 - 3.341 \times 10^{-7} \times \alpha_{Nin}^4$$

$$+ 3.035 \times 10^{-7} \times \alpha_{Nin}^3 \times \alpha_2 + 1.758 \times 10^{-6} \times \alpha_{Nin}^2 \times \alpha_2^2$$

$$- 1.952 \times 10^{-6} \times \alpha_{Nin} \times \alpha_2^3 - 5.388 \times 10^{-7} \times \alpha_2^4$$

$$+ 4.641 \times 10^{-9} \times \alpha_{Nin}^4 \times \alpha_2 - 4.783 \times 10^{-9} \times \alpha_{Nin}^3 \times \alpha_2^2$$

$$+ 1.157 \times 10^{-10} \times \alpha_{Nin}^2 \times \alpha_2^3 + 4.891 \times 10^{-9} \times \alpha_{Nin} \times \alpha_2^4$$

$$+ 1.373 \times 10^{-9} \times \alpha_2^5$$

$$C_{mN} = \frac{F_{LN} \times s_N}{b_N} \quad 5$$

where  $\alpha_{Nin}$  is the fluid outlet angle.

and  $\alpha_2$  is the fluid inlet angle at minimum loss angle.

To determine the basic profile loss, a quadratic equation for each contraction ratio was prepared, as shown in equations 6 to 11. These values were adjusted for zero trailing edge thickness loss and assigned a weightage, as shown in equations 12 to 16. An increase in the Profile loss was noted by increasing the pitch to chord ratio, as in figure 3.

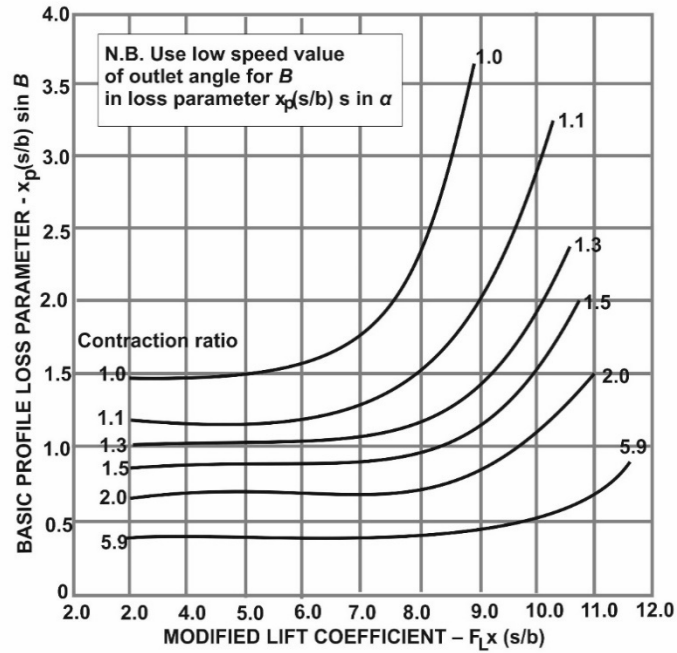


Figure 3 – Basic profile loss derived from the lift coefficient

For  $CR_N = 1.0$  6

$$Z_{n1} = 0.0278 LC_{mN}^3 - 0.3845 LC_{mN}^2 + 1.7306 LC_{mN} - 1.0024$$

For  $CR_N = 1.1$  7

$$Z_{n2} = 0.016 LC_{mN}^3 - 0.2398 LC_{mN}^2 + 1.1452 LC_{mN} - 0.531$$

For  $CR_N = 1.3$  8

$$Z_{n3} = 0.0102 LC_{mN}^3 - 0.1598 LC_{mN}^2 + 0.7972 LC_{mN} - 0.2512$$

For  $CR_N = 1.5$  9

$$Z_{n4} = 0.0049 LC_{mN}^3 - 0.0701 LC_{mN}^2 + 0.3212 LC_{mN} + 0.381$$

For  $CR_N = 2.0$  10

$$Z_{n5} = 0.0188 LC_{mN}^2 - 0.2 LC_{mN} + 1.179$$

For  $CR_N = 5.0$  11

$$Z_{n6} = 0.0045 LC_{mN}^2 - 0.0467 LC_{mN} + 0.5104$$

If  $CR_N \leq 1.1$ , then 12

$$\frac{X_{pbN} \times s_N \times \sin \alpha_2}{b_N} = Z_{n1} \times \frac{1.1 - CR_N}{1.1 - 1} + Z_{n2} \times \frac{CR_N - 1}{1.1 - 1}$$

If  $CR_N > 1.1$  and  $\leq 1.3$ , then

13

$$\frac{X_{pbN} \times s_N \times \sin \alpha_2}{b_N} = Z_{n2} \times \frac{1.3 - CR_N}{1.3 - 1.1} + Z_{n3} \times \frac{CR_N - 1.1}{1.3 - 1.1}$$

If  $CR_N > 1.3$  and  $\leq 1.5$ , then

14

$$\frac{X_{pbN} \times s_N \times \sin \alpha_2}{b_N} = Z_{n3} \times \frac{1.5 - CR_N}{1.5 - 1.3} + Z_{n4} \times \frac{CR_N - 1.3}{1.5 - 1.3}$$

If  $CR_N > 1.5$  and  $\leq 2$ , then

15

$$\frac{X_{pbN} \times s_N \times \sin \alpha_2}{b_N} = Z_{n4} \times \frac{2 - CR_N}{2 - 1.5} + Z_{n5} \times \frac{CR_N - 1.5}{2 - 1.5}$$

If  $CR_N > 2$  and  $\leq 5$ , then

16

$$\frac{X_{pbN} \times s_N \times \sin \alpha_2}{b_N} = Z_{n5} \times \frac{5 - CR_N}{5 - 2} + Z_{n6} \times \frac{CR_N - 2}{5 - 2}$$

Profile loss due to trailing edge thickness  $N_{pt}$ , derived from Stewart [347], as shown in equation 17. An additional trailing edge incremental loss was derived, as seen in equation 18.

$$N_{ptN} = 1.189 + 25.35 \times \left(\frac{te_N}{s_N}\right) - 0.05721 \times \alpha_2 + 160.9 \times \left(\frac{te_N}{s_N}\right)^2 \quad 17$$

$$\begin{aligned} & - 3.033 \times \left(\frac{te_N}{s_N}\right) \times \alpha_2 + 0.005574 \times \alpha_2^2 + 504.7 \times \left(\frac{te_N}{s_N}\right)^3 \\ & - 13.3 \times \left(\frac{te_N}{s_N}\right)^2 \times \alpha_2 + 0.1267 \times \left(\frac{te_N}{s_N}\right) \times \alpha_2^2 - 0.000195 \times \alpha_2^3 \\ & + 346.9 \times \left(\frac{te_N}{s_N}\right)^4 - 11.64 \times \left(\frac{te_N}{s_N}\right)^3 \times \alpha_2 + 0.2035 \times \left(\frac{te_N}{s_N}\right)^2 \times \alpha_2^2 \\ & - 0.001499 \times \left(\frac{te_N}{s_N}\right) \times \alpha_2^3 + 2.099 \times 10^{-6} \times \alpha_2^4 \end{aligned}$$

$$\text{Lossincr}_N = 172.2 \times \left(\frac{te_N}{s_N}\right)^2 - 6.526 \times \left(\frac{te_N}{s_N}\right) + 0.05865 \quad 18$$

Where ,

$te_N$  is the trailing edge thickness;

$s_N$  is the profile pitch.

Mach number loss for convergent profiles was applicable for the outlet isentropic Mach number greater than 1.1, as shown in equation 19, derived from Figure 4. It was a function of the Mach determiner  $M_{detN}$  and relative outlet isentropic Mach number  $RelMachW_{outisenB}$ .

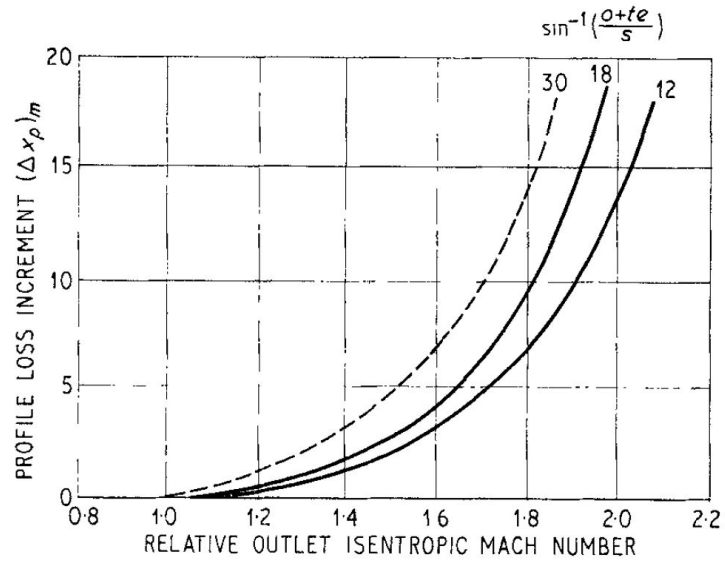


Figure 4 – Mach number loss for convergent blading

$$\begin{aligned}
 \Delta X_{pmN} = & -26.67 + 68.09 \times \text{RelMach}W_{\text{outisenN}} + 0.3699 \times M_{\text{detN}} & 19 \\
 & - 56.65 \times \text{RelMach}W_{\text{outisenN}}^2 - 0.9062 \times \text{RelMach}W_{\text{outisenN}} \times M_{\text{detN}} \\
 & + 0.002599 \times M_{\text{detN}}^2 + 15.49 \times \text{RelMach}W_{\text{outisenN}}^3 \\
 & + 0.5014 \times \text{RelMach}W_{\text{outisenN}}^2 \times M_{\text{detN}} \\
 & - 0.001435 \times \text{RelMach}W_{\text{outisenN}} \times M_{\text{detN}}^2
 \end{aligned}$$

where

$$M_{\text{detN}} = \frac{\arcsin(\text{thr}_N + \text{te}_N)}{s_N};$$

$$\text{RelMach}W_{\text{outisenB}} = \frac{V_{3s}}{SS_{\text{outB}}}$$

Blade back radius loss  $\Delta X_{PseN}$  was determined by the pitch to blade back radius ratio, profile loss increment  $\Delta X_{Pse}$  and outlet isentropic Mach number  $Mach_{\text{outisen}}$ . It was applicable on outlet isentropic Mach numbers greater than 0.8, and has been defined in Figure 5 and equation 20.

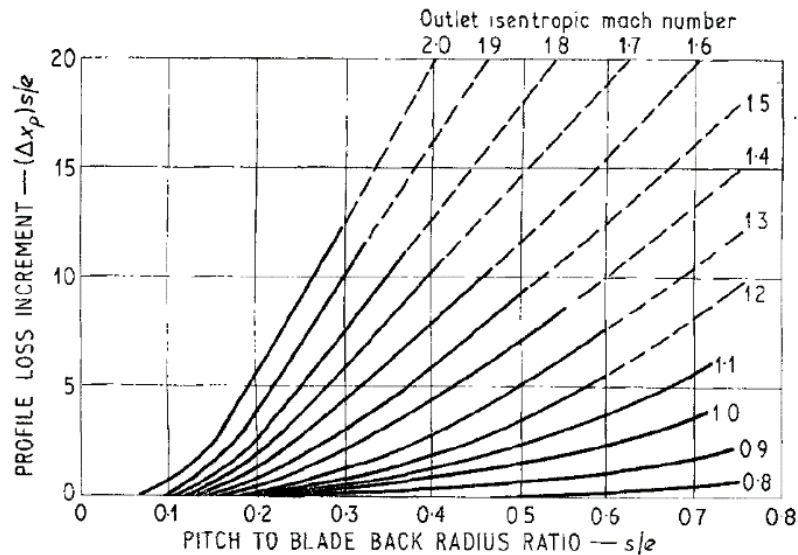


Figure 5 – Blade back radius ratio loss

$$\begin{aligned}
\Delta X_{pse_N} = & -9.176 + 93.52 \times \left(\frac{S_N}{b_N}\right) + 11.15 \times \text{Machoutisen}_N - 197.2 \times \left(\frac{S_N}{b_N}\right)^2 \\
& - 140.5 \times \left(\frac{S_N}{b_N}\right) \times \text{Machoutisen}_N + 4.793 \times \text{Machoutisen}_N^2 \\
& + 88.67 \times \left(\frac{S_N}{b_N}\right)^3 + 261.3 \times \left(\frac{S_N}{b_N}\right)^2 \times \text{Machoutisen}_N \\
& + 34.38 \times \left(\frac{S_N}{b_N}\right) \times \text{Machoutisen}_N^2 - 8.748 \times \text{Machoutisen}_N^3 \\
& - 83.59 \times \left(\frac{S_N}{b_N}\right)^3 \times \text{Machoutisen}_N - 56.58 \times \left(\frac{S_N}{b_N}\right)^2 \times \text{Machoutisen}_N^2 \\
& + 10.13 \times \left(\frac{S_N}{b_N}\right)^2 \times \text{Machoutisen}_N^3 + 2.157 \times \text{Machoutisen}_N^4
\end{aligned}$$

## Secondary losses

$N_{SaspectratN}$  indicated the secondary loss due to the aspect ratio, determined by the camber length and height, as shown in equation 21 and Figure 6.  $X_{sbN}$  indicated the basic secondary loss factor which was a function of the relative velocities across the blading, pitch, lift parameter and backbone length, as shown in equation 22 and Figure 7.

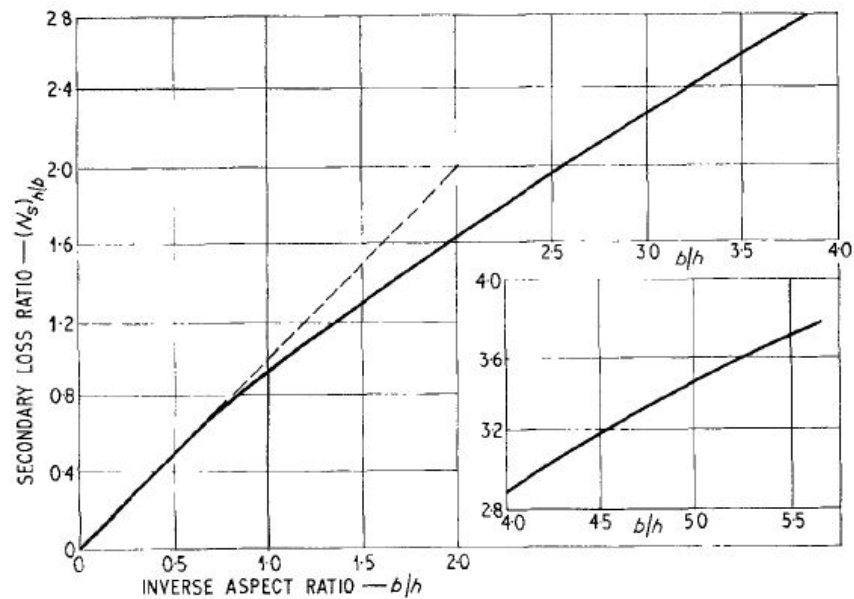


Figure 6 – Secondary loss aspect ratio factor

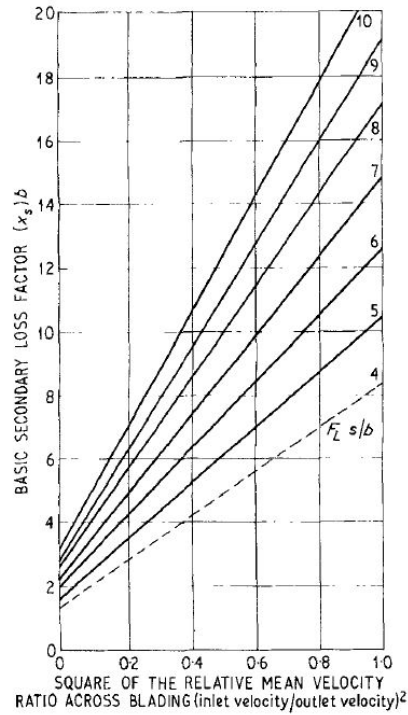


Figure 7 – Secondary loss and basic loss factor

$$N_{SaspectratN} = -0.08718 \times \left(\frac{b_N}{ht_N}\right)^3 - 0.08718 \times \left(\frac{b_N}{ht_N}\right)^2 + 0.9544 \times \left(\frac{b_N}{ht_N}\right) + 0.02289 \quad 21$$

$$\begin{aligned} X_{sbN} = & 0.4842 + 0.4659 \times V_{ratiosqrN} + 0.07775 \times \left(\frac{F_{LN} \times S_N}{b_N}\right) - 0.2736 \times V_{ratiosqrN}^2 \quad 22 \\ & + 1.694 \times V_{ratiosqrN} \times \left(\frac{F_{LN} \times S_N}{b_N}\right) + 0.04304 \times \left(\frac{F_{LN} \times S_N}{b_N}\right)^2 \\ & - 0.05759 \times V_{ratiosqrN}^2 \times \left(\frac{F_{LN} \times S_N}{b_N}\right) \\ & + 0.01489 \times V_{ratiosqrN} \times \left(\frac{F_{LN} \times S_N}{b_N}\right)^2 - 0.002299 \times \left(\frac{F_{LN} \times S_N}{b_N}\right)^3 \end{aligned}$$

## APPENDIX 2

### Engineering Equation Solver (EES) Code for the Craig and Cox Loss Model

The EES code using the Craig and Cox design point and Moustapha off-design point loss model has been presented below. The polynomial equations presented in Appendix 1 were used to determine turbine and cycle efficiency.

```
Function noz_5(CR_n,Z_n1,Z_n2,Z_n3,Z_n4,Z_n5,Z_n6)
```

```
If (CR_n<1.1) Then
```

$$A:=Z_{n1}*(1.1-CR_n)/(1.1-1)+(Z_{n2})*((CR_n-1)/(1.1-1))$$

```
Endif
```

```
If(CR_n<1.3) AND (CR_n>=1.1) Then
```

$$A:=Z_{n2}*(1.3-CR_n)/(1.3-1.1)+(Z_{n3})*((CR_n-1.1)/(1.3-1.1))$$

```
Endif
```

```
If (CR_n<1.5) AND (CR_n>=1.3) Then
```

$$A:=Z_{n3}*(1.5-CR_n)/(1.5-1.3)+(Z_{n4})*((CR_n-1.3)/(1.5-1.3))$$

```
Endif
```

```
If (CR_n<2) AND (CR_n>=1.5) Then
```

$$A:=Z_{n4}*(2-CR_n)/(2-1.5)+(Z_{n5})*((CR_n-1.5)/(2-1.5))$$

```
Endif
```

```
If (CR_n<5) AND (CR_n>=2.0) Then
```

$$A:=Z_{n5}*(5-CR_n)/(5-2)+(Z_{n6})*((CR_n-2)/(5-2))$$

```
Else A:= Z_n6
```

```
noz_5:=A
```

```
End
```

```
Function bl_5(CR_b,Z_b1,Z_b2,Z_b3,Z_b4,Z_b5,Z_b6)
```

```
If (CR_b<1.1) Then
```

$$B:=Z_{b1}*(1.1-CR_b)/(1.1-1)+(Z_{b2})*((CR_b-1)/(1.1-1))$$

```
Endif
```

```
If(CR_b<1.3) AND (CR_b>=1.1) Then
```

$$B:=Z_{b2}*(1.3-CR_b)/(1.3-1.1)+(Z_{b3})*((CR_b-1.1)/(1.3-1.1))$$

```
Endif
```

```
If (CR_b<1.5) AND (CR_b>=1.3) Then
```

$$B:=Z_{b3}*(1.5-CR_b)/(1.5-1.3)+(Z_{b4})*((CR_b-1.3)/(1.5-1.3))$$

```
Endif
```

```
If (CR_b<2) AND (CR_b>=1.5) Then
```

$$B:=Z_{b4}*(2-CR_b)/(2-1.5)+(Z_{b5})*((CR_b-1.5)/(2-1.5))$$

```
Endif
```

```
If (CR_b<5) AND (CR_b>=2.0) Then
```

$$B:=Z_{b5}*(5-CR_b)/(5-2)+(Z_{b6})*((CR_b-2)/(5-2))$$

```
Else B:=Z_b6
```

```
bl_5:=B
```

```
End
```

```
Function noz_7(ZZ_n,ZZ_n1,ZZ_n2,ZZ_n3)
```

If (ZZ\_n<=0.4) Then  
A:=ZZ\_n1  
Endif

If(ZZ\_n<0.8) AND (ZZ\_n>0.4) Then  
A:=ZZ\_n1\*(ZZ\_n2-ZZ\_n1)\*(ZZ\_n-0.4)/(0.8-0.4)  
Endif

If (ZZ\_n<1.2) AND (ZZ\_n>=0.8) Then  
A:=ZZ\_n2\*(ZZ\_n3-ZZ\_n2)\*(ZZ\_n-0.8)/(1.2-0.8)  
Endif

If (ZZ\_n>=1.2) Then  
A:=ZZ\_n3  
Endif

noz\_7:=A  
End

"Total loss is the sum of Group 1 and Group 2 Losses"

"Group 1 Losses include Nozzle Profile Loss, Nozzle Secondary Loss, Nozzle Annulus Loss, Blade Profile Loss, Blade Secondary Loss and Blade Annulus loss"

"Group 2 losses include Nozzle Gland Leakage loss, balance hole loss Tip leakage loss, Lacing Wire Loss, Wetness Loss Disc Windage Loss, Partial Admission Loss"

"Group 1 losses can be divided in 2 parts - Nozzle losses and Blade losses"

"Further Nozzle losses have 3 parts- Primary , Secondary and Annulus. Blade losses also have 3 parts- Primary , Secondary and Annulus."

"Terminology  
1 is before Nozzle  
2 is between Nozzle and Blade  
3 is after Blade"

"INPUTS"

"Mass flow Rate in TPH through entire turbine,Hub Diameter in m ,RPM"  
MFR=10  
D\_hub= 0.660  
N=3000  
DoR=0.1

" R245fa Conditions before stage. P in ata , Temp in Celsius"  
P\_1=16  
T\_1=160

"R245fa Parameters After Stage. P in ata , Temp in Celsius"  
P\_3 = 2  
T\_aftcondenser=28  
Boiler\_Heatinput = 5.5\*(178)

"Nozzle"  
No\_Nozzles=40  
alpha\_2=14 "Nozzle exit Angle / Fluid outlet angle  
from Nozzle, used in fig 4 "  
Ht\_N= 0.02524 "Nozzle Height "

thr_N=0.004978	" Throat Width"
s_N=0.0294	"Nozzle pitch"
b_N =0.07364	"Nozzle backbone length (Camber length) "
te_N=0.0003	"Nozzle Trailing edge thickness"
leadedgedia_N = 0.003236	" Nozzle leading edge dia"
alphametal_Nout = 14	" Nozzle exit metal angle "
alphametal_Nin = 90	" Nozzle inlet metal angle"
stagger_N = 30	" nozzle stagger angle"
"Blade"	
Overlap=0.00254	"Overlap of Blade over Nozzle"
Ht_B=Ht_N+Overlap	"Blade Height"
thr_B=0.0035299	" Throat Width"
s_B=0.0112268	"Blade pitch"
b_B=0.0217	"Blade backbone length (Camber length)"
te_B=0.0003	"Blade Trailing edge thickness"
"No of Blades"	
No_Blades=90	"shroud thickness"
thk_shr=0.003	"Shroud to casing clearance"
Clearance_ShroudCasing=0.0254	"Nozzle Blade Gap"
E_nb=0.024	" Blade inlet metal angle"
alphametal_Bin = 23	
alphametal_Bout=45	
leadedgedia_B = 0.01	
stagger_B = 30	
"Equivalent Grain Size ks*1000/b"	
ks=2	
b=100000	
"Fluid inlet angle to Nozzle"	
alpha_Nin=90	
"CALCULATIONS"	
"Loss Composition"	
"Nozzle Primary Loss"	
$G_{pN}=(X_{pbN}*N_{prN}*N_{piN}*N_{ptN})+lossincr_N+delX_{PseN}+delX_{pmN}$	
"Nozzle Secondary Loss"	
$G_{sN}=(N_{prN}*N_{SaspectratN}*X_{sbN})*(N_{siN})$	
"Blade Primary Loss"	
$G_{pB}=(X_{pbB}*N_{prB}*N_{piB}*N_{ptB})+lossincr_B+delX_{PseB}+delX_{pmB}$	
"Blade Secondary Loss"	
$G_{sB}=(N_{prB}*N_{SaspectratB}*X_{sbB})*(N_{siB})$	
"Annulus Loss"	
$G_a=X_{a1}$	
$G_{Group1Nozzle}=(G_{pN}+G_{sN}+G_a)/100$	
$G_{Group1Blade}=(G_{pB}+G_{sB}+G_a*(C_3)^2/(V_3)^2)/100$	
$G_{total}=(G_{Group1Nozzle}+G_{Group1Blade})$	

MFR\_persec=MFR\*1000/3600

Y. C. Engineer, PhD Thesis, Aston University, 2022

$SpVol\_1 = volume(R245fa, T=T\_1, P=P\_1)$   
 $Vol\_1 = SpVol\_1 * MFR\_persec$   
 $Inlet\_Area = No\_Nozzles * s\_N * Ht\_N$   
 $C\_1 = Vol\_1 / Inlet\_Area$   
 $SpVol\_2 = volume(R245fa, T=T\_2, P=P\_2)$   
 $Vol\_2 = SpVol\_2 * MFR\_persec$   
 $Vol\_2eachNozzle = Vol\_2 / No\_Nozzles$   
 $SpVol\_3 = volume(R245fa, T=T\_3, P=P\_3)$   
 $Vol\_3 = SpVol\_3 * MFR\_persec$   
 $Vol\_3eachNozzle = Vol\_3 / No\_Nozzles$

"Thermodynamic Calculations"

"Working fluid Properties"

$H\_01 = enthalpy(R245fa, T=T\_1, P=P\_1)$   
 here"

"Enthalpy of Inlet velocity  $C\_1$  is ignored

$H\_1 = H\_01$

"Static Enthalpy = Stagnation Enthalpy"

$S\_01 = entropy(R245fa, T=T\_1, P=P\_1)$

$H\_2s = H\_1s * DoR + (1 - DoR) * H\_3s$

"Isentropic Enthalpy after nozzle"

$P\_2s = pressure(R245fa, h=H\_2s, s=S\_2s)$

$T\_2s = temperature(R245fa, h=H\_2s, s=S\_2s)$

$S\_2s = S\_01$

$C\_2s = sqrt(2 * (H\_01 - H\_2s)) * (sqrt(1000))$

$C\_w2s = (C\_2s * cos(alpha\_2))$

$C\_a2s = (C\_2s * sin(alpha\_2))$

$C\_2 = sqrt(2 * 1000 * (H\_01 - H\_2s) / (1 + G\_Group1Nozzle))$

$C\_w2 = C\_2 * cos(alpha\_2)$

$C\_a2 = C\_2 * sin(alpha\_2)$

$H\_02 = H\_2 + (0.5 * (C\_2)^2) / 1000$

$S\_3s = S\_2s$

$H\_1s = H\_01$

"assuming Isentropic expansion"

$H\_3s = enthalpy(R245fa, s=S\_3s, P=P\_3)$

$T\_3s = temperature(R245fa, P=P\_3, h=H\_3s)$

"Assuming Complete isentropic Stage"

$H\_2 = H\_2s + G\_Group1Nozzle * ((C\_2s)^2) / 2000$

$P\_2 = P\_2s$

$T\_2 = temperature(R245fa, P=P\_2, h=H\_2)$

$S\_2 = entropy(R245fa, P=P\_2, h=H\_2)$

"Speed of sound"

$SS\_outN = soundspeed(R245fa, T=T\_2, P=P\_2)$

$SS\_outB = soundspeed(R245fa, T=T\_3, P=P\_3)$

"Mean, Tip Diameter"

$D\_mean = D\_hub + Ht\_B$

$D\_tip = D\_hub + 2 * Ht\_B + 2 * thk\_shr$

"Nozzle Throat Area"

$TotalThroatArea\_N = No\_Nozzles * Ht\_N * thr\_N$

$AreaPer\_N = Ht\_N * thr\_N$

"Blade Throat Area"

$TotalThroatArea\_B = No\_Blades * Ht\_B * thr\_B$

"Velocity Triangle Nozzle Calculation"

$U = pi * D\_mean * N / 60$

$U\_tip = pi * D\_tip * N / 60$

$$V_2 = \sqrt{(C_2)^2 + (U)^2 - (2 * C_2 * U * \cos(\alpha_2))}$$

$$V_{w2} = (C_2 * \cos(\alpha_2)) - U$$

$$V_{a2} = \sqrt{(V_2)^2 - (V_{w2})^2}$$

$$V_{2s} = \sqrt{(C_{2s})^2 + (U)^2 - (2 * C_{2s} * U * \cos(\alpha_2))}$$

$$V_{w2s} = (C_{2s} * \cos(\alpha_2)) - U$$

$$V_{a2s} = \sqrt{(V_{2s})^2 - (V_{w2s})^2}$$

$$\beta_2 = \arctan(V_{a2}/V_{w2})$$

$$UVRatio = U/C_{2s}$$

"Velocity triangle tip values"

$$V_{2tip} = \sqrt{(C_2)^2 + (U_{tip})^2 - (2 * C_2 * U_{tip} * \cos(\alpha_2))}$$

$$V_{w2tip} = (C_2 * \cos(\alpha_2)) - U_{tip}$$

$$V_{a2tip} = \sqrt{(V_{2tip})^2 - (V_{w2tip})^2}$$

"Velocity Triangle Blade Calculation"

$$\beta_3 = \beta_2$$

"Relative velocity after blade"

$$V_3 = \sqrt{(V_2^2 + 2000 * (H_2 - H_{3s})) / (1 + G_{Group1Blade}))}$$

$$V_{w3} = V_3 * \cos(\beta_3)$$

$$V_{w3tip} = V_3 * \cos(\beta_3)$$

"Power and Efficiency"

$$MFRKgperSec = MFR/3.6$$

$$ActualWorkDoneperKG = U * (V_{w2} + V_{w3}) / 1000$$

$$Power = MFRKgperSec * U * (V_{w2} + V_{w3}) / 1000$$

"Total to Total efficiency"

$$Workideal\_TT = MFRKgperSec * (H_{01} - H_{3s})$$

$$efficiencyTT = Power / Workideal\_TT$$

"Total to Static Efficiency"

$$V_{a3} = V_3 * \sin(\beta_3)$$

$$C_3 = \sqrt{(V_{w3} - U)^2 + (V_{a3})^2}$$

$$C_{w3} = (C_3 * \cos(\alpha_3))$$

$$C_{a3} = V_{a3}$$

$$\alpha_3 = \arcsin(c_{a3}/c_3)$$

$$Workideal\_TS = MFRKgperSec * (H_{01} - H_{3s} + ((C_3)^2) / 2000)$$

$$EfficiencyTS = Power / Workideal\_TS$$

"Flow Coefficient"

$$PHI\_FlowCoeff = C_{a2} / U$$

"Load Coefficient"

$$PSI\_LoadCoeff = (C_{w2} - C_{w3}) / U$$

"Ideal velocity after blade"

$$V_{3s} = V_2 + \sqrt{2 * 1000 * (H_2 - H_{3s})}$$

$$V_{w3s} = V_{3s} * \cos(\beta_2)$$

$$V_{a3s} = V_{3s} * \sin(\beta_2)$$

$$C_{3s} = \sqrt{(V_{w3s} - U)^2 + (V_{a3s})^2}$$

$$C_{w3s} = C_{3s} * \cos(\beta_2)$$

$$C_{a3s} = C_{3s} * \sin(\beta_2)$$

"After Blade"

$H_3 = H_2 + G_{\text{Group1Blade}} \cdot (C_3)^2 / 2000$   
 $T_3 = \text{temperature}(R245fa, h=H_3, s=S_3)$   
 $S_3 = \text{entropy}(R245fa, P=P_3, h=H_3)$   
 $\text{LeavingLoss} = ((C_3)^2) / 2000$   
 $\text{DELTAH}_{13\text{isen}} = (H_1) - (H_{3s})$

"Nozzle Reynolds Number"

$\rho_N = \text{density}(R245fa, P=P_2, s=S_{01})$   
 $\mu_n = \text{viscosity}(R245fa, P=P_2, h=H_1)$   
 $Re_n = (\rho_N \cdot (\text{Vol}_{2\text{eachNozzle}} / \text{AreaPer}_N) \cdot D_{\text{hydrN}}) / \mu_n$

"Nozzle Hydraulic Diameter"

$D_{\text{hydrN}} = (4 \cdot H_t \cdot \text{thr}_N) / (2 \cdot (H_t + \text{thr}_N))$

"Blade Reynolds Number"

$\rho_b = \text{density}(R245fa, P=P_3, s=S_3)$   
 $\mu_b = \text{viscosity}(R245fa, P=P_3, s=S_3)$   
 $Re_b = (\rho_b \cdot (\text{Vol}_{2\text{eachNozzle}} / \text{AreaPer}_N) \cdot D_{\text{hydrB}}) / \mu_b$

"Blade Hydraulic Diameter"

$D_{\text{hydrB}} = (4 \cdot H_t \cdot \text{thr}_B) / (2 \cdot (H_t + \text{thr}_B))$

"Off Design"

$\text{alphametal}_{N\text{axial}} = 90 - \text{alphametal}_{N\text{in}}$   
 $\text{alphametal}_{N\text{outaxial}} = 90 - \text{alphametal}_{N\text{out}}$   
 $\text{stagger}_{N\text{axial}} = 90 - \text{stagger}_N$

$\text{alphametal}_{B\text{inaxial}} = 90 - \text{alphametal}_{B\text{in}}$   
 $\text{alphametal}_{B\text{outaxial}} = 90 - \text{alphametal}_{B\text{out}}$   
 $\text{stagger}_{B\text{axial}} = 90 - \text{stagger}_B$

$\text{incidence} = \text{alphametal}_{N\text{outaxial}} - \text{alphametal}_{B\text{inaxial}}$

"Ratio of Nozzle Area to Blade Area"

$\text{Area}_{NB} = \text{TotalArea}_N / \text{TotalArea}_B$   
 $\text{TotalArea}_N = (3.14 \cdot ((D_{\text{mean}}/2) + (H_t/2))^2) - (3.14 \cdot ((D_{\text{mean}}/2) - (H_t/2))^2)$   
 $\text{TotalArea}_B = (3.14 \cdot ((D_{\text{mean}}/2) + (H_t/2))^2) - (3.14 \cdot ((D_{\text{mean}}/2) - (H_t/2))^2)$

"Ratio of Blade Area to Casing Area"

$\text{TotalArea}_{\text{Shrouded}} = (3.14 \cdot (D_{\text{tip}})^2) / 4$   
 $\text{TotalArea}_{\text{Casing}} = (3.14 \cdot (D_{\text{tip}} + (2 \cdot \text{Clearance}_{\text{ShroudCasing}}))^2) / 4$

"Pressure Ratio"

$\text{PressureRatio} = P_1 / P_3$

"Specific Speed"

$N_s = (N/60) \cdot \sqrt{\text{Vol}_3} / (\text{DELTAH}_{13\text{isen}} \cdot 1000^{0.75})$

"Size Parameter"

$\text{SizeParameter} = \sqrt{\text{Vol}_3} / (\text{DELTAH}_{13\text{isen}}^{0.25})$

"Volume Ratio"

$\text{VolumeRatio} = \text{Vol}_3 / \text{Vol}_1$

"NOZZLE LOSSES"

"Profile loss Ratio"

$$\text{ValN\_prN} = 0.9135 + (-4.299) \cdot (10)^{-8} \cdot \text{Re}_n + 0.7864 \cdot \text{ks}/b + 2.158 \cdot (10)^{-15} \cdot (\text{Re}_n)^2 + 1.255 \cdot (10)^{-8} \cdot \text{Re}_n \cdot \text{ks}/b + (-0.136) \cdot (\text{ks}/b)^2 + 1.333 \cdot (10)^{-14} \cdot (\text{Re}_n)^2 \cdot \text{ks}/b + (-1.092) \cdot (10)^{-9} \cdot \text{Re}_n \cdot (\text{ks}/b)^2 + 0.00787 \cdot (\text{ks}/b)^3$$

$$\text{N\_prN} = \max(0, \text{ValN\_prN})$$

"Lift Parameter"

"Fluid inlet Angle at minimum Loss Condition (alpha-i\_min) is 90"

$$\begin{aligned} \text{ValF\_LN} = & 9.807 + 0.2042 \cdot \alpha_2 + 0.1345 \cdot \alpha_{\text{Nin}} + 0.004977 \cdot (\alpha_2)^2 - \\ & 0.004855 \cdot \alpha_2 \cdot \alpha_{\text{Nin}} - 0.005104 \cdot (\alpha_{\text{Nin}})^2 + 3.081 \cdot (10)^{-5} \cdot (\alpha_2)^3 - \\ & 0.0002772 \cdot (\alpha_2)^2 \cdot \alpha_{\text{Nin}} + 0.0001862 \cdot \alpha_2 \cdot (\alpha_{\text{Nin}})^2 + 7.86 \cdot (10)^{-5} \cdot (\alpha_{\text{Nin}})^3 - \\ & 3.341 \cdot (10)^{-7} \cdot (\alpha_2)^4 + 3.035 \cdot (10)^{-7} \cdot (\alpha_2)^3 \cdot \alpha_{\text{Nin}} + \\ & 1.758 \cdot (10)^{-6} \cdot (\alpha_2)^2 \cdot (\alpha_{\text{Nin}})^2 - 1.952 \cdot (10)^{-6} \cdot \alpha_2 \cdot (\alpha_{\text{Nin}})^3 + \\ & - 5.388 \cdot (10)^{-7} \cdot (\alpha_{\text{Nin}})^4 + 4.641 \cdot (10)^{-9} \cdot (\alpha_2)^4 \cdot (\alpha_{\text{Nin}}) - 4.783 \cdot (10)^{-9} \cdot (\alpha_2)^3 \cdot (\alpha_{\text{Nin}})^2 + \\ & 1.157 \cdot (10)^{-10} \cdot (\alpha_2)^2 \cdot (\alpha_{\text{Nin}})^3 + 4.891 \cdot (10)^{-9} \cdot (\alpha_2) \cdot (\alpha_{\text{Nin}})^4 + 1.373 \cdot (10)^{-9} \cdot (\alpha_{\text{Nin}})^5 \end{aligned}$$

$$\text{F\_LN} = \max(0, \text{ValF\_LN})$$

"Modified Lift Coefficient & Basic Profile Loss"

$$\text{LC\_mN} = \text{F\_LN} \cdot s_N / b_N$$

"1 "

$$\text{Z\_n1} = 0.0278 \cdot \text{LC\_mN}^3 - 0.3845 \cdot \text{LC\_mN}^2 + 1.7306 \cdot \text{LC\_mN} - 1.0024$$

"1.1"

$$\text{Z\_n2} = 0.016 \cdot \text{LC\_mN}^3 - 0.2398 \cdot \text{LC\_mN}^2 + 1.1452 \cdot \text{LC\_mN} - 0.531$$

"1.3"

$$\text{Z\_n3} = 0.0102 \cdot \text{LC\_mN}^3 - 0.1598 \cdot \text{LC\_mN}^2 + 0.7972 \cdot \text{LC\_mN} - 0.2512$$

"1.5"

$$\text{Z\_n4} = 0.0049 \cdot \text{LC\_mN}^3 - 0.0701 \cdot \text{LC\_mN}^2 + 0.3212 \cdot \text{LC\_mN} + 0.381$$

"2"

$$\text{Z\_n5} = 0.0188 \cdot \text{LC\_mN}^2 - 0.2 \cdot \text{LC\_mN} + 1.179$$

"5"

$$\text{Z\_n6} = 0.0045 \cdot \text{LC\_mN}^2 - 0.0467 \cdot \text{LC\_mN} + 0.5104$$

$$(\text{ValX\_pbn} \cdot s_N \cdot \sin(\alpha_2)) / b_N = \text{noz}_5(\text{CR}_n, \text{Z\_n1}, \text{Z\_n2}, \text{Z\_n3}, \text{Z\_n4}, \text{Z\_n5}, \text{Z\_n6})$$

$$\text{X\_pbN} = \max(0, \text{ValX\_pbn})$$

"Trailing edge Thickness loss"

$$\text{tetopitchratio\_N} = \text{te}_N / s_N$$

$$\begin{aligned} \text{ValN\_ptN} = & 1.189 + 25.35 \cdot \text{tetopitchratio\_N} + -0.05721 \cdot \alpha_2 + \\ & 160.9 \cdot (\text{tetopitchratio\_N})^2 + -3.033 \cdot \text{tetopitchratio\_N} \cdot \alpha_2 + 0.005574 \cdot (\alpha_2)^2 + \\ & 504.7 \cdot (\text{tetopitchratio\_N})^3 - 13.3 \cdot (\text{tetopitchratio\_N})^2 \cdot (\alpha_2) + \\ & 0.1267 \cdot (\text{tetopitchratio\_N}) \cdot (\alpha_2)^2 + -0.000195 \cdot (\alpha_2)^3 + 346.9 \cdot (\text{tetopitchratio\_N})^4 + \\ & -11.64 \cdot (\text{tetopitchratio\_N})^3 \cdot \alpha_2 + 0.2035 \cdot (\text{tetopitchratio\_N})^2 \cdot (\alpha_2)^2 + \\ & -0.001499 \cdot (\text{tetopitchratio\_N}) \cdot (\alpha_2)^3 + 2.099 \cdot 10^{-6} \cdot (\alpha_2)^4 \end{aligned}$$

$$\text{N\_ptN} = \max(1, \text{ValN\_ptN})$$

"Trailing Edge thickness Loss increment"

$$\text{Vallossincr\_N} = 172.2 \cdot (\text{tetopitchratio\_N})^2 + -6.526 \cdot (\text{tetopitchratio\_N}) + 0.05865$$

$$\text{lossincr\_N} = \max(0, \text{Vallossincr\_N})$$

"contraction Ratio"

$$\text{Sinalpha\_Nin} = \sin(\alpha_{\text{Nin}})$$

$$\text{Sinalpha\_2} = \sin(\alpha_2)$$

CR\_DeterminerN=1-(Sinalpha\_2/Sinalpha\_Nin)  
ZZ\_n=(s\_N/b\_N)

"0.4"

ZZ\_n1= 2.8225\*CR\_DeterminerN^3+ 0.9693\*CR\_DeterminerN^2+  
0.3523\*CR\_DeterminerN + 1.107

"0.8"

ZZ\_n2 = 1.6255\*CR\_DeterminerN^3 + 1.1095\*CR\_DeterminerN^2 +  
0.2963\*CR\_DeterminerN + 1.081

"1.2"

ZZ\_n3= 1.4543\*CR\_DeterminerN^2 + 0.2455\*CR\_DeterminerN+ 1.0402

ValCR\_n=noz\_7(ZZ\_n,ZZ\_n1,ZZ\_n2,ZZ\_n3)

CR\_n=max(1,ValCR\_n)

"Mach No Loss"

RelMachW\_outisenN=C\_2s/SS\_outN

Mach\_determinerN=arcsin((thr\_N+te\_N)/s\_N)

ValdelX\_pmN =-26.67 + 68.09\*RelMachW\_outisenN +0.3699\*Mach\_determinerN +-  
56.65\*(RelMachW\_outisenN)^2 + -0.9062\*RelMachW\_outisenN\*Mach\_determinerN  
+0.002599\*(Mach\_determinerN)^2 + 15.49\*(RelMachW\_outisenN)^3 +  
0.5014\*(RelMachW\_outisenN)^2\*(Mach\_determinerN) + -  
0.001435\*(RelMachW\_outisenN)\*(Mach\_determinerN)^2

delX\_pmN=max(0,ValdelX\_pmN)

"Blade back radius Loss/ Profile Loss"

Mach\_outisenN = C\_2S/SS\_outN

ValdelX\_PseN = -9.176 + 93.52 \*(s\_N/b\_N) + 11.15 \*Mach\_outisenN + -197.2\*(s\_N/b\_N)^2  
+ -140.5\*(s\_N/b\_N)\*Mach\_outisenN + 4.793\*(Mach\_outisenN)^2 + 88.67 \*(s\_N/b\_N)^3 +  
261.3\*(s\_N/b\_N)^2\*(Mach\_outisenN) + 34.38\*(s\_N/b\_N)\*(Mach\_outisenN)^2 + -  
8.748\*(Mach\_outisenN)^3 + -83.59 \*(s\_N/b\_N)^3\*(Mach\_outisenN) + -56.58  
\*(s\_N/b\_N)^2\*(Mach\_outisenN)^2 + 10.13\*(s\_N/b\_N)\*(Mach\_outisenN)^3 +  
2.157\*(Mach\_outisenN)^4

delX\_PseN=max(0,ValdelX\_PseN)

"Secondary Loss Aspect Ratio Factor"

ValN\_SaspectratN = 0.006704\*(b\_N/Ht\_N)^3 - 0.08718\*(b\_N/Ht\_N)^2 + 0.9544\*(b\_N/Ht\_N)  
+0.02289

N\_SaspectratN = max(1,ValN\_SaspectratN)

"Basic Secondary Loss Factor"

V\_ratiosqrN=(C\_1/C\_2)^2

ValX\_sbN= 0.4842 + 0.4659 \*V\_ratiosqrN + 0.07775\*(F\_LN\*s\_N/b\_N) + - 0.2736  
\*(V\_ratiosqrN)^2 + 1.694 \*(V\_ratiosqrN)\*(F\_LN\*s\_N/b\_N) + 0.04304\*(F\_LN\*s\_N/b\_N)^2 + -  
0.05759\*(V\_ratiosqrN)^2\*(F\_LN\*s\_N/b\_N) + 0.01489\*(V\_ratiosqrN)\*(F\_LN\*s\_N/b\_N)^2 + -  
0.002299\*(F\_LN\*s\_N/b\_N)^3

X\_sbN=max(1,ValX\_sbN)

"BLADE LOSSES"

"Profile loss Ratio"

$$\text{ValN\_prB} = 0.9135 + (-4.299) \cdot (10)^{-8} \cdot \text{Re}_b + 0.7864 \cdot \text{ks}/b + 2.158 \cdot (10)^{-15} \cdot (\text{Re}_b)^2 + 1.255 \cdot (10)^{-8} \cdot \text{Re}_b \cdot \text{ks}/b + (-0.136) \cdot (\text{ks}/b)^2 + 1.333 \cdot (10)^{-14} \cdot (\text{Re}_b)^2 \cdot \text{ks}/b + (-1.092) \cdot (10)^{-9} \cdot \text{Re}_b \cdot (\text{ks}/b)^2 + 0.00787 \cdot (\text{ks}/b)^3$$

$$\text{N\_prB} = \max(0, \text{ValN\_prB})$$

"Lift Parameter"

"Fluid inlet Angle at minimum Loss Condition (alpha-i\_min) is 90"

$$\begin{aligned} \text{ValF\_LB} = & 9.807 + 0.2042 \cdot \beta_3 + 0.1345 \cdot \beta_2 + 0.004977 \cdot (\beta_3)^2 - \\ & 0.004855 \cdot \beta_3 \cdot \beta_2 - 0.005104 \cdot (\beta_2)^2 + 3.081 \cdot (10)^{-5} \cdot (\beta_3)^3 - \\ & 0.0002772 \cdot (\beta_3)^2 \cdot \beta_2 + 0.0001862 \cdot \beta_3 \cdot (\beta_2)^2 + 7.86 \cdot (10)^{-5} \cdot (\beta_2)^3 - \\ & 3.341 \cdot (10)^{-7} \cdot (\beta_3)^4 + 3.035 \cdot (10)^{-7} \cdot (\beta_3)^3 \cdot \beta_2 + 1.758 \cdot (10)^{-6} \cdot (\beta_3)^2 \cdot (\beta_2)^2 - \\ & 1.952 \cdot (10)^{-6} \cdot \beta_3 \cdot (\beta_2)^3 + -5.388 \cdot (10)^{-7} \cdot (\beta_2)^4 + 4.641 \cdot (10)^{-9} \cdot (\beta_3)^4 \cdot (\beta_2) - \\ & 4.783 \cdot (10)^{-9} \cdot (\beta_3)^3 \cdot (\beta_2)^2 + 1.157 \cdot (10)^{-10} \cdot (\beta_3)^2 \cdot (\beta_2)^3 + 4.891 \cdot (10)^{-9} \cdot (\beta_3) \cdot (\beta_2)^4 + \\ & 1.373 \cdot (10)^{-9} \cdot (\beta_2)^5 \end{aligned}$$

$$\text{F\_LB} = \max(0, \text{ValF\_LB})$$

"Modified Lift Coefficient & Basic Profile Loss"

$$\text{LC\_mB} = \text{F\_LB} \cdot s_B / b_B$$

"1 "

$$\text{Z\_b1} = 0.0278 \cdot \text{LC\_mB}^3 - 0.3845 \cdot \text{LC\_mB}^2 + 1.7306 \cdot \text{LC\_mB} - 1.0024$$

"1.1"

$$\text{Z\_b2} = 0.016 \cdot \text{LC\_mB}^3 - 0.2398 \cdot \text{LC\_mB}^2 + 1.1452 \cdot \text{LC\_mB} - 0.531$$

"1.3"

$$\text{Z\_b3} = 0.0102 \cdot \text{LC\_mB}^3 - 0.1598 \cdot \text{LC\_mB}^2 + 0.7972 \cdot \text{LC\_mB} - 0.2512$$

"1.5"

$$\text{Z\_b4} = 0.0049 \cdot \text{LC\_mB}^3 - 0.0701 \cdot \text{LC\_mB}^2 + 0.3212 \cdot \text{LC\_mB} + 0.381$$

"2"

$$\text{Z\_b5} = 0.0188 \cdot \text{LC\_mB}^2 - 0.2 \cdot \text{LC\_mB} + 1.179$$

"5"

$$\text{Z\_b6} = 0.0045 \cdot \text{LC\_mB}^2 - 0.0467 \cdot \text{LC\_mB} + 0.5104$$

$$(\text{ValX\_pbb} \cdot s_B \cdot \sin(\beta_3)) / b_B = \text{bl}_5(\text{CR}_b, \text{Z\_b1}, \text{Z\_b2}, \text{Z\_b3}, \text{Z\_b4}, \text{Z\_b5}, \text{Z\_b6})$$

$$\text{X\_pbb} = \max(0, \text{ValX\_pbb})$$

"Trailing edge Thickness loss"

$$\text{tetopitchratio\_B} = \text{te}_B / s_B$$

$$\begin{aligned} \text{ValN\_ptB} = & 1.189 + 25.35 \cdot \text{tetopitchratio\_B} + -0.05721 \cdot \beta_3 + 160.9 \cdot (\text{tetopitchratio\_B})^2 \\ & + -3.033 \cdot \text{tetopitchratio\_B} \cdot \beta_3 + 0.005574 \cdot (\beta_3)^2 + 504.7 \cdot (\text{tetopitchratio\_B})^3 - 13.3 \\ & \cdot (\text{tetopitchratio\_B})^2 \cdot (\beta_3) + 0.1267 \cdot (\text{tetopitchratio\_B}) \cdot (\beta_3)^2 + - \\ & 0.000195 \cdot (\beta_3)^3 + 346.9 \cdot (\text{tetopitchratio\_B})^4 + -11.64 \cdot (\text{tetopitchratio\_B})^3 \cdot \beta_3 + \\ & 0.2035 \cdot (\text{tetopitchratio\_B})^2 \cdot (\beta_3)^2 + -0.001499 \cdot (\text{tetopitchratio\_B}) \cdot (\beta_3)^3 + \\ & 2.099 \cdot 10^{-6} \cdot (\beta_3)^4 \end{aligned}$$

$$\text{N\_ptB} = \max(1, \text{ValN\_ptB})$$

"Trailing Edge thickness Loss increment"

$$\text{Vallossincr\_B} = 172.2 \cdot (\text{tetopitchratio\_B})^2 + -6.526 \cdot (\text{tetopitchratio\_B}) + 0.05865$$

$$\text{lossincr\_B} = \max(0, \text{Vallossincr\_B})$$

"Contraction Ratio"

$$\sin \beta_2 = \sin(\beta_2)$$

$$\text{Sinbeta}_3 = \sin(\text{beta}_3)$$

$$\text{CR\_DeterminerB} = 1 - (\text{Sinbeta}_3 / \text{Sinbeta}_2)$$

$$\text{ValCR}_b = 1.098 + 0.7112 * \text{CR\_DeterminerB} + -0.02163 * (s_B / b_B) + 2.549 * (\text{CR\_DeterminerB})^2 + -0.8594 * \text{CR\_DeterminerB} * (s_B / b_B) + -0.008569 * (s_B / b_B)^2$$

$$\text{CR}_b = \max(1, \text{ValCR}_b)$$

"Mach No Loss"

$$\text{RelMachW\_outisenB} = V_3s / \text{SS\_outB}$$

$$\text{Mach\_determinerB} = \arcsin((\text{thr}_B + \text{te}_B) / s_B)$$

$$\text{ValdelX\_pmB} = -26.67 + 68.09 * \text{RelMachW\_outisenB} + 0.3699 * \text{Mach\_determinerB} + -56.65 * (\text{RelMachW\_outisenB})^2 + -0.9062 * \text{RelMachW\_outisenB} * \text{Mach\_determinerB} + 0.002599 * (\text{Mach\_determinerB})^2 + 15.49 * (\text{RelMachW\_outisenB})^3 + 0.5014 * (\text{RelMachW\_outisenB})^2 * (\text{Mach\_determinerB}) + -0.001435 * (\text{RelMachW\_outisenB}) * (\text{Mach\_determinerB})^2$$

$$\text{delX\_pmB} = \max(0, \text{ValdelX\_pmB})$$

"Blade back radius Loss/ Profile Loss"

$$\text{Mach\_outisenB} = C_3s / \text{SS\_outB}$$

$$\text{ValdelX\_PseB} = -9.176 + 93.52 * (s_B / b_B) + 11.15 * \text{Mach\_outisenB} + -197.2 * (s_B / b_B)^2 + -140.5 * (s_B / b_B) * \text{Mach\_outisenB} + 4.793 * (\text{Mach\_outisenB})^2 + 88.67 * (s_B / b_B)^3 + 261.3 * (s_B / b_B)^2 * (\text{Mach\_outisenB}) + 34.38 * (s_B / b_B) * (\text{Mach\_outisenB})^2 + -8.748 * (\text{Mach\_outisenB})^3 + -83.59 * (s_B / b_B)^3 * (\text{Mach\_outisenB}) + -56.58 * (s_B / b_B)^2 * (\text{Mach\_outisenB})^2 + 10.13 * (s_B / b_B) * (\text{Mach\_outisenB})^3 + 2.157 * (\text{Mach\_outisenB})^4$$

$$\text{delX\_PseB} = \max(0, \text{ValdelX\_PseB})$$

"Secondary Loss Aspect Ratio Factor"

$$\text{ValN\_SaspectratB} = 0.006704 * (b_B / \text{Ht}_B)^3 - 0.08718 * (b_B / \text{Ht}_B)^2 + 0.9544 * (b_B / \text{Ht}_B) + 0.02289$$

$$\text{N\_SaspectratB} = \max(1, \text{ValN\_SaspectratB})$$

"Basic Secondary Loss Factor"

$$\text{ValV\_ratiosqrB} = (V_2 / V_3)^2$$

$$V\_ratiosqrB = \min(1, \text{ValV\_ratiosqrB})$$

$$\text{ValX\_sbB} = 0.4842 + 0.4659 * V\_ratiosqrB + 0.07775 * (F_{LB} * s_B / b_B) + -0.2736 * (V\_ratiosqrB)^2 + 1.694 * (V\_ratiosqrB) * (F_{LB} * s_B / b_B) + 0.04304 * (F_{LB} * s_B / b_B)^2 + -0.05759 * (V\_ratiosqrB)^2 * (F_{LB} * s_B / b_B) + 0.01489 * (V\_ratiosqrB) * (F_{LB} * s_B / b_B)^2 + -0.002299 * (F_{LB} * s_B / b_B)^3$$

$$X\_sbB = \max(1, \text{ValX\_sbB})$$

"Annulus Wall Loss/ Uncontrolled Expansion loss"

$$\text{ValX\_a1} = 9.424 + -1.539 * (10)^{-9} * (\text{Area}_{NB}) + -12.98 * (E_{nb} / \text{Ht}_N) + 1.932 * (10)^{-9} * (\text{Area}_{NB})^2 + 3.352 * (10)^{-10} * (\text{Area}_{NB}) * (E_{nb} / \text{Ht}_N) + 14.53 * (E_{nb} / \text{Ht}_N)^2 + -8.973 * (10)^{-10} * (\text{Area}_{NB})^3 + -3.416 * (10)^{-10} * (\text{Area}_{NB})^2 * (E_{nb} / \text{Ht}_N) + -2.542 * (10)^{-11} * (\text{Area}_{NB}) * (E_{nb} / \text{Ht}_N)^2 + -3.81 * (E_{nb} / \text{Ht}_N)^3 + (2.244) * (10)^{-10} * (\text{Area}_{NB})^3 * (E_{nb} / \text{Ht}_N) + -3.54 * (10)^{-11} * (\text{Area}_{NB})^2 * (E_{nb} / \text{Ht}_N)^2 + 9.455e-12 * (\text{Area}_{NB}) * (E_{nb} / \text{Ht}_N)^3 + 0.3394 * (E_{nb} / \text{Ht}_N)^4$$

$$X_{a1} = \max(0, \text{Val}X_{a1})$$

" OFF-DESIGN MOUSTAPHA LOSS MODEL"

" Nozzle Primary Off design loss"

$$X_{NPoffdesign} = ((\text{leadedgedia}_N/s_N)^{-1.6}) * (\cos(\text{alphametal}_{Ninaxial}) / \cos(\text{alphametal}_{Noutaxial}))^{-2} * \text{incidence}$$

"X<sub>NPoff</sub> design should be between 0 and +800"

$$\text{del\_phiNoffdesign} = \sqrt{(0.778 * 10^{-5}) * X_{NPoffdesign} + 0.56 * 10^{-7} * (X_{NPoffdesign})^2 + (0.4 * 10^{-10}) * (X_{NPoffdesign})^3 + 2.054 * 10^{-19}}$$

$$\text{Val}N_{piN} = ((1 - (\text{stagger}_{Naxial} - 1)/2) * (\text{mach}_{outisenN})^2 * (1 / (\text{del\_phiNoffdesign})^{2-1})^{(-\text{stagger}_{Naxial} / (\text{stagger}_{Naxial} - 1) - 1) / (1 - (1 + ((\text{stagger}_{Naxial} - 1)/2) * (\text{mach}_{outisenN})^2)^{(-\text{stagger}_{Naxial} / (\text{stagger}_{Naxial} - 1)))})$$

$$N_{piN} = \text{abs}(\text{Val}N_{piN})$$

"Nozzle Secondary Offdesign loss"

$$N_{siN} = (2.718)^{(0.9 * X_{NSoffdesign})} + 13 * (X_{NSoffdesign})^2 + 400 * (X_{NSoffdesign})^4$$

$$X_{NSoffdesign} = (\text{incidence} / (180 - (\text{alphametal}_{Ninaxial} + \text{alphametal}_{Noutaxial}))) * ((\cos(\text{alphametal}_{Ninaxial}) / \cos(\text{alphametal}_{Noutaxial}))^{-1.5}) * ((\text{leadedgedia}_N/s_N)^{-0.3})$$

" Blade Primary Off design loss"

$$X_{BPoffdesign} = ((\text{leadedgedia}_B/s_B)^{-1.6}) * (\cos(\text{alphametal}_{Binaxial}) / \cos(\text{alphametal}_{Boutaxial}))^{-2} * \text{incidence}$$

"X<sub>BPoff</sub> design should be between 0 and +800"

$$\text{del\_phiBoffdesign} = \sqrt{(0.778 * 10^{-5}) * X_{BPoffdesign} + 0.56 * 10^{-7} * (X_{BPoffdesign})^2 + (0.4 * 10^{-10}) * (X_{BPoffdesign})^3 + 2.054 * 10^{-19}}$$

$$\text{Val}N_{piB} = ((1 - (\text{stagger}_{Baxial} - 1)/2) * (\text{mach}_{outisenB})^2 * (1 / (\text{del\_phiBoffdesign})^{2-1})^{(-\text{stagger}_{Baxial} / (\text{stagger}_{Baxial} - 1) - 1) / (1 - (1 + ((\text{stagger}_{Baxial} - 1)/2) * (\text{mach}_{outisenB})^2)^{(-\text{stagger}_{Baxial} / (\text{stagger}_{Baxial} - 1)))})$$

$$N_{piB} = \text{abs}(\text{Val}N_{piB})$$

"Nozzle Secondary Offdesign loss"

$$N_{siB} = (2.718)^{(0.9 * X_{BSoffdesign})} + 13 * (X_{BSoffdesign})^2 + 400 * (X_{BSoffdesign})^4$$

$$X_{BSoffdesign} = (\text{incidence} / (180 - (\text{alphametal}_{Binaxial} + \text{alphametal}_{Boutaxial}))) * ((\cos(\text{alphametal}_{Binaxial}) / \cos(\text{alphametal}_{Boutaxial}))^{-1.5}) * ((\text{leadedgedia}_B/s_B)^{-0.3})$$

"ANNULUS LOSSES"

"Shroud Loss"

$$A_k = \text{TotalArea}_{Casing} - \text{TotalArea}_{Shrouded}$$

$$A_t = \text{TotalThroatArea}_B$$

$$x = \text{Blade\_TipLeakageCoeff}$$

$$y = (\text{Overlap}/2) / \text{Ht}_B$$

$$si = V_3 / V_2$$

"Moving blade velocity coefficient"

$$F_k = 0.1025 + 0.8093 * x + - 1.928 * y + - 0.3397 * x^2 + - 8.332 * x * y + 18.59 * y^2 + 5.272 * x^2 * y + 13.68 * x * y^2 + - 35.69 * y^3$$

$$\text{Blade\_TipLeakageCoeff} = (((1 - (si)^2) / (si)^2) + ((V_{w3tip})^2 - (V_{w2tip})^2) / (V_{w3tip})^2)$$

$$(\text{DELTA}_{\text{eta\_Shroud}}) = (F_k) * (A_k) / (A_t) * (\text{eta\_afterUncontrolledExpLoss})"$$

"CYCLE EFFICIENCY"

"1 After phase change Condenser 2"

$P_{aftcondenser} = p_{sat}(R245fa, T=T_{aftcondenser})$   
 $H_{aftcondenser} = \text{enthalpy}(R245fa, P=P_{aftcondenser}, x=0)$   
 $S_{aftcondenser} = \text{entropy}(R245fa, P=P_{aftcondenser}, x=0)$

"2 After Pump "

$P_{pump} = P_1$   
 $S_{pump} = \text{entropy}(R245fa, P=P_1, T=T_{pump})$   
 $H_{pump} = \text{enthalpy}(R245fa, P=P_{pump}, T=T_{pump})$   
 $T_{pump} = T_{aftcondenser} + 4.74$

"3 After Economiser"

$P_{economiser} = P_{pump}$   
 $T_{economiser} = T_{boiler} - 1$   
 $H_{economiser} = \text{enthalpy}(R245fa, P=P_{economiser}, T=T_{economiser})$   
 $S_{economiser} = \text{entropy}(R245fa, P=P_{economiser}, T=T_{economiser})$

"4 After Boiler"

$P_{boiler} = P_{pump}$   
 $T_{boiler} = t_{sat}(R245fa, P=P_{boiler})$   
 $H_{boiler} = \text{enthalpy}(R245fa, P=P_{boiler}, x=1)$   
 $S_{boiler} = \text{entropy}(R245fa, P=P_{boiler}, x=1)$

"5 After Turbine"

"All data taken from Loss model"

" 6 After desuperheating Condenser"

$P_{aftmidcondenser} = P_{aftcondenser}$   
 $H_{aftmidcondenser} = \text{enthalpy}(R245fa, P=P_3, x=1)$   
 $S_{aftmidcondenser} = \text{entropy}(R245fa, P=P_3, x=1)$   
 $T_{aftmidcondenser} = \text{temperature}(R245fa, P=P_3, x=1)$

"Turbine Work Done"

$W_{actual} = \text{MFRKgperSec} * (H_1 - H_3)$

"Pump Work Done"

$W_{Pump} = \text{MFRKgperSec} * (H_{pump} - H_{aftcondenser})$

"Boiler Heat Energy Used"

$\text{Heatabsorbed}_{Boiler} = \text{MFRKgperSec} * (H_{boiler} - H_{pump})$

"Condenser Heat Energy Used"

$\text{HeatLoss}_{Cond} = \text{MFRKgperSec} * (H_3 - H_{aftcondenser})$   
 $\text{HeatLoss}_{Cond1} = \text{MFRKgperSec} * (H_3 - H_{aftmidcondenser})$   
 $\text{HeatLoss}_{Cond2} = \text{MFRKgperSec} * (H_{aftmidcondenser} - H_{aftcondenser})$

$\text{Heatdrop}_{Cond} = (H_3 - H_{aftcondenser})$

$\text{Heatdrop}_{Cond1} = (H_3 - H_{aftmidcondenser})$

$\text{Heatdrop}_{Cond2} = (H_{aftmidcondenser} - H_{aftcondenser})$

"Cycle Efficiency"

$\text{Efficiency}_{cycle} = \text{Power} * 100 / (W_{Pump} + \text{Boiler}_{Heatinput})$

$\text{Superheat}_{inlet} = T_1 - t_{sat}(R245fa, P=P_1)$

$\text{Superheat}_{outlet} = T_3 - t_{sat}(R245fa, P=P_3)$

"T-S DIAGRAM"

"Superheater Outlet / Turbine Inlet"

$P[4] = P\_1$   
 $T[4] = T\_1$   
 $H[4] = H\_1$   
 $S[4] = S\_01$

"Turbine Outlet"

$P[5] = P\_3$   
 $T[5] = T\_3$   
 $H[5] = H\_3$   
 $S[5] = S\_3$

"Mid Condenser Outlet"

$P[6] = P\_aftmidcondenser$   
 $T[6] = T\_aftmidcondenser$   
 $H[6] = H\_aftmidcondenser$   
 $S[6] = S\_aftmidcondenser$

"Condenser Outlet"

$P[7] = P\_aftcondenser$   
 $T[7] = T\_aftcondenser$   
 $H[7] = H\_aftcondenser$   
 $S[7] = S\_aftcondenser$

$P[8] = P[1]$   
 $T[8] = T[1]$   
 $H[8] = H[1]$   
 $S[8] = S[1]$

"Pump outlet"

$P[1] = P\_pump$   
 $T[1] = T\_pump$   
 $H[1] = H\_pump$   
 $S[1] = S\_pump$

"Economiser outlet"

$P[2] = P\_pump$   
 $T[2] = T\_economiser$   
 $H[2] = H\_economiser$   
 $S[2] = S\_economiser$

"Evaporator Outlet"

$P[3] = P\_boiler$   
 $T[3] = T\_boiler$   
 $H[3] = H\_boiler$   
 $S[3] = S\_boiler$

## APPENDIX 3

### Engineering Equation Solver (EES) Code for the Soderberg loss model

The EES code used to determine turbine and cycle efficiency applying the Soderberg design point and Moustapha off-design point loss model is presented below.

"INPUTS"

"Mass flow Rate in TPH through entire turbine, Hub Diameter and RPM"

MFR=10

Dhub= 0.660

N=5000

" R245fa Parameters before stage"

P1=16

T1=160

"R245fa Parameters After Stage"

P2= 2

"Nozzle Metal Exit Angle, Height, Throat and Axial Length"

alpha\_2=14

htn= 0.02524

thrn= 0.004978

bn=0.036

"Blade height and Axial Length"

htb=0.02778

bb=0.0143

" Condenser temperature"

T\_aftcondenser=40

"RESULTS"

"R245fa Properties"

C1=0

C1s=0

H01=enthalpy(R245fa, T=T1, P=P1)

H1=H01

S01=entropy(R245fa, T=T1, P=P1)

H2s=enthalpy(R245fa, P=P2, s=S2s)

H2=H01-(C2)^2/(2\*1000)

S2=entropy(R245fa, P=P2, h=H2)

H02s=H2s+((C2s)^2)/2000

H02=H2+((C2)^2)/2000

H03s=H3s+(C3s)^2/2000

H03=H3+((C3)^2)/2000

"Mean Diameter"

Dmean=Dhub+htb

"Hydraulic Diameter"  
 $D_{hydr} = (4 * h_{tn} * t_{hrn}) / (2 * (h_{tn} + t_{hrn}))$   
 "Throat Area"  
 $A_{rea} = (h_{tn} * t_{hrn})$   
 "Nozzle Area for 1' Vane with full arc"  
 $A_{reaTotal} = 40 * A_{rea}$

" Velocity after nozzle ignoring losses"  
 $C_{2s} = \sqrt{2 * (h_{01} - h_{2s})} * (\sqrt{1000})$

"assuming Isentropic expansion"  
 $S_{2s} = S_{01}$   
 $S_{3s} = S_{2s}$

"Finding Reynolds Number "  
 $\rho = \text{density}(R245fa, P=P2, s=S_{2s})$   
 $\mu = \text{viscosity}(R245fa, P=P2, s=S_{2s})$   
 $Re = (\rho * C_{2s} * D_{hydr}) / \mu$

"U/C2s Ratio"  
 $U_{tip} = U + (2 * h_{tb})$   
 $UVRatio = U / C_{2s}$

"NOZZLE LOSSES"  
 "Placing Nozzle in Soderberg's model"  
 $defln = 90 - \alpha_2$   
 $G_{sn} = 0.04 + 0.06 * (defln / 100)^2$   
 "Height correction"  
 $HtCFn = b_n / h_{tn}$   
 $1 + G_{1n} = (1 + G_{sn}) * (0.993 + 0.021 * HtCFn)$   
 "Reynold's Number Correction Factor "  
 $ReCF = (100000 / Re)^{0.25}$   
 $G_n = G_{1n} * ReCF$

"C2"  
 $C_2 = C_{2s} / \sqrt{1 + G_n}$

$C_{\text{tangential}2} = (C_2 * \cos(\alpha_2))$   
 $C_{\text{axial}2} = (C_2 * \sin(\alpha_2))$

"Velocity Triangle, U , V2, Vw2, Va2, beta2"

$U = \pi * D_{mean} * N / 60$   
 $V_2 = \sqrt{(C_2)^2 + (U)^2 - (2 * C_2 * U * \cos(\alpha_2))}$   
 $V_{w2} = (C_2 * \cos(\alpha_2)) - U$   
 $V_{a2} = \sqrt{(V_2)^2 - (V_{w2})^2}$   
 $\beta_{a2} = \arctan(V_{a2} / V_{w2})$

"BLADE LOSSES"  
 "Placing blade in Soderberg's model"  
 $Inletangleb = \beta_{a2}$   
 $Exitangleb = \beta_{a2}$   
 $Deflb = 180 - (inletangleb + exitangleb)$   
 $G_{sb} = 0.04 + 0.06 * (deflb / 100)^2$   
 "Height Correction"  
 $1 + G_{1b} = (1 + G_{sb}) * (0.975 + 0.075 * (B_b / h_{tb}))$   
 "Reynold's Number Correction Factor"  
 "Taking ReCF From Above"  
 $G_b = G_{1b} * ReCF$

"Relative velocity after blade"

$$V3=V2/(\text{sqrt}(1+Gb))$$

$$Vw3=V3*\cos(\text{inletangleb})$$

"Power and Efficiency"

$$\text{MFRKgperSec}=\text{MFR}/3.6$$

$$\text{ActualWorkDoneperKG}=U*(Vw2+Vw3)/1000$$

$$\text{Power}=\text{MFRKgperSec}*U*(Vw2+Vw3)/1000$$

"Total to Total Efficiency"

$$H3s=H2s$$

$$\text{WorkidealTT}=\text{MFRKgperSec}*(H01-H3s)$$

$$\text{efficiencyTT}=\text{Power}/\text{WorkidealTT}$$

"Total to Static Efficiency"

$$Va3=V3*\sin(\text{Inletangleb})$$

$$C3=\text{sqrt}((Vw3-U)^2+(Va3)^2)$$

$$C_{\text{tangential3}}=(C3*\cos(\text{alphab}))$$

$$C_{\text{axial3}}=Va3$$

$$\text{alphab}=\arcsin(c_{\text{axial3}}/c3)$$

$$\text{WorkidealTS}=\text{MFRKgperSec}*(H01-H3s+((C3)^2)/2000)$$

$$\text{EfficiencyTS}=\text{Power}/\text{WorkidealTS}$$

"Ideal velocity after blade"

$$V3s=V2$$

$$Vw3s=V3s*\cos(\text{inletangleb})$$

$$Va3s=V3s*\sin(\text{Inletangleb})$$

$$C3s=\text{sqrt}((Vw3s-U)^2+(Va3s)^2)$$

"Actual velocity after blade"

$$H3=H2+((C2)^2)/(2000)-\text{ActualWorkDoneperKG}-((C3)^2)/(2000)$$

$$T3=\text{temperature}(R245fa,P=P2,h=H3)$$

$$S3=\text{entropy}(R245fa,P=P2,h=H3)$$

"Leaving Loss"

$$\text{LeavingLoss}=((C3)^2)/2000$$

$$T2=\text{temperature}(R245fa,P=P2,h=H2)$$

$$\text{densityafternozzle}=\text{density}(R245fa,P=P2,h=H2)$$

"T-S Diagram"

"Ideal Nozzle"

$$S\text{Nolsen}[1]=1$$

$$P\text{Isen}[1]=P1$$

$$T\text{Isen}[1]=T1$$

$$H0\text{Isen}[1]=H01$$

$$H\text{Isen}[1]=H01$$

$$S\text{Isen}[1]=S01$$

$$K\text{EIsen}[1]=((C1s)^2)/2000$$

"Actual Before Nozzle"

$$S\text{No}[1]=2$$

$$P[1]=P1$$

$$T[1]=T1$$

$$H0[1]=H01$$

H[1]=H01  
S[1]=S01  
KE[1]=((C1)^2)/2000

"Ideal after Nozzle"  
SNolsen[2]=3  
PIsen[2]=P2  
TIsen[2]=T2  
H0Isen[2]=H02s  
HIsen[2]=H2s  
SIsen[2]=S2s  
KEIsen[2]=((C2s)^2)/2000

"Actual after Nozzle"  
SNo[2]=4  
P[2]=P2  
T[2]=T2  
H0[2]=H02  
H[2]=H2  
S[2]=S2  
KE[2]=((C2)^2)/2000

"Ideal after Blade"  
SNolsen[3]=5  
PIsen[3]=P2  
TIsen[3]=T3  
H0Isen[3]=H03s  
HIsen[3]=H3s  
SIsen[3]=S3s  
KEIsen[3]=((C3s)^2)/2000

"Actual After Blade"  
SNo[3]=6  
P[3]=P2  
T[3]=T3  
H0[3]=H03  
H[3]=H3  
S[3]=S3  
KE[3]=((C3)^2)/2000

MachoutIsenB = V3s/Mach\_Number  
Mach\_Number=soundspeed(R245fa, T=T3, P=P2)  
Phi\_Flowcoeff = C\_axial2/U

"CYCLE EFFICIENCY"

"1 After phase change Condenser 2"  
P\_aftcondenser=p\_sat(R245fa, T=T\_aftcondenser)  
H\_aftcondenser=enthalpy(R245fa, P=P\_aftcondenser, x=0)  
S\_aftcondenser=entropy(R245fa, P=P\_aftcondenser, x=0)

"2 After Pump "  
P\_pump=p\_sat(R245fa, T=T\_1)  
S\_pump=S\_aftcondenser  
H\_pump=enthalpy(R245fa, P=P\_pump, s=S\_pump)

"3 After Economiser"  
P\_economiser=P\_pump

H\_economiser=enthalpy(R245fa,P=P\_economiser,x=0)

S\_economiser=entropy(R245fa,P=P\_economiser,x=0)

"4 After Boiler"

P\_boiler=P\_pump

T\_boiler= T\_1

H\_boiler=enthalpy(R245fa,P=P\_pump,x=1)

S\_boiler=entropy(R245fa,P=P\_pump,x=1)

"5 After Turbine"

"All data taken from Loss model"

" 6 After desuperheating Condenser"

P\_1=P1

P\_3 = P2

T\_1=T1

T\_3=T2

H\_3 = H2

H\_aftmidcondenser=enthalpy(R245fa,P=P\_3,x=1)

S\_aftermidcondenser=entropy(R245fa,P=P\_3,x=1)

T\_aftermidcondenser=entropy(R245fa,P=P\_3,x=1)

"Turbine Work Done"

W\_actual = MFRKgperSec \* (H1-H\_3)

"Pump Work Done"

W\_Pump = MFRKgperSec\*(H\_pump-H\_aftcondenser)

"Boiler Heat Energy Used"

Heat\_Boiler=MFRKgperSec\*(H\_boiler-H\_pump)

"Condenser Heat Energy Used"

Heat\_Cond = MFRKgperSec\*(H\_3-H\_aftcondenser)

Heat\_Cond1= MFRKgperSec\*(H\_3-H\_aftmidcondenser)

Heat\_Cond2= MFRKgperSec\*(H\_aftmidcondenser-H\_aftcondenser)

Heatdrop\_Cond = (H\_3-H\_aftcondenser)

Heatdrop\_Cond1= (H\_3-H\_aftmidcondenser)

Heatdrop\_Cond2= (H\_aftmidcondenser-H\_aftcondenser)

"Cycle Efficiency"

Efficiency\_cycle =W\_actual\*100/(Heat\_Boiler)

Superheat\_inlet = T\_1 - t\_sat(R245fa,P=P\_1)

Superheat\_outlet = T\_3 - t\_sat(R245fa,P=P\_3)